UNIVERSITY OF CALIFORNIA
RIVERSIDE

Fate, Transport, and Removal of Engineered Nanomaterials in the Aquatic Environment

A Dissertation submitted in partial satisfaction
of the requirements for the degree of

Doctor of Philosophy

in

Chemical and Environmental Engineering

by

Indranil Chowdhury

June 2012

Dissertation Committee:
Dr. Sharon L. Walker, Chairperson
Dr. Mark R. Matsumoto
Dr. Jay Gan

The Dissertation of Indranil Chowdhury is approved:

Committee Chairperson

University of California, Riverside

Acknowledgments

First of all, I would like to thank my advisor Dr. Sharon L. Walker for her great guidance and support throughout my PhD research. Without her enormous amount of time, effort and patience in advising me from the beginning to end of my doctoral research, my dissertation was not possible at all. Her excellent mentoring and pursuit for perfection always drove me to get better in my research throughout my program.

I would also like to thank my all of my dissertation committee members for their comments and valuable suggestions: Professor Mark R. Matsumoto (Chemical and Environmental Engineering, UCR) and Professor Jay Gan (Environmental Science, UCR). I would also like to thank Dr. David M. Cwiertny (Civil and Environmental Engineering, The University of Iowa) for his helpful suggestions and collaboration in my doctoral research.

My sincere appreciation goes to all of our collaborators including Dr. Arturo A. Keller (University of California, Santa Barbara), Dr. Patricia Holden (University of California, Santa Barbara), Dr. Lutz Mädler (University of Bremen, Germany), Dr. Suman Pokhrel (University of Bremen, Germany), Dr. Mark C. Hersam (Northwestern University), Dr. David M. Cwiertny (The University of Iowa), Dr. Steven E. Mylon (Lafayette College, PA) and Dr. Jeffrey Zink (University of Caliornia, Los Angeles). I would also like to thank Dr. Yadong Yin (UCR), Dr. Tanapon Phenrat (Naresuan University, Thailand), Dr. Scott Bradford (USDA-ARS Salinity Laboratory), Dr. Zhaoxia

Ji (University of California, Los Angeles) and Dr. Wilfred Chen (University of Delaware, Delaware) for their help in different parts of my PhD research.

I am also grateful to numerous former and current members from Dr. Walker lab group, particularly Dr. Yongsuk Hong, Dr. Gexin Chen, Dr. Hyun Jung "Nick" Kim, Dr. Berat Haznedaroglu, Dr. Amy Gong, Olgun Zorlu, Ian Marcus and Ryan J. Honda. Special thanks to the undergraduate researchers worked with me including Chad Thomson, James Kim, Jose Valle and Elizabeth Horstman. I would like to extend my thanks to the professors in the CEE Department and staff members for their excellent support. I am also grateful to my MS advisor Dr. David A. Dzombak (Civil and Environmental Engineering, Carnegie Mellon University, PA) and Dr. M. Ashraf Ali (Civil Engineering, Bangladesh University of Engineering and Technology, Bangladesh) for their excellent mentoring.

Finally, I would like to thank my parents and family for their kind support and sacrifice throughout my doctoral program.

The research was primarily supported by the University of California Center for the Environmental Implications of Nanotechnology (National Science Foundation and Environmental Protection Agency under Cooperative Agreement # DBI-0830117). Other sources were UCR Dissertation Year Program fellowship and Graduate Dean's Dissertation Research Grant.

Dedication

This dissertation is dedicated to my family including my mother, brothers, and to my late father Promode Kanti Chowdhury for their sacrifice and inspiration.

ABSTRACT OF THE DISSERTATION

Fate, Transport, and Removal of Engineered Nanomaterials
In the Aquatic Environment

by

Indranil Chowdhury

Doctor of Philosophy, Graduate Program in Chemical and Environmental Engineering
University of California, Riverside, June 2012
Dr. Sharon L. Walker, Chairperson

The overall goal of this research was to identify the mechanisms involved in the fate, transport, and removal of nanomaterials in both natural and engineered systems. The project was developed based upon the hypothesis that nanomaterial properties (type, size, shape) and environmental parameters including solution chemistry (pH, ionic strength, and ion valence), as well as the presence of natural organic matter (NOM) and bacteria will control the transport and removal of nanomaterials. Nine different nanomaterials were used including three metal oxides, three sizes of TiO_2 and three types of single walled carbon nanotubes(SWNTs). Wide variation in physicochemical properties among these nanomaterials allowed the comparison with respect to size, shape, type, and synthesis method. Complementary transport studies were conducted in both macroscopic (column) and microscopic (flow cells) systems.

This dissertation work has allowed for the following critical observations to be made. Sonication, nanoparticle concentration and solution chemistry can significantly alter physicochemical properties of metal oxide nanoparticles to ensure reproducible

dispersion of metal oxide nanoparticles for transport and toxicity studies. Transport of TiO_2 nanoparticles (TNPs) through macroscopic porous media showed that a combination of mechanisms including straining, blocking, DLVO and hydrodynamic forces were involved. Additionally experiments in the parallel plate chamber indicated that deposition of TNPs was controlled by a combination of DLVO and non-DLVO-type forces, aggregation, shear and gravitational forces. Also, the presence of both NOM and bacteria resulted in much less deposition than NOM or bacteria alone, indicating a combination of factors involved in deposition including electrosteric, electrostatic effects, and aggregation state of TNPs and TNP-bacteria. Another study with three distinctly sized TNPs revealed that heterogeneity in the nanoparticle aggregate – due to its composition of primary nanoparticles – plays a significant role in the transport and aggregate breakup. Finally, SWNTs synthesized by different methods resulted in distinctive breakthrough curves due to catalysts used in synthesis, whereas metal content of SWNTs affects the relative elution of SWNTs through column. This collection of studies suggests that consideration of these mechanisms is necessary to improve our ability to predict fate, transport and removal nanomaterials in the aquatic environments as well as set-up environmental regulations.

Table of Contents

List of Figures

List of Tables

Chapter 1

Introduction

1.1 Motivation and Background

Human advancement is usually defined by the materials used in different ages including stone, bronze, iron ages and recently the silicon age. Technology to fabricate materials at the nanoscale is ushering a new era of advanced materials, which hold the promise of creating new techniques to manufacture devices and develop advanced information technology. The capacity of building materials at the nanolevel is fundamentally changing the way materials and devices are produced, as large surface to volume ratio provides nanomaterials very unique properties from their bulk counterparts (1, 2,3). Commercial applications of nanomaterials range from drug delivery, electronics, cosmetics, textiles, water purification and environmental remediation (4, 5).

Most commonly used nanomaterials are metal and carbon-based materials. Metal oxide nanomaterials including titanium dioxide (TiO_2) and zinc oxide (ZnO) have made their way into personal care products and catalytic applications (4,6). Nano silver, primarily known for antibacterial properties, is used in approximately 20% of the nanomaterial containing products in US (7). Quantum dot (QD) is another type of nanomaterial, which is usually made of core materials as CdTe, CdSe, ZnSe, or PbSe with zinc or cadmium sulfide shells (8). Quantum dots have been used extensively due to their optical properties (9). One of the most widely used nanomaterials is magnetic nanostructure used in data storage devices (10), audio speakers (11) and drug delivery (12). Fe_xNi_{1-x} alloys with different compositions have also been utilized in many

industrial fields including magnetic recording heads (13) and precision instruments such as shadow masks for color televisions (14, 15).

Carbon based nanomaterials are also widely used nanostructures, which are particularly desirable for their mechanical, electrical, optical and thermal properties (16). These materials can be synthesized in a variety of shapes and sizes including C_{60} "bucky balls", carbon nanotubes and graphenes (16, 17). While fullerene is spherical carbon-based nanomaterial, both single walled and multi walled carbon nanotubes (SWNT and MWNT, respectively) can be synthesized with nanometer in diameter but typical lengths on the micron scale (16). Graphene, on the other hand, is basically two dimensional nanostructure with nanometer in thickness (16).

Environmental remediation and membrane applications are emerging areas for nanomaterial applications. Nanosorbents, nanocatalysts, and nanostructured membranes to nanoparticles enhanced filtration have been reported to be used in the water and wastewater treatment (18). For example, the high adsorption capacity of nanoscale magnetite and maghemite has been utilized to remove arsenic from water (2, 19). Iron based nanoparticles like zero-valent iron have been used for groundwater remediation (20, 21). Carbon-based nanomaterials including carbon nanotubes and fullerenes can adsorb heavy metals and organics (23).

Nanomaterial-based industries are growing exponentially due to the rapid rise of information technology and advanced materials. For example, TiO_2 is one of the most widely used nanomaterials with production rate of 40,000 metric tons/year in US (24).

With this rapid production, nanomaterials will be ubiquitous in both the natural and engineered environments in future and has created notable concern with environmental regulators (25) and industrial associations (26). Recent studies found TiO_2 nanoparticles in wastewater effluent and biosolids (27). Nanosilver and carbon nanotubes have been reported to be present in wastewater (28). Release of nanosilver from fabrics used for sock production was reported by Benn and Westerhoff (7). Due to the growing concern of potential risks from exposure to nanomaterials, both National Science Foundation and U.S. Environmental Protection Agency have committed more than $25 million since 2002 to determine the environmental sustainability of nanotechnology (25).

Toxicity of different nanomaterials is being investigated to understand the interactions between nanomaterials and organisms. Small size and high surface areas of nanomaterials provide higher toxic potential at the nanolevel (3). Metal oxide nanomaterials (ZnO and TiO_2) showed cytotoxic to cytoprotective towards organisms (29). Toxicity studies of carbon-based nanomaterials revealed that fullerene showed toxicity to fish and humans (4), while carbon nanotubes are reported as cytotoxic to bacteria and mice (30,31). The toxicity of nano-TiO_2 is primarily attributed to the oxidative stress generated from the photoreactivity of these nanomaterials (32). Both colloidal and ionic forms of nanosilver have been found to be toxic to bacteria (7). Toxicity of QDs is mainly generated from the release of cadmium from the core (8,9).

Fate and transport of these emerging contaminants in the environment will govern their toxic exposure towards living organisms. Only a few studies have been done to

understand fate, transport and removal processes of different nanomaterials in both natural and engineered environments. Chen et al. (33, 34) investigated the transport mechanisms of fullerene nanomaterials in the aquatic environments through aggregation and deposition studies. Phenrat et al. (20, 35, 36) observed the role of magnetic properties on the transport of iron oxide nanomaterials. In the engineered system, Kiser et al. (27) conducted research on the capacity of our current wastewater facilities to remove TiO_2 and observed that most of nanomaterials were found in biosolids. Study on transport of nano-TiO_2 through porous media (37) reported that electrostatic forces were the dominant factors in the filtration of TiO_2. These few publications have by no means answered comprehensively the question of what mechanisms control nanoparticle fate.

Nanotechnology has great potential to improve environmental quality and water treatment. Usage of nanomaterials in membranes, adsorption and catalysis can revolutionize the water treatment technologies. While most of industries are embracing nanotechnology in the manufacturing processes for the novel properties of nanomaterials, natural waters and ecosystems will likely face unknown consequences from the introduction of these advanced materials in the environment. Moreover, unique size, shape and properties of nanomaterials may challenge the engineered systems, as the current treatment facilities did not consider these anthropogenic contaminants in design. Environmental monitoring and regulations will also be challenging task for the rapid growth of numerous nanomaterials. Furthermore, environmental degradation is quite possible from manufacturing, usage and disposal of nanomaterials. Although the

potential for nanotechnology in environmental engineering is immense, the challenge is to ensure the sustainable development of nanotechnology instead of future environmental liability. Understanding the fate, transport and removal processes is essential for regulation, and monitoring the potential contaminants generated from this nanotechnology. It is clear there is a need for preventative steps for monitoring, regulating and removal of nanomaterials and the policy to ensure that these steps are implemented based upon best science available. Hence, this doctoral research addresses fundamental mechanisms involved in the fate, transport and removal of nanoparticles in both the natural and engineered environments and fills the current gap in both literature and the knowledge base.

1.2 Objective and Scope

The overall goal of this research was to shed a light on the fundamental mechanisms involved in the transport and removal of nanomaterials in both natural and engineered systems, which can be useful for both regulatory and treatment perspectives of these emerging contaminants. Figure 1.1 summarizes the overall research framework. It was hypothesized that transport and removal of engineered nanomaterials will be governed by nanomaterial physicochemical properties and environmental parameters including solution chemistry (pH, ionic strength, and ion valence), as well as the presence of natural organic matter (NOM) and bacteria. In this PhD research, both metal oxide and carbon-based nanomaterials were used including three different metal oxides (TiO_2,

CeO_2, ZnO), three differently sized TiO_2 (6, 13, 23 nm) and three differently synthesized single walled carbon nanotubes (HiPco-D, SG65-D, P2-D) (Figure 1.2). Fate and transport of these nanomaterials can be compared with respect to size, shape, types, and synthesis methods due to the wide variation in physicochemical properties. Solution chemistry was utilized in this research to simulate natural and engineered environments including pH 5-7, ionic strength (0.1-100 mM), ion valence (K^+, Ca^{2+}) and presence of bacteria (10^7 cells/mL) and NOM (1 mg/L). Outcomes of this study will allow us to understand the mechanisms involved in the transport of nanomaterials in the environment, which will improve our ability to predict the fate, transport and removal of nanomaterials in both natural and engineered environments.

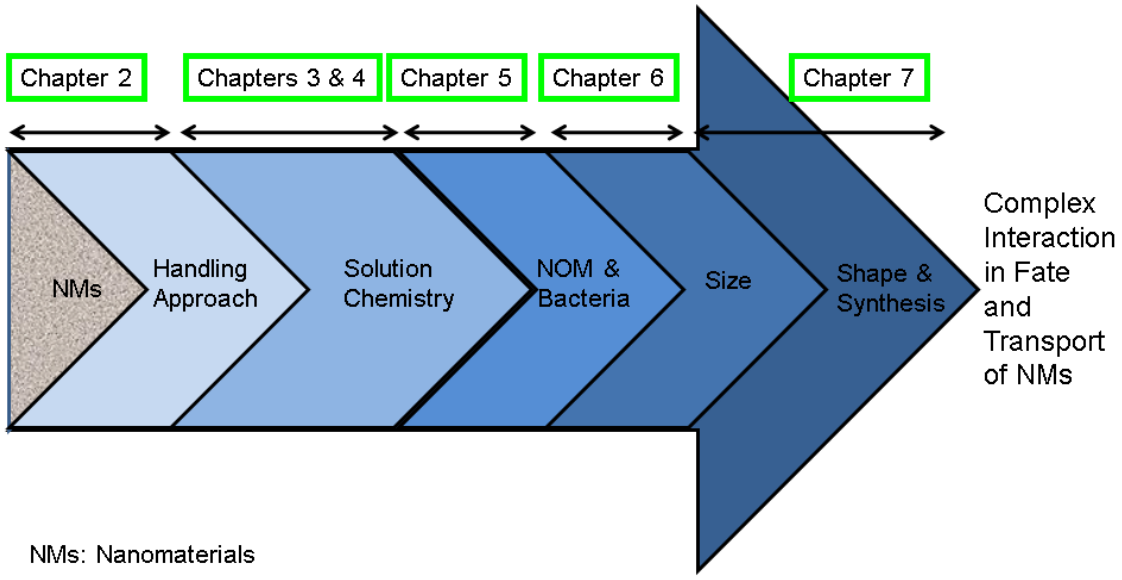

Figure 1.1. Overall research framework

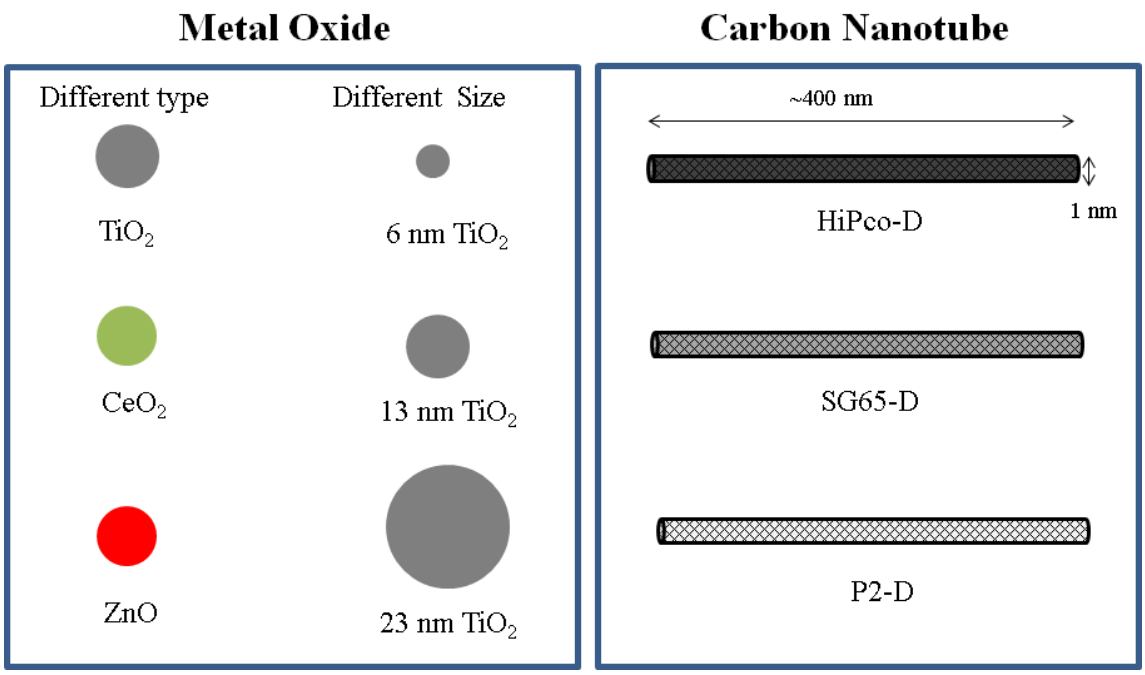

Figure 1.2. Nanomaterials used in this study. HiPco-D, SG65-D and P2-D are three differently synthesized single walled carbon nanotubes as mentioned in Chapter 7.

1.2.1 Hypotheses and Specific Objectives

To achieve the overall goal of this doctoral research, the hypotheses and specific objectives were developed and are presented below (note that each specific objective has been addressed in a chapter of this dissertation):

Hypothesis 1: Physicochemical characteristics of metal oxide nanomaterials are dependent on the handling approach to disperse nanomaterials in an aqueous suspension, which can influence their transport.

The specific objective of this study was to develop a dispersion protocol for metal oxide nanomaterials, which can be used for reproducible transport and toxicity studies. Three commonly used metal oxide nanomaterials (TiO_2, CeO_2 and ZnO) were used to develop this handling approach (38). For this study, optimum dispersion time was determined by varying the sonication time over a wide range of nanomaterial concentration. Influence of nanomaterial concentration on the solution chemistry was also investigated in this study (Chapter 2).

Hypothesis 2: Solution chemistry, nanoparticle concentration, and hydrodynamic conditions will influence the transport of nanoparticles through porous media by influencing the surface charge, size and hydrodynamic forces on the nanoparticles.

To test this hypothesis, the specific objective was set to determine the mechanisms involved in the transport of TiO_2 nanoparticles through porous media. After developing the dispersion protocol, the purpose of this study was to determine how this handling approach can ultimately affect the transport. In this study, transport experiments were carried out in a saturated packed-bed column over a wide range of TiO_2 concentration (100-800 mg/L) and solution chemistry including pH (pH 5 and 7) and ionic strength (1 and 10 mM) (39-41) (Chapter 3).

Hypothesis 3: Deposition of nanoparticle on the collector surface will be governed by aggregate formation.

The specific objective was to develop a novel microscope-based technique for nanoparticle deposition study in the parallel plate system. This study was primarily motivated by the results observed in Chapter 3, which showed that aggregate formation is one of the most dominant factors in the transport of metal oxide nanomaterials. In this study, further investigation was carried out to determine how this aggregate formation can affect the physicochemical properties of aggregates and subsequently interaction with collector surfaces in the parallel plate chamber. In this study, a microscope-based technique was utilized to understand the fundamental mechanisms involved in the deposition of TiO_2 nanoparticles. Transport and deposition studies were conducted in a parallel plate (PP) flow chamber with TNP labeled with fluorescein isothiocyanate (FITC) for visualization (Chapter 4).

Hypothesis 4: Both natural organic matter and bacteria will affect the aggregation state of nanomaterials, which subsequently can affect the transport.

To test this hypothesis, the specific objective was to determine the mechanisms involved in the combined role of bacteria and natural organic matter in transport and removal of nanomaterials. Based on the previous studies (Chapters 3 and 4), it has been found that aggregate formation is the most dominant factor in the transport of metal oxide nanomaterials. In this study, the purpose was to investigate how two most common natural parameters (NOM and bacteria) can influence the nanoparticle aggregate and

subsequent transport. In this study, transport experiments with TiO_2 nanoparticles were conducted in a microscopic parallel plate system and a macroscopic packed-bed column using fluorescently tagged *E. coli* as a model organism and Suwannee River Humic Acid as a representative NOM (Chapter 5).

Hypothesis 5: Nanoparticle aggregates with different primary particle size can form similarly sized aggregates; however, the heterogeneity of particle size within the aggregate will affect the deposition in several ways including stability and interactions with surfaces.

The objective was set to determine the role of primary particle size on nanoparticle aggregate formation and transport. From the earlier studies, it was revealed that aggregate formation is critical parameter controlling the nanoparticle transport. To further analyze the aggregate transport, this study seeks to understand what role the primary particle size within aggregate will play in the transport. In this study, three distinctly sized TNPs (6, 13, 23 nm) were synthesized using flame spray pyrolysis. Aggregate formation and transport behavior of TiO_2 nanoparticle aggregates were evaluated in the column packed with quartz sand over a range of solution chemistries and natural organic matter presence (Chapter 6).

Hypothesis 6: Synthesis methods and purifications will affect the transport of single walled carbon nanotubes in the aquatic environment by influencing the physicochemical properties of nanotubes.

The specific objective was to evaluate the influence of synthesis methods and purifications in the transport of single walled carbon nanotubes. In this study, a systematic approach was followed to investigate the fate and transport of single walled carbon nanotubes (SWNTs) from synthesis to environmentally relevant conditions. Three widely used SWNT synthesis methods have been investigated in this study including high pressure carbon monoxide (HiPco), chemical vapor deposition (CVD) and electric arc discharge technique (EA) (Chapter 7).

1.2.2 Experimental Approach

This doctoral research involved extensive characterization and transport studies using model nanomaterials (TiO_2, CeO_2, ZnO and carbon nanotubes), NOM (humic acids), and bacteria (*E. coli*). Characterization techniques including electrokinetic characterization, particle size by dynamic light scattering, aggregate morphology by static light scattering, potentiometric titration, transmission electron microscopy (TEM) and environmental scanning electron microscopy were utilized to understand the physicochemical properties of nanomaterials. Stability of nanomaterials in aqueous suspension was determined by a combination of aggregation and sedimentation tests. For bacteria, additional characterization was done including evaluation of extracellular

polymeric substance content, cell size, and hydrophobicity. Transport studies were conducted in both macroscopic (packed-bed column) and microscopic (flow cells) systems with fluorescently labeled nanoparticles (green FITC coating) and bacteria (red mCherry plasmid). In the column, deposition rates of nanoparticles were determined from breakthrough curves. In the flowcell, deposition of nanoparticles was determined by taking real time images of deposited nanoparticles and bacteria with a fluorescent microscope.

1.3 Organization of the Dissertation

This whole dissertation is composed of eight chapters including the Introduction (Chapter 1) and Conclusion (Chapter 8). Following the Introduction, Chapter 2 describes the impact of experimental handling approach on the state of model nanoparticles, from the container of dry particles to the characterization of suspended particles. Specifically, the effects of sonication, nanoparticle concentration, and ionic strength upon the size, electrophoretic mobility, and stability of the model metal oxides (TiO_2, CeO_2 and ZnO) were investigated. It was found that duration of sonication has significant effect on dispersion of metal oxide nanomaterials. In addition, the nanoparticle concentration showed a notable role on the solution chemistry. This dispersion protocol is thoroughly described in Chapter 2 entitled, "Container to Characterization: Impacts of Metal Oxide Handling, Preparation, and Solution Chemistry on Particle Stability".

Chapter 3, entitled "Mechanisms of TiO_2 Nanoparticle Transport in Porous Media: Role of Solution Chemistry, Nanoparticle Concentration, and Flowrate" investigates the role of solution chemistry, nanoparticle concentration and hydrodynamic effects in the transport and deposition of TiO_2 nanoparticles through porous media. Solution chemistry including pH and ionic strength showed a significant influence on the transport due to their involvement in the aggregation of the nanoparticles and interaction with quartz sand. Overall, a combination of mechanisms including straining, blocking, and DLVO-type forces (combination of Van der Waals and electrostatic forces) were involved over the range of solution chemistry and nanoparticle concentrations tested.

Chapter 4, entitled "Deposition Mechanisms of TiO_2 Nanoparticles in a Parallel Plate System" describes a novel microscope based approach for investigating nanoparticle deposition. In this study, a microscope-based technique was utilized to understand the fundamental mechanisms involved in the deposition of TiO_2 nanoparticles. Transport and deposition studies were conducted in a parallel plate (PP) flow chamber with TiO_2 nanoparticle labeled with fluorescein isothiocyanate (FITC) for visualization. This study revealed that attachment of FITC-labeled TiO_2 nanoparticles on surfaces was a function of a combination of parameters, including ionic strength (IS), pH and flowrate. Comparisons between experimental and theoretical approximations indicate that non-DLVO type forces also play a significant role.

Chapter 5, entitled "Combined Factors Influencing the Aggregation and Deposition of nano-TiO_2 in the Presence of Humic Acids and Bacteria" highlights the

contributions of natural organic matter and bacteria to the aggregation and deposition of TiO_2 nanoparticles (TNPs) in the aquatic environments. In this study, transport experiments with TiO_2 nanoparticles were conducted in a microscopic parallel plate system (used in Chapter 4) and a macroscopic packed-bed column (used in Chapter 3) using fluorescently tagged *E. coli* as a model organism and Suwannee River Humic Acid as a representative NOM. Notably, TiO_2 nanoparticles were labeled with FITC (as mentioned in Chapter 4) allowing particles and cells to be simultaneously visualized with a fluorescent microscope. Results from both experimental systems revealed that interactions among TiO_2 nanoparticles, NOM and bacteria exhibited a significant dependence on solution chemistry (pH 5 and 7) and ion valence (K^+ and Ca^{2+}), and that these interactions subsequently affect nanoparticle deposition. Nanoparticle transport in the presence of both NOM and *E. coli* resulted in much less deposition than in the presence of NOM or *E. coli* alone, indicating a complex combination of interactions involved in stabilization.

Chapter 6, entitled "Influence of Primary Particle Size on Nano-TiO_2 Aggregate Formation and Transport" set out to determine the influence of primary particle size on the aggregate formation and transport of TiO_2 nanoparticles through porous media. Three distinctly sized TiO_2 nanoparticles (6, 13, 23 nm) were synthesized using flame spray pyrolysis. Aggregate formation and transport behavior of TNP aggregates were evaluated in the column packed with quartz sand over a range of solution chemistries and natural organic matter presence. Transport results revealed deposition rates of TNP

aggregates composed with three distinctly sized primary nanoparticles were significantly different, even though the aggregate size and electrokinetic properties of these particles were similar. The size of primary nanoparticles was demonstrated to play a dramatic role on the aggregate breakup process. Primary nanoparticle size as well as surface area effected the aggregate density, surface roughness, hydrodynamic force and strength, which subsequently impacts the transport of TNP aggregates.

Chapter 7, entitled "Impact of Synthesis and Purification Methods on the Transport of Single Walled Carbon Nanotubes in the Aquatic Environments" investigates the fate and transport of single walled carbon nanotubes (SWNTs) from synthesis to environmentally relevant conditions. Three widely used SWNT synthesis methods were investigated in this study including high pressure carbon monoxide (HiPco), chemical vapor deposition (CVD) and electric arc discharge technique (EA). This study related the transport of three SWNTs (HiPco-D, SG65-D and P2-D) with different synthesis methods and residual catalyst content revealing their influence on the subsequent fate of the nanoparticles. To eliminate the heterogeneity in nanotube length and diameter, a sample preparation procedure was utilized by dispersing SWNTs using biocompatible triblock copolymer Pluronic, which allowed the comparison in the transport trends among these SWNTs. Overall SWNTs synthesized by different methods resulted distinctive breakthrough curves due to catalysts used in synthesis, whereas metal content of SWNTs affected the relative elution of SWNTs through column.

Chapter 8, entitled “Summary and Conclusions” summarizes the findings from this PhD research. Most of the work in this dissertation has already been published, while most recent studies are still under review in refereed journals. Below is a list of manuscripts, which have been resulted from this research:

1. Chowdhury, I., Hong, Y., Walker, S. L. (2010) Container to Characterization: Impacts of Metal Oxide Handling, Preparation and Solution Chemistry on Particle Stability, *Colloids and Surfaces A: Physicochemical and Engineering Aspects*, 368(1-3): 91-95.
2. Chowdhury, I., Hong, Y., Honda, R., Walker, S. L. (2011) Mechanisms of TiO_2 Nanoparticles Transport in Saturated Porous Media: Role of Solution Chemistry, Nanoparticle Concentration and Flow rate, *Journal of Colloid and Interface Science*, 362 (2): 548-555.
3. Chowdhury, I. and Walker, S. L. (2012) Deposition Mechanisms of TiO_2 Nanoparticles in a Parallel Plate System, *Journal of Colloid and Interface Science*, 369 (1), 16-22.
4. Chowdhury, I., Cwiertny, D. M. and Walker, S. L. (2012) Combined Factors Influencing the Aggregation and Deposition of nano-TiO_2 in the Presence of Humic Acid and Bacteria, *Environmental Science and Technology*. doi/abs/10.1021/es2034747.

5. Chowdhury, I., Pokhrel, S., Mädler, L., Mylon, S. E. and Walker, S. L. (2012) Influence of Primary Particle Size on Nano-TiO_2 Aggregate Formation and Transport, *Environmental Science and Technology* (in preparation).
6. Chowdhury, I., Duch, M. C., Gits, C. C., Hersam, M. C. and Walker, S. L. (2012) Impact of Synthesis and Purification Methods on the Transport of Single Walled Carbon Nanotubes in the Aquatic Environments, *Environmental Science and Technology* (in preparation).

1.4 References

(1) Alivisatos, A. P., Semiconductor Clusters, Nanocrystals, and Quantum Dots. *Science* **1996,** *271*, (5251), 933-937.

(2) Park, H.; Ayala, P.; Deshusses, M. A.; Mulchandani, A.; Choi, H.; Myung, N. V., Electrodeposition of maghemite (gamma-Fe2O3) nanoparticles. *Chemical Engineering Journal* **2008,** *139*, (1), 208-212.

(3) Nel, A.; Xia, T.; Madler, L.; Li, N., Toxic Potential of Materials at the Nanolevel. *Science* **2006,** *311*, (5761), 622-627.

(4) Wiesner, M. R.; Lowry, G. V.; Alvarez, P.; Dionysiou, D.; Biswas, P., Assessing the Risks of Manufactured Nanomaterials. *Environmental Science & Technology* **2006,** *40*, (14), 4336-4345.

(5) Dunphy Guzman, K. A.; Taylor, M. R.; Banfield, J. F., Environmental Risks of Nanotechnology: National Nanotechnology Initiative Funding, 2000-2004. *Environmental Science & Technology* **2006,** *40*, (5), 1401-1407.

(6) Chen, Z.; Westerhoff, P.; Herckes, P., Quantification of C60 Fullerene Concentrations in Water. *Environmental Toxicology and Chemistry* **2008,** *27*, (9), 1852-1859.

(7) Benn, T. M.; Westerhoff, P., Nanoparticle Silver Released into Water from Commercially Available Sock Fabrics. *Environmental Science & Technology* **2008,** *42*, (11), 4133-4139.

(8) Zhang, Y.; Chen, Y.; Westerhoff, P.; Crittenden, J. C., Stability and Removal of Water Soluble CdTe Quantum Dots in Water. *Environmental Science & Technology* **2008,** *42*, (1), 321-325.

(9) Mahendra, S.; Zhu, H.; Colvin, V. L.; Alvarez, P. J., Quantum Dot Weathering Results in Microbial Toxicity. *Environmental Science & Technology* **2008,** *42*, (24), 9424-9430.

(10) Sharrock, M. P., Particulate magnetic recording media: a review. *Magnetics, IEEE Transactions on* **1989,** *25*, (6), 4374.

(11) Miller, M. M.; Prinz, G. A.; Cheng, S. F.; Bounnak, S., Detection of a micron-sized magnetic sphere using a ring-shaped anisotropic magnetoresistance-based sensor: A model for a magnetoresistance-based biosensor. *Applied Physics Letters* **2002,** *81*, (12), 2211.

(12) Rudge, S. R.; Kurtz, T. L.; Vessely, C. R.; Catterall, L. G.; Williamson, D. L., Preparation, characterization, and performance of magnetic iron-carbon composite microparticles for chemotherapy. *Biomaterials* **2000,** *21*, (14), 1411.

(13) Zech, N.; Podlaha, E. J.; Landolt, D., Rotating cylinder Hull cell study of anomalous codeposition of binary iron-group alloys. *Journal of Applied Electrochemistry* **1998,** *28*, (11), 1251.

(14) Shiga, M., Invar alloys. *Current Opinion in Solid State and Materials Science* **1996,** *1*, (3), 340.

(15) Jiao, Q.-Z.; Tian, Z.-L.; Zhao, Y., Preparation of nickel hydroxide nanorods/nanotubes and microscopic nanorings under hydrothermal conditions. *Journal of Nanoparticle Research* **2007,** *9*, (3), 519.

(16) Mauter, M. S.; Elimelech, M., Environmental Applications of Carbon-Based Nanomaterials. *Environmental Science & Technology* **2008,** *42*, (16), 5843-5859.

(17) Wiesner, M. R.; Hotze, E. M.; Brant, J. A.; Espinasse, B., Nanomaterials as possible contaminants: the fullerene example. *Water Science and Technology* **2008,** *57*, (3), 305-310.

(18) Savage, N.; Diallo, M. S., Nanomaterials and water purification: Opportunities and challenges. *Journal of Nanoparticle Research* **2005,** *7*, (4-5), 331-342.

(19) Yavuz, C. T.; Mayo, J. T.; Yu, W. W.; Prakash, A.; Falkner, J. C.; Yean, S.; Cong, L.; Shipley, H. J.; Kan, A.; Tomson, M.; Natelson, D.; Colvin, V. L., Low-Field Magnetic Separation of Monodisperse Fe3O4 Nanocrystals. *Science* **2006,** *314*, (5801), 964-967.

(20) Phenrat, T.; Saleh, N.; Sirk, K.; Tilton, R. D.; Lowry, G. V., Aggregation and Sedimentation of Aqueous Nanoscale Zerovalent Iron Dispersions. *Environmental Science & Technology* **2007,** *41*, (1), 284-290.

(21) Saleh, N.; Kim, H.-J.; Phenrat, T.; Matyjaszewski, K.; Tilton, R. D.; Lowry, G. V., Ionic Strength and Composition Affect the Mobility of Surface-Modified Fe0 Nanoparticles in Water-Saturated Sand Columns. *Environmental Science & Technology* **2008,** *42*, (9), 3349-3355.

(22) Schrick, B.; Blough, J. L.; Jones, A. D.; Mallouk, T. E., Hydrodechlorination of Trichloroethylene to Hydrocarbons Using Bimetallic Nickel-Iron Nanoparticles. *Chemistry of Materials* **2002,** *14*, (12), 5140.

(23) Christian, P.; Von der Kammer, F.; Baalousha, M.; Hofmann, T., Nanoparticles: structure, properties, preparation and behaviour in environmental media. *Ecotoxicology* **2008,** *17*, (5), 326.

(24) Robichaud, C. O.; Uyar, A. E.; Darby, M. R.; Zucker, L. G.; Wiesner, M. R., Estimates of Upper Bounds and Trends in Nano-TiO2 Production As a Basis for Exposure Assessment. *Environmental Science & Technology* **2009,** *43*, (12), 4227-4233.

(25) Savage, N.; Thomas, T. A.; Duncan, J. S., Nanotechnology applications and implications research supported by the US Environmental Protection Agency STAR grants program. *Journal of Environmental Monitoring* **2007,** *9*, (10), 1046-1054.

(26) Fairbrother, A.; Fairbrother, J. R., Are environmental regulations keeping up with innovation? A case study of the nanotechnology industry. *Ecotoxicology and Environmental Safety* **2009,** *72*, (5), 1327-1330.

(27) Kiser, M. A.; Westerhoff, P.; Benn, T.; Wang, Y.; PeÌ • rez-Rivera, J.; Hristovski, K., Titanium Nanomaterial Removal and Release from Wastewater Treatment Plants. *Environmental Science & Technology* **2009,** *43*, (17), 6757-6763.

(28) Mueller, N. C.; Nowack, B., Exposure Modeling of Engineered Nanoparticles in the Environment. *Environmental Science & Technology* **2008,** *42*, (12), 4447.

(29) Xia, T.; Kovochich, M.; Liong, M.; Mädler, L.; Gilbert, B.; Shi, H.; Yeh, J. I.; Zink, J. I.; Nel, A. E., Comparison of the Mechanism of Toxicity of Zinc Oxide and

Cerium Oxide Nanoparticles Based on Dissolution and Oxidative Stress Properties. *ACS Nano* **2008,** *2*, (10), 2121-2134.

(30) Kang, S.; Pinault, M.; Pfefferle, L. D.; Elimelech, M., Single-Walled Carbon Nanotubes Exhibit Strong Antimicrobial Activity. *Langmuir* **2007,** *23*, (17), 8670-8673.

(31) Narr, J.; Viraraghavan, T.; Jin, Y. C., Applications of nanotechnology in water/wastewater treatment: A review. *Fresenius Environmental Bulletin* **2007,** *16*, (4), 320-329.

(32) Long, T. C.; Saleh, N.; Tilton, R. D.; Lowry, G. V.; Veronesi, B., Titanium Dioxide (P25) Produces Reactive Oxygen Species in Immortalized Brain Microglia (BV2): Implications for Nanoparticle Neurotoxicity. *Environmental Science & Technology* **2006,** *40*, (14), 4346-4352.

(33) Chen, K. L.; Elimelech, M., Aggregation and Deposition Kinetics of Fullerene (C60) Nanoparticles. *Langmuir* **2006,** *22*, (26), 10994-11001.

(34) Chen, K. L.; Elimelech, M., Interaction of Fullerene (C60) Nanoparticles with Humic Acid and Alginate Coated Silica Surfaces: Measurements, Mechanisms, and Environmental Implications. *Environmental Science & Technology* **2008,** *42*, (20), 7607-7614.

(35) Phenrat, T.; Song, J. E.; Cisneros, C. M.; Schoenfelder, D. P.; Tilton, R. D.; Lowry, G. V., Estimating Attachment of Nano- and Submicrometer-particles Coated with Organic Macromolecules in Porous Media: Development of an Empirical Model. *Environmental Science & Technology* **2010**, *44*, (12), 4531.

(36) Phenrat, T.; Kim, H.-J.; Fagerlund, F.; Illangasekare, T.; Tilton, R. D.; Lowry, G. V., Particle Size Distribution, Concentration, and Magnetic Attraction Affect Transport of Polymer-Modified Fe0 Nanoparticles in Sand Columns. *Environmental Science & Technology* **2009,** *43*, (13), 5079.

(37) Joo, S. H.; Al-Abed, S. R.; Luxton, T., Influence of Carboxymethyl Cellulose for the Transport of Titanium Dioxide Nanoparticles in Clean Silica and Mineral-Coated Sands. *Environmental Science & Technology* **2009,** *43*, (13), 4954-4959.

(38) Chowdhury, I.; Hong, Y.; Walker, S. L., Container to characterization: Impacts of metal oxide handling, preparation, and solution chemistry on particle stability. *Colloids and Surfaces A: Physicochemical and Engineering Aspects* **2010,** *368*, (1-3), 91-95.

(39) Chowdhury, I.; Hong, Y.; Honda, R. J.; Walker, S. L., Mechanisms of TiO2 nanoparticle transport in porous media: Role of solution chemistry, nanoparticle concentration, and flowrate. *Journal of Colloid and Interface Science* **2011,** *360*, (2), 548-555.

(40) Chen, G.; Hong, Y.; Walker, S. L., Colloidal and Bacterial Deposition: Role of Gravity. *Langmuir* **2009**. *26*, (1), 314-319.

(41) Crittenden, J. C.; Montgomery Watson, H., *Water treatment principles and design*. J. Wiley: Hoboken, N.J., 2005.

Chapter 2

Container to Characterization: Impacts of Metal Oxide Handling, Preparation, and Solution Chemistry on Particle Stability

Chowdhury, I., Hong, Y. Walker, S. L., Container to characterization: Impacts of metal oxide handling, preparation, and solution chemistry on particle stability. *Colloids and Surfaces A: Physicochemical and Engineering Aspects* **2010,** *368*, (1-3), 91-95.

Abstract

A study has been conducted to investigate the impact of experimental handling approaches on the state of model nanoparticles, from the container of dry particles to the characterization of suspended particles. Specifically, the effects of sonication, nanoparticle concentration, and ionic strength upon the size, electrophoretic mobility, and stability of the model metal oxides (TiO_2, CeO_2 and ZnO) were investigated. For initial breakup of dried nanoparticles in water, results indicate 30 min is the optimum sonication duration (120 W) all three metal oxide nanoparticles over the solution chemistry tested. Since aggregation is evident in metal oxide nanoparticles, sonication to achieve a proper dispersion of nanoparticles in solution is necessary prior to further experimentation. No more than 30 s sonication is needed for preparing well dispersed test sample from the diluted stock suspension. Effects of nanoparticle concentration on the solution chemistry were also studied. TiO_2 or CeO_2 addition can reduce pH with increase of nanoparticle concentration; whereas pH increases with ZnO concentration. Consideration of these parameters (effects of sonication, nanoparticle concentration, and solution chemistry) is necessary to ensure successful subsequent toxicity and transport studies.

2.1 Introduction

Nanotechnology is one of the fastest growing business sectors, predicted to grow to $1 trillion by 2015 (1). Commercial applications of nanomaterials range from drug delivery, electronics, cosmetics, textiles, and detergents (2, 3). With the rapid growth of nanoparticles usage, these materials have found their way in the environment (4-6). Though nanomaterials have been studied extensively for their wide range of applications, their fate, transport and toxicity is not well understood (7, 8).

Characterization is one of the main challenges for fate, transport and toxicity studies of nanomaterials (9). Fate and transport of these nanomaterials in an aquatic environment will be governed by these properties and how they impact nanoparticle stability in aqueous suspensions. For example, particle size, size distribution, and stability in cell culture media have been found to control the toxic potential (10). Though different protocols have been developed for extensive characterization of nanomaterials, lack of reproducible dispersion of dry nanomaterials in environmental media may pose challenges to get consistent results in fate, transport and toxicity studies (10-12). Even in industrial applications, the lack of reproducibility in characterization of nanomaterials can impede quality control of nanomaterial-based products (13).

Sonication is commonly used for the dispersion of nanoparticles in suspension (14-16); however, the range of time that the dispersion is sonicated varies considerably (14-16). Sonication time varied from as low as 1 min to 3 hours using both bath and probe sonicators and various approaches were followed for preparation of nanoparticle suspension by sonication (14-16). Sonication can change the agglomeration of

nanomaterials as well as surface properties which can consequently affect toxicity studies (17). Hence, in order to get reproducible results for transport and toxicity studies, linking the nanoparticle preparation and handling to physical-chemical properties is critical. It is essential to understand how handling procedures impact subsequent characterization and studies so that results can properly inform and allow for consistent protocol development; and hence the rationale behind this particular study. The impact of three experimental handling approaches (resuspension via sonication, solution ionic strength, and nanoparticle concentration) on the state of model metal oxides has been investigated and the resultant nanoparticles have been characterized as a function of the size, electrophoretic mobility, and stability. titanium dioxide (TiO_2), cerium dioxide (CeO_2) and zinc oxide (ZnO) were selected as they are commonly used metal oxide nanomaterials in a wide array of applications including sunscreens, catalyst, gasoline additives, and polymer filters (3, 18-20). The detailed analyses of these three metal oxide nanoparticles is discussed along with recommendations for particle handling to ensure a reproducible, consistent suspension of particles.

2.2 Materials and Methods

2.2.1 Metal Oxide Nanoparticle Stock Solution and Test Sample Preparation

Titanium dioxide (Evonik Degussa Coorporation, NJ), cerium dioxide (Meliorum Technologies, NY) and zinc oxide (Meliorum Technologies, NY) nanoparticles were used in all experiments. According to the manufacturers, all the materials were more than

99.5% pure. The reported primary particle size for TiO_2, CeO_2 and ZnO were 21 nm, 10 nm and 10 nm, respectively. The detailed physicochemical characteristics of these model metal oxide nanoparticles were mentioned elsewhere (21). To prepare the nanoparticle suspension, an amount of dry nanoparticles was added to the background solution (nanopure water at >18.2 MΩ at 25^{o}C or electrolyte solution) and stirred with a magnetic stir bar for 1 minute. The concentration of nanoparticle stock suspension was 200 mg/L in these experiments. For initial breakup of dry nanoparticles into solution, sonication was employed in a water bath at 120 W (Transsonic 460/H, Barnstead/Lab-line, Melrose Park, IL). Sonication time was initially varied to identify the ideal sonication time needed to obtain a well- dispersed suspension. A sonication time of 30 minutes was employed for creating stock solutions for all subsequent experiments.

After preparing the stock solution of nanoparticles with the 30 minute sonication step, the stock was used to make a diluted suspension in the desired electrolyte. The concentration of nanoparticle test suspension was 100 mg/L in these experiments. Following the addition of the stock suspension into the background electrolyte, the unadjusted pH of these test samples were 5.21, 5.38, and 7.59 for TiO_2, CeO_2, and ZnO at nanoparticle concentration of 100 mg/L respectively. The test sample was sonicated again prior to experiment to minimize aggregation. Sonication time was varied to optimize the length of sonication needed to achieve a well-dispersed suspension. A sonication time of 30 s for the test sample was employed for all subsequent experiments.

2.2.2 Nanoparticle Characterization

Electrokinetic characterization was measured over a wide range ionic strength (0.1-100 mM KCl, Fisher, ACS reagent grade) and nanoparticle concentration (10-1000 mg/L) using a ZetaPALS analyzer (Brookhaven Instruments Corp., Holtsville, NY). Prior to each experiment, electrolyte solutions were filtered through 100 nm filters (Anotop 25, Whatman, Middlesex, UK) to eliminate any possible contamination. During these characterization techniques, the pH of the test samples was unadjusted.

Hydrodynamic diameter was measured by using dynamic light scattering (DLS, Brookhaven model BI-9000AT digital correlator, Holtsville, NY) at a wavelength of 661 nm (15 mW solid-state laser) and a scattering angle of 90°. Average hydrodynamic diameter was determined by taking an arithmetic average of 10 runs for 3 separate samples, with each run involving a measurement taken as an average over 30 s.

2.3 Results and Discussion

2.3.1 Effects of Sonication

In order to determine the optimal sonication time for complete suspension of dry metal oxide nanoparticles when put in an aqueous solution, different sonication times (0-60 min) were tested for 200 mg/L TiO_2, CeO_2 and ZnO nanoparticles at 1 mM KCl (Figure 2.1). For all three nanoparticles, the initial hydrodynamic diameter measured decreased with longer periods of sonication over the course of the first thirty minutes. However, beyond 30 minutes, the hydrodynamic diameter began to increase with further

sonication. The magnitude of the change in hydrodynamic diameter differs between particle types, although the overall trend is the same. Hence, for metal oxide nanoparticles under the low ionic strength solution conditions tested, a 30 minute sonication after the addition of dry nanoparticles to solution appears to be the optimum to ensure a well-dispersed nanoparticle suspension. All subsequent experiments in this study involved the preparation of stock solution with the 30 min sonication step.

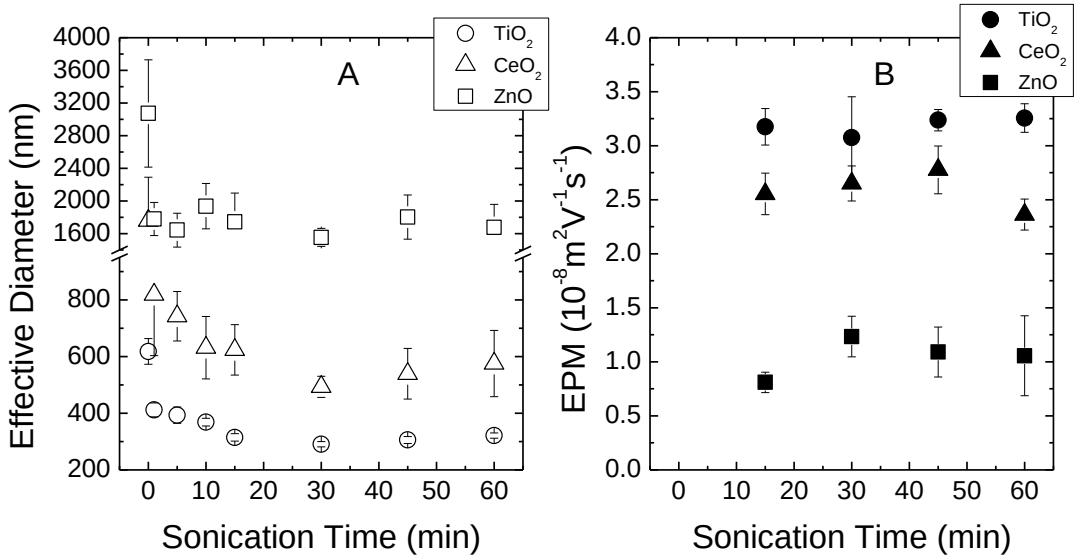

Figure 2.1. Effects of sonication duration on TiO_2, CeO_2 and ZnO nanoparticles stock solutions A) particle size (hydrodynamic diameter) and B) electrophoretic mobility (EPM). Measurements conducted at a nanoparticle concentration of 200 mg/L, unadjusted pH (5.14, 5.28, and 7.85 for TiO_2, CeO_2, and ZnO, respectively), 1 mM ionic strength (KCl), and temperature (25^{o}C).

It is not entirely clear why the hydrodynamic diameter increases after the 30 min sonication, particularly as the temperature in the water bath was maintained at 20-25^{o}C

by frequently adding ice in the sonication bath during sonication. Though sonication can significantly affect thermal behavior of particles as well as particle size (22, 23), the fact the system was maintained at a very narrow range of temperature suggests that the hydrodynamic diameter trends cannot be attributed to changes in thermal energy. Moreover, electrophoretic mobility (EPM) results (Figure 2.1B) showed that EPM did not change significantly during the sonication period. Since EPM is a measure of surface potential of particles, stable EPM values indicate that change of surface charge may not be responsible for observed sonication effects. Other possible mechanisms include higher collisions and changes in structural properties of particles due to extended sonication (24-29). Delgado and Matijević (24) study on latex and several oxide particles showed that prolonged sonication can enhance reaggregation and defeat the purpose of sonication. This study also identified 30 min sonication as ideal for hematite, as beyond this time there was reaggregation. Vibration created by sound waves due to sonication disperses particles in suspension. However, smaller particles are strongly influenced by sonic waves, which can lead to attachment of particles as well as aggregation (24, 30, 31). As nanoparticle aggregates are dispersed to smaller size, prolonged sonication may increase collisions between smaller particles and subsequently reaggregation. Moreover, nanoparticles are much smaller than traditional colloids which imply that nanoparticles may be more strongly affected by prolonged sonic waves.

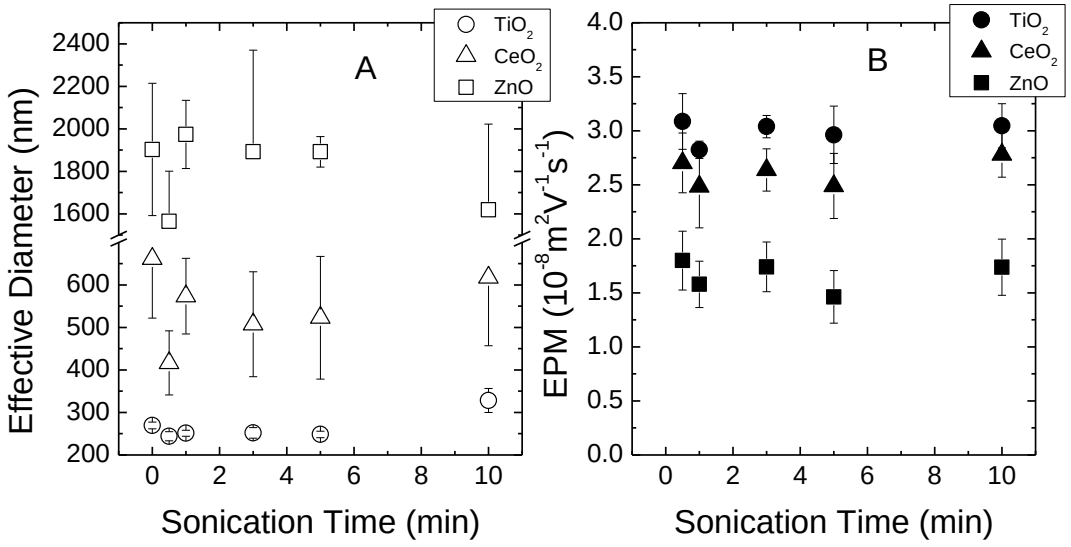

Figure 2.2. Effects of sonication duration on TiO_2, CeO_2 and ZnO nanoparticles solution test samples as a function of A) particle size (hydrodynamic diameter) and B) electrophoretic mobility (EPM). Measurements conducted at a nanoparticle concentration of 100 mg/L, unadjusted pH (5.14, 5.28, and 7.85 for TiO_2, CeO_2, and ZnO, respectively), 1 mM ionic strength (KCl), and temperature (25^{o}C).

Metal oxide nanoparticles have been reported to aggregate in solution over time (20, 32), suggesting that an additional sonication step is needed following the addition of an aliquot of the nanoparticles stock solution to another more dilute solution prior to any further experimentation. In order to determine the optimal sonication time for a diluted dispersion of nanoparticles made from stock solution, also referred to as a test sample, sonication duration was varied for all three metal oxide nanoparticles from 0 to ten minutes (Figure 2.2). Results indicate for all three metal oxide nanoparticles the hydrodynamic diameter decreases initially (from time 0 to approximately 1 min), and beyond this time hydrodynamic diameter of nanoparticles increased. Like stock solution

preparation, EPM of particles remained unchanged during sonication (Figure 2.2B). This suggests that for the metal oxide nanoparticles, 30s to 60s is the ideal range of time for sonication prior to experiment, This is attributed to enhanced number of collisions between particles that is achieved with longer sonication, leading to greater aggregation (24, 30). However, test sample preparation required a much shorter sonication time than the stock solution, whereas as the test sample is prepared from already dispersed stock solution. Delgado and Matijević (24) also recommended a moderate sonication prior to experiment in order to reduce aggregation. Hence, a 30s duration of sonication was selected for test samples, or diluted nanoparticle samples, prior to subsequent experiments.

2.3.2 Effects of Ionic Strength

The effect of ionic strength on measured EPM and hydrodynamic diameter of the model nanoparticles is presented in Figure 2.3. At unadjusted pH, all the three nanoparticles showed positive EPM over the range of ionic strength (0.1–100 mM) (Figure 2.3A). For TiO_2, the EPM decreased from 3.11 x 10^{-8} $m^2V^{-1}s^{-1}$ to 1.90 x 10^{-8} $m^2V^{-1}s^{-1}$, corresponding to the anticipated compression of the electrical double layer occurring with the increase of ionic strength. This double layer compression effect was also observed by the notable increase in hydrodynamic diameter of TiO_2 nanoparticles occurring at greater ionic strength (Figure 2.3B). At the lower range of ionic strength (0.1-1 mM KCl) the effective diameters were in the range of 300-350 nm; whereas, at ionic strength greater than 10mM, the hydrodynamic diameters increased sharply to the

range of 850-900 nm. Similarly, electrical double layer compression was observed for CeO_2 over the same range of ionic strength, with the EPM decreasing from 2.88 x 10^{-8} $m^2V^{-1}s^{-1}$ to 2.03 x 10^{-8} $m^2V^{-1}s^{-1}$ and the hydrodynamic diameter increasing from approximately 400 nm –800 nm.

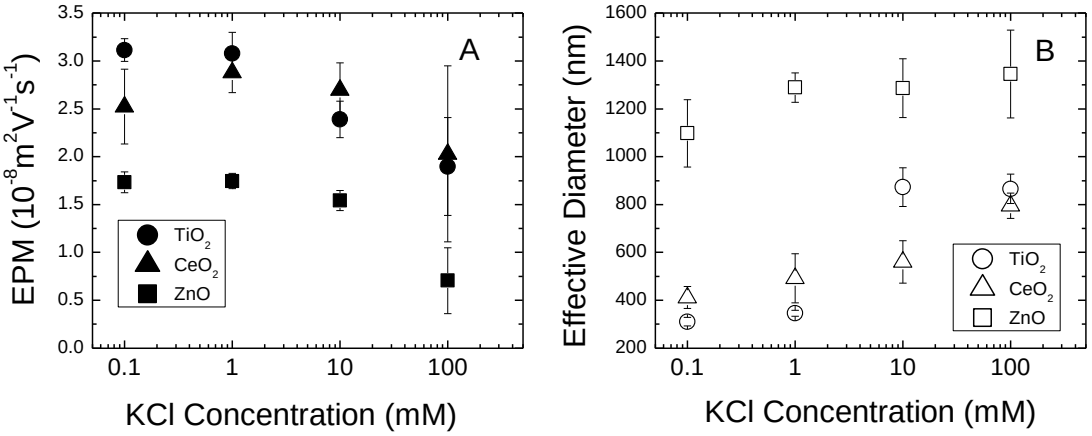

Figure 2.3. Effects of ionic strength on TiO_2, CeO_2 and ZnO A) electrophoretic mobility (EPM) and b) particle size (hydrodynamic diameter). Measurements conducted at a nanoparticle concentration of 100 mg/L, unadjusted pH (5.14, 5.28, and 7.85 for TiO_2, CeO_2, and ZnO, respectively), 1 mM ionic strength (KCl), and temperature (25^{o}C).

ZnO displayed a slightly different trend than the other metal oxides with respect to ionic strength. The EPM was also observed to decrease from 1.81x 10^{-8} $m^2V^{-1}s^{-1}$ to 0.70 x 10^{-8} $m^2V^{-1}s^{-1}$ as ionic strength increased from 0.1 mM to 100 mM KCl. However, for ionic strength below 10 mM KCl, the EPM appeared to be independent of ionic strength. This may be attributed to the dissolution of ZnO nanoparticles which can contribute divalent cation Zn^{2+} to the solution, and this divalent cation may shield the

effects of changing concentration of monovalent cations particularly across a range of low ionic strength (0.1-1 mM) (33). Evidence of dissolution of ZnO was also observed in later study on effects of nanoparticle concentration from conductivity measurement during the experiment (Figure 2.4B). The hydrodynamic diameter increased from about 1100 nm to 1350 nm as ionic strength increased from 0.1 mM to 100 mM KCl. However, compared to the other two metal oxide nanoparticles (TiO_2 and CeO_2), although the size of ZnO aggregates are much bigger, the sensitivity of ZnO aggregation to ionic strength is lower than other two metal oxide nanoparticles.

2.3.3 Effects of Nanoparticle Concentration

For all three metal oxide nanoparticles, the concentration of nanoparticles in the test samples were varied from 0 to 1000 mg/L to observe the effects of particle concentration on the subsequent solution chemistry – notably the background pH and ionic strength– and the resulting EPM and hydrodynamic diameter of the particles. Results are presented in Figure 2.4. For both TiO_2 and CeO_2 suspensions, pH was observed to become more acidic as the concentration of nanoparticles was increased (Figure 2.4A). For both of these metal oxide test samples, the pH decreased approximately 1 pH unit (starting at pH 5.7 reduced to 4.7 and 4.8 for TiO_2 and CeO_2, respectively over the range of particle concentration tested). As indicated by the EPM data in Figure 2.4C, these particles remain positively charged. This is due to the fact the isolectric points of TiO_2 and CeO_2 are above pH 6.0 (18, 34). Hence, both TiO_2 and CeO_2

are acidic metal oxides where hydroxylated surfaces of nanoparticles have a tendency to donate protons by dissociating water, binding the OH^- ions and releasing H^+ ions (35). The increased proton concentration in solution resulted in the observed drop in pH.

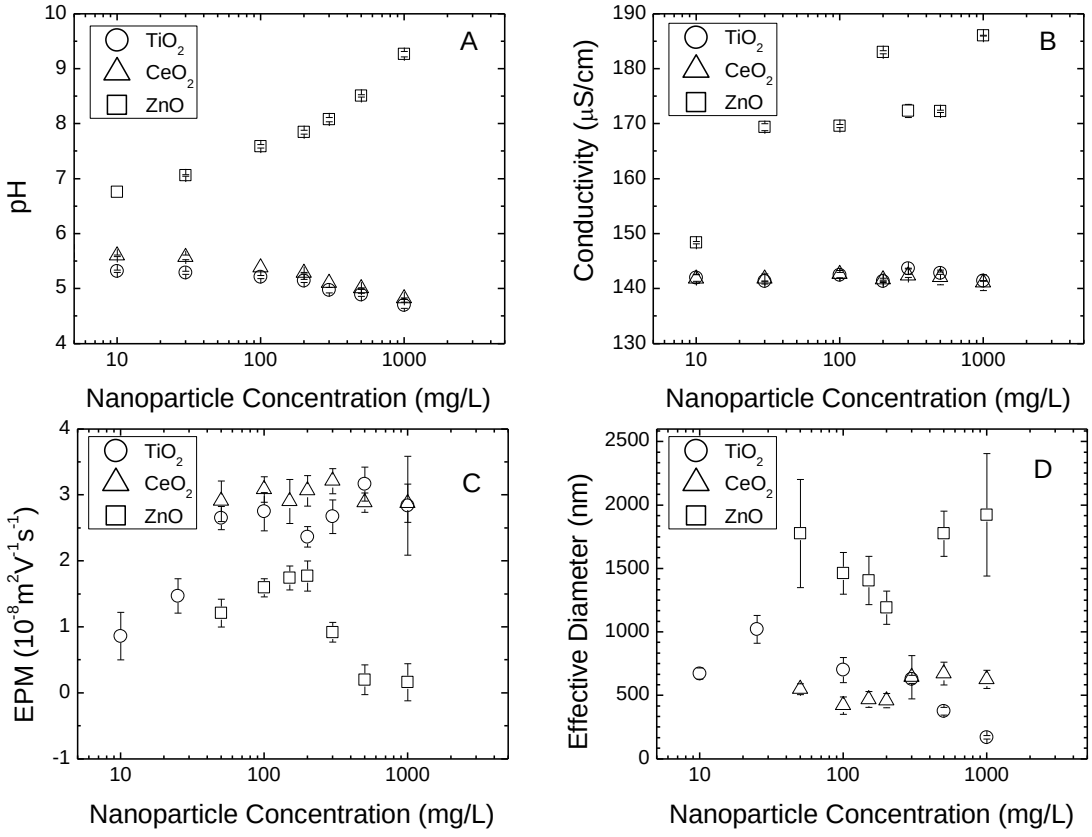

Figure 2.4. Effects of TiO_2, CeO_2 and ZnO nanoparticle concentration on the A) pH of solution, B) conductivity of solution, C) EPM of nanoparticles, and D) particle size (hydrodynamic diameter) of nanoparticles at fixed ionic strength (1 mM KCl) and temperature (25^oC). Each measurement was determined with test sample after at least 1 hour of equilibration with atmosphere for stable pH.

The implications of the pH change were minor for CeO_2. The subsequent EPM, ionic strength (conductivity), and particle size were altered slightly due to the modified solution chemistry (Figure 2.4B, C, and D). However, a simple t-test results showed that the changes were negligible, with no measureable change in ionic strength, EPM, and hydrodynamic diameter for CeO_2. The observed effect of pH change on stability of TiO_2 nanoparticles is significant. The hydrodynamic diameter of TiO_2 decreased with greater particle concentration. This change in diameter is attributed to the pH-induced increase in EPM which increases the electrical double layer repulsive forces between nanoparticles and consequently enhances particles dispersion. Moreover, as the pH drops further away from the IEP, the extent of interparticle repulsion and particle stability increases further.

Conversely, the data also indicated an increasing pH trend with ZnO nanoparticle concentration (Figure 2.4A). The increase in ZnO concentration resulted in a pH increase from 5.7 to 9.3 for 0 to 1000 mg/L ZnO, respectively. The IEP of ZnO has been reported around pH 9 (18); therefore, within the measured pH range the ZnO nanoparticles are positively charged (Figure 2.4C). However, the increase in ZnO concentration leads to the reduction in EPM approaching neutrality. This is due to ZnO being a basic metal oxide (35)where hydroxylated ZnO dissociates to Zn^{2+} and OH^-, allowing the particles to remain positive charged, although leading to a higher solution pH. There is evidence of ZnO dissolution (the conductivity data, Figure 2.4B) at the varied particle concentrations which contributes to the solution becoming basic. The conductivities of TiO_2 and CeO_2 nanoparticle suspensions in 1 mM KCl solution is close to 140 µS/cm, which is actually the predicted conductivity for 1 mM KCl solution at 25^oC (36) suggesting that both TiO_2

and CeO_2 did not dissolve during the experiments; in case of ZnO, there was an increase of conductivity with ZnO concentration. This implies that ZnO was dissolving even at the lowest nanoparticle concentration (as evident from the conductivity being greater than that for TiO_2 and CeO_2). Dissolution of ZnO produces free Zn^{2+} ions and OH^- ions which can contributed to the increased pH (35, 37, 38). This change in pH subsequently led to a decreased EPM and enhanced aggregation of particles with the greater ZnO nanoparticles concentration.

2.4 Conclusions

This study showed the effects of handling approaches on the resulting metal oxide nanoparticle suspensions and proposed a guideline for an optimum handling approach for preparing reproducible dispersion of nanoparticles in aqueous solution which is very crucial for consistent and comparable results for toxicity and transport studies (17, 39, 40). Optimization of sonication protocol for dispersion of nanoparticles is critical to achieve reproducible particle characterization results. This study found sonication of the nanoparticle stock suspension and the diluted test suspension to be optimum at 30 minutes and 30 seconds, respectively for the metal oxide nanoparticles tested in this study. However, the sonication protocol needs to be customized and optimized for each type of nanoparticle. Toxicity of nanoparticle depends on the dose of particles; hence, different concentrations of nanoparticles are usually tested in toxicity studies. However, maintaining same solution chemistry including pH, and ionic strength over different

concentrations of nanoparticles is essential for quantitative studies of toxicity and transport, as pH and ionic strength can change the surface properties of particles (41, 42). Our experimental results showed that nanoparticle concentration can significantly affect solution chemistry, particularly pH. Both TiO_2 and CeO_2 can decrease pH with nanoparticle concentration whereas ZnO can raise pH as well as ionic strength significantly as concentration increases. Therefore, it is necessary to control or carefully select experimental conditions (nanoparticle concentration, sonication protocol, and solution chemistry) to maintain a consistent and reproducible nanoparticle suspension being investigated.

2.5 References

(1) Nel, A.; Xia, T.; Mädler, L.; Li, N., Toxic Potential of Materials at the Nanolevel. *Science* **2006,** *311*, (5761), 622-627.

(2) Wiesner, M. R.; Lowry, G. V.; Alvarez, P.; Dionysiou, D.; Biswas, P., Assessing the Risks of Manufactured Nanomaterials. *Environmental Science & Technology* **2006,** *40*, (14), 4336-4345.

(3) Dunphy Guzman, K. A.; Taylor, M. R.; Banfield, J. F., Environmental Risks of Nanotechnology: National Nanotechnology Initiative Funding, 2000-2004. *Environmental Science & Technology* **2006,** *40*, (5), 1401-1407.

(4) Benn, T. M.; Westerhoff, P., Nanoparticle silver released into water from commercially available sock fabrics. *Environmental Science & Technology* **2008,** *42*, (11), 4133-4139.

(5) Mueller, N. C.; Nowack, B., Exposure Modeling of Engineered Nanoparticles in the Environment. *Environmental Science & Technology* **2008,** *42*, (12), 4447.

(6) Kiser, M. A.; Westerhoff, P.; Benn, T.; Wang, Y.; Pelì□rez-Rivera, J.; Hristovski, K., Titanium Nanomaterial Removal and Release from Wastewater Treatment Plants. *Environmental Science & Technology*, **2009**, 43 (17), pp 6757–6763.

(7) Colvin, V. L., The potential environmental impact of engineered nanomaterials. *Nat Biotech* **2003,** *21*, (10), 1166.

(8) Auffan, M.; Rose, J.; Bottero, J.-Y.; Lowry, G. V.; Jolivet, J.-P.; Wiesner, M. R., Towards a definition of inorganic nanoparticles from an environmental, health and safety perspective. *Nat Nano* **2009,** *4*, (10), 634.

(9) Baer, D. R.; Amonette, J. E.; Engelhard, M. H.; Gaspar, D. J.; Karakoti, A. S.; Kuchibhatla, S.; Nachimuthu, P.; Nurmi, J. T.; Qiang, Y.; Sarathy, V.; Seal, S.; Sharma, A.; Tratnyek, P. G.; Wang, C. M., Characterization challenges for nanomaterials. *Surface and Interface Analysis* **2008,** *40*, (3-4), 529-537.

(10) Powers, K. W.; Brown, S. C.; Krishna, V. B.; Wasdo, S. C.; Moudgil, B. M.; Roberts, S. M., Research Strategies for Safety Evaluation of Nanomaterials. Part VI. Characterization of Nanoscale Particles for Toxicological Evaluation. *Toxicol. Sci.* **2006,** *90*, (2), 296-303.

(11) Burleson, D. J.; Driessen, M. D.; Penn, R. L., On the Characterization of Environmental Nanoparticles. *Journal of Environmental Science and Health, Part A: Toxic/Hazardous Substances and Environmental Engineering* **2005,** *39*, (10), 2707 - 2753.

(12) Warheit, D. B.; Borm, P. J. A.; Hennes, C.; Lademann, J., Testing Strategies to Establish the Safety of Nanomaterials: Conclusions of an ECETOC Workshop. *Inhalation Toxicology: International Forum for Respiratory Research* **2007,** *19*, (8), 631 - 643.

(13) Richman, E. K.; Hutchison, J. E., The Nanomaterial Characterization Bottleneck. *ACS Nano* **2009,** *3*, (9), 2441.

(14) Saleh, N. B.; Pfefferle, L. D.; Elimelech, M., Aggregation Kinetics of Multiwalled Carbon Nanotubes in Aquatic Systems: Measurements and Environmental Implications. *Environmental Science & Technology* **2008,** *42*, (21), 7963-7969.

(15) Chen, K. L.; Elimelech, M., Relating Colloidal Stability of Fullerene (C60) Nanoparticles to Nanoparticle Charge and Electrokinetic Properties. *Environmental Science & Technology* **2009,** *43*, (19), 7270.

(16) Phenrat, T.; Saleh, N.; Sirk, K.; Tilton, R. D.; Lowry, G. V., Aggregation and Sedimentation of Aqueous Nanoscale Zerovalent Iron Dispersions. *Environmental Science & Technology* **2007,** *41*, (1), 284-290.

(17) Murdock, R. C.; Braydich-Stolle, L.; Schrand, A. M.; Schlager, J. J.; Hussain, S. M., Characterization of Nanomaterial Dispersion in Solution Prior to In Vitro Exposure Using Dynamic Light Scattering Technique. *Toxicol. Sci.* **2008,** *101*, (2), 239-253.

(18) Xia, T.; Kovochich, M.; Liong, M.; Mädler, L.; Gilbert, B.; Shi, H.; Yeh, J. I.; Zink, J. I.; Nel, A. E., Comparison of the Mechanism of Toxicity of Zinc Oxide and Cerium Oxide Nanoparticles Based on Dissolution and Oxidative Stress Properties. *ACS Nano* **2008,** *2*, (10), 2121-2134.

(19) Long, T. C.; Saleh, N.; Tilton, R. D.; Lowry, G. V.; Veronesi, B., Titanium Dioxide (P25) Produces Reactive Oxygen Species in Immortalized Brain Microglia: Implications for Nanoparticle Neurotoxicity. *Environmental Science & Technology* **2006,** *40*, (14), 4346-4352.

(20) French, R. A.; Jacobson, A. R.; Kim, B.; Isley, S. L.; Penn, R. L.; Baveye, P. C., Influence of Ionic Strength, pH, and Cation Valence on Aggregation Kinetics of Titanium Dioxide Nanoparticles. *Environmental Science & Technology* **2009,** *43*, (5), 1354-1359.

(21) Keller, A. A.; Wang, H.; Zhou, D.; Lenihan, H. S.; Cherr, G.; Cardinale, B. J.; Miller, R.; Ji, Z., Stability and Aggregation of Metal Oxide Nanoparticles in Natural Aqueous Matrices. *Environmental Science & Technology,* **2010**. *44*, (6), 1962-1967.

(22) Pérez-Maqueda, L. A.; Franco, F.; Pérez-Rodríguez, J. L., Comparative study of the sonication effect on the thermal behaviour of 1:1 and 2:1 aluminium phyllosilicate clays. *Journal of the European Ceramic Society* **2005,** *25*, (9), 1463.

(23) Franco, F.; Pérez-Maqueda, L. A.; Pérez-Rodríguez, J. L., The influence of ultrasound on the thermal behaviour of a well ordered kaolinite. *Thermochimica Acta* **2003,** *404*, (1-2), 71.

(24) Angel, D.; Egon, M., Particle Size Distribution of Inorganic Colloidal Dispersions: A comparison of different techniques. *Particle and Particle Systems Characterization* **1991,** *8*, (1-4), 128-135.

(25) Franco, F.; Pérez-Maqueda, L. A.; Pérez-Rodríguez, J. L., The effect of ultrasound on the particle size and structural disorder of a well-ordered kaolinite. *Journal of Colloid and Interface Science* **2004,** *274*, (1), 107.

(26) Franco, F.; Cecila, J. A.; Pérez-Maqueda, L. A.; Pérez-Rodríguez, J. L.; Gomes, C. S. F., Particle-size reduction of dickite by ultrasound treatments: Effect on the structure, shape and particle-size distribution. *Applied Clay Science* **2007,** *35*, (1-2), 119.

(27) Kim, S. H.; Haimovich-Caspi, L.; Omer, L.; Talmon, Y.; Franses, E. I., Effect of sonication and freezing-thawing on the aggregate size and dynamic surface tension of aqueous DPPC dispersions. *Journal of Colloid and Interface Science* **2007,** *311*, (1), 217.

(28) Pérez-Rodríguez, J. L.; Wiewióra, A.; Drapala, J.; Pérez-Maqueda, L. A., The effect of sonication on dioctahedral and trioctahedral micas. *Ultrasonics Sonochemistry* **2006,** *13*, (1), 61.

(29) Pérez-Maqueda, L. A.; Duran, A.; Pérez-Rodríguez, J. L., Preparation of submicron talc particles by sonication. *Applied Clay Science* **2005,** *28*, (1-4), 245.

(30) Poli, A. L.; Batista, T.; Schmitt, C. C.; Gessner, F.; Neumann, M. G., Effect of sonication on the particle size of montmorillonite clays. *Journal of Colloid and Interface Science* **2008,** *325*, (2), 386.

(31) Hueter, T. F.; Bolt, R. H., *Sonics : techniques for the use of sound and ultrasound in engineering and science*. Wiley ; Chapman & Hall: New York; London, 1955.

(32) Chen, K. L.; Mylon, S. E.; Elimelech, M., Enhanced Aggregation of Alginate-Coated Iron Oxide (Hematite) Nanoparticles in the Presence of Calcium, Strontium, and Barium Cations. *Langmuir* **2007,** *23*, (11), 5920-5928.

(33) Elimelech, M., Gregory, J., Jia, X., Williams, R.A., *Particle Deposition and Aggregation: Measurement, Modeling and Simulation*. Butterworth-Heinemann: 1995; p 441.

(34) Fatisson, J.; Domingos, R. F.; Wilkinson, K. J.; Tufenkji, N., Deposition of TiO2 Nanoparticles onto Silica Measured Using a Quartz Crystal Microbalance with Dissipation Monitoring. *Langmuir* **2009,** *25*, (11), 6062.

(35) Stumm, W.; Morgan, J. J., *Aquatic chemistry : chemical equilibria and rates in natural waters*. 3rd Year: 1996 ed.; p xvi, 1022.

(36) Crittenden, J. C.; Montgomery Watson, H., *Water treatment principles and design*. J. Wiley: Hoboken, N.J., 2005.

(37) Fruhwirth, O.; Herzog, G. W.; Hollerer, I.; Reitsamer, G., ZnO dissolution kinetics by means of A 65Zn tracer method. *Surface Technology* **1982,** *15*, (1), 43.

(38) Fruhwirth, O.; Herzog, G. W.; Poulios, J., Dark dissolution and photodissolution of ZnO. *Surface Technology* **1985,** *24*, (3), 293.

(39) Zhang, Y.; Chen, Y.; Westerhoff, P.; Crittenden, J. C., Stability and Removal of Water Soluble CdTe Quantum Dots in Water. *Environmental Science & Technology* **2008,** *42*, (1), 321-325.

(40) Zhang, Y.; Chen, Y.; Westerhoff, P.; Hristovski, K.; Crittenden, J. C., Stability of commercial metal oxide nanoparticles in water. *Water Research* **2008,** *42*, (8-9), 2204.

(41) Domingos, R. F.; Baalousha, M. A.; Ju-Nam, Y.; Reid, M. M.; Tufenkji, N.; Lead, J. R.; Leppard, G. G.; Wilkinson, K. J., Characterizing Manufactured Nanoparticles in the Environment: Multimethod Determination of Particle Sizes. *Environmental Science & Technology* **2009,** *43*, (19), 7277.

(42) Dunphy Guzman, K. A.; Finnegan, M. P.; Banfield, J. F., Influence of Surface Potential on Aggregation and Transport of Titania Nanoparticles. *Environmental Science & Technology* **2006,** *40*, (24), 7688-7693.

Chapter 3

Mechanisms of TiO_2 Nanoparticle Transport in Porous Media: Role of Solution Chemistry, Nanoparticle Concentration, and Flowrate

Chowdhury, I., Hong, Y., Honda, R. J., Walker, S. L., Mechanisms of TiO_2 nanoparticle transport in porous media: Role of solution chemistry, nanoparticle concentration, and flowrate. *Journal of Colloid and Interface Science* **2011,** *360*, (2), 548-555.

Abstract

The role of solution chemistry, nanoparticle concentration and hydrodynamic effects in the transport and deposition of TiO_2 nanoparticles through porous media has been systematically investigated. Two solution chemistry variables, pH and ionic strength (IS), showed a significant influence on the transport due to their involvement in the aggregation of the nanoparticles and interaction with quartz sand. An electrostatically unfavorable condition for deposition existed at pH 7, at which the greatest retention occurred in the column, likely due to aggregation (>1000 nm) and straining effects. Under electrostatically favorable conditions (pH 5) significant elution from the column was observed and attributed to smaller aggregate size (~300 nm) and blocking effects. Nanoparticle concentration was found to contribute to the increased breakthrough of nanoparticles at pH 5 due to blocking and subsequent particle-particle repulsion. Increased flowrate resulted in greater elution of nanoparticles due to hydrodynamic forces acting on aggregates and subsequently contributed to blocking. Overall, a combination of mechanisms including straining, blocking, and DLVO-type forces were involved over the range of solution chemistry and nanoparticle concentrations tested. Consideration of these mechanisms is necessary for improved removal of TiO_2 nanoparticles via filtration and reliable prediction of transport of these potentially problematic nanoparticles through the subsurface.

3.1 Introduction

With rapid growth of the nanotechnology industry, nanomaterials will ultimately end up in the aquatic environment (1). Titanium dioxide (TiO_2) is one of the most widely used nanomaterials in consumer products including sunscreens, cosmetics, paints and other products (1). Research has shown that TiO_2 nanoparticles (TNPs) can be introduced to the environment from such processes such as mining, TiO_2-enabled product fabrication, product use, product recycling and disposal to the aquatic environment (2). TNPs become problematic and are viewed as an emerging pollutant due to their neurotoxicity to animals, capability of causing oxidative stress in human cells (3, 4) and genetic instability in mice (5).

After release into the environment, TNPs have the potential to be transported in the subsurface. Subsequently nanoparticles may get into groundwater (6) and enter into food web through bioaccumulation (7). Therefore, it is critical to understand the movement of TNPs in natural porous media. One of the essential methods of removing particles in conventional treatment plants is filtration (8, 9). Moreover, since TNPs have been found in effluent from current treatment systems (10), the fundamental physicochemical processes involved in the transport and removal of TNPs in engineered porous media must be considered as well. Another factor involved in the fate of TNPs is the degree of aggregation. Aggregation studies have shown that TNPs are very stable at low IS and pH (11) or in the presence of natural organic matter (12); whereas, high IS leads to micron-sized aggregate formation (11). Aggregate size also increases with particle concentration and decreasing primary particle size (13). The impact of this

aggregation is substantial; for example, it has been reported that aggregation of metal oxide nanoparticles (including TiO_2) was irreversible and 90% of these agglomerated nanoparticles can be subsequently removed by filtration (14).

Though aggregation behavior of TNPs has been investigated previously (11, 12, 14, 15), very few studies have been conducted on the filtration mechanisms (6, 16, 17). It was observed that the elution of fullerene and metal oxide nanoparticles from a glass bead column increased with velocity (16). Another study showed that TNPs are highly stable in soil, and a significant amount can pass through sand at low IS (0.15 - 1.00 mM), while higher clay content and salinity resulted in greater retention (6). Others investigated the effects of pH on TNPs aggregation and transport in a two dimensional pore structure model (17) and found substantial elution (>80% of nanoparticles injected) across the range of pH 1-12 with the exception of pH 7 at which elution was negligible. Interestingly, at the electrostatically favorable condition under this particular experimental scenario (pH 3), a considerable amount of particles eluted (84%) a phenomenon current transport theories cannot explain (17).

This paper presents work that has been conducted in saturated porous media in order to address some of these gaps in knowledge. The specific goals were to understand the sensitivity of transport and removal of TNPs to the effects of three critical parameters: solution chemistry (pH and IS), nanoparticle concentration, and flowrate. These parameters were selected to simulate what would occur in a range of natural and engineered systems (8). The combined contributions of these parameters to the fate of

TNPs provide greater insight to the potential for transport and the subsequent risk to the environment.

3.2 Materials and Methods

3.2.1 Metal Oxide Nanoparticle Stock Solution and Sample Preparation

Titanium dioxide (Aeroxide TiO_2 P25, Evonik Degussa Corporation, NJ) was used in all experiments. According to the manufacturer, nanomaterials were >99.5% pure with a primary particle size of 21 nm. Following the protocol developed from our past research (18), a stock suspension of TNPs was prepared prior to experiment by sonicating 30 min in a water bath (Transsonic 460/H, Barnstead/Lab-line, Melrose Park, IL). The protocol for preparation of metal oxide nanoparticles suspension and sample preparation has been mentioned elsewhere (18). An amount of dry TiO_2 nanoparticles (TNPs) was added to the desired electrolyte solution, stirring with a magnetic stir bar for 1 min. Subsequently, the nanoparticle stock solution of 1 g/L was prepared by sonicating for 30 min in a water bath at 120 W (Transsonic 460/H, Barnstead/Lab-line, Melrose Park, IL). The test sample was prepared by diluting stock suspension in desired concentration and electrolyte solution, followed by another 15 min sonication step. The test sample was again sonicated for 30 s prior to experiments to minimize aggregation.

3.2.2 Nanoparticles Characterization

Nanoparticle size was determined by transmission electron microscopy (TEM, FEI-PHILIPS CM300, Hillsboro, OR) operated at 300 kV. Electron microscopy was

performed at the Central Facility for Advanced Microscopy and Microanalysis at UCR. More than 200 nanoparticles from ten different images were used for size determination. The isoelectric point (IEP) of TNPs was determined by conducting electrokinetic characterization using a ZetaPALS analyzer (Brookhaven Instruments Corp., Holtsville, NY) from pH 5 to 10 at 10 mM KCl. Electrophoretic mobilities (EPM) were measured over a wide range of IS (1-100 mM) at constant pH (5 and 7). Hydrodynamic diameter was measured using dynamic light scattering (DLS) (Brookhaven model BI-9000AT Holtsville, NY) at a wavelength of 661 nm and scattering angle of 90°. The average diameter was determined from the arithmetic average of ten runs for three separate samples, with each run involving an average of measurements taken over 30 s. All solutions were made with ACS reagent grade chemicals (Fisher Scientific, Pittsburgh, PA), and pH was controlled with 10 mM HCl or KOH.

3.2.3 Column Experiments

Experiments were conducted using columns packed with 275 μm ultra-pure quartz (Iota® quartz, Unimin Corp., NC), which represents the typical size range of sand in filters (8). For each experiment a borosilicate glass column (Omnifit, Boonton, NJ) was wet packed with cleaned and rehydrated sand, with a resulting average bed porosity of 0.46. Further details regarding preparation procedures for the sand are described elsewhere (19-21).

Following the packing step, deionized water (nanopure water at >18.2 MΩ at 25^{o}C) was used for flushing the column for at least 10 pore volumes (PV) which was

followed by electrolyte solution for more than 10 PV (22). Then 6 PV of the nanoparticle suspension was injected into the column, followed by a nanoparticles-free electrolyte solution (>6 PV). Column effluent was collected in 15 mL centrifuge tubes (Thermo Fisher Scientific Inc. Waltham, MA) using a fraction collector (CF 1 Fraction Collector, Spectrum Chromatography, Houston, TX). During the injection phase of the experiments, the nanoparticle suspension was continuously sonicated and stirred to maintain a consistent dispersion of nanoparticles over the course of the experiment. The distribution of retained nanoparticles remaining in the column was determined after the column experiment using a previously reported method (22). Briefly, after the column experiment, quartz sand was excavated in 1 cm segments into 50 mL centrifuge tubes. The TiO_2 concentration in each of stock nanoparticles suspension, effluent, and column dissections was determined by Inductively Coupled Plasma Atomic Emission Spectroscopy (ICP-AES) (Optima 2100 DV, PerkinElmer Inc., Shelton, CT.) in concentrated H_2SO_4 (Fisher, trace metal grade) by following standard methods (23). The samples of quartz from the column dissection were heated in H_2SO_4 at 250^oC for more than 2 hours and the resulting TiO_2 suspension was diluted at least 10 times with deionized water (nanopure water at >18.2 MΩ at 25^oC) prior to ICP-AES measurement.

Column experiments were conducted at two representative flowrates, 2 mL/min (1.9×10^{-4} m/s) and 10 mL/min (9.5×10^{-4} m/s), simulating groundwater or slow sand filtration and rapid sand filtration respectively (8, 24). The injected concentration of

nanoparticles was varied (100-800 mg/L) and experiments were conducted across a range of IS (1-10 mM KCl).

3.2.4 Aggregation Studies

Stability was evaluated using dynamic light scattering at 10 s intervals for 100 min for nanoparticle suspensions at pH 5 and 7 at 25°C. For these measurements, a weighed sample was added into the KCl solution and adjusted to pH 5 or 7 with HCl or KOH. Without further buffering the solution, pH was stable within ± 0.1 units during the experiments. All the experiments were initiated after 30 s of sonication in a water bath.

3.3 Results and Discussion

3.3.1 Characterization of Nanoparticles

The effective diameter of TNPs was determined as 18.4 ± 6.0 nm through TEM images analysis, similar to the 21 nm reported by the manufacturer (Figure 3.1). TNPs ranged from 5 to 45 nm, with the majority in the 10-25 nm size range. TEM images showed the particle shape to be virtually spherical. The IEP of TNPs was determined to be pH 6.2 (Figure 3.2). Electrokinetic analysis determined that at pH 5 and across the range of IS, EPM was positive; whereas, above the IEP at pH 7, the EPM was negative. Increasing IS resulted in greater charge screening and hence less negative or positive electrophoretic mobility, as anticipated due to double layer compression (9, 25).

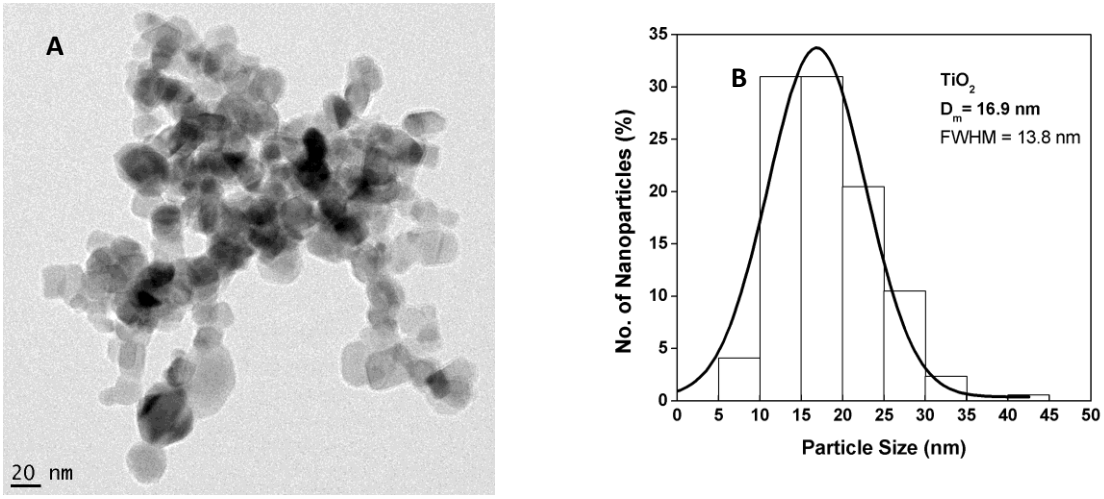

Figure 3.1. A) Transmission Electron Microscope (TEM) image of TNPs at 300 kV. B) Particle Size Distribution of TNPs. Particle size was determined from 10 different TEM images over 200 particles.

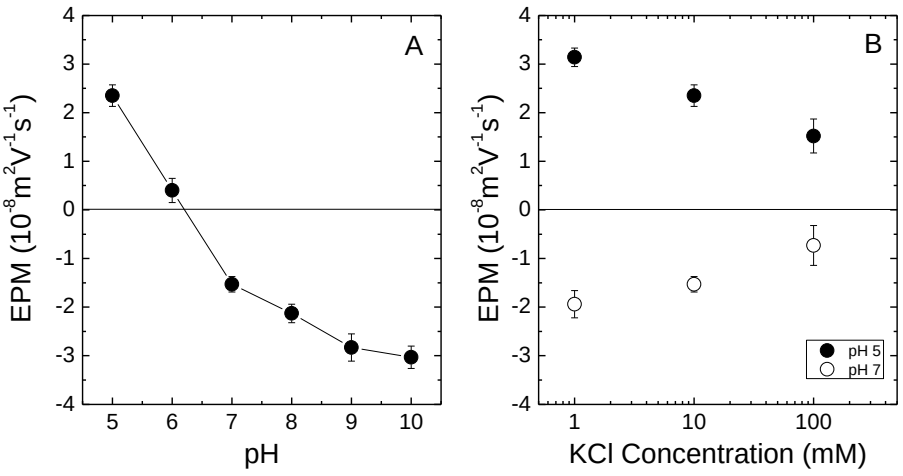

Figure 3.2. Electrophoretic mobility (EPM) values for TNPs A) EPM of TNPs as a function of pH at fixed IS (10 mM KCl), nanoparticle concentration (100 mg/L), and temperature (25^{o}C); and B) as a function of IS at 2 different pHs (pH 5, and 7) , fixed nanoparticle concentration (100 mg/L) and temperature (25^{o}C).

3.3.2 Column Experiments

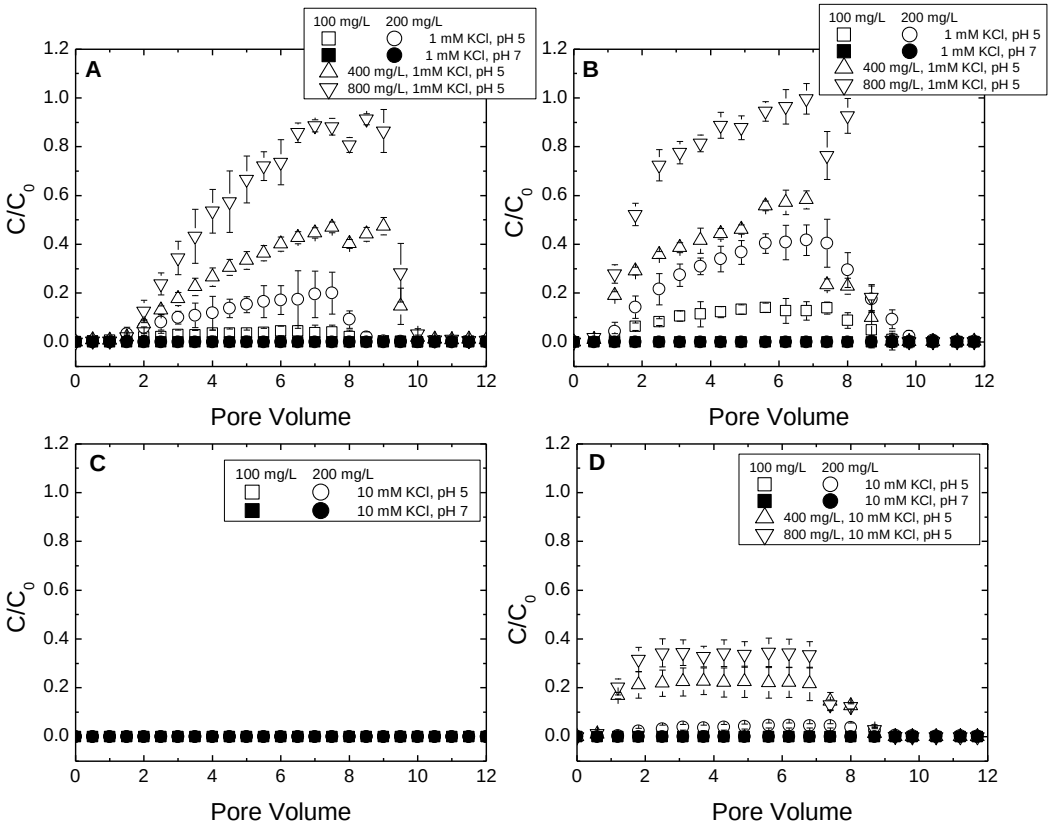

Figure 3.3. TiO_2 nanoparticle breakthrough curves for experiments conducted in the column at A) 2 mL/min and 1 mM KCl , B) 10 mL/min and 1 mM KCl, C) 2 mL/min and 10 mM KCl and D) 10 mL/min and 10 mM KCl as function of pH and nanoparticle concentration. C_0 and C represent influent and effluent nanoparticle concentration respectively.

Column breakthrough curves (BTCs) for TNPs obtained at 2 mL/min are reported in Figure 3.3. pH played a significant role in the transport of TNPs. At pH 7, TNPs and quartz were negatively charged, indicating the existence of sufficient repulsive forces to lead to an electrostatically "unfavorable" condition for deposition. Still, TNPs were

retained in the column and no elution was observed under all conditions. Conversely, at pH 5, TNPs successfully passed through the column at the lower IS condition; whereas increased IS resulted complete retention of TNPs in the column. At the lower IS and pH 5 condition, a significant increase of elution was observed with greater nanoparticle concentration. The maximum C/C_0 observed in the BTCs increased from 0.04 to 0.91 with TNPs from 100 mg/L to 800 mg/L, respectively. At pH 5, TNPs are presumably under "favorable" conditions; hence, it is not entirely clear why any elution was observed.

Similar BTCs were observed at the higher flowrate (Figure 3.3). At 10 mL/min, no elution was observed at pH 7 under any of the tested conditions; whereas at low IS and pH 5, particles passed through the column. However, the extent of elution was higher with increased flowrate. The maximum breakthrough levels (C/C_0) increased (0.04 -0.14 and 0.20 to 0.41 for 100 and 200 mg/L TiO_2, respectively) with as the flowrate increased from 2 to 10 mL/min. Similar to the lower flowrate, at high IS and pH 5, no elution was observed at low nanoparticle concentration (100 mg/L). However, increased elution was observed at the greater nanoparticle concentration (C/C_0 increased from 0.05 to 0.35 with 200-800 mg/L) at high IS and pH 5.

3.3.3 Column Mass Balance

A mass balance of the TNPs was determined to further evaluate the mechanisms involved in the removal of nanoparticles (Table 3.1). The relative amount (% by mass)

of nanoparticles eluted and retained in the column is presented in Table 3.1. The mass balance accounted for 90% to 110% of the particles. These levels suggest that almost all retained particles were released from the sand based on the protocol used in determination of the mass balance for column experiments (19, 22, 26). Since an acid digestion method was applied, even particles irreversibly attached to the sand were dissolved and quantified. Results at pH 7 indicate that 95%-110% of injected nanoparticles were retained in the column, which corroborates the lack of elution observed in the column experiments at both flow rates. At pH 5, the mass balance results were more complex. At 2 mL/min, elution was only observed at pH 5 and 1 mM KCl ($M_E/M_T>0$ when M_E and M_T represent mass of TNPs in effluent and mass of TNPs injected, respectively) regardless of nanoparticle concentration injected (100-800 mg/L). The ratio of M_E/M_T increased with nanoparticle concentration, corroborating the observed trend of greater elution with nanoparticle concentration under these particular conditions. A similar trend was also observed at the higher flow rate; albeit the relative amount eluted (as indicated by the ratio of M_E/M_T) was higher at 10 mL/min than at 2 mL/min. M_E/ M_T ratios increased from 0.028 to 0.107 and from 0.126 to 0.347, as flowrates increased from 2 to 10 mL/min for nanoparticle concentration of 100 and 200 mg/L respectively (Table 3.1). This further indicates that flowrate has significant effects on the transport of TNPs through the column.

Table 3.1. Mass balance results from column experiments

Experimental Conditions							
Flow Velocity (mL/min)	Concentration (mg/L)	pH	IS (mM)	M_E[a]	M_C[b]	M_T[c]	M_E/M_T
2 mL/min	100 mg/L	5	1	0.03	1.00	1.03	0.03
			10	0	1.06	1.06	0
		7	1	0	1.03	1.03	0
			10	0	0.98	0.98	0
	200 mg/L	5	1	0.12	0.85	0.98	0.13
			10	0	1.05	1.05	0
		7	1	0	1.03	1.03	0
			10	0	0.97	0.97	0
	400 mg/L	5	1	0.17	0.74	0.91	0.19
	800 mg/L	5	1	0.33	0.59	0.93	0.36
10 mL/min	100 mg/L	5	1	0.11	0.93	1.04	0.11
			10	0	1.07	1.07	0
		7	1	0	0.93	0.93	0
			10	0	1.09	1.09	0
	200 mg/L	5	1	0.33	0.62	0.95	0.35
			10	0.04	1.07	1.11	0.03
		7	1	0	0.95	0.95	0
			10	0	1.07	1.07	0
	400 mg/L	5	1	0.16	0.66	0.82	0.20
			10	0.09	0.89	0.98	0.09
	800 mg/L	5	1	0.32	0.49	0.82	0.39
			10	0.11	0.97	1.07	0.09

[a] M_E: Mass of TNPs in effluent

[b] M_C: Mass of TNPs retained in the column

[c] M_T: Total mass of TNPs injected

3.3.4 Column Retention Profiles

To further understand the mechanisms involved in column experiments, retention profiles were developed (Figure 3.4). At the lower flowrate and pH 7, > 90% of nanoparticles injected were retained at the column inlet (at a dimensionless depth of 0.1). Similarly at higher flowrate, the greatest retention was observed at the top of the column. However, for the higher flowrate, greater IS resulted in more retention at the inlet of column at pH 7 as follows: 200 mg/L, 10 mM KCl> 100 mg/L, 10 mM KCl> 100 mg/L, 1 mM KCl> 200 mg/L, 1mM KCl. Retention levels corroborate the lack of elution observed in BTCs.

The retention profile trends for pH 5 differed from those at pH 7. At 10 mM KCl, > 60% of TNPs were retained at the top of the column with the extent of retention in this region notably less than what was observed at pH 7 (80-99% retained at pH 7 versus 60-75% at pH 5). At pH 5 and 2 mL/min, retention at the column inlet follows this order: 200 mg/L, 10 mM KCl> 100 mg/L, 10 mM KCl> 100 mg/L, 1 mM KCl> 200 mg/L, 1 mM KCl. The higher flowrate experiments conducted at pH 5 resulted in the similar trend of retention at a dimensionless depth of 0.1, albeit the retention in the column is less as compared to the lower flowrate. Retention was greatest in the first 1 cm of the column, and less substantial below the initial 1 cm past the inlet. TNPs retention was observed throughout the column, even at solution conditions of pH 5 and low IS, indicating that nanoparticles remained mobile through the column and were not entirely retained under these conditions.

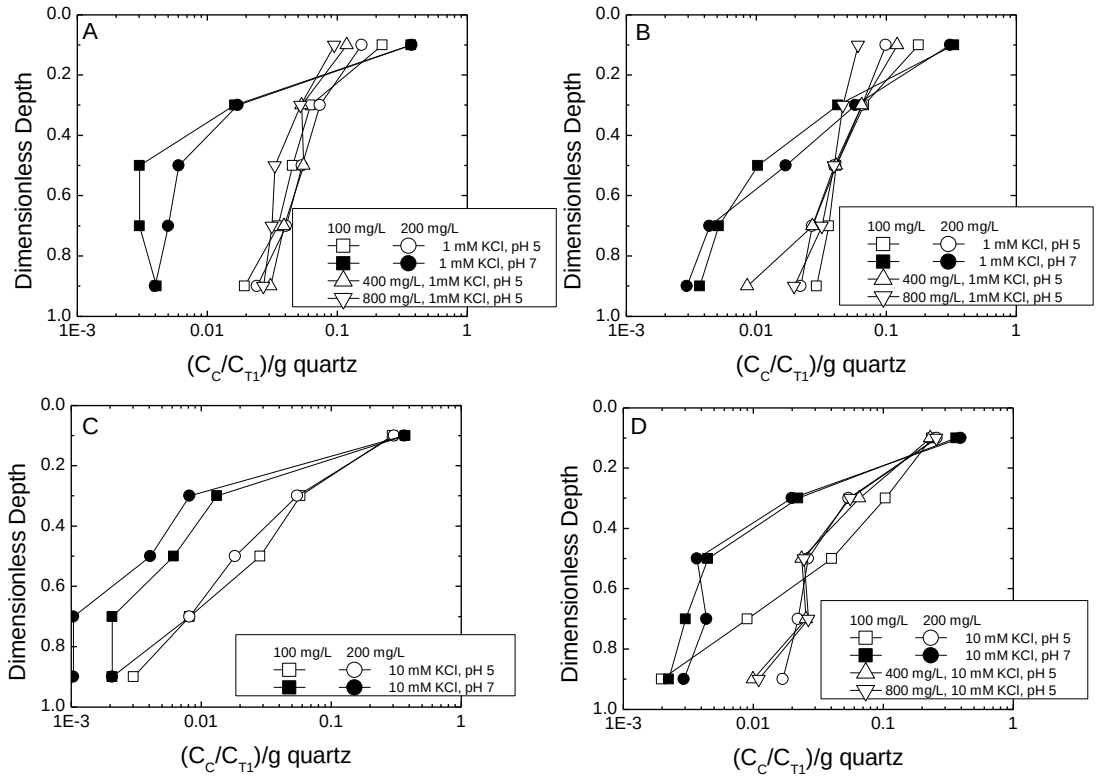

Figure 3.4. Retention profiles of TNPs in the column at A) 2 mL/min and 1 mM KCl , B) 10 mL/min and 1 mM KCl, C) 2 mL/min and 10 mM KCl and D) 10 mL/min and 10 mM KCl as function of pH and nanoparticle concentration. C_c and C_{T1} represent particle concentration recovered from column and total concentration of particles injected, respectively.

From the relative trends observed, further mechanistic insight can be gained by comparing results with theoretical predictions. According to classical filtration theory deposition of colloids through porous media decreases with travel distance following a hyper-exponential distribution (20, 21, 27, 28). At pH 5 (favorable conditions) the amount of particle retention monotonically decreased with distance from the top of the column as predicted by classical filtration theory under the range of nanoparticle concentration and IS tested (Figure 3.4). Conversely, at pH 7 under unfavorable

conditions, retention profiles were non-exponential, specifically at high IS (10 mM) and both flowrates (Figure 3.4). Retention profiles showed deviation from theory at the top part of the column, which indicates mechanisms involved in particle retention are more than those accounted for in classical filtration theory. These other retention mechanisms likely include aggregation and straining, which are not considered in traditional clean bed attachment theory and the contribution of each will be discussed below.

3.3.5 Mechanisms of Nanoparticle Retention

3.3.5.1 Interpretation with DLVO Theory

Derjaguin-Landau-Verwey-Overbeek (DLVO) theory was applied to further evaluate the relative contribution of electrostatic and van der Waals interactions upon the interaction between the TNPs and the quartz surfaces in the column (22, 29, 30). Interaction profiles for the TiO_2-quartz systems were developed assuming sphere-plate geometry and following equations were utilized (22, 31, 32):

$$V_{el} = \pi\varepsilon_0 \varepsilon a_p \left\{ 2\psi_p \psi_c \ln\left[\frac{1+\exp(-\kappa h)}{1-\exp(-\kappa h)}\right] + (\psi_p^2 + \psi_c^2)\ln\left[1-\exp(-2\kappa h)\right]\right\} \quad (3.1)$$

$$V_{vdW} = -\frac{A_{102}\, a_p}{6h}\left[1+\frac{14\,h}{\lambda}\right]^{-1} \quad (3.2)$$

Permittivity of free space (ε_0) and the dielectric constant of water (ε) were assumed to be 8.854×10^{-12} C/V/m and 78.5 respectively (9, 22). Hamaker constant

(A_{102}) for the quartz-TiO_2-water system was assumed to be 10^{-20} J (33). In the place of surface potentials, zeta potential values of TNPs (ψ_p) were utilized. EPM values for the TNPs were converted to zeta potential values using Smoluchowski equation (9) (summarized in Figure 3.2) and previously reported streaming potential values (ψ_c) for quartz sand were applied (27). A characteristic wavelength (λ) of 100 nm was assumed (9).

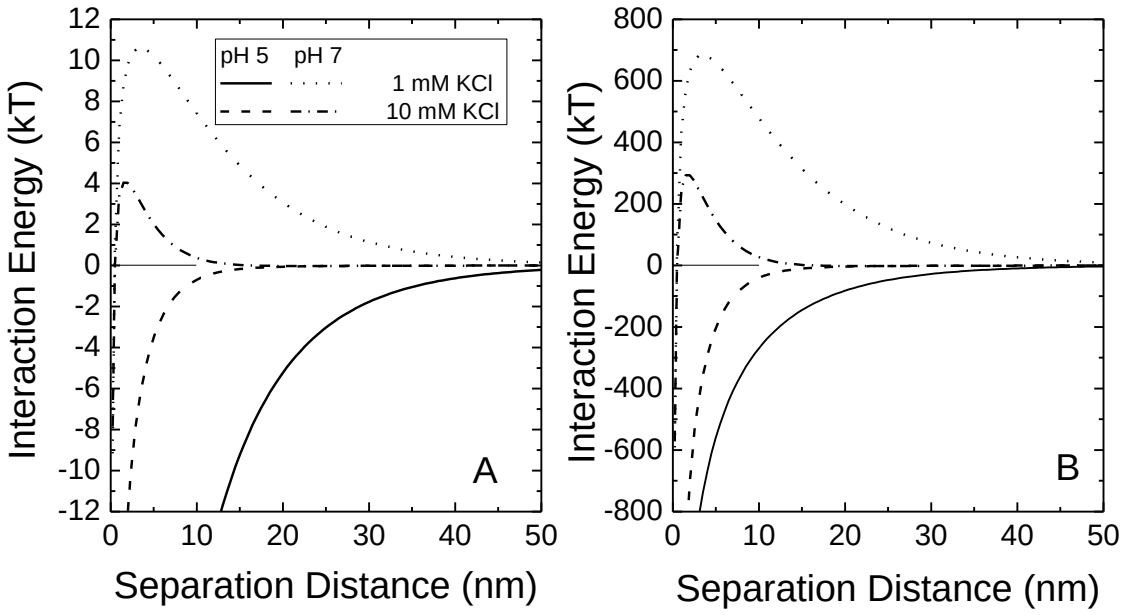

Figure 3.5. Interaction energy profiles generated with DLVO theory between a nanoparticle and quartz collector at pH 5 and pH 7 as a function of separation distance and based on A) primary particle size (18.4 nm) and B) aggregate sizes.

Table 3.2. Total Interaction Energy Parameters for TNPs-quartz system as a function of pH and IS

pH	IS	Based on Primary Particle Size			Based on Aggregate Size			Separation Distance[a] (nm)
		1^o Max (kT)	Energy Barrier (kT)	2^o Min (kT)	1^o Max (kT)	Energy Barrier (kT)	2^oMin (kT)	
5	1	-156.9	NB[b]	NB[b]	-2472.7	NB[b]	NB[b]	NB[b]
	10	-50.9	NB[b]	NB[b]	-2953.5	NB[b]	NB[b]	NB[b]
7	1	-9.2	10.6	-0.002	-591.1	683.5	-0.114	105.5
	10	-7.9	4.0	-0.031	-571.8	294.2	-2.262	22.0

[a] Calculated distance between the TNP and quartz surface where secondary energy minimum exists
[b]NB: No barrier

Interaction profiles across the range of solution conditions were generated considering both primary particle and aggregate sizes (Figure 3.5). The profiles indicated unfavorable conditions at pH 7 with energy barriers of 4-11 and 300-700 kT, considering primary particle and aggregate size, respectively (Table 3.2). Depth of the secondary energy minimum was also quite shallow (< 3 kT for aggregates). If the DLVO-type interactions dominate, then one would anticipate the relative transport in the column to mirror the observed DLVO profiles (1 mM KCl and pH 7, which is the most repulsive and unfavorable condition due to the negatively charged surfaces, should result in the

greatest elution). However, column results did not follow these anticipated trends. Conversely, an electrostatically favorable condition was observed at pH 5 with no energy barrier. Deep primary energy well (-50 kT to -150 kT for primary particle size; -2400 kT to - 3000 kT for aggregate) were observed indicating that most of TNPs should be irreversibly attached to quartz sand and no elution should occur at pH 5 (Table 3.2). Although DLVO predictions align with observed deposition trends at higher IS, low flowrate, and pH 5, significant elution was observed at low IS with increasing elution as a function of nanoparticle concentration. Hence, DLVO theory cannot fully explain the phenomena observed in the column experiments at either pH. However, these phenomena may be explained by aggregation and subsequent straining, as aggregation is very common phenomenon for metal oxide nanoparticles (11, 14).

3.3.5.2 Contribution of Nanoparticle Aggregation and Straining

DLVO theory predicts only particle-particle and particle-quartz interactions and it is insufficient for describing physicochemical interactions including straining, ripening and blocking (9). The aggregation of nanoparticles, a common phenomenon, may be contributing to these other physicochemical interactions. Hence, aggregation studies of TNPs were conducted to further investigate the mechanisms involved in TiO_2 filtration (Figure 3.2). The extent of aggregation was evaluated by the hydrodynamic diameter as a function of time for the various solution chemistry conditions and nanoparticle concentrations. TNPs stability was observed to be sensitive to IS, pH and concentration.

Particles at pH 5 and 1mM KCl remained at a stable size (~ 300 nm) across the range of nanoparticle concentrations tested (100-800 mg/L) (Fig. S2); whereas it was observed that the aggregate size increased with IS at pH 5. At pH 7, aggregate size > 1000 nm was observed at all IS and nanoparticle concentrations (Figure 3.2). These trends, as a function of pH, are attributed to the pH relative to the IEP. Above the IEP at pH 7, the extent of aggregation was greater than that at pH 5. Additionally, higher TNPs concentration and IS led to increased aggregate size at pH 7.

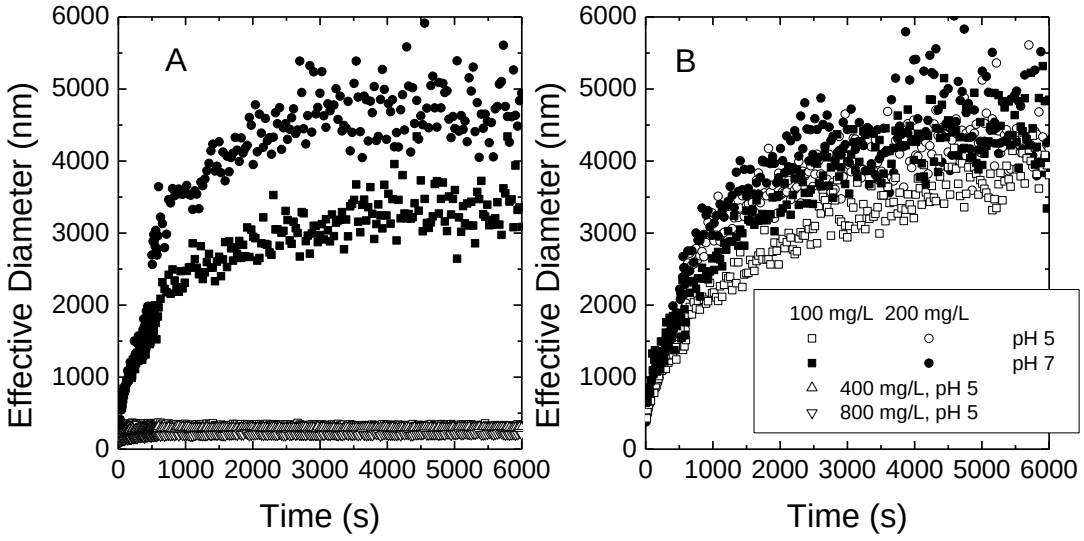

Figure 3.6. Aggregation of TNPs as a function of nanoparticle concentration (100-800 mg/L) and pH (pH 5, 7) at IS of A) 1 mM KCl and B) 10 mM KCl

The aggregation trends provide further insight into the mechanisms involved in TiO_2 retention in the packed column. In the case of pH 7, greater aggregation (aggregate >1000 nm) was observed as well as a higher degree of retention in the column (and no

elution). This was also the case at pH 5 at 10mM and low flowrate for all concentrations (100-800 mg/L) tested. These trends suggest greater aggregate size leads to more retention in the column presumably due to a physical mechanism such as straining. Conversely, a smaller aggregate size (~ 300 nm) was measured at 1 mM KCl and pH 5, which allowed for greater nanoparticle transport compared to the other conditions when aggregate sizes were >1000 nm. These trends were observed despite DLVO predictions suggested that 1 mM and pH 5 was the most favorable of all conditions tested for quartz-TNPs interactions.

The retention of TNPs in the pore structure, referred to as straining, has been reported to occur when the ratio of particle to collector diameter is approximately <0.15 (34) and also as low as 0.002 (35-38). Based upon the primary nanoparticle sizes (18.4 nm) measured by TEM and the quartz grain size, the ratio is 6.7×10^{-5} which is notably lower than the literature values at which straining should occur (ratio> 0.002) (Table 3.3). This suggests straining may not be involved; however, aggregation studies showed that aggregation occurred across the range of IS, pH and nanoparticle concentration to varying degrees, and likely the particles are not at their primary size. Hence, the ratio of particle to collector size has been calculated for the aggregates, resulting in values between 0.0009 and 0.005 (>0.002), suggesting that straining is a likely phenomenon involved in the majority of scenarios. For pH 7, ratios are >0.004 at all IS and TNPs concentration indicating that straining is likely involved in the retention of aggregated nanoparticles. This can explain the 100% retention observed at pH 7 for both flowrates, even though pH 7 is an electrostatically unfavorable condition according to DLVO

theory. This further implicates straining mechanisms dominating over DLVO-type forces at pH 7, which consequently caused the retention of TNPs.

Table 3.3. Ratio of particle and collector grain diameter as a function of IS, TNPs concentration and pH

pH	IS (mM KCl)	TNP[b] concentration (mg/L)	TNP aggregate size (nm)	Ratio of TNP aggregate and collector grain diameter[a]
5	1	100	290.0±13.2	0.0011
		200	286.6±16.3	0.0010
		400	260.3±11.2	0.0009
		800	260.0±10.02	0.0009
	10	100	1066.0±160.5	0.0039
		200	1044.3±154.5	0.0038
		400	1095.2±140.2	0.0040
		800	1115.5±170.8	0.0041
7	1	100	1186.8±73.0	0.0043
		200	1353.2±154.3	0.0049
	10	100	1338.7±140.1	0.0049
		200	1279.9±124.8	0.0047

[a] Collector grain diameter 275 µm

[b] TiO_2 nanoparticle

At pH 5, the contribution of straining is not as clear cut. At low IS the aggregate-collector ratios are below the reported threshold value for straining (Table 3.3) suggesting this mechanism is unlikely. This agrees with experimental results, which showed that TNPs successfully pass through the column at all concentrations. However, at high IS, more substantial aggregation was observed and led to a ratio of particle to collector diameter of 0.004, above the threshold value defined for straining. This is corroborated by column experiments where no elution at pH 5 and 10 mM KCl was observed at each condition except at higher flowrate (10 mL/min) and high concentrations (200-800 mg/L).

Straining can provide an explanation of the observed retention at pH 7 (all conditions) and pH 5 (most higher IS conditions). Neither DLVO theory nor straining mechanisms can provide a clear explanation for why substantial levels of eluted particles were observed with higher nanoparticle concentration (100-800 mg/L) at pH 5 and the lower IS condition. This disparity suggests an additional mechanism is involved. Blocking is a possible candidate, as it is a common phenomenon under favorable conditions.

3.3.5.3 Consideration of Blocking Effects

Since elution was only observed at pH 5 where particle-quartz interaction is favorable and particle-particle interaction is unfavorable, blocking may be involved. Blocking refers to a decline in the deposition rate due to reduced availability of

attachment sites on the collector surfaces, and this is a key mechanism under favorable conditions (39-41). However, blocking is quite unlikely under the conditions at pH 7 due to unfavorable conditions. The conditions for which the transport and retention have not been fully explained were at pH 5, at which TNPs may be considered experiencing electrostatically "favorable" interactions with the quartz. TNPs may be able to attach to the sand and form clusters of TNPs on the collectors. At pH 5, particle-particle interactions are considered "unfavorable" and may result in limiting further nanoparticle deposition after this initial layer deposits. The extent of blocking should also be sensitive to the injection concentration of nanoparticles, with a greater number of TNPs leading to more coverage of the collector surfaces and limiting the availability of collectors for further deposition (42). Indeed, greater elution was observed with increasing nanoparticle concentration at pH 5 and 1 mM (Figure 3.3).

Dynamics of blocking can be determined by the rate at which the collector surfaces are covered by particles. In a packed bed column, the collector surface coverage θ may be calculated as a function of time from experimental particle breakthrough data and assuming spherical collectors according to relationship (39, 42)

$$\theta = \frac{\pi\, a_p^2\, U\, a_c\, C_o \int_0^t (1 - C / C_o)\, dt}{3\, L\, (1 - \varepsilon)} \tag{3.3}$$

where θ is fractional surface coverage, a_p is particle radius, a_c is collector radius, U is fluid approach velocity, C_o is the column inlet nanoparticle concentration and C is the column effluent nanoparticle concentration, L is the column length, and ε is the porosity.

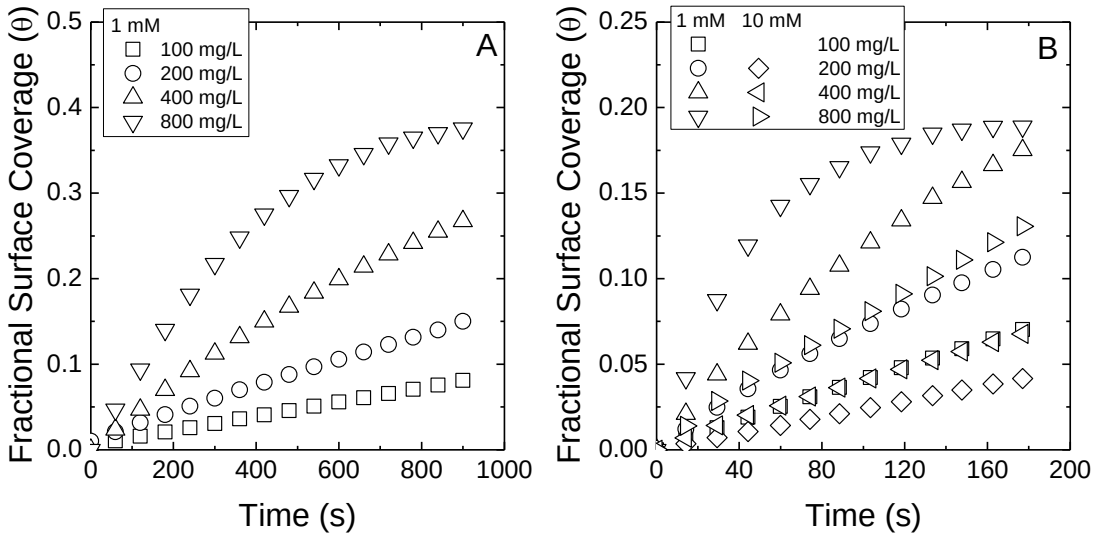

Figure 3.7. Fractional surface coverage of collectors for TNPs at pH 5 and 1 mM KCl based on aggregate sizes at A) 2 mL/min and B) 10 mL/min.

The fractional surface coverage of quartz sand by TNPs was calculated using equation 3 based upon data for pH 5 and considering both primary particle and aggregate sizes. Results were summarized in Figure 3.7 with the change of surface coverage with time by TNPs on quartz collectors at both 2 mL/min and 10 mL/min based on aggregate size. Surface coverage was observed to increase with nanoparticle concentration based on both primary particle and aggregate size. Increased coverage of collector surfaces with TNPs due to nanoparticle concentration indicates that greater numbers of nanoparticles fill up the surface sites faster. Once the collector surfaces are covered by TNPs, particle-particle repulsion becomes the dominating mechanism. TNP interaction profiles were developed using DLVO theory assuming sphere-sphere interactions (Figure 3.8). At pH 5 and 1 mM, DLVO profiles showed a high energy barrier of 8.88 kT based on primary

particle size and 140.02 kT based on aggregate size. Hence, higher elution was observed with nanoparticle concentration likely due to blocking, which may subsequently lead to particle-particle repulsion between those deposited and in suspension. A similar trend was also observed at 10 mL/min, with higher nanoparticle concentration leading to increased surface coverage by TNPs, though higher flowrate resulted in faster coverage of quartz (Figure 3.7B). Similar results were observed in a favorable transport study with 0.48 µm and 2.51 µm positively charged latex particles and glass beads conducted by Lie et al. (2002). Greater elution with increasing nanoparticle concentration was reported, although the calculated fractional surface coverage decreased with particle size (43).

Though blocking can explain the transport of TNPs at pH 5 and 1 mM under both flowrates, it is not clear why elution was observed at the higher flowrate of 10 mL/min and concentration (200-800 mg/L) suspended in 10 mM KCl and pH 5 (Figure 3.3D). It may be due to higher drag force causing aggregate breakup. During the experiments, nanoparticles did not remain in the primary form, rather aggregates formed at ~1000 nm (Figure 3.6). Due to hydrodynamic affects, these aggregates may break apart and release smaller aggregates or primary nanoparticles, and these phenomena were not considered in theoretical calculation of DLVO, straining, or blocking effects.

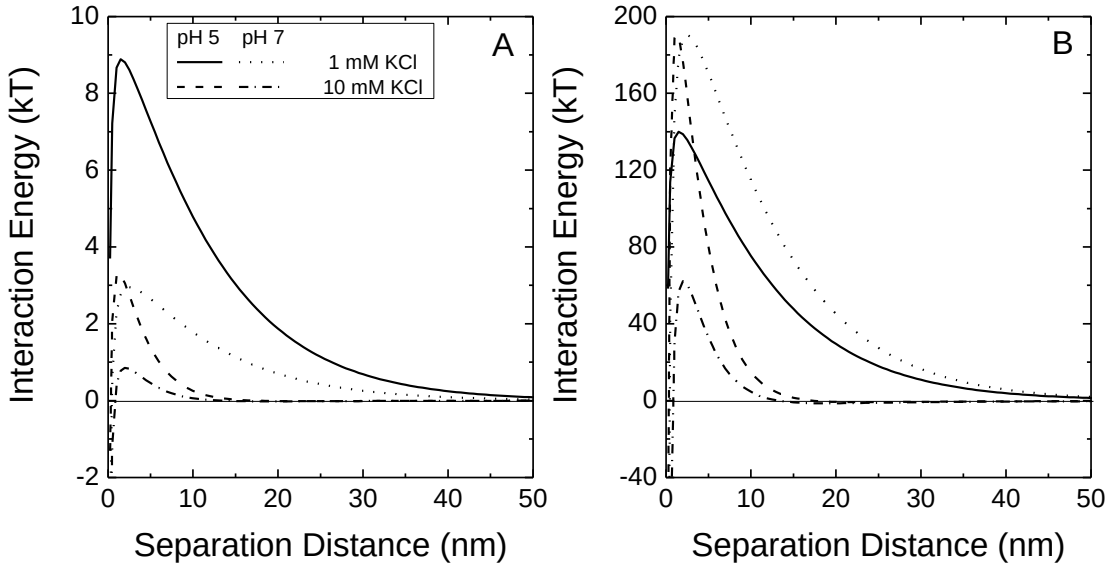

Figure 3.8. Interaction energy profiles generated with DLVO theory between TiO_2-TiO_2 at pH 5 and pH 7 as a function of separation distance .A) based on primary particle size of 18.4 nm and B) nanoparticle aggregate.

3.3.5.4 Contribution of Hydrodynamic Forces and Breakup of Nanoparticle Aggregates

At pH 5 and 10 mM, experiments at 400 and 800 mg/L resulted higher elution than at 200 mg/L. Maximum C/C_0 increased from 0 to 0.35 with nanoparticle concentrations from 100 to 800 mg/L, respectively. However, aggregation studies showed that TNPs under these conditions aggregated rapidly to >1000 nm and straining likely is the main mechanism for retention. Moreover, at lower flowrate no elution was observed under these conditions. This may be due to aggregate break up from greater flowrate and hydrodynamic forces acting on them in the pore spaces.

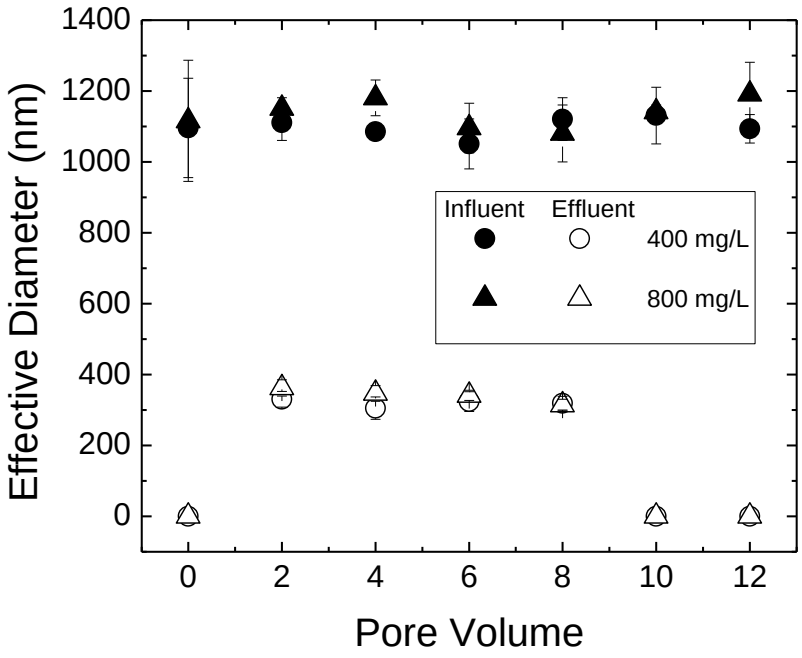

Figure 3.9. Hydrodynamic diameter in influent and effluent suspension from column experiments at pH 5, 10 mM KCl, two different nanoparticle concentrations (400 and 800 mg/L) and flowrate of 10 mL/min.

Evidence of aggregate breakup was observed by measuring the hydrodynamic diameter of the TNPs in the influent and effluent of the column experiments (pH 5, 10 mM KCl, and 10 mL/min; Figure 3.9). The influent particle sizes were within the range of 1000-1200 nm at both nanoparticle injection concentrations (400, 800 mg/L). However, effluent particle sizes were much smaller (~300 nm) than influent particle sizes. This confirms that nanoparticle aggregates were breaking up within the column under the experimental conditions tested. Under favorable conditions, TNPs aggregates were attached to the surface irreversibly and higher flowrate could detach the adhered

particles loosely bound with other particles. As the concentration of nanoparticles injected into the column was increased, the propensity for aggregates to form also was greater. In the presence of greater hydrodynamic forces acting on aggregates, they can break up and/or detach, releasing a greater number of TNPs further in the column or allowing for elution via blocking (22, 44). At pH 7, the size of aggregates formed was similar to those at pH 5 (Table 3.3 and Figure 3.7). However, unlike at pH 5, no elution was observed at the higher flowrate and NP concentrations at pH 7 (Figure 3.3D). This is attributed to aggregate breakup being unlikely, as a considerable energy barrier exists between TNPs and quartz at pH 7, as opposed to pH 5. Even at the higher flowrate, elution was not observed at pH 7.

3.4 Conclusions

In light of the concern that TNPs may become ubiquitous in our environment in future, it is important that our capacity to remove these particles via natural or engineered filtration is understood. Results indicate that a complex combination of mechanisms involving DLVO-type interactions, aggregation, straining, blocking, and aggregate breakup can dominate the transport and removal of TNPs through porous media. Removal mechanisms appeared to have a significant dependence on nanoparticle concentration, flowrate, and solution pH and IS. Aggregation of nanoparticles and subsequent straining were the dominant mechanisms of TNPs retention. At pH 7, a condition with a huge energy barrier, the highest retention level was likely due to larger

aggregates suggesting straining dominates over DLVO forces. Even under favorable conditions (pH 5), smaller and stable particles result in elution of TNPs, and blocking leads to greater elution with nanoparticle concentration. Hence, favorable conditions may not be the most effective scenario for nanoparticle removal, specifically at low IS. For optimization of TNPs removal through filters, either pH must be close to IEP for greater aggregation or the water must be adjusted to a higher IS (>10 mM). Increased flowrate leads to more elution due to aggregate breakup, indicating that slow sand filtration is most appropriate for removal of TNPs. Further consideration of these parameters, and the mechanisms described above, are necessary to optimize removal of TNPs in natural and engineered porous media.

3.5 References

(1) Wiesner, M. R.; Lowry, G. V.; Alvarez, P.; Dionysiou, D.; Biswas, P., Assessing the Risks of Manufactured Nanomaterials. *Environmental Science & Technology* **2006,** *40*, (14), 4336-4345.

(2) Robichaud, C. O.; Uyar, A. E.; Darby, M. R.; Zucker, L. G.; Wiesner, M. R., Estimates of Upper Bounds and Trends in Nano-TiO2 Production As a Basis for Exposure Assessment. *Environmental Science & Technology* **2009,** *43*, (12), 4227-4233.

(3) Xia, T.; Kovochich, M.; Liong, M.; Mädler, L.; Gilbert, B.; Shi, H.; Yeh, J. I.; Zink, J. I.; Nel, A. E., Comparison of the Mechanism of Toxicity of Zinc Oxide and Cerium Oxide Nanoparticles Based on Dissolution and Oxidative Stress Properties. *ACS Nano* **2008,** *2*, (10), 2121-2134.

(4) Long, T. C.; Saleh, N.; Tilton, R. D.; Lowry, G. V.; Veronesi, B., Titanium Dioxide (P25) Produces Reactive Oxygen Species in Immortalized Brain Microglia (BV2): Implications for Nanoparticle Neurotoxicity. *Environmental Science & Technology* **2006,** *40*, (14), 4346-4352.

(5) Trouiller, B.; Reliene, R.; Westbrook, A.; Solaimani, P.; Schiestl, R. H., Titanium Dioxide Nanoparticles Induce DNA Damage and Genetic Instability In vivo in Mice. *Cancer Res* **2009,** *69*, (22), 8784-8789.

(6) Fang, J.; Shan, X.-q.; Wen, B.; Lin, J.-m.; Owens, G., Stability of titania nanoparticles in soil suspensions and transport in saturated homogeneous soil columns. *Environmental Pollution* **2009,** *157*, (4), 1101.

(7) Jaisi, D. P.; Saleh, N. B.; Blake, R. E.; Elimelech, M., Transport of Single-Walled Carbon Nanotubes in Porous Media: Filtration Mechanisms and Reversibility. *Environmental Science & Technology* **2008,** *42*, (22), 8317-8323.

(8) Crittenden, J. C.; Montgomery Watson, H., *Water treatment principles and design*. J. Wiley: Hoboken, N.J., 2005.

(9) Elimelech, M., Gregory, J., Jia, X., Williams, R.A., *Particle Deposition and Aggregation: Measurement, Modeling and Simulation*. Butterworth-Heinemann: 1995; p 441.

(10) Kiser, M. A.; Westerhoff, P.; Benn, T.; Wang, Y.; PeÌ • rez-Rivera, J.; Hristovski, K., Titanium Nanomaterial Removal and Release from Wastewater Treatment Plants. *Environmental Science & Technology* **2009**, *43,* 6757.

(11) French, R. A.; Jacobson, A. R.; Kim, B.; Isley, S. L.; Penn, R. L.; Baveye, P. C., Influence of Ionic Strength, pH, and Cation Valence on Aggregation Kinetics of Titanium Dioxide Nanoparticles. *Environmental Science & Technology* **2009,** *43*, (5), 1354-1359.

(12) Domingos, R. F.; Tufenkji, N.; Wilkinson, K. J., Aggregation of Titanium Dioxide Nanoparticles: Role of a Fulvic Acid. *Environmental Science & Technology* **2009,** *43*, (5), 1282.

(13) Pettibone, J. M.; Cwiertny, D. M.; Scherer, M.; Grassian, V. H., Adsorption of Organic Acids on TiO2 Nanoparticles: Effects of pH, Nanoparticle Size, and Nanoparticle Aggregation. *Langmuir* **2008,** *24*, (13), 6659.

(14) Zhang, Y.; Chen, Y.; Westerhoff, P.; Hristovski, K.; Crittenden, J. C., Stability of commercial metal oxide nanoparticles in water. *Water Research* **2008,** *42*, (8-9), 2204.

(15) Keller, A. A.; Wang, H.; Zhou, D.; Lenihan, H. S.; Cherr, G.; Cardinale, B. J.; Miller, R.; Ji, Z., Stability and Aggregation of Metal Oxide Nanoparticles in Natural Aqueous Matrices. *Environmental Science & Technology,* **2010**, *44,* 1962.

(16) Lecoanet, H. F.; Wiesner, M. R., Velocity Effects on Fullerene and Oxide Nanoparticle Deposition in Porous Media. *Environmental Science & Technology* **2004,** *38*, (16), 4377-4382.

(17) Dunphy Guzman, K. A.; Finnegan, M. P.; Banfield, J. F., Influence of Surface Potential on Aggregation and Transport of Titania Nanoparticles. *Environmental Science & Technology* **2006,** *40*, (24), 7688-7693.

(18) Chowdhury, I.; Hong, Y.; Walker, S. L., Container to characterization: Impacts of metal oxide handling, preparation, and solution chemistry on particle stability. *Colloids and Surfaces A: Physicochemical and Engineering Aspects* **2010,** *368*, (1-3), 91-95.

(19) Kim, H. N.; Bradford, S. A.; Walker, S. L., Escherichia coli O157:H7 Transport in Saturated Porous Media: Role of Solution Chemistry and Surface Macromolecules. *Environmental Science & Technology* **2009**, *43*, 4340.

(20) Haznedaroglu, B. Z.; Kim, H. N.; Bradford, S. A.; Walker, S. L., Relative Transport Behavior of Escherichia coli O157:H7 and Salmonella enterica Serovar Pullorum in Packed Bed Column Systems: Influence of Solution Chemistry and Cell Concentration. *Environmental Science & Technology* **2009,** *43*, (6), 1838.

(21) Bradford, S. A.; Kim, H. N.; Haznedaroglu, B. Z.; Torkzaban, S.; Walker, S. L., Coupled Factors Influencing Concentration-Dependent Colloid Transport and Retention in Saturated Porous Media. *Environmental Science & Technology* **2009,** *43,* (18), 6996.

(22) Hong, Y.; Honda, R. J.; Myung, N. V.; Walker, S. L., Transport of Iron-Based Nanoparticles: Role of Magnetic Properties. *Environmental Science & Technology* **2009,** *43*, (23), 8834.

(23) American Public Health, A.; American Water Works, A.; Water Pollution Control, F., Standard methods for the examination of water and wastewater. *Standard methods for the examination of water and wastewater.* **1905**.

(24) Chen, G.; Hong, Y.; Walker, S. L., Colloidal and Bacterial Deposition: Role of Gravity. *Langmuir* **2009,** *26,* 314.

(25) Gregory, J., *Particles in water : properties and processes*. IWA Pub. ; Taylor & Francis: London; Boca Raton, FL, 2006.

(26) Bradford, S. A.; Kim, H. N.; Haznedaroglu, B. Z.; Torkzaban, S.; Walker, S. L., Coupled Factors Influencing Concentration-Dependent Colloid Transport and Retention in Saturated Porous Media. *Environmental Science & Technology* **2009,** *43,* 6996.

(27) Kim, H. N.; Bradford, S. A.; Walker, S. L., Escherichia coli O157:H7 Transport in Saturated Porous Media: Role of Solution Chemistry and Surface Macromolecules. *Environmental Science & Technology* **2009,** *43*, (12), 4340.

(28) Yao, K. M.; Habibian, M. T.; O'Melia, C. R., Water and waste water filtration: Concepts and applications. *Environmental Science and Technology* **1971,** *5*, 1105-1112.

(29) Derjaguin, B. V.; Landau, L., *Acta Physicochim U.S.S.R.* **1941,** *14*, 300.

(30) Verwey, E. J.; Overbeek, J. T. G., *Theory of the Stability of Lyophobic Colloids*. Elsevier: New York, N.Y., 1948.

(31) Gregory, J., Approximate Expressions for Retarded Vanderwaals Interaction. *Journal of Colloid and Interface Science* **1981,** *83*, (1), 138-145.

(32) Hogg, R.; Healy, T. W.; Fuerstenau, D. W., Mutual Coagulation of Colloidal Dispersions. *Transactions of the Faraday Society* **1966,** *62*, (522P), 1638-1651.

(33) Fatisson, J.; Domingos, R. F.; Wilkinson, K. J.; Tufenkji, N., Deposition of TiO_2 Nanoparticles onto Silica Measured Using a Quartz Crystal Microbalance with Dissipation Monitoring. *Langmuir* **2009,** *25*, (11), 6062.

(34) Xu, S.; Gao, B.; Saiers, J. E., Straining of colloidal particles in saturated porous media. *Water Resour. Res.* **2006,** *42*.

(35) Bradford, S. A.; Simunek, J.; Bettahar, M.; Tadassa, Y. F.; van Genuchten, M. T.; Yates, S. R., Straining of colloids at textural interfaces. *Water Resour. Res.* **2005,** *41*.

(36) Bradford, S. A.; Torkzaban, S.; Walker, S. L., Coupling of physical and chemical mechanisms of colloid straining in saturated porous media. *Water Research* **2007,** *41*, (13), 3012.

(37) Auset, M.; Keller, A. A., Pore-scale processes that control dispersion of colloids in saturated porous media. *Water Resources Research* **2004,** *40*, (3).

(38) Auset, M.; Keller, A. A., Pore-scale visualization of colloid straining and filtration in saturated porous media using micromodels. *Water Resources Research* **2006,** *42*, (12).

(39) Song, L.; Elimelech, M., Dynamics of colloid deposition in porous media: Modeling the role of retained particles. *Colloids and Surfaces A: Physicochemical and Engineering Aspects* **1993,** *73*, 49.

(40) Johnson, P. R.; Elimelech, M., Dynamics of Colloid Deposition in Porous Media: Blocking Based on Random Sequential Adsorption. *Langmuir* **2002,** *11*, (3), 801.

(41) Adamczyk, Z.; Siwek, B.; Zembala, M.; Belouschek, P., Kinetics of localized adsorption of colloid particles. *Advances in Colloid and Interface Science* **1994,** *48*, 151.

(42) Johnson, P. R.; Sun, N.; Elimelech, M., Colloid Transport in Geochemically Heterogeneous Porous Media: Modeling and Measurements. *Environmental Science & Technology* **1996,** *30*, (11), 3284.

(43) Liu, D.; Johnson, P. R.; Elimelech, M., Colloid Deposition Dynamics in Flow-Through Porous Media: Role of Electrolyte Concentration. *Environmental Science & Technology* **2002,** *29*, (12), 2963.

(44) Phenrat, T.; Kim, H.-J.; Fagerlund, F.; Illangasekare, T.; Tilton, R. D.; Lowry, G. V., Particle Size Distribution, Concentration, and Magnetic Attraction Affect Transport of Polymer-Modified Fe0 Nanoparticles in Sand Columns. *Environmental Science & Technology* **2009,** *43*, (13), 5079.

Chapter 4

Deposition Mechanisms of TiO_2 Nanoparticles in a Parallel Plate System

Chowdhury, I., Walker, S. L., Deposition mechanisms of TiO_2 nanoparticles in a parallel plate system. *Journal of Colloid and Interface Science* **2012,** *369*, (1), 16-22.

Abstract

In this study, a microscope-based technique was utilized to understand the fundamental mechanisms involved in deposition of TiO_2 nanoparticles (TNPs). Transport and deposition studies were conducted in a parallel plate (PP) flow chamber with TNP labeled with fluorescein isothiocyanate (FITC) for visualization. Attachment of FITC-labeled TNPs on surfaces is a function of a combination of parameters, including ionic strength (IS), pH and flowrate. Significantly higher deposition rates were observed at pH 5 versus pH 7. This is attributed to the conditions being chemically favorable for deposition at pH 5 as compared to pH 7, as predicted by DLVO theory. Additionally, deposition rates at pH 5 were reduced with IS below 10 mM due to the decrease in range of electrostatic attractive forces. Above 10 mM, aggregate size increased, resulting in higher deposition rates. At pH 7, no deposition was observed below 10 mM and above this concentration, deposition increased with IS. The impact of flowrate was also observed, with decreasing flowrate leading to greater deposition due to the reduction in drag force acting on the aggregate (regardless of pH). Comparisons between experimental and theoretical approximations indicate that non-DLVO type forces also play a significant role. This combination of observations suggest that the deposition of these model nanoparticles on glass surfaces was controlled by a combination of DLVO and non-DLVO-type forces, shear rate, aggregation state, and gravitational force acting on TNPs.

4.1 Introduction

Nanotechnology provides tremendous opportunities for future technological advancement including energy, medical, information technology, electronic devices, and environmental applications (1-5). The nanomaterial industry is growing with an excellent pace, predicted to become trillion dollar industry by 2015(1) with nanomaterial-based products expected to capture a significant portion of the consumer market (2, 6). Hence, nanomaterials will become ubiquitous in the environment, demanding an understanding of the fate, transport and toxicity of these novel materials to predict and respond to the potential environmental and public health implications.

Fate, transport and removal of nanomaterials in the environment depend on the nanomaterial interactions with surfaces (7, 8). These mechanisms apply to the fate of nanomaterials in the human body, with the aggregation and deposition of the nanomaterials affecting the extent of toxicity and transport (9). In aquatic environments, nanoparticles can attach to other particles resulting in colloid-facilitated transport (7, 10). One of the important steps for toxicity to organisms is the deposition and attachment of nanomaterials to eukaryotic and prokaryotic cell surfaces (11-13), hence the aggregation state of nanomaterials can impact the subsequent toxicity.

Deposition and attachment of nanoparticles have been extensively studied in porous media (8, 14-16). Additionally, deposition studies with nanoparticles have been examined with quartz crystal microbalance with dissipation monitoring (QCM-D) (9, 17-19). Though QCM-D is very effective tool for studying deposition trends, determination of mass transfer rates is complicated and not entirely reliable for nanoparticles due to

heterogeneous nanoparticle populations and high measured shifts (18, 19). Moreover, the deposited mass calculated by Sauerbrey relation used in QCM-D can be lower than the actual value (18, 19). Since investigations in porous media and the QCM-D are complex, well-characterized microscopic flow cells such as the parallel plate (PP) chamber and radial stagnation point flow (RSPF) system may be utilized to understand the fundamental physical-chemical mechanisms involved in the particle-surface interactions. Previously these systems have only been involved in bacterial and colloidal deposition studies (20-23). Therefore, in this study, the microscopic PP technique was utilized to understand the fundamental mechanisms involved in attachment of nanoparticles to surfaces.

TiO_2 nanoparticles (TNPs) were used as model nanoparticles, as nano-TiO_2 is widely used in consumer products (2, 24, 25) and approximately 40,000 metric tons/year is produced in the US alone (26). TNPs have shown toxic effects to both eukaryotic and prokaryotic cells (11, 27-29). Recent work showed that TNPs have been found in wastewater treatment effluent, mostly in biosolids (30). Therefore, the main objectives of this study were 1) to demonstrate a direct experimental method for real time visualization of nanoparticles and 2) to elucidate the deposition and attachment behavior of TNPs on surfaces under attractive and repulsive conditions and to identify the role of ionic strength (IS), pH and flowrate on the deposition kinetics.

4.2 Materials and Methods

4.2.1 Fluorescent Labeling and Characterization of TNPs

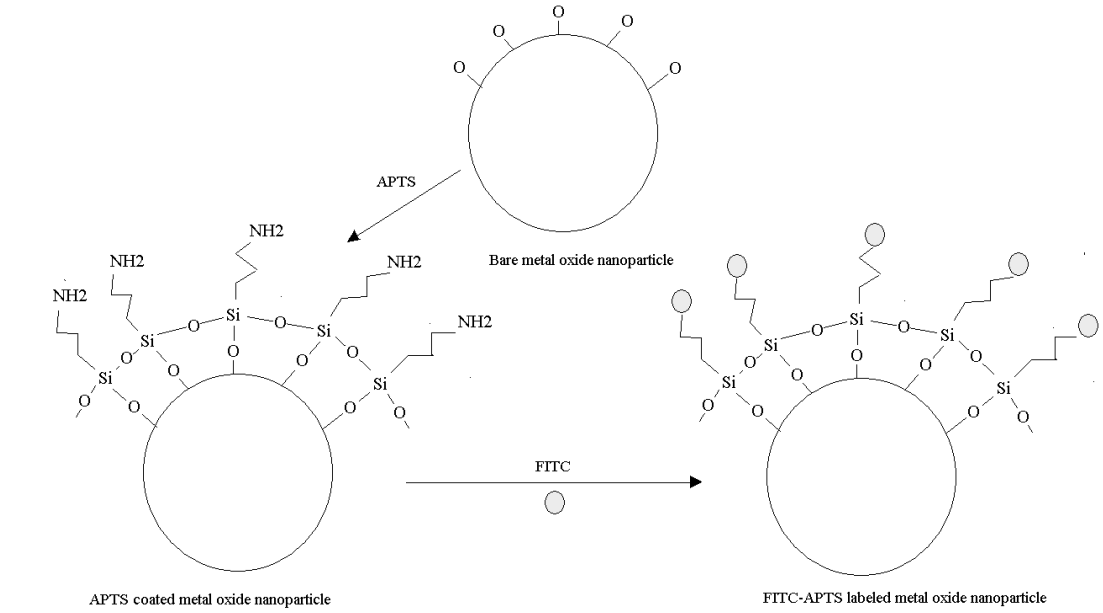

Figure 4.1. Flow diagram of labeling of bare TiO_2 nanoparticle with Flourescein Isothiocyanate Isomer I (modified from Xia et al. (31)).

TNPs were labeled for visualization with fluorescent microscopy following a procedure developed by Xia et al. (31). Fluorescein Isothiocyanate Isomer I (FITC) was used as a flourophor for the TNP (31). FITC cannot be attached to TNPs directly; hence, TNPs were functionalized with aminopropyltriethoxysilane (APTS) so that amine functional groups were available to attach FITC. Anhydrous dimethylformamide (DMF) was used as solvent for dispersing 4 mg TNPs in 3 mL DMF. Then 2% APTS (diluted in DMF) was added in the TNPs suspension and sonicated for 30 min under nitrogen. The

TNPs suspension was kept at room temperature (23-25^{o}C) for 20 h to complete functionalization reaction. TNPs functionalized with APTS were rinsed twice by centrifuging at 3700 g for 15 min and washing with DMF. 1 mg of FITC was added 0.5 mL DMF and mixed with the APTS-modified TNPs resuspended in 0.5 mL DMF. After stirring the suspension for 4 h, FITC-modified TNPs were collected by centrifuging at 3700 g for 15 min, followed by washing with DMF twice. Then FITC-labeled TNPs were dried under vacuum and stored as dry powder at 4^{o}C. These chemicals were purchased from Sigma Aldrich (St. Louis, MO). The procedure for fluorescent labeling of TNPs is shown schematically in Figure 4.1. The modified FITC-labeled TNPs are referred to as TiO_2-FITC.

Surface coverage of TNPs by FITC was determined from thermogravimetric analysis (TGA/SDTA 851, Mettler-Toledo Inc., Columbus, OH). Both bare TiO_2 and TiO_2-FITC of 100 mg were used for TGA where the sample was heated at a constant temperature range of 10^{o}C /min up to 700^{o}C in the presence of oxygen. During the heating process, the weight loss of the sample was recorded.

Transmission electron microscopy (TEM) (FEI-PHILIPS CM300 electron microscope (Hillsboro, OR)) operated at 300 kV was utilized to determine the particle size of the TiO_2-FITC. Average primary particle size was determined by measuring the size of at least 200 nanoparticles from 10 different TEM images using ImageJ software (National Institute of Health, US). A ZetaPALS analyzer (Brookhaven Instruments Corp., Holtsville, NY) was used to determine the isoelectric point (IEP) of the TiO_2-FITC at 10 mM. ZetaPALS was also used to measure the electrophoretic mobility (EPM) over a

wide range of IS (1-100 mM) at both pH 5 and 7. Dynamic light scattering (DLS, Brookhaven model BI-9000AT digital correlator, Holtsville, NY) was utilized at a wavelength of 661 nm and a scattering angle of 90° to determine the particle size in aqueous suspension, typically referred to as the hydrodynamic diameter (7, 10). Average hydrodynamic diameter was determined by taking an arithmetic average of the measured diameters over 30 min. pH was controlled by adding 10 mM HCl or 10 mM KOH. pH was measured at the beginning and end of experiments to confirm no changes beyond ±0.1 pH units. All chemicals described here were ACS reagent grade (Fisher Scientific, PA).

The stability of TiO_2-FITC in aqueous suspension was determined by measuring the optical density and the hydrodynamic diameter of 10 mg/L of TiO_2-FITC suspension at pH 5.0 and 7.0 at 25°C. The sedimentation experiments were conducted by measuring the absorbance with 1 cm light path at a wavelength of 500 nm via a UV/Vis spectrophotometer (DU 800 Spectrophotometer, Beckman Coulter, CA). Absorbance value was recorded at 30 s intervals for 60 min. The initial absorbance value of nanoparticles suspension at time = 0 is set as C_0 and sedimentation rate was analyzed by normalized C/C_0 plot. The hydrodynamic diameter of nanoparticles was evaluated using dynamic light scattering (DLS, Brookhaven model BI-9000AT digital correlator, Holtsville, NY) at 30 s intervals for 60 min for the nanoparticle suspension at pH 5.0 and 7.0 at 25°C. All the experiments were initiated after 30 s of sonication in a water bath

(Transsonic 460/H, Barnstead/Lab-line, Melrose Park, IL). For selected experiments, cerium dioxide nanoparticles labeled with FITC (CeO_2-FITC) was used.

4.2.2 TiO_2-FITC Deposition Experiments Using a Parallel Plate System

Nanoparticle deposition experiments were conducted in a parallel plate (PP) flow chamber system (Product # 31-010, GlycoTech, Rockville, MA) (Figure 4.2), which has been described previously (32-34). Briefly, the inner dimensions of the PP chamber are 6 cm x 1 cm x 0.0762 cm consist of a Plexiglass block, a flexible silicon elastomer gasket, and a microscope glass slide.

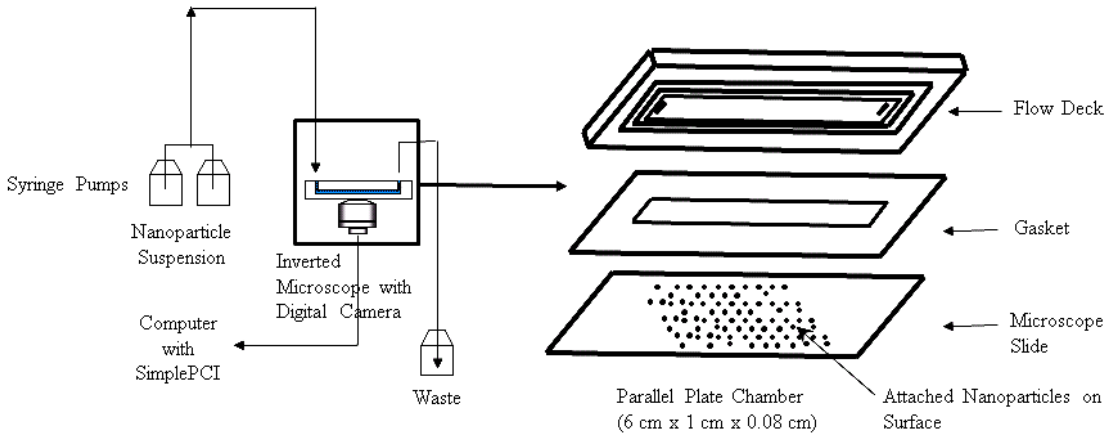

Figure 4.2. Schematic diagram of deposition experimental setup using a parallel plate system.

The parallel plate (PP) system was installed on the stage of an inverted fluorescent microscope (IX70, Olympus, Center Valley, PA). Images of TiO_2-FITC onto the glass were captured by infinity- corrected 40x objective (Olympus UPlanF1, N.A., 0.75). A Xe lamp with a fluorescent filter set (excitation 480 nm/emission 510 nm, Chroma Technology Corp., Brattleboro, VT) was used to take images.

Before deposition experiments and characterization, all glass slides (Fisher Scientific, Pittsburgh, PA) were rinsed extensively with surfactant, ethanol and deionized water as mentioned elsewhere (21, 35). 2% Extran MA02 solution (EM Science, Gibbs-town, NJ) was used for cleaning, and ethanol and deionized water were used for rinsing. Then glass slides were immersed in a 2% RBS 35 detergent solution (Pierce, Rockford, IL) and sonicated for 15 mins and ethanol and deionized water was used for final cleaning. The electrokinetic properties of the glass were determined by using a streaming potential analyzer (EKA, Anton Paar, US) with an asymmetric clamping cell (36). Measurements were obtained over the solution chemistry used in deposition experiments.

A digital camera (Retiga EXI 1394, Qimaging, British Columbia) fitted with the microscope was used to acquire images of TiO_2-FITC deposited on the glass surfaces every 30 s for 30 min, which were then analyzed with the supplied software (SimplePCI, Precision Instruments, Inc., Minneapolis, MN). The number of deposited TiO_2-FITC was determined for each time interval by comparing the changes between successive images. Injection concentrations of TiO_2-FITC nanoparticles were 10 mg/L (~10^{12} primary TiO_2-FITC / mL). Nanoparticles were sonicated for 30 s prior to experiment. Flowrates of 1 mL/min and 0.1 mL/min were employed, corresponding to average flow velocities of 7.9

m/hr and 0.79 m/hr, respectively. These values correspond to a typical range of rates in rapid granular filtration bed and groundwater environments (33, 37). TiO_2-FITC Reynolds numbers (10^{-5} and 10^{-3}), corresponding to Peclet numbers (1.59×10^{-3} and 1.40×10^{-2}), indicate a diffusion-dominated transport regime (7). All experiments were conducted in triplicate at two different pH conditions and at ambient temperature (22-25^{o}C). All chemicals were ACS research grade (Fisher Scientific, PA).

The number of particles deposited versus time was plotted from the acquired images. The deposition flux (J) was calculated by dividing the initial slope of this curve by the microscope viewing area (211 μm x 168 μm). The experimental particle transfer rate coefficient, $k_{experimental}$, which is a measure of the deposition kinetics of the nanoparticles, was determined using the following equation (7, 32, 33, 38):

$$k_{experimental}=J/C_0 \quad (4.1)$$

where C_0 is injected nanoparticle concentration.

4.3 Results and Discussion

4.3.1 Characterization of Nanoparticles

TEM image of TiO_2-FITC nanoparticles are shown in Figure 4.3A. From the TEM image analysis, the average particle size of bare TiO_2 was insignificantly different from TiO_2-FITC (17.7 ± 6.1 nm). The particle size distribution of TiO_2-FITC nanoparticles is shown in Figure 4.3B. TiO_2-FITC nanoparticles were between 5 and 45 nm with most of nanoparticles within 10-20 nm (approximately 70% of nanoparticles).

IEP of TiO_2-FITC was found to be about pH 5.6 (Figure 4.4). TGA of TiO_2-FITC is summarized in Figure 4.5. Bare TiO_2 was stable up to 700^oC with only 1.5 % a decrease in mass observed; whereas, a 4.5% of decrease of mass was observed for TiO_2-FITC, indicating FITC being only 3% of total mass of the TiO_2-FITC complex.

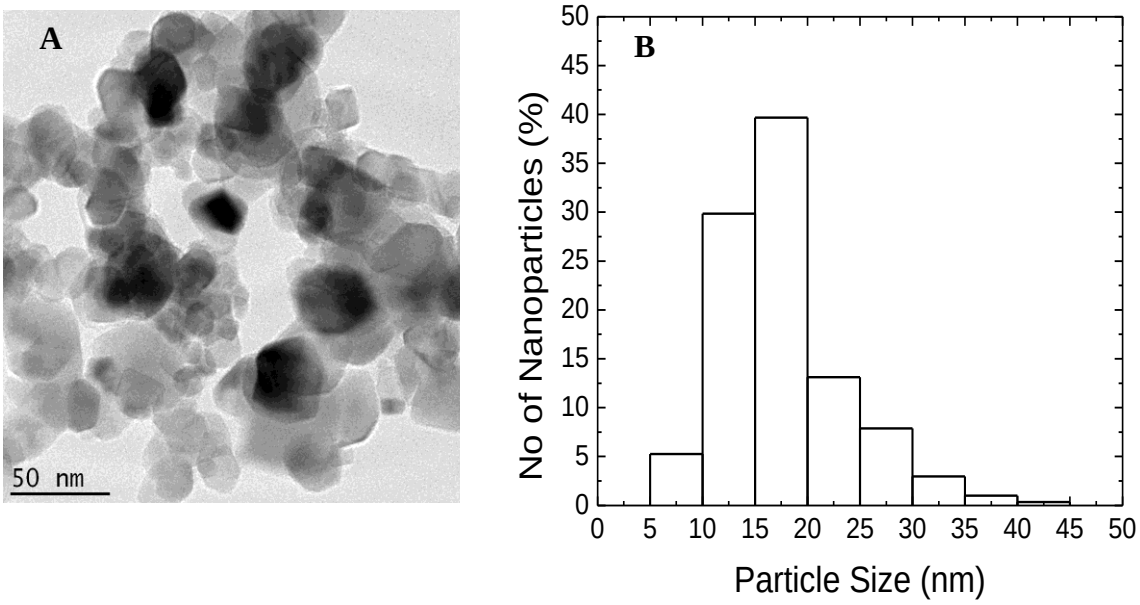

Figure 4.3. A) Transmission electron microscope (TEM) FITC-coated TiO_2 nanoparticles taken at 300 kV. B) Particle size distribution of FITC-coated TiO_2 from the TEM image

The average effective hydrodynamic diameter of TiO_2-FITC was measured over 30 min and is presented as a function of pH and IS (Figure 4.6A). The particle size of TiO_2-FITC was stable from 1 mM through 10 mM at both pH values. The average hydrodynamic diameter was ~700 nm at lower IS conditions through 10 mM and pH 5, with aggregate size reaching ~1200 nm at 100 mM. The average hydrodynamic diameter was ~800 nm from 1 to 10 mM and pH 7, and increased to ~1000 nm at 100 mM.

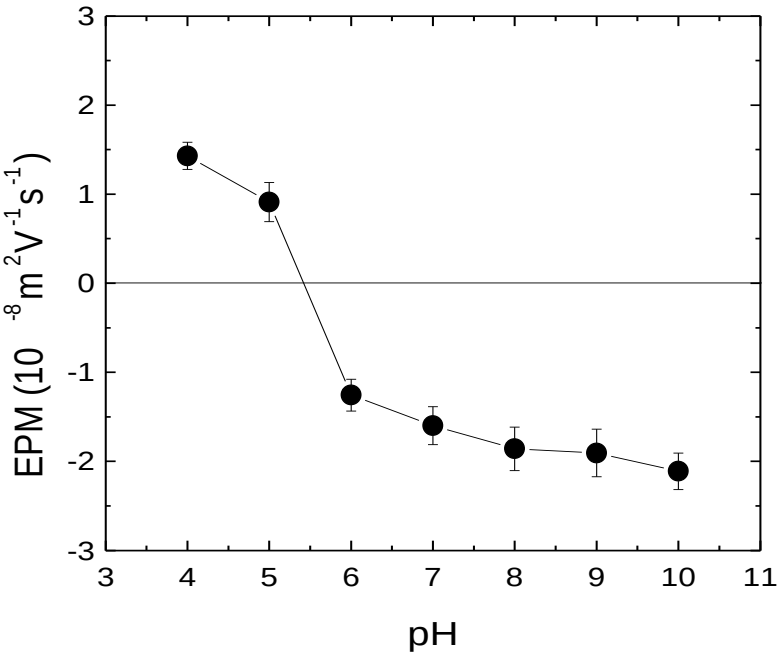

Figure 4.4. Electrophoretic mobility (EPM) of FITC-coated TiO_2 as a function of pH at a fixed nanoparticle concentration (100 mg/L), ionic strength (10 mM KCl) and temperature (25^{o}C).

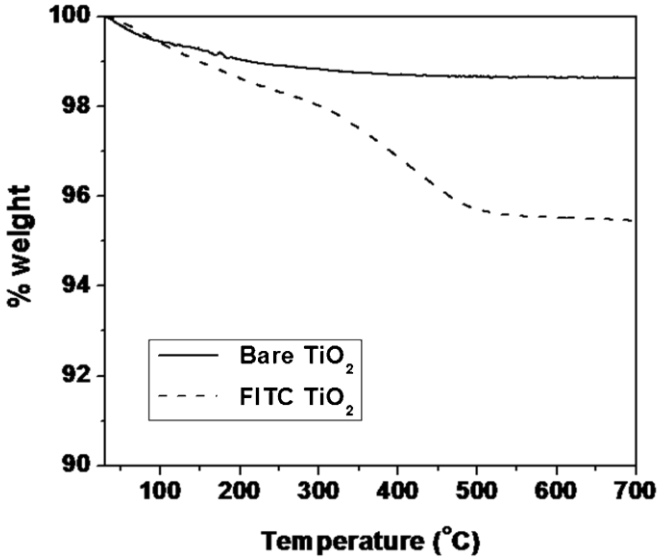

Figure 4.5. Thermogravimetric analysis of bare and FITC-coated TiO_2

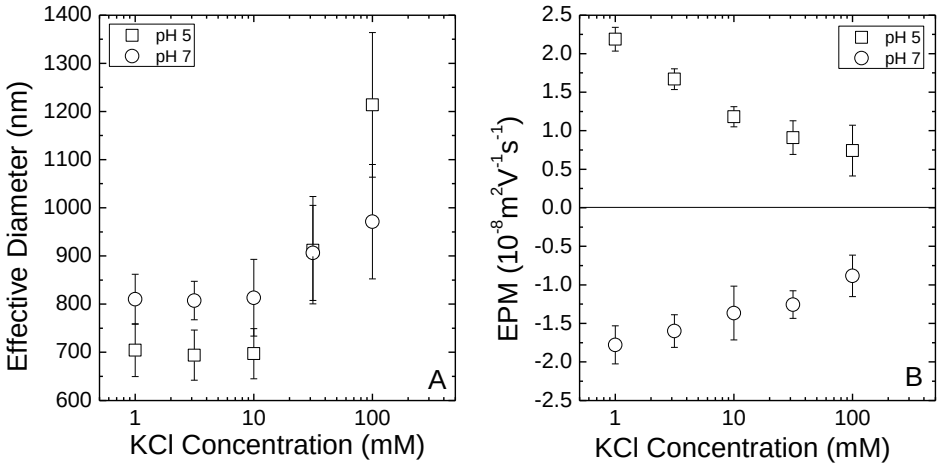

Figure 4.6. (A) Effective hydrodynamic diameter and (B) Electrophoretic mobility (EPM) of TiO_2-FITC as a function IS at both pH 5 and 7. Effective diameter was determined as the arithmetic average of nanoparticle effective diameter over 30 min.

4.3.2 Electrokinetic Data and Interpretation with DLVO Theory

Electrokinetic characterization data for TiO_2-FITC are presented in Figure 4.6B. At pH 5, the EPM of TiO_2-FITC was positive across the range of IS; whereas, at pH 7 negative EPM values were observed. At pH 5, EPM of TiO_2-FITC nanoparticles changed from (2.19±0.16) x 10^{-8} $m^2V^{-1}s^{-1}$ to (0.74±0.33) x 10^{-8} $m^2V^{-1}s^{-1}$ for IS 1 and 100 mM respectively. At pH 7, increased IS resulted in the EPM changing from (-1.78±0.25) x 10^{-8} $m^2V^{-1}s^{-1}$ to (-0.88±0.27) x 10^{-8} $m^2V^{-1}s^{-1}$. At both pH values, the increased IS resulted in a reduced EPM, which is attributed to electrical double layer compression (7).

In order to predict the deposition behavior of TiO_2-FITC nanoparticles on glass surfaces, the classical Derjaguin-Landau-Verwey-Overbeek (DLVO) theory was applied to generate interaction profiles between TiO_2-FITC nanoparticles and glass surfaces assuming a sphere-plate geometry (15, 39, 40) :

$$V_{el} = \pi\varepsilon_0\varepsilon a_p \left\{ 2\psi_p\psi_c \ln\left[\frac{1+\exp(-\kappa h)}{1-\exp(-\kappa h)}\right] + (\psi_p^2 + \psi_c^2)\ln\left[1-\exp(-2\kappa h)\right] \right\} \quad (4.2)$$

$$V_{vdW} = -\frac{A_{102}\, a_p}{6h}\left[1+\frac{14\,h}{\lambda}\right]^{-1} \quad (4.3)$$

Values of 8.854 × 10^{-12} C/V/m and 78.5 were assumed for permittivity of free space (ε_0) and the dielectric constant of water (ε) respectively (7, 15). Hamaker constant (A_{102}) of 10^{-20} J was assumed for the quartz-TiO_2-FITC -water system (18). In case of surface potentials (ψ_p, ψ_c), zeta potentials of both TiO_2-FITC and glass surfaces

were used for DLVO interaction energy profile calculations. A characteristic wavelength (λ) of 100 nm was assumed (7).

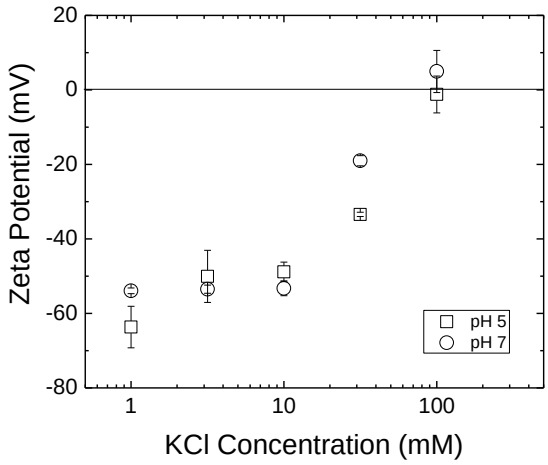

Figure 4.7. Streaming potential of glass surface as a function of ionic strength at both pH 5 and pH 7.

Smoluchowski equation was applied to convert EPM data of TiO_2-FITC nanoparticles to zeta potential (7). Both DLVO and Smoluchowski equation are applicable when Debye length of particle is much less than particle size (7, 41). The zeta potential of the glass surfaces was measured as a function of pH and IS (Figure 4.7) and these values were used to generate DLVO interaction profiles between TiO_2-FITC and glass surfaces (shown in Figure 4.8). Calculations were done with two different particle sizes, assuming an aggregate (size measured by DLS) at given pH and IS and a non-aggregated primary particle. The total interaction energy calculated based on primary particle size is much lower than for aggregates. Since some degree of aggregation was observed for TiO_2-FITC nanoparticles under all conditions in a batch system, likely the

actual extent of interaction occurs somewhere in between these two assumed extremes (primary particle and large aggregate size measured by DLS). Hence the DLVO calculations based on aggregate size are considered appropriate for predicting the extent of surface-nanoparticle interactions.

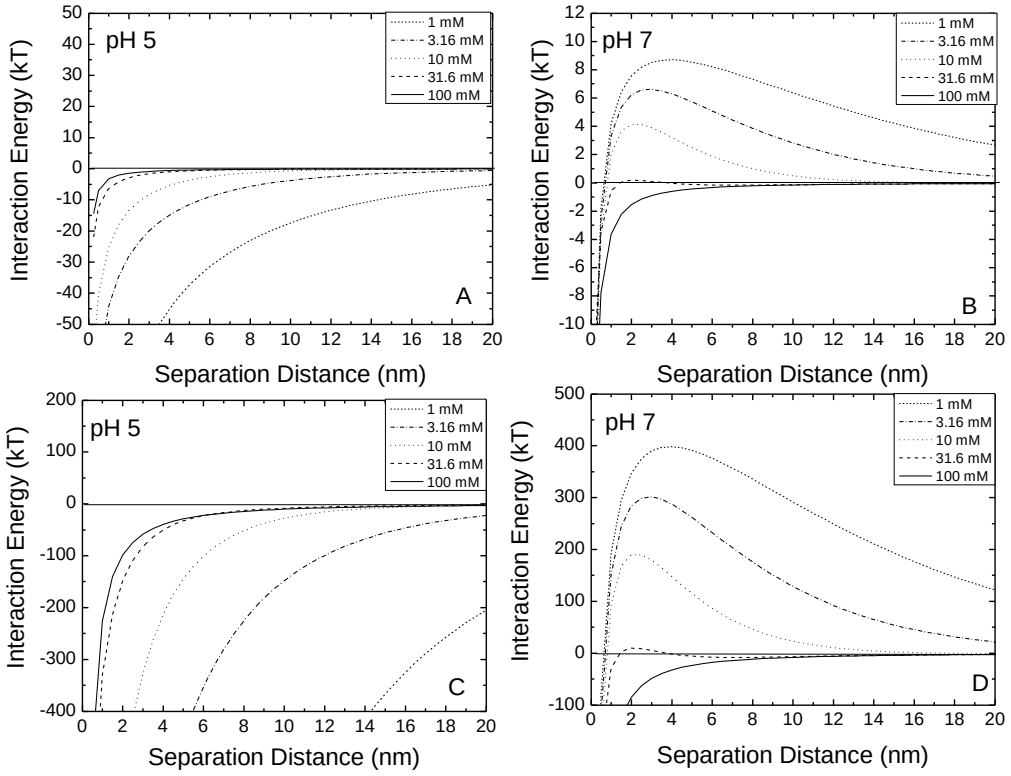

Figure 4.8. Interaction energy profiles between TNP and glass surface generated with DLVO theory at pH 5 and 7 as a function of separation distance. Interaction energies in (A) and (B) were calculated using primary particle size. Interaction energies in (C) and (D) were calculated with aggregate size.

DLVO interaction profiles (based on both primary particle and aggregate size) indicate that pH 5 is an electrostatically favorable condition with no energy barrier to interaction and deep primary minimum. However, the magnitude of the primary energy minimum is sensitive to solution chemistry and decreases from -173 kT to -15 kT based on primary particle size and -6895 kT to -993 kT based on aggregate size from IS 1-100 mM at 0.5 nm separation distance. Hence, the range of the attractive forces between the particle and glass decreased with IS due to electrostatic double layer compression (7). If DLVO forces were to dominate this system, it would predict that the interaction of nanoparticles with glass would be the most substantial at pH 5, and interactions would be reduced with increased IS as the range of attractive forces decreased. At pH 7, a virtually insurmountable energy barrier was observed under almost all conditions considering either primary particles or aggregates. However, increased IS showed a lower energy barrier existing (changed from 8.7 kT to 0 kT and from 398.2 kT to 0 kT based on primary particle and aggregate size, respectively). Secondary minima were observed in the lower to mid IS range (1-31.6 mM) from -0.002 kT to -0.16 kT and -0.08 kT to -8.21 kT with IS 1-31.6 mM based on both primary particle size and aggregate size, respectively. No energy barrier or secondary minimum was observed at 100 mM and pH 7. Hence, less nanoparticle deposition should be observed at pH 7 (unfavorable condition) with respect to pH 5 (favorable condition). Deposition rate of nanoparticles should be enhanced with increasing IS due to the reduced energy barrier to interactions of the TiO_2-FITC with the glass surface, following DLVO predictions. These DLVO predictions were verified by our experimental deposition studies as presented below.

4.3.3 Deposition Studies

To understand the mechanisms of deposition and attachment of nanoparticles, transport studies were conducted in the PP system as a function of pH, IS and flowrate. Deposition results of TiO_2-FITC on glass surfaces are shown in Figure 4.9. $k_{experimental}$ values at pH 5 based on primary particle size showed a decreasing trend from 2.14×10^{-12} m/s to 8.43×10^{-13} m/s with IS (1-100 mM) at 1 mL/min which follows DLVO predictions. However, $k_{experimental}$ values based on the aggregate size showed different trend at pH 5 (Figure 4.9B). Overall, $k_{experimental}$ values based on aggregate size were approximately 10^5 times higher than based on primary particle size. Since substantial aggregation was observed in the TiO_2-FITC suspension (Figure 4.2A), $k_{experimental}$ values based on the aggregate size appear more appropriate for quantifying TiO_2-FITC nanoparticle deposition in the parallel plate system. At 1 mL/min and pH 5, $k_{experimental}$ values decreased from 1.35×10^{-7} m/s to 8.43×10^{-8} m/s with increasing IS from 1 mM to 10 mM which is aligned with DLVO predictions. Above 10 mM, $k_{experimental}$ values increased from 8.43×10^{-8} m/s to 2.74×10^{-7} m/s with greater IS which is in contrast to DLVO predictions. A similar trend was observed at the lower flowrate as well. Approximately a 50-80% increase in $k_{experimental}$ values were observed with respect to the higher flowrate, although overall trend remained same. This may be due to less drag force acting on the TiO_2-FITC particles at the lower flowrate, as drag force is linearly dependent on fluid velocity and particle size (7, 10).

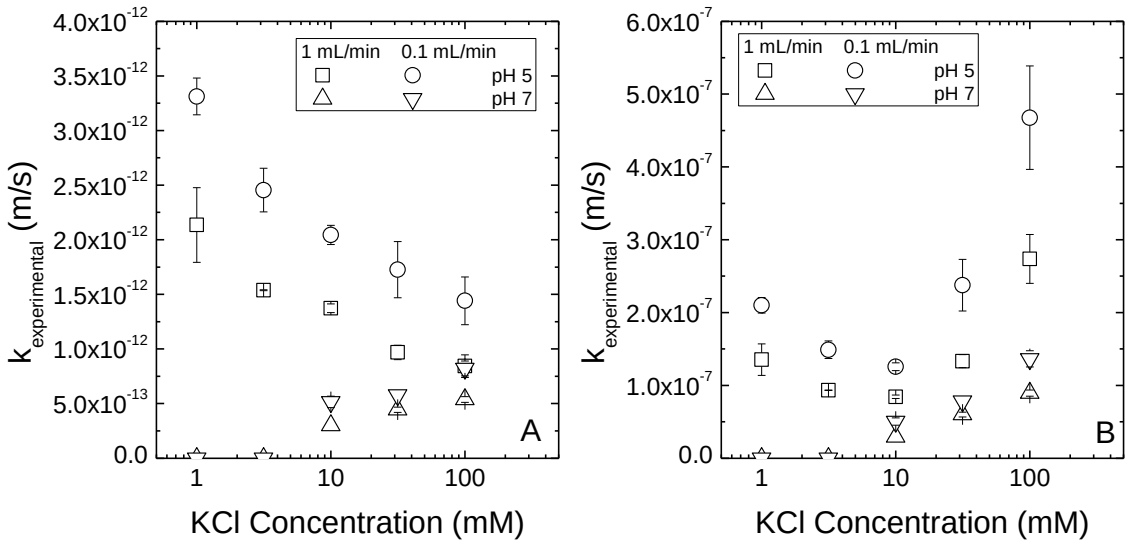

Figure 4.9. Particle transfer coefficient ($k_{experimental}$) of TiO_2-FITC on glass surface as a function of IS at two different pHs (pH 5 and pH 7) and flow rates (1 mL/min and 0.1 mL/min) based on (A) primary particle size and (B) aggregate size.

At pH 7, $k_{experimental}$ values were approximately 2-4 times lower than at pH 5, which was predicted by DLVO theory. There was no measurable $k_{experimental}$ value below 10 mM, which indicates that high energy barrier at low IS and pH 7 inhibits the deposition of TiO_2-FITC nanoparticles on glass surfaces. However, deposition was observed across the range of 10 mM to 100 mM KCl, which is attributed to interactions in a secondary minimum. Based on primary particle size, at 1 mL/min, $k_{experimental}$ values increased from 3 x 10^{-13} m/s to 5.38 x 10^{-13} m/s with IS from 10 to 100 mM. Based on aggregate size, approximately 10^5 times higher $k_{experimental}$ values were determined (2.93 x 10^{-8} m/s to 8.94 x 10^{-8} m/s with IS from 10 to100 mM). Although trends remained the

same considering primary particle size or aggregate size at pH 7, a higher sensitivity to IS was observed when particles were considered as aggregates.

Observed phenomena followed the DLVO predictions; however, calculations based on aggregate size showed a different trend. Specifically at high IS (>10 mM) DLVO failed to explain the observed phenomena. Aggregation studies (Figure 4.2A) indicated that nanoparticle aggregates were similar size up to 10 mM and a sharp increase of aggregate size was observed above this IS at both pH. At this greater IS, large aggregate size (>1000 nm) coupled with high particle density (3.8 g/cm^3) (42) for TiO_2-FITC can result in additional mechanisms contributing to deposition of nanoparticles on surfaces. Further discussion of the mechanisms involved in the observed deposition trends of TNPs is found in the next section.

4.3.4 Mechanistic Interpretation

4.3.4.1 Comparisons with Theoretical Predictions

Colloidal particle transport and deposition have been modeled by using classical convection-diffusion equation for granular filtration, radial stagnation point flow, and PP systems (7, 10, 43). Since it is difficult to achieve an analytical solution for this equation, Smoluchowski-Levich (SL) approximation was used (44, 45). However, there are few assumptions in the SL approximation that limit the prediction of a real condition (7, 33, 44). This approximation is only applicable for favorable conditions (perfect sink model) assuming van der Waals attraction between nanoparticles and surfaces are offset by

hydrodynamic forces. The SL approximation does not consider effects of external forces (gravity, hydrodynamic corrections, electrostatic interactions) on the mass transfer. In fact, the SL approximation considers only the effect of diffusion in the deposition process (7, 10). The SL approximation is based upon the following equations for calculation of a theoretical particle transfer rate coefficient (k_{ideal}) (7, 33):

$$k_{ideal} = \frac{D_{\infty}}{\Gamma\left(\frac{4}{3}\right) a_p} \left(\frac{2\,Pe}{9\,x/b} \right)^{1/3} \qquad (4.4)$$

where primary particle and aggregate size are used for nanoparticle radius (a_p); Stokes-Einstein equation is used for calculating bulk diffusion coefficient ($D_\infty = k_B T/(6\pi\mu a_P)$) (7) ; Peclet number (Pe) is calculated by using equation $3\,u a_p^3/(2\,b^2 D)$ (7) for PP system; u and μ are the fluid velocity and fluid dynamic viscosity respectively; x (half of the flow chamber length), and b (midway depth of PP system) are determined from the PP configuration.

At pH 5 and 1 mL/min, k_{ideal} varied from 3.14×10^{-7} m/s to 2.19×10^{-7} m/s with IS from 1 to 100 mM based on aggregate size; whereas, a constant k_{ideal} value of 3.67×10^{-6} m/s was calculated based on primary particle size. Calculation based on aggregate size would be more appropriate as aggregation was observed due to increased IS. Comparisons between $k_{experimental}$ and k_{ideal} showed that at pH 5 and 1 mL/min, experimental values were lower than ideal values up to 31.6 mM (Figure 4.10A). However, at 100 mM, $k_{experimental}$ was 25% greater than k_{ideal}. This may be due to the higher aggregate size (1214 nm), which exceeded the limit of 1000 nm where

gravitational force can significantly influence the deposition of particles (7, 10). These observed effects were substantial at the lower flowrate (0.1 mL/min). At the lower flowrate, k_{ideal} values varied from 1.46 x 10^{-7} m/s to 1.01 x 10^{-7} m/s; whereas, $k_{experimental}$ varied from 2.09 x 10^{-7} m/s to 4.68 x 10^{-7} m/s. $k_{experimental}$ exceeded k_{ideal} at almost all IS conditions tested. However, the aggregate size remained 700 nm for IS conditions l-10 mM, which is within the range of 1 µm where diffusion can dominate (10). However, $k_{experimental} > k_{ideal}$ indicates that external forces dominate over diffusive forces. This may be due to the high density of TiO_2 nanoparticles (3.8 g/cm^3) (42) as the influence of external forces was disregarded in SL approximations.

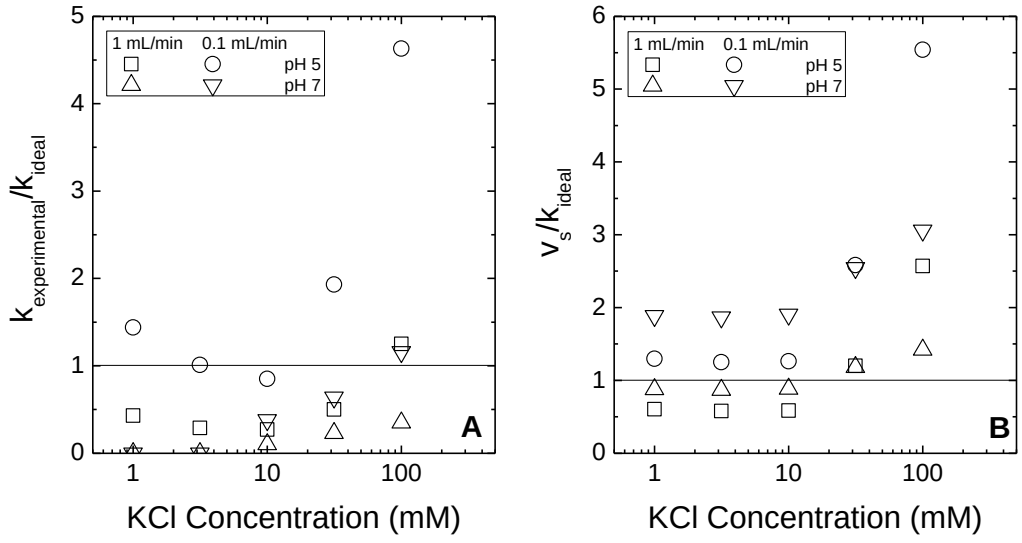

Figure 4.10. Relative mass transfer of TiO_2-FITC nanoparticles presented as (A) $k_{experimental}/k_{ideal}$ and (B) v_s/k_{ideal} as a function of IS, pH and flowrate.

At pH 7 and 1 mL/min, k_{ideal} was varied from 2.86 x 10^{-7} m/s to 2.53 x 10^{-7} m/s with IS from 1 to 100 mM. The ratios of $k_{experimental}$ /k_{ideal} were between 0.10 and 0.35 which indicates that an unfavorable condition at pH 7 reduces deposition rates due to high energy barrier. Though other external forces still may be involved, these effects were limited due to the unfavorable physical-chemical conditions (substantial energy barrier and high shear rate). Hence, at the lower flowrate, a significant increase was observed in the ratios of $k_{experimental}$ /k_{ideal} (0.38 to 1.16 with IS 10-100mM). At pH 7 and 100 mM, $k_{experimental}$ actually exceeded k_{ideal} because at the higher IS, there was a substantial attractive force resulting in no interaction energy barrier. Hence, external forces other than diffusion can significantly affect the deposition rates at low flowrate due to reduction of shear forces.

Comparisons between experimental results and theoretical values by SL approximations indicate that external forces are more dominant than diffusive forces, especially at IS>10 mM. Analyses of DLVO interaction profiles in the previous section showed that DLVO theory failed to explain the deposition process at high IS, further indicating the involvement of another, external force. At constant flowrate, the hydrodynamic forces will also be similar for all experiments assuming no aggregation. However, aggregation is occurring and the extent to which gravitational and hydrodynamic forces are contributing is a function of particle density, aggregate size and morphology (7, 10).

4.3.4.2 Role of Settling on Deposition and Attachment of TiO_2-FITC

The contribution of gravity to the interaction forces can be estimated by calculating the particle settling velocity for TiO_2-FITC nanoparticles using Stoke's law (37):

$$v_s = \frac{(\rho_p - \rho) g d_p^2}{18\,\mu} \tag{4.5}$$

where v_s is the particle settling velocity, ρ_p is the specific density of the particle, ρ is the specific density of fluid, μ is the fluid dynamic viscosity, d_p is the particle diameter, g is the gravitational acceleration, and t is time.

Settling rates were on the order of 10^{-10} m/s and 10^{-7} m/s based on primary particle size and aggregate size respectively. At pH 5, settling rates increased from 1.89 x 10^{-7} m/s to 5.62 x 10^{-7} m/s with IS ranging from 1 to 100 mM, although at lower IS (1-10 mM) settling rates were constant. Settling rates at pH 7 followed a similar trend at lower IS and increasing from 2.50 x 10^{-7} m/s to 3.60 x 10^{-7} m/s with IS ranging from 1 to 100 mM.

Both diffusion and sedimentation can contribute to the deposition of TiO_2-FITC nanoparticles in the parallel plate system (10, 46, 47). Particle deposition flux by sedimentation can be determined by $v_s C_0$ whereas $k_{ideal} C_0$ can represent the particle deposition flux by diffusion (33, 48, 49). For higher flowrate (1 mL/min) and at pH 5, k_{ideal} was greater than v_s until 10 mM (Figure 4.5B), which indicates that diffusion was dominant under these conditions. However above 10 mM, v_s exceeded k_{ideal} suggesting

that sedimentation contributes more than convective diffusion at these IS. It is due to the higher IS leading to larger aggregate size which reduced diffusion coefficient and increased settling rates (7, 10). Hence, $k_{experimental}$ exceeded k_{ideal} under those conditions. The influence of settling was substantial at low flowrate (Figure 4.10B). The settling rate exceeded k_{ideal} under all conditions indicating that sedimentation was dominating over diffusive transport. Due to the high settling rates, $k_{experimental}$ exceeded k_{ideal} almost all conditions (Figure 4.9A).

For pH 7, v_s was smaller than k_{ideal} up to 10 mM indicating that diffusive transport was dominant over gravitational forces on deposition of TiO_2-FITC nanoparticles on surfaces. Like pH 5, increased aggregate size due to higher IS (> 10 mM) resulted in $v_s > k_{ideal}$. However, $k_{experimental}$ was still less than k_{ideal} as the condition was electrostatically unfavorable at pH 7. At the lower flowrate, k_{ideal} was less than v_s under all conditions indicating that high density and large aggregate size of TiO_2-FITC resulted in dominance of gravitational forces over diffusive force. Hence, $k_{experimental}$ values were significantly higher at the lower flowrate.

4.3.4.3 Further Evidence of Gravity Effect with Cerium Dioxide Nanoparticles

To confirm the role of gravitational forces on nanoparticle deposition, selected experiments were conducted with Cerium dioxide (CeO_2) nanoparticles (Meliorum Technologies, NY) which have a density (7.132 g/cm^3) much higher than TiO_2 (3.8 g/cm^3). Deposition rates of CeO_2-FITC were much higher than those of TiO_2-FITC (Figure 4.11) at pH 5 and IS 1-100 mM. Though both TiO_2-FITC and CeO_2-FITC

showed very similar EPMs and aggregate size ranges under those conditions, higher deposition rates with CeO_2-FITC confirmed that gravitation force is one of the main parameters that need to be considered in prediction of nanoparticle deposition rates.

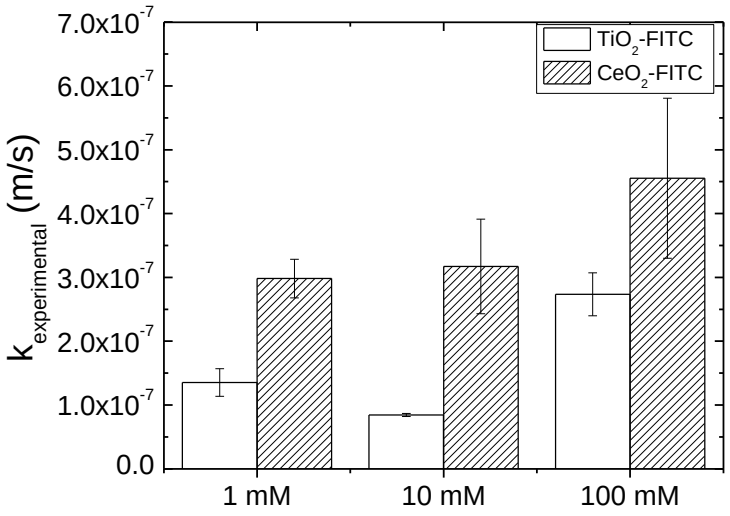

Figure 4.11. Comparative deposition rates of TiO_2-FITC and CeO_2-FITC as a function of IS at pH 7 and 1 mL/min flowrate. $k_{experimental}$ values have been calculated based on aggregate size.

4.4 Conclusions

In this study, a combination of mechanisms including DLVO-type forces and gravitational forces contribute to the deposition of TiO_2-FITC. For the same IS and flowrate, as long as the aggregate size was sufficiently small as not to induce gravitational forces the DLVO interactions appear to control the deposition of nanoparticles, as the favorable condition (pH 5) showed significantly higher deposition

than the unfavorable condition (pH 7). Like the model glass surface used in this study, most natural surfaces are negatively charged (10, 37) under ambient aquatic conditions. Therefore, if the pH or IS leads to electrostatically favorable conditions (i.e. positively charged particles), higher deposition and attachment of TiO_2-FITC will result. All three of the parameters (pH, IS and flowrate) tested here impact the deposition of TiO_2-FITC nanoparticles; however, the highest sensitivity of deposition was observed with pH. These aforementioned mechanisms (DLVO, gravitational, hydrodynamic forces) will play significant roles in the fate of TNPs in both natural and engineered environments and considerations of these mechanisms will be essential for minimizing toxic exposure and designing effective removal processes.

4.5 References

(1) Nel, A.; Xia, T.; Mädler, L.; Li, N., Toxic Potential of Materials at the Nanolevel. *Science* **2006,** *311*, (5761), 622-627.

(2) Wiesner, M. R.; Lowry, G. V.; Alvarez, P.; Dionysiou, D.; Biswas, P., Assessing the Risks of Manufactured Nanomaterials. *Environmental Science & Technology* **2006,** *40*, (14), 4336-4345.

(3) Mauter, M. S.; Elimelech, M., Environmental Applications of Carbon-Based Nanomaterials. *Environmental Science & Technology* **2008,** *42*, (16), 5843-5859.

(4) Richman, E. K.; Hutchison, J. E., The Nanomaterial Characterization Bottleneck. *ACS Nano* **2009,** *3*, (9), 2441.

(5) Marambio-Jones, C.; Hoek, E., A review of the antibacterial effects of silver nanomaterials and potential implications for human health and the environment. *Journal of Nanoparticle Research* **2010,** *12*, 1531.

(6) Auffan, M.; Rose, J.; Bottero, J.-Y.; Lowry, G. V.; Jolivet, J.-P.; Wiesner, M. R., Towards a definition of inorganic nanoparticles from an environmental, health and safety perspective. *Nat Nano* **2009,** *4*, (10), 634.

(7) Elimelech, M., Gregory, J., Jia, X., Williams, R.A., *Particle Deposition and Aggregation: Measurement, Modeling and Simulation*. Butterworth-Heinemann: 1995; p 441.

(8) Jaisi, D. P.; Saleh, N. B.; Blake, R. E.; Elimelech, M., Transport of Single-Walled Carbon Nanotubes in Porous Media: Filtration Mechanisms and Reversibility. *Environmental Science & Technology* **2008,** *42*, (22), 8317-8323.

(9) Chen, K. L.; Elimelech, M., Aggregation and Deposition Kinetics of Fullerene (C60) Nanoparticles. *Langmuir* **2006,** *22*, (26), 10994-11001.

(10) Gregory, J., *Particles in water : properties and processes*. IWA Pub. ; Taylor & Francis: London; Boca Raton, FL, 2006.

(11) Trouiller, B.; Reliene, R.; Westbrook, A.; Solaimani, P.; Schiestl, R. H., Titanium Dioxide Nanoparticles Induce DNA Damage and Genetic Instability In vivo in Mice. *Cancer Res* **2009,** *69*, (22), 8784-8789.

(12) Xu, S.; Gao, B.; Saiers, J. E., Straining of colloidal particles in saturated porous media. *Water Resour. Res.* **2006,** *42*.

(13) Li, Z.; Greden, K.; Alvarez, P. J. J.; Gregory, K. B.; Lowry, G. V., Adsorbed Polymer and NOM Limits Adhesion and Toxicity of Nano Scale Zerovalent Iron to E. coli. *Environmental Science & Technology*. **2010,** *44*, (9), 3462-3467.

(14) Saleh, N.; Kim, H.-J.; Phenrat, T.; Matyjaszewski, K.; Tilton, R. D.; Lowry, G. V., Ionic Strength and Composition Affect the Mobility of Surface-Modified Fe0 Nanoparticles in Water-Saturated Sand Columns. *Environmental Science & Technology* **2008,** *42*, (9), 3349-3355.

(15) Hong, Y.; Honda, R. J.; Myung, N. V.; Walker, S. L., Transport of Iron-Based Nanoparticles: Role of Magnetic Properties. *Environmental Science & Technology* **2009,** *43*, (23), 8834.

(16) Lecoanet, H. F.; Wiesner, M. R., Velocity Effects on Fullerene and Oxide Nanoparticle Deposition in Porous Media. *Environmental Science & Technology* **2004,** *38*, (16), 4377-4382.

(17) Chen, K. L.; Elimelech, M., Interaction of Fullerene (C60) Nanoparticles with Humic Acid and Alginate Coated Silica Surfaces: Measurements, Mechanisms, and Environmental Implications. *Environmental Science & Technology* **2008,** *42*, (20), 7607-7614.

(18) Fatisson, J.; Domingos, R. F.; Wilkinson, K. J.; Tufenkji, N., Deposition of TiO2 Nanoparticles onto Silica Measured Using a Quartz Crystal Microbalance with Dissipation Monitoring. *Langmuir* **2009,** *25*, (11), 6062.

(19) Quevedo, I. R.; Tufenkji, N., Influence of Solution Chemistry on the Deposition and Detachment Kinetics of a CdTe Quantum Dot Examined Using a Quartz Crystal Microbalance. *Environmental Science & Technology* **2009,** *43*, 3176.

(20) Walker, S. L.; Hill, J. E.; Redman, J. A.; Elimelech, M., Influence of growth phase on adhesion kinetics of *Escherichia coli D21g*. *Applied And Environmental Microbiology* **2005,** *71*, (6), 3093-3099.

(21) Walker, S. L.; Redman, J. A.; Elimelech, M., Influence of growth phase on bacterial deposition: Interaction mechanisms in packed-bed column and radial stagnation point flow systems. *Environmental Science & Technology* **2005,** *39*, (17), 6405-6411.

(22) Sjollema, J.; Busscher, H. J.; Weerkamp, A. H., Real-Time Enumeration of Adhering Microorganisms in a Parallel Plate Flow Cell Using Automated Image-Analysis. *Journal of Microbiological Methods* **1989,** *9*, (2), 73-78.

(23) McClaine, J. W.; Ford, R. M., Characterizing the adhesion of motile and nonmotile Escherichia coli to a glass surface using a parallel-plate flow chamber. *Biotechnology and Bioengineering* **2002,** *78*, (2), 179-189.

(24) Dunphy Guzman, K. A.; Finnegan, M. P.; Banfield, J. F., Influence of Surface Potential on Aggregation and Transport of Titania Nanoparticles. *Environmental Science & Technology* **2006,** *40*, (24), 7688-7693.

(25) Dunphy Guzman, K. A.; Taylor, M. R.; Banfield, J. F., Environmental Risks of Nanotechnology: National Nanotechnology Initiative Funding, 2000-2004. *Environmental Science & Technology* **2006,** *40*, (5), 1401-1407.

(26) Robichaud, C. O.; Uyar, A. E.; Darby, M. R.; Zucker, L. G.; Wiesner, M. R., Estimates of Upper Bounds and Trends in Nano-TiO2 Production As a Basis for Exposure Assessment. *Environmental Science & Technology* **2009,** *43*, (12), 4227-4233.

(27) Long, T. C.; Saleh, N.; Tilton, R. D.; Lowry, G. V.; Veronesi, B., Titanium Dioxide (P25) Produces Reactive Oxygen Species in Immortalized Brain Microglia

(BV2): Implications for Nanoparticle Neurotoxicity. *Environmental Science & Technology* **2006,** *40*, (14), 4346-4352.

(28) Ramsden, C.; Smith, T.; Shaw, B.; Handy, R., Dietary exposure to titanium dioxide nanoparticles in rainbow trout, (Oncorhynchus mykiss): no effect on growth, but subtle biochemical disturbances in the brain. *Ecotoxicology* **2009,** *18*, (7), 939.

(29) Zhu, X.; Chang, Y.; Chen, Y., Toxicity and bioaccumulation of TiO2 nanoparticle aggregates in Daphnia magna. *Chemosphere* **2010**, *78*, (3), 209.

(30) Kiser, M. A.; Westerhoff, P.; Benn, T.; Wang, Y.; PeÌ • rez-Rivera, J.; Hristovski, K., Titanium Nanomaterial Removal and Release from Wastewater Treatment Plants. *Environmental Science & Technology* **2009,** *43*, (17), 6757-6763.

(31) Xia, T.; Kovochich, M.; Liong, M.; Mädler, L.; Gilbert, B.; Shi, H.; Yeh, J. I.; Zink, J. I.; Nel, A. E., Comparison of the Mechanism of Toxicity of Zinc Oxide and Cerium Oxide Nanoparticles Based on Dissolution and Oxidative Stress Properties. *ACS Nano* **2008,** *2*, (10), 2121-2134.

(32) Chen, G.; Beving, D. E.; Bedi, R. S.; Yan, Y. S.; Walker, S. L., Initial Bacterial Deposition on Bare and Zeolite-Coated Aluminum Alloy and Stainless Steel. *Langmuir* **2009,** *25*, (3), 1620.

(33) Chen, G.; Hong, Y.; Walker, S. L., Colloidal and Bacterial Deposition: Role of Gravity. *Langmuir* **2009**, *26*, 314.

(34) Kline, T. R.; Chen, G.; Walker, S. L., Colloidal Deposition on Remotely Controlled Charged Micropatterned Surfaces in a Parallel-Plate Flow Chamber. *Langmuir* **2008,** *24*, (17), 9381-9385.

(35) Redman, J. A.; Walker, S. L.; Elimelech, M., Bacterial adhesion and transport in porous media: Role of the secondary energy minimum. *Environmental Science & Technology* **2004,** *38*, (6), 1777-1785.

(36) Walker, S. L.; Bhattacharjee, S.; Hoek, E. M. V.; Elimelech, M., A novel asymmetric clamping cell for measuring streaming potential of flat surfaces. *Langmuir* **2002,** *18*, (6), 2193-2198.

(37) Crittenden, J. C.; Montgomery Watson, H., *Water treatment principles and design*. J. Wiley: Hoboken, N.J., 2005.

(38) Chen, G.; Walker, S. L., Role of Solution Chemistry and Ion Valence on the Adhesion Kinetics of Groundwater and Marine Bacteria. *Langmuir* **2007,** *23*, (13), 7162-7169.

(39) Derjaguin, B. V.; Landau, L., *Acta Physicochim U.S.S.R.* **1941,** *14*, 300.

(40) Verwey, E. J.; Overbeek, J. T. G., *Theory of the Stability of Lyophobic Colloids*. Elsevier: New York, N.Y., 1948.

(41) Hogg, R.; Healy, T. W.; Fuerstenau, D. W., Mutual Coagulation of Colloidal Dispersions. *Transactions of the Faraday Society* **1966,** *62*, (522P), 1638-1651.

(42) Keller, A. A.; Wang, H.; Zhou, D.; Lenihan, H. S.; Cherr, G.; Cardinale, B. J.; Miller, R.; Ji, Z., Stability and Aggregation of Metal Oxide Nanoparticles in Natural Aqueous Matrices. *Environmental Science & Technology* **2010,** *44*, 1962.

(43) Adamczyk, Z.; Vandeven, T. G. M., Deposition of Particles under External Forces in Laminar-Flow through Parallel-Plate and Cylindrical Channels. *Journal of Colloid and Interface Science* **1981,** *80*, (2), 340-356.

(44) Wit, P. J.; Poortinga, A.; Noordmans, J.; van der Mei, H. C.; Busscher, H. J., Deposition of Polystyrene Particles in a Parallel Plate Flow Chamber under Attractive and Repulsive Electrostatic Conditions. *Langmuir* **1999,** *15*, (8), 2620.

(45) Yang, J.; Bos, R.; Poortinga, A.; Wit, P. J.; Belder, G. F.; Busscher, H. J., Comparison of Particle Deposition in a Parallel Plate and a Stagnation Point Flow Chamber. *Langmuir* **1999,** *15*, (13), 4671.

(46) Jennifer, W. M.; Roseanne, M. F., Characterizing the adhesion of motile and nonmotile *Escherichia coli* to a glass surface using a parallel-plate flow chamber. *Biotechnology and Bioengineering* **2002,** *78*, (2), 179-189.

(47) Adamczyk, Z.; Van De Ven, T. G. M., Deposition of particles under external forces in laminar flow through parallel-plate and cylindrical channels. *Journal of Colloid and Interface Science* **1981,** *80*, (2), 340.

(48) Yiantsios, S. G.; Karabelas, A. J., Deposition of micron-sized particles on flat surfaces: effects of hydrodynamic and physicochemical conditions on particle attachment efficiency. *Chemical Engineering Science* **2003,** *58*, (14), 3105.

(49) Yiantsios, S. G.; Karabelas, A. J., The effect of gravity on the deposition of micron-sized particles on smooth surfaces. *International Journal of Multiphase Flow* **1998,** *24*, (2), 283.

Chapter 5

Combined Factors Influencing the Aggregation and Deposition of nano-TiO_2 in the Presence of Humic Acids and Bacteria

Chowdhury, I., Cwiertny, D. M., Walker, S. L., Combined Factors Influencing the Aggregation and Deposition of nano-TiO_2 in the Presence of Humic Acid and Bacteria. *Environmental Science & Technology* **2012**.

Abstract

This study investigates the contributions of natural organic matter (NOM) and bacteria to the aggregation and deposition of TiO_2 nanoparticles (TNPs) in aquatic environments. Transport experiments with TNPs were conducted in a microscopic parallel plate system and a macroscopic packed-bed column using fluorescently tagged *E. coli* as a model organism and Suwannee River Humic Acid as a representative NOM. Notably, TNPs were labeled with fluorescein isothiocyanate allowing particles and cells to be simultaneously visualized with a fluorescent microscope. Results from both experimental systems revealed that interactions among TNPs, NOM and bacteria exhibited a significant dependence on solution chemistry (pH 5 and 7) and ion valence (K^+ and Ca^{2+}), and that these interactions subsequently affect TNPs deposition. NOM and *E. coli* significantly reduced deposition of TNPs, with NOM having a greater stabilizing influence than bacteria. Ca^{2+} ions played a significant role in these interactions, promoting formation of large clusters of TNPs, NOM and bacteria. TNPs transport in the presence of both NOM and *E. coli* resulted in much less deposition than in the presence of NOM or *E. coli* alone, indicating a complex combination of interactions involved in stabilization. Generally, over the aquatic conditions considered, the extent of TNPs deposition follows: without NOM or bacteria > with bacteria only > with NOM only > combined bacteria and NOM. This trend should allow better prediction of the fate of TNPs in complex aquatic systems.

5.1 Introduction

Titanium dioxide (TiO_2) is one of the most widely used nanomaterials in industry (1, 2), yet it is also demonstrated to be toxic to eukaryotic and prokaryotic cells (3-5). The extent of their use and their known toxicological risks make studies of the environmental fate of TiO_2 nanoparticles (TNPs) an urgent priority. Upon their release to natural and engineered aquatic environments, natural organic matter (NOM) and bacteria, both of which are ubiquitous(6), are likely to influence the transport of TNPs.

Interactions of NOM (e.g., humic and fulvic acids) with nanomaterials have been studied quite extensively. For example, interactions between humic acid and fullerenes (C60) have been shown to decrease C60 deposition significantly (7-12). Moreover, both monovalent and divalent ions affected the nature of these interactions, and in turn the subsequent deposition of the humic-coated fullerenes. Association with NOM is also known to influence non-carbonaceous nanoparticle stability; for example, NOM increased the fractal dimension of hematite (13), stabilized gold nanoparticles (14), and contributed to electrosteric and electrostatic repulsion for TNPs (15). Consensus is that NOM plays a vital role in the fate of nanomaterials, primarily reducing the size of aggregates and contributing to steric effects (16).

Though interactions of nanoparticles with bacteria have been studied (5, 17), research thus far has been limited to toxicity studies and nanoparticle-cell interactions, and not necessarily the associated implications for transport. One such toxicity study found NOM and an adsorbed polymer coating can reduce interactions of nano-iron with *E. coli*, decreasing their toxic effect (18). A significant change in the aggregation state of

TNPs was observed after interaction with *Pseudomonas aeruginosa* due to preferential biosorption of TNPs, which in turn increased nanoparticle stability in solution (19). This type of cell-nanoparticle interaction has also been observed between nanoparticles and biosolids (20-25). During wastewater treatment, a majority of cerium oxide nanoparticles were deposited within biosolids, although smaller aggregates (size <200 nm) passed through the model treatment plant (20). Similarly, Kiser et al.(21) observed TNPs in both wastewater biosolids (1-6 µg/mg) and effluent (5-15 µg/L). Another investigation with TNPs reported 96% removal during treatment but that smaller nanoparticles (4-30 nm) remained in wastewater effluent below 25 µg/L (22). Studies in a pilot wastewater treatment plant reported that nanoscale silver (Ag) mostly sorbed to wastewater biosolids (sludge and effluent) and individual Ag nanoparticles were observed in the influent only (23, 25). Another study showed a paramount role for surface coatings on the fate of silica nanoparticles during simulated primary wastewater treatment; uncoated nanoparticles passed through the effluent, whereas surfactant-coated nanoparticles were mainly found in sewage sludge (24). Given these results from an engineered system heavy with NOM and bacteria, one would expect similar stabilizing effects in natural systems, yet the extent of this effect has not been examined. While the fate of nanoparticles was investigated in treatment plants, so far there has been no systematic study on how the interactions of nanoparticles with planktonic bacteria will affect nanoparticle transport through porous media.

Be it in natural or engineered systems, interactions with, NOM and bacteria will be determining factors in the fate of nanomaterials in aquatic environments. To date,

however, most studies have considered nanomaterial transport in relatively idealized systems that have tended to focus on the influence of a single environmental variable (e.g., pH, ion concentration or charge, the presence or absence of NOM). It remains unclear whether trends in nanoparticle transport established in such single variable systems will remain relevant in more complex aquatic environments where multiple factors may impact nanomaterial stability in parallel. Here, we take one of the first steps toward establishing the combined effect of environmental variables known or suspected to impact nanomaterial fate. We focus on the role of NOM and bacteria, both independently and in combination, in the transport of a model nanoparticle (TNPs). Particularly, the influence of ionic strength, ion valence and pH on transport of TNPs in the presence of NOM, bacterial cells, and a mixture of NOM and bacterial cells was investigated. In addition to providing new insights into the influence of bacteria on nanomaterial transport, we also report relative trends in TNP stability and transport in multi-component (i.e., bacteria and NOM) aquatic systems exhibiting a range of chemical complexity.

5.2 Materials and Methods

5.2.1 Selection and Characterization of Nanoparticles

Titanium dioxide (Aeroxide TiO_2 P25, Evonik Degussa Corporation, NJ) was selected as the model nanoparticle. Detailed characterization of these particular TNPs has been described previously (26). TNPs were labeled with fluorescein isothiocyanate

isomer I (Sigma Aldrich, St. Louis, MO) for visualization under a fluorescent microscope according to established procedures (27, 28). The primary particle size of coated TNPs was 17.7 ± 6.1 nm. Electrophoretic mobilities (EPMs) of TNPs were measured using a ZetaPALS analyzer (Brookhaven Instruments Corp., Holtsville, NY) at both pH 5 and 7. pH was maintained within ±0.1 units by the addition of hydrochloric acid or potassium hydroxide (both Fisher, ACS reagent grade). Both monovalent (KCl) and divalent ($CaCl_2$) cations were used in preparing solutions at 10 mM. Suwannee River Humic Acid (SRHA) (International Humic Substances Society, MN) was used as the model NOM. The student t-test was utilized to determine the statistical differences between mean data, assuming significant difference when $P < 0.05$ (95% confidence level).

Aggregation and sedimentation studies were utilized to determine the stability of TNPs suspension as would occur during transport experiments by dynamic light scattering (DLS, Brookhaven model BI-9000AT digital correlator, Holtsville, NY) at a wavelength of 661 nm (15 mW solid state laser) and UV/Vis spectrophotometer (DU800, UV/Vis Spectrophotometer, Beckman Coulter, CA) and as mentioned elsewhere (26, 29).

Batch sorption studies were conducted to understand the mechanisms involved interactions of TNPs and Suwannee River Humic Acid (SRHA) (Standard II, International Humic Substances Society, MN) following the procedure mentioned elsewhere (30, 31). SRHA stock solution was prepared following the protocol mentioned in the literature (11). 1 mg/L SRHA solution was prepared in 10 mM KCl or $CaCl_2$. After the addition of 10 mg/L TNPs in the suspension, TNPs suspension was sonicated for 30 min following a nanoparticle dispersion protocol mentioned elsewhere.(29) Next

the suspension was stirred during the sorption process. 1.5 mL of samples was taken into microcentrifuge tube from the suspension after 10 min, 1 h, 2 h, 3 h, 4 h and 24 h. Then the samples were centrifuged for 10 min at 15000 g. Concentration of NOM in the supernatant separated from the suspension was determined by measuring absorbance at 254 nm wavelength (31, 32).

Effects of SRHA on the acid-base properties of TNPs were investigated by potentiometric titration (33, 34). Carbon dioxide from background solution (10 mM KCl or $CaCl_2$) was purged using nitrogen gas (Puritan Medical Products, Inc., Overland Park, KS) for at least 50 min prior to experiments. Titration was conducted in a sealed titration vessel with 10 mL volume for TNPs. Nanoparticle concentration was maintained at 4 g/L. After lowering the pH of the suspension below 4.0 with 0.1 N HCl, an automatic titrator (798 Titrino, Metrohm Ltd., Switzerland) was utilized to conduct potentiometric titrations with 0.1 N NaOH titrant over the pH range of 4.0-10.0 at room temperature (23 $\pm$ 2 ^{o}C) in the presence of nitrogen gas purging and continuous stirring. Monotonic equivalence point (MET) mode was used in automatic titrator with a maximum drift of electric potential of pH electrode less than 4 mV/min. All titration experiments were conducted in triplicate. Overall surface charge densities and acidities of TNPs under the experimental conditions were also determined from the titration study following the procedure mentioned elsewhere (35, 36).

5.2.2 Selection and Characterization of Bacteria

In this study, *Escherichia coli* from a human isolate (HU1) was chosen as model bacteria (37). *E. coli* was tagged with mCherry plasmid (38) so that both red *E. coli* and green TNPs could be simultaneously visualized with fluorescent microscopy during transport studies. *E. coli* HU1 tagged with mCherry plasmid was named and will hitherto be referred to as *E. coli* HU1R. A wide range of characterization was conducted for *E. coli* including electrokinetic characterization, cell size, hydrophobicity, potentiometric titration studies and extracellular polymeric substances.

All of the bacterial characterization methods were carried out on *E. coli* HU1R harvested at stationary growth phase in 10 mM KCl and $CaCl_2$ with and without SRHA at pH 5 and 7 following the procedure mentioned in details elsewhere (37, 39). Live/Dead BacLight kit (L-7012, Molecular Probes, Eugene, OR) were used to determine cell viability. Electrokinetic characterization of bacteria was determined by measuring electrophoretic mobility (EPM) using a ZetaPALS analyzer (Brookhaven Instruments Corporation, Holtsville, NY). Potentiometric titrations were performed to determine relative acidities and surface charge densities of the bacterial surfaces by using a microtitrator (798 Titrino, Metroohm, Switzerland) for bacterial concentration of 5×10^8 cells/ml. Microbial adhesion to hydrocarbon (MATH) test(34) was used to determine the hydrophobicity of *E. coli* HU1R by measuring the degree of partitioning between n-dodecane (Fischer Scientific, PA) and the electrolyte solution. An inverted fluorescence microscope (IX70, Olympus, Japan) operated in phase-contrast mode was used to determine bacterial size by capturing images of bacterial cells harvested in stationary

growth phase (10^7 cells/mL) by analyzing the captured images with software (Simple PCI 5.8). An established extraction method was utilized for the isolation and analysis of extracellular polymeric substances (EPS) from bacterial cells (40). Sugar content was determined by phenol sulfuric acid method (41) using Xanthan gum (Fisher Scientific) as the standard. Protein content was determined by Lowry method (42) at 500 nm wavelength with Bovine Serum Albumin (BSA) as the standard.

5.2.3 Transport Experiments

The transport of TNPs was investigated in both a parallel plate (PP) chamber and packed-bed column systems. An inverted fluorescent microscope (IX70, Olympus, Center Valley, PA) was utilized for visualization and imaging of deposited nanoparticles on a glass slide (Fisher Scientific, Pittsburgh, PA) in a rectangular PP chamber (Glyco Tech, Rockville, MA) with inner dimensions of 6 cm x 1 cm x 0.0762 cm (43, 44). A 10 mg/L suspension of TNPs (10^{12} primary TNPs/mL) was prepared following a procedure mentioned elsewhere (29) and was injected in the chamber at 0.06 mL/min (corresponding to 0.47 m/h which is within the range for groundwater and sand filtration (6)). The Peclet (6.22×10^{-7} - 6.22×10^{-3}) and Reynolds numbers (1.31×10^{-5} – 1.31×10^{-4}) were within the range of diffusion dominated regime. The background electrolyte was 10 mM KCl and $CaCl_2$ at pH 5 and 7. The SRHA concentration was maintained at 1 mg/L and the *E. coli* concentration was 10^7 cells/mL (45). Deposition kinetics for both TNPs and *E. coli* were determined by utilizing a novel approach in which both the green TNPs and red *E. coli* were imaged simultaneously as described in the Supporting

Information. For selected conditions, transport experiments were conducted in a packed-bed column following the procedures described elsewhere (26, 46). In brief, a 5-cm borosilicate glass column (Omnifit, Boonton, NJ) packed with ultrapure quartz sand (Iota quartz, Unimin Corp., NC) of 275 μm size was utilized to investigate the transport of TNPs in the presence and absence of SRHA and *E. coli* at pH 7 in 10 mM KCl and $CaCl_2$. The suspension was injected into the column at 2 mL/min, simulating similar hydrodynamic conditions to the PP chamber.

5.2.4 Environmental Scanning Electron Microscopy

Environmental scanning electron microscopy (ESEM) was utilized to further validate the findings from deposition studies and DLS results. Interactions among TNPs, *E. coli* and SRHA were investigated by taking ESEM images of wet samples (19). An FEI Co. XL30 FEG ESEM (Philips Electron Optics, Eindoven, Netherlands) was used to acquire at least 10 images of each experimental condition at 5000x magnification. For imaging by ESEM, 7 μL of each well-mixed sample was dispensed onto an aluminum stub (Ted Pella, Inc., Redding, CA) and analyzed in wet mode at ~4.0 Torr and 20 kV accelerating voltage, using a gaseous secondary electron detector at a working distance of 10.3 mm.

5.3 Results and Discussion

5.3.1 Characterization

5.3.1.1 Characterization of TNPs

Detailed characterization of TNPs as a function of pH, ion valence and in the presence and absence of SRHA is presented in Table 5.1. At pH 5 without SRHA, TNPs showed positive EPM at both 10 mM KCl and $CaCl_2$, though in the presence of $CaCl_2$ the mobility was lower due to ion valence effects (47). After the addition of SRHA, a negative mobility was observed at both IS conditions. Since SRHA has predominantly negative functional groups(6), these can interact with and coat positive TNPs, producing an overall negative surface charge. However, with SRHA, TNPs in KCl resulted in almost a three-fold more negative surface potential than in $CaCl_2$ due to greater electrical double layer compression occurring in the divalent salt solution (47). Moreover, Ca^{2+} is able to bind to available carboxyl functional groups in SRHA, in turn decreasing the negative surface charge (13).

At pH 7, TNPs had negative EPMs at both IS. With the addition of SRHA, the TNPs became more negative in the presence of both monovalent (K^+) and divalent (Ca^{2+}) ions. Also, particles with SRHA were more charged in the presence of monovalent ions than divalent ions. Similar to pH 5, the TNPs sensitivity to the presence of organic matter and its conferred stability were more pronounced in KCl relative to $CaCl_2$. These results are consistent with other studies on gold and hematite NPs with SRHA (8, 14).

The size of TNPs aggregates was significantly affected by SRHA. With addition of SRHA, aggregation decreases resulting in lower aggregate size at both IS. However, the reduction in aggregate size in the presence of SRHA was notably higher with monovalent ions than with divalent ions. This may be due to the lower EPM of nanoparticles with divalent ions relative to monovalent ions, increasing the electrostatic forces among particles (47, 48). Moreover, SRHA may adsorb to the nanoparticle surfaces, creating electrosteric repulsion, which can be a function of ion valence (49, 50). Overall, SRHA reduced the aggregate size of TNPs and increased the negativity of TNPs surfaces, which may subsequently increase the transport of TNPs.

5.3.1.2 E. coli Characterization

Characterization of *E. coli* has been summarized in Table 5.1. EPM results indicate that *E. coli* is negatively charged under all conditions investigated. Unlike TNPs, addition of SRHA did not change the mobility of *E. coli* significantly ($P >> 0.05$) in the presence of either monovalent (K^+) or divalent (Ca^{2+}) ions. *E. coli* has an effective diameter of ~1.14 µm, which is approximately 60 times larger than the primary particle size of TNPs (17.7 ± 6.1 nm) (28). Microbial adhesion to hydrocarbons (MATH) results indicate that this particular *E. coli* strain is highly hydrophobic under all conditions (80 - 90%). The addition of SRHA decreased the hydrophobicity to some extent with both monovalent and divalent ions (reduced by 7.7% and 9.4%, respectively).

Table 5.1. Characterization of TNPs and *E. coli* HU1R as a function of ion valence, pH and SRHA

Condition	TNPs					*E. coli*					
		EPM (10^{-8} m^2 V^{-1} s^{-1})	**Aggregate Size (nm)**	**q_e (mg SRHA/g TNPs)**	**Surface charge density (μC/mg TNPs)**	**EPM (10^{-8} m^2 $V^{-1}s^{-1}$)**	**Cell Size (μm)**	**MATH (%)**	**Viability (%)**	**Surface charge density (μC/cm^2)**	**Sugar and Protein ($mg/10^{10}$ cells)**
10 mM KCl	pH 5	1.18 ± 0.13	697.0 ± 51.9	NA[j]	8643.45	-2.58 ± 0.22	Radius: 0.57 ± 0.15 Length: 1.72 ± 0.7 Width: 0.76 ± 0.16	87.15 ± 1.14	97.60 ± 1.11	171.44	Sugar: 4.05 ± 0.82 Protein 183.52 ± 6.51
	pH 7	-1.37 ± 0.35	813.2 ± 79.6	NA							
10 mM KCl + SRHA	pH 5	-2.78 ± 0.13	239.4 ± 5.8	16.29	8265.50	-2.68 ± 0.26		80.42 ± 2.97	99.50 ± 0.86	226.31	
	pH 7	-2.54 ± 0.44	409.7 ± 60.7	ND							
10 mM $CaCl_2$	pH 5	0.62 ± 0.13	1120.8 ± 80.5	NA	25078.06	-1.19 ± 0.20		90.44 ± 0.56	97.22 ±0.53	164.02	
	pH 7	-0.59 ± 0.14	1227.4 ± 139.8	NA							
10 mM $CaCl_2$ + SRHA	pH 5	-0.71 ± 0.16	966.1 ± 73.1	37.18	28885.20	-1.15 ± 0.26		81.93 ± 10.69	98.82 ± 1.03	150.24	
	pH 7	-0.78 ± 0.13	930.4 ± 93.4	34.60							

Potentiometric titration studies revealed that the surface charge densities of *E. coli* were dependent on ion valence and SRHA. Similar to the EPM trends, the addition of SRHA significantly ($P < 0.05$) increased the surface charge densities of *E. coli* in KCl, suggesting that SRHA binds with the bacterial surface. However, in the presence of $CaCl_2$ and SRHA, there was an observed slight decrease in the surface charge densities of *E. coli*, indicating Ca^{2+} bridging with the cell surface (32, 49). Finally, the compositional analysis of extracellular polymeric substances demonstrates that the protein content is 45 times higher than sugar content. This is similar to trends for other *E. coli* in the literature (37, 39), where protein is the greater exopolymeric component. Hence, this charged polymeric matrix can interact with ions, SRHA and surfaces and can affect the interaction among TNPs, *E. coli* and NOM and subsequent deposition.

5.3.2 Deposition of TNPs in the Absence of *E. coli*

Results for deposition of TNPs in the PP chamber are summarized in Figure 5.1 and additional data are provided in Table 5.2. Overall deposition trends of TNPs in the parallel plate followed the order: pH 5, $CaCl_2$ > pH 7, $CaCl_2$ > pH 5, $CaCl_2$ + SRHA > pH 5, KCl > pH 7, $CaCl_2$ + SRHA > pH 7, KCl > pH 7, KCl + SRHA > pH 5, KCl + SRHA. Mass transfer rates (k_{pp}) at 10 mM and pH 5 were six times higher in the presence of $CaCl_2$ than KCl. This is likely due to charge screening and reduced Debye length by divalent Ca^{2+}(47), leading to increased aggregate size and electrostatic attraction towards the surface. However, with the addition of SRHA, the impact of valence was even more pronounced. For monovalent ions, k_{pp} in the presence of SRHA

was significantly ($P < 0.05$) (62 times) less than without SRHA. Similarly, in $CaCl_2$, a four-fold decrease in mass transfer was observed due to the addition of the organic matter. At pH 7, k_{pp} in $CaCl_2$ was almost six times higher than in KCl. In the presence of SRHA, k_{pp} decreased 16.5 and 4.8 times in KCl and $CaCl_2$, respectively. These trends indicate a stabilizing influence of the organic matter, although the extent of stabilization is influenced by ion valence and pH.

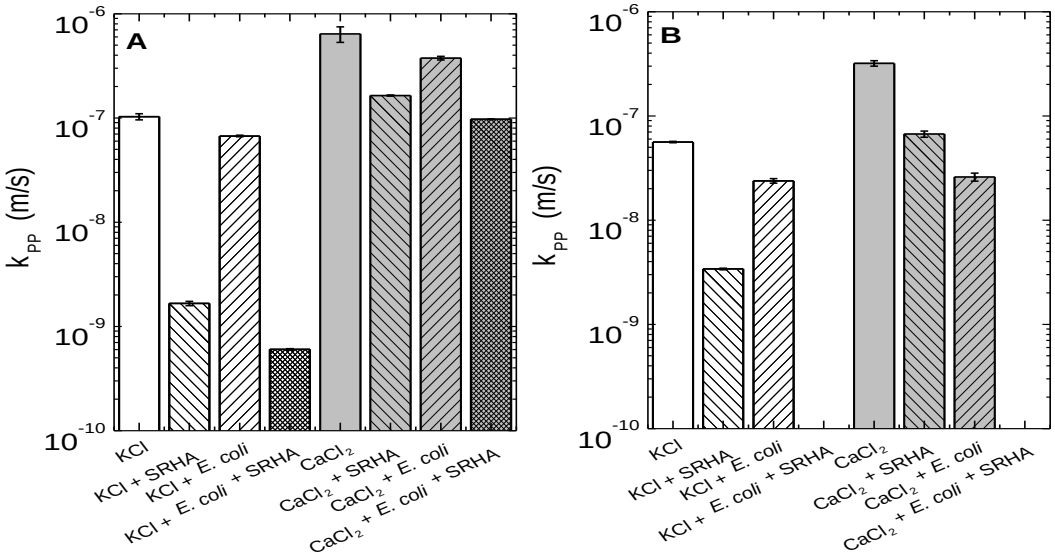

Figure 5.1. Mass transfer rate coefficients of TNPs on glass surfaces in parallel plate chamber in the presence and absence of SRHA and *E. coli* at A) pH 5 and B) pH 7. 10 mM KCl and $CaCl_2$ have been used as solution chemistry. TNPs, SRHA and *E. coli* concentrations have been maintained at 10 mg/L, 1 mg/L and 10^7 cells/mL. Flowrate was maintained at 0.06 mL/min. Error bars indicate one standard deviation of triplicate experiments.

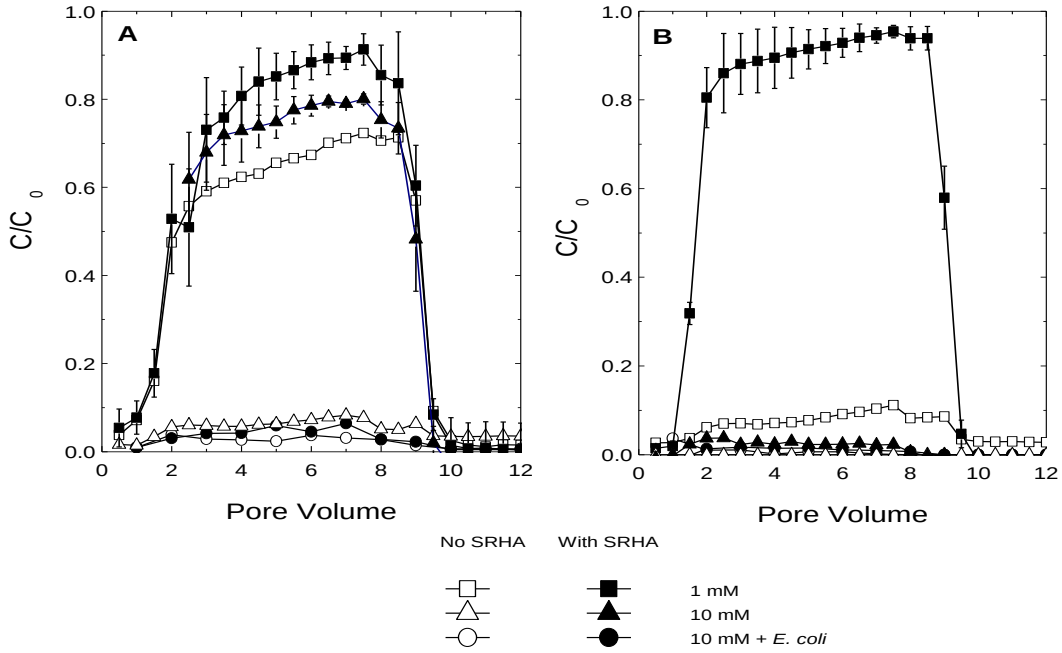

Figure 5.2. Column breakthrough curves for TNPs at pH 7 in the absence and presence of SRHA and *E. coli* at A) KCl and B) $CaCl_2$. TNPs, SRHA and *E. coli* concentrations have been maintained at 10 mg/L, 1 mg/L and 10^7cells/mL. Other experimental conditions: approach velocity = 0.019 cm/s, packed column length = 5.0 cm, column diameter = 1.5 cm, porosity = 0.465, temperature = 25 ^oC. Error bars indicate the one standard deviation of triplicate experiments.

To further understand the transport mechanisms of TNPs through porous media, experiments were conducted in a packed-bed for select conditions at pH 7. Column breakthrough curves (Figure 5.2) show that without SRHA, deposition rates of TNPs increased significantly ($P<0.05$) (8 times) with IS (1 to 10 mM) in KCl (Table 5.2). Similarly, with divalent ions little elution (maximum $C/C_0 = 0.11$) was observed at 1 mM, whereas increased IS (10 mM) resulted in complete retention of TNPs within the column. Deposition rates of TNPs decreased significantly ($P< 0.05$) from monovalent to

divalent ions (7x), which is similar to trends observed in the PP system. In the presence of SRHA, a significant ($P< 0.05$) drop in deposition rates of TNPs was observed with both monovalent and divalent ions (4x in 1 mM KCl; 11x in 10 mM KCl; 46x in 1 mM $CaCl_2$). Deposition rates of TNPs decreased notably at 1-10 mM KCl and also 1 mM $CaCl_2$, whereas 10 mM $CaCl_2$ resulted in very little elution, even with SRHA.

Overall deposition trends of TNPs are similar in both the PP and column systems with and without SRHA, indicating that changes in aggregate size and EPMs of TNPs induced by SRHA decreases their deposition. We note that changes in deposition rates in the PP were significantly higher than those in the column, indicating that additional removal mechanisms are involved in the column. Straining and pore blocking may increase deposition in the column due to increased aggregate size and reduced surface charge at high IS and ion valence (26).

Table 5.2. Mass transfer rate coefficients (k_{pp}) of TNPs and *E. coli* in parallel plate chamber as a function of ionic strength, ion valence, pH and absence and presence of SRHA

		TNPs (m/s)	*E. coli* (m/s)
pH 5	**10 mM KCl**	$(1.03 \pm 0.07) \times 10^{-7}$	NA
	10 mM KCl + SRHA	$(1.66 \pm 0.08) \times 10^{-9}$	NA
	10 mM KCl + HU1R	$(6.71 \pm 0.11) \times 10^{-8}$	$(6.43 \pm 0.09) \times 10^{-8}$
	10 mM KCl + HU1R +SRHA	$(6.01 \pm 0.10) \times 10^{-10}$	$(7.05 \pm 0.16) \times 10^{-9}$
	10 mM $CaCl_2$	$(6.39 \pm 1.08) \times 10^{-7}$	NA
	10 mM $CaCl_2$+ SRHA	$(1.64 \pm 0.02) \times 10^{-7}$	NA
	10 mM $CaCl_2$ + HU1R	$(3.74 \pm 0.15) \times 10^{-7}$	$(1.95 \pm 0.08) \times 10^{-8}$
	10 mM $CaCl_2$ + HU1R + SRHA	$(9.72 \pm 0.08) \times 10^{-8}$	$(6.21 \pm 0.14) \times 10^{-9}$
pH 7	**10 mM KCl**	$(5.61 \pm 0.09) \times 10^{-8}$	NA
	10 mM KCl + SRHA	$(3.40 \pm 0.06) \times 10^{-9}$	NA
	10 mM KCl + HU1R	$(2.38 \pm 0.12) \times 10^{-8}$	$(2.23 \pm 0.08) \times 10^{-8}$
	10 mM KCl + HU1R +SRHA	ND	ND
	10 mM $CaCl_2$	$(3.19 \pm 0.19) \times 10^{-7}$	NA
	10 mM $CaCl_2$+ SRHA	$(6.69 \pm 0.45) \times 10^{-8}$	NA
	10 mM $CaCl_2$ + HU1R	$(2.59 \pm 0.23) \times 10^{-8}$	$(4.57 \pm 0.17) \times 10^{-8}$
	10 mM $CaCl_2$ + HU1R + SRHA	ND	$(1.78 \pm 0.11) \times 10^{-8}$

NA: Not available; ND: Negligible deposition

5.3.2.1 Contribution of Aggregate Size and EPM to deposition trends

Additional insights into TNP deposition mode were obtained via correlation of aggregate size and EPMs of TNP with values of k_{pp} for TNPs in the parallel plate system (Figure 5.3). Overall, the extent of TNPs mass transfer increased with aggregate size, revealing an exponential correlation (R^2 = 0.90) between k_{pp} and aggregate size. The lowest k_{pp} value was observed for the smallest aggregate size with the highest EPM (10 mM KCl with SRHA). Though aggregate size was largest at pH 7/10 mM $CaCl_2$, the greatest k_{pp} was observed at pH 5/10 mM $CaCl_2$ due to the electrostatically favorable EPM. Until the EPM approached zero (isoelectric point), mass transfer rates of TNPs increased as EPM values became less positive or negative, showing an exponential correlation (R^2 = 0.96) between k_{pp} and EPM. Though larger aggregate sizes and lower EPM were observed at pH 7/10 mM $CaCl_2$/SRHA relative to pH 7/10 mM KCl/SRHA, mass transfer rates were very similar. Values of k_{pp} were also similar at pH 5/10 mM KCl and pH 5/10 mM $CaCl_2$/SRHA though the latter condition resulted in larger aggregate size and more unfavorable EPM than pH 5/10 mM KCl.

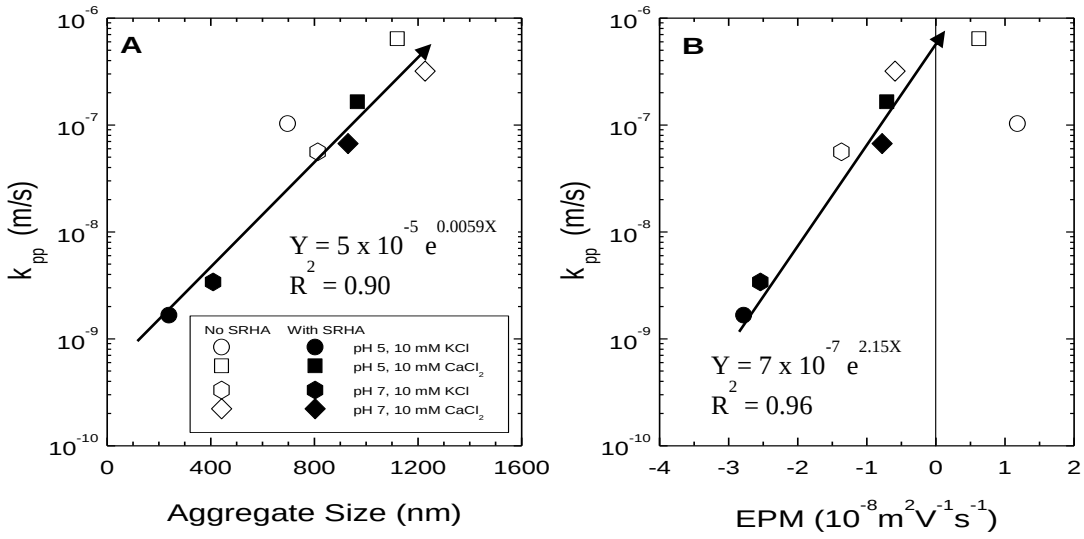

Figure 5.3. Deposition rates of TNPs in parallel plate chamber under different conditions as a function of A) Aggregate size and B) EPM. The line in Figure B was fitted using the data points before neutral EPM. The legends in Figure A are also applicable to Figure B. Here k_{pp} denotes mass transfer rate coefficients of TNPs.

Mass transfer of TNPs with and without SRHA can be correlated with EPM and aggregate size, specifically for monovalent ions in the PP. Deviation was observed under the conditions investigated with divalent ions, particularly in the presence of SRHA. Derjaguin–Landau–Verwey–Overbeek (DLVO) theory has been applied to quantify the influence of electrostatic and van der Waals forces on the interaction between nanoparticles and a glass surface with and without SRHA (51, 52). Outcomes of these calculations are reported in Figure 5.4.

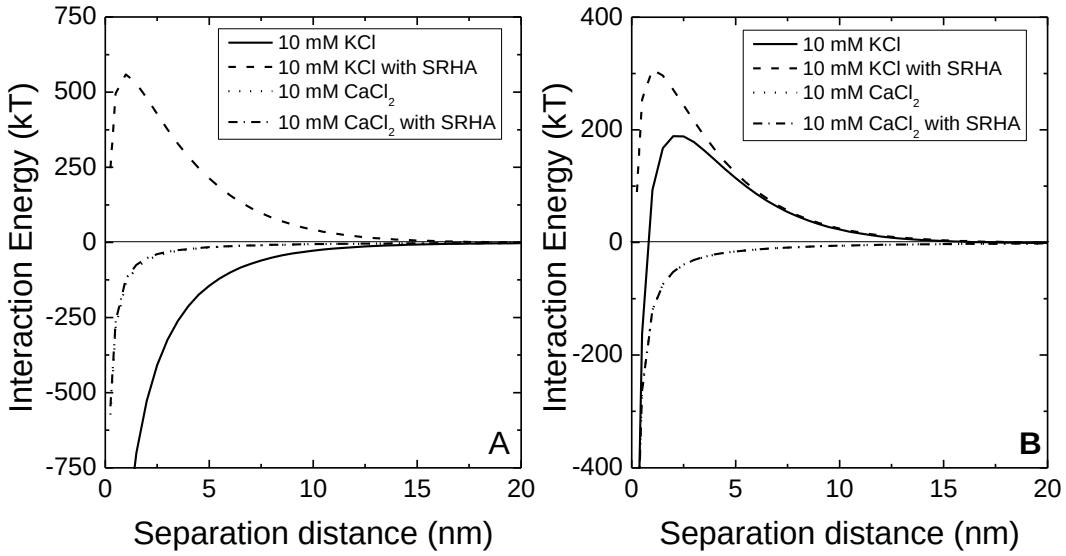

Figure 5.4. DLVO interaction profiles for TNPs-glass-water system as a function of ion valence and SRHA at A) pH 5 and B) pH 7.

DLVO interaction profiles in pH 5 solutions of KCl indicate that the addition of SRHA resulted in a high energy barrier (544.8 kT), decreasing the interaction and subsequent deposition of TNPs significantly. In pH 5/10 mM $CaCl_2$/SRHA, the interaction profiles remained unchanged as compared to that in the absence of SRHA even though deposition of TNPs decreased significantly with SRHA. Similar trends were observed in DLVO interaction profiles at pH 7 indicating that deposition trends in the presence of divalent cations cannot be explained by DLVO and aggregate size effects alone. Other studies with organic matter, micoorganisms, and nanoparticles have demonstrated that electrosteric effects can significantly influence the transport of

particles in the presence of divalent ions and NOM (11, 53). Hence, this phenomenon may also be at play in our systems due to the sorption of SRHA on TNPs.

5.3.2.2 Influence of Electrosteric Interactions

Sorption of SRHA to TNPs has been found to contribute to electrosteric interactions with TNPs (54). To identify whether electrosteric interactions are involved, the amount of sorbed SRHA on TNPs was determined as a function of pH and ion valence in batch adsorption experiments (Table 5.1). Overall, sorption of SRHA with TNPs was notably dependent on ion valence and pH. Sorption of SRHA on TNPs in the presence of Ca^{2+} ions was considerably higher than with K^{+} ions possibly due to cation bridging, which occurs as the SRHA carboxylate groups bind with TNPs via Ca^{2+} (11, 49). A slight decrease in sorption of SRHA to TNPs was observed from pH 5 to pH 7 in either salt due to the electrostatically favorable conditions between TNPs and SRHA at pH 5 with respect to pH 7.

Sorption studies indicate that the presence of organic matter clearly impacts the physicochemical properties of TNPs surfaces, and to better elucidate this contribution, potentiometric titration experiments of TNPs suspension were conducted. Acidities of TNPs were measured from pH 4 to 10 under different conditions, and surface charge densities were calculated from acidities (Table 5.1). Overall, the surface charge densities of nanoparticles were significantly higher in the presence of divalent (25078 μC/mg TNPs) versus monovalent cations (8643 μC/mg TNPs), indicating an increase in the concentration of surface functional groups available on the aggregate surface. Addition

of SRHA did not change the TNPs surface charge densities significantly for monovalent ions. Sorption studies also showed very low amount of SRHA sorbed to nanoparticles in the presence of monovalent ions. However, increased surface charge densities were observed with divalent cations upon addition of SRHA, as SRHA can introduce ion-dissociable functional groups that can add to the measured level of charge density (6). It was also observed that there were greater levels of sorbed SRHA on nanoparticles in the presence of divalent cations, as Ca^{2+} can bridge between particles and SRHA. Hence, determination of sorbed SRHA layer properties is necessary to understand the contribution of SRHA conformation in interactions with TNPs.

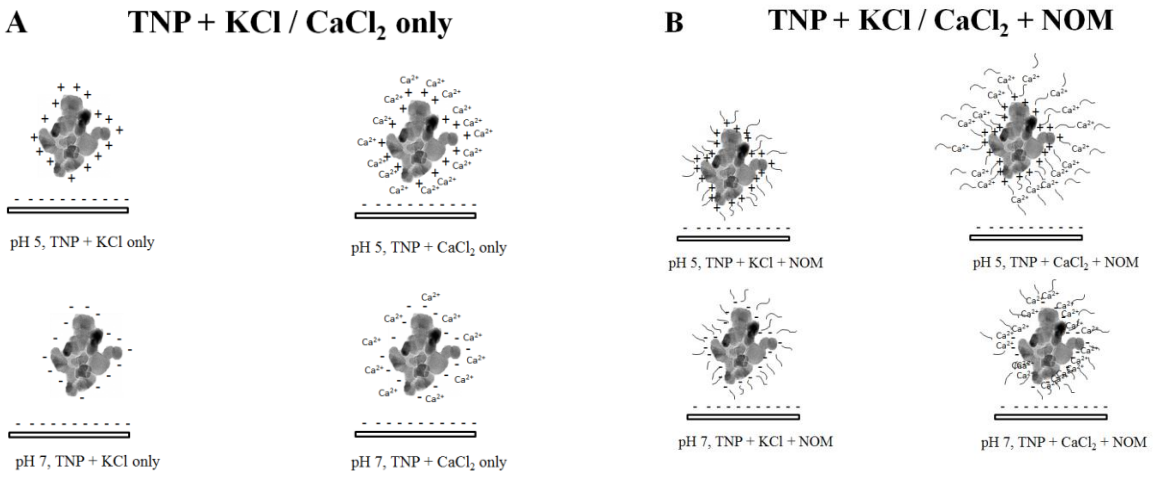

Figure 5.5. Schematic of mechanisms involved in interactions between TNPs, NOM and bacteria and combined effects on deposition of TNPs. A) Mechanisms involved TNPs and KCl/$CaCl_2$ only; B) Mechanisms involved TNPs and NOM in KCl/$CaCl_2$. In this figure, the trends (up or down) for Figure B are compared to trends observed in Figure A.

Table 5.3. Characteristics of adsorbed SRHA on TNPs estimated by Ohshima's soft particle analysis

	fixed charge density (ZN/N_A) (mol/m^3)	**ψ_o (mV)**	**ψ_{don} (mV)**	**thickness of sorbed SRHA (nm)**	**Electrophoretic softness ($1/\lambda$) (nm)**
pH 5, 10 mM KCl + SRHA 1 mg/L	1.99	-1.30	-2.60	72.00	11.00
pH 5, 10 mM $CaCl_2$ + SRHA 1 mg/L	0.66	-0.05	-0.11	86.00	13.00
pH 7, 10 mM KCl + SRHA 1 mg/L	1.33	-0.90	-1.70	94.00	14.00
pH 7, 10 mM $CaCl_2$ + SRHA 1 mg/L	7.97	-0.60	-1.30	22.00	4.00

Ohshima soft particle theory (55) was applied to determine the layer properties of SRHA-coated TNPs under different aquatic conditions. Ohshima soft particle theory has been widely used in determining the layer properties of polyelectrolyte coated nanoparticles (30, 56) and bacteria (57). Details of the calculation for Ohshima soft particle analysis are provided in Table 5.3. Calculated values of surface charge (ψ_o) were significantly lower than zeta potentials calculated from the Smoluchowski equation, in agreement with previous studies (30, 56, 58). The Smoluchowski equation is applicable for only hard spheres (47, 48), whereas for Ohshima's soft particle theory the assumption of a hard sphere is not valid (55). Values of ψ_o were close to neutral within the range of -

0.05 to -1.30 mV, which indicates that electrostatic repulsion is unlikely to occur between SRHA-coated TNPs and quartz surfaces under the experimental conditions investigated herein. Hence, the stability of nanoparticles with addition of SRHA is mainly due to electrosteric repulsion (30, 39). The sorbed SRHA layer thickness and electrophoretic softness showed a significant dependence on solution chemistry following the trend: pH 7, KCl + SRHA> pH 5, $CaCl_2$ + SRHA > pH 5, KCl + SRHA > pH 7, $CaCl_2$ +SRHA. Fixed charge density on the sorbed layer of SRHA follows the opposite trend of layer thickness. Hence, sorption, potentiometric titration, and Ohshima analysis demonstrated that solution chemistry significantly affected sorbed SRHA layer properties on the TNPs surfaces (in addition to aggregate size and EPM), which in turn influenced the electrosteric impact on deposition of TNPs.

5.3.3 Deposition of TNPs in the Presence of *E. coli* only

Deposition of TNPs was also investigated in the presence of *E. coli* in both the PP and packed-bed column. The deposition trends of TNPs in the presence of bacteria are: pH 5, $CaCl_2$ + *E. coli* > pH 5, KCl + *E. coli* > pH 7, $CaCl_2$ + *E. coli* > pH 7, KCl + *E. coli*. In the PP, k_{pp} of TNPs decreased almost 2-fold at pH 5 and 10 mM KCl in the presence of cells relative to the same solution conditions without cells. Deposition of TNPs and *E. coli* is comparable, indicating that mass transfer of bacteria is also significant (Table 5.2). The decrease of deposition in the presence of *E. coli* may be due to the change of TNPs and TNPs-bacteria aggregate size resulting from nanoparticle association with the bacterial surface (19). In the presence of divalent ions, deposition

trends were similar to monovalent ions with bacteria at pH 5. At 10 mM $CaCl_2$ and pH 5, k_{pp} values in the presence of bacteria were half of those measured without bacteria. However, the deposition of *E. coli* was negligible at this condition. Similarly, at pH 7, addition of *E. coli* resulted in a 2.4-fold decrease in deposition of TNPs in KCl. Under this condition, mass transfer of *E. coli* is also comparable with TNPs deposition. Addition of bacteria decreased mass transfer rate of TNPs by a factor of ~12 in $CaCl_2$ with significant bacteria deposition (~2 times less than TNPs deposition). Overall, mass transfer rates of TNPs were considerably higher in the presence of bacteria than SRHA under the experimental conditions investigated in this study.

In the column, addition of *E. coli* affected the transport of TNPs significantly. At 10 mM KCl and pH 7, elution of TNPs was very low (maximum C/C_0 is 4%) and the deposition rate of TNPs increased 1.5 times in the presence of *E. coli* than without *E. coli*, which notably is opposite to observations from the PP. With divalent ions, only 1% of TNPs eluted through the column, indicating their increased deposition rate after addition of *E. coli*.

Though the results from the PP showed a significant drop of nanoparticle deposition with addition of bacteria, column studies resulted in higher deposition rates with bacteria. This may be due to the variation in aggregate size with addition of bacteria and subsequent straining of aggregates in porous media. The column retains particles not only by chemical interactions but also via particles being retained in the pore structure. This can be due to such means as physical roughness of the grains, packing, and straining (26, 29, 59). In the column, the *E. coli* + TNPs aggregates are retained more (as

compared to TNPs alone) due to their larger size and irregular shape, whereas in the PP the difference in size and shape influences the transport somewhat, but nothing as substantial as observed within the column pore structure.

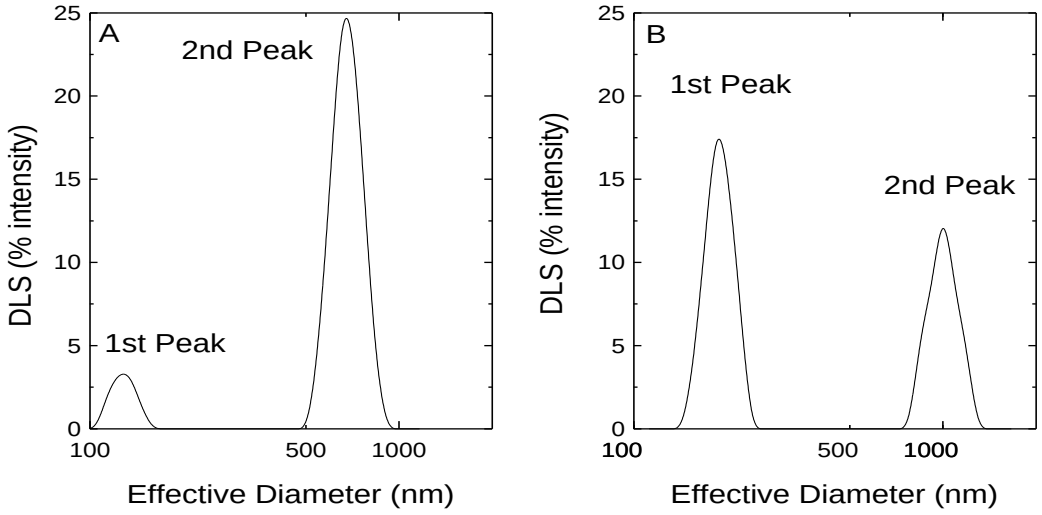

Figure 5.6. Representative intensity-based multimodal size distribution of TNPs and bacteria aggregates from DLS. A) TNPs only in 10 mM KCl at pH 5. B) Both TNPs and bacteria in 10 mM KCl at pH 5.

Previous work revealed that bacteria can influence the agglomeration of nanoparticles (19). Both DLS and ESEM imaging were utilized to understand the aggregation state of TNPs with bacteria. The intensity-based multimodal size distribution of TNP aggregates and TNPs-bacteria aggregate was determined from DLS according to procedures mentioned in the literature (60). A representative DLS multimodal size distribution plot is shown in Figure 5.6 for TNPs with and without bacteria. Without bacteria, TNPs aggregates were mainly distributed around 700 nm, with a small peak

around 150 nm. However, addition of bacteria significantly altered the aggregate condition with the 1st peak at ~200 nm. Because bacteria size is 1140 nm (Table 5.1), we refer to the first peak as "TNPs aggregate". The second peak's location is around 1000 nm, which is assumed to be the "TNPs-bacteria aggregate". Similar analyses have been conducted for other experimental conditions and are summarized in Table 5.4.

Mechanisms governing interactions between TNPs and bacteria, and their subsequent effect on TNPs deposition, are shown schematically in Figure 5.7A. At pH 5 and KCl, positive TNPs can attract negative *E. coli*. Hence, TNPs aggregate size will decrease due to reduced collision among TNPs aggregates. DLS results (Table 5.4) indicated that addition of *E. coli* increased TNPs aggregate fraction (189.6 nm from 5% to 58.33%) and reduced the TNPs-bacteria aggregate fraction (1000.5 nm from 95% to 41.67%) as compared to TNPs without *E. coli*. The addition of cells may have reduced the nanoparticle aggregate size, possibly due to decreased nanoparticle collision. Similarly, at pH 7 and KCl, negative *E. coli* can repel negative TNPs aggregates and increase TNP-TNP collision, enhancing TNPs aggregation. DLS results are also consistent with these hypotheses at pH 7 and KCl. In $CaCl_2$, mechanisms are similar to KCl; however, increased electrical double layer compression at $CaCl_2$ can reduce TNPs aggregate size more at pH 5 and increase TNPs aggregate size at pH 7 due to bacterial interactions. DLS data demonstrated that addition of *E. coli* in the presence of $CaCl_2$ decreased both TNPs aggregate size and TNPs-bacteria aggregate at pH 5. At pH 7, divalent ions increased both TNPs aggregate and TNPs-bacteria aggregate size.

Table 5.4. Aggregate size distribution from intensity-based multimodal size distribution

	1 min sorption		**60 min sorption**	
Condition	effective diameter (nm)		effective diameter (nm)	
	1st peak	2nd peak	1st peak	2nd peak
pH 5, 10 mM KCl + *E. coli*	104.4 (5%)	676.6 (95%)	189.6 (58.33%)	1005.2 (41.67%)
pH 5, 10 mM KCl + *E. coli* +SRHA	237.5 (36.29%)	748.8 (63.71%)	250.8 (29.15%)	1188.6 (70.85%)
pH 5, 10 mM $CaCl_2$ + *E. coli*	291.1 (49%)	1118.4 (51%)	135.4 (23.47%)	851.6 (76.53%)
pH 5, 10 mM $CaCl_2$ + *E. coli* + SRHA	134.0 (14.25%)	766.3 (85.75%)	198.9 (4.92%)	4554.6 (95.08%)
pH 7, 10 mM KCl + *E. coli*	253.4 (52.17%)	1302.4 (47.83%)	311.2 (66.40%)	2876.5 (33.60 %)
pH 7, 10 mM KCl + *E. coli* +SRHA	220.1 (65.46%)	852.9 (34.54%)	123.3 (5.86%)	839.3 (94.14%)
pH 7, 10 mM $CaCl_2$ + *E. coli*	296.9 (66.66%)	3550.6 (33.34%)	367.6 (50.01%)	4030.1 (49.99%)
pH 7, 10 mM $CaCl_2$ + *E. coli* + SRHA	174.9 (20.15%)	819.7 (79.85%)	401.5 (21.7%)	8909.5 (78.3%)

1 min sorption: Effective diameter was measured after 1 min of contact with bacteria and nanoparticles

60 min sorption: Effective diameter was measured after 60 min of contact with bacteria and nanoparticles

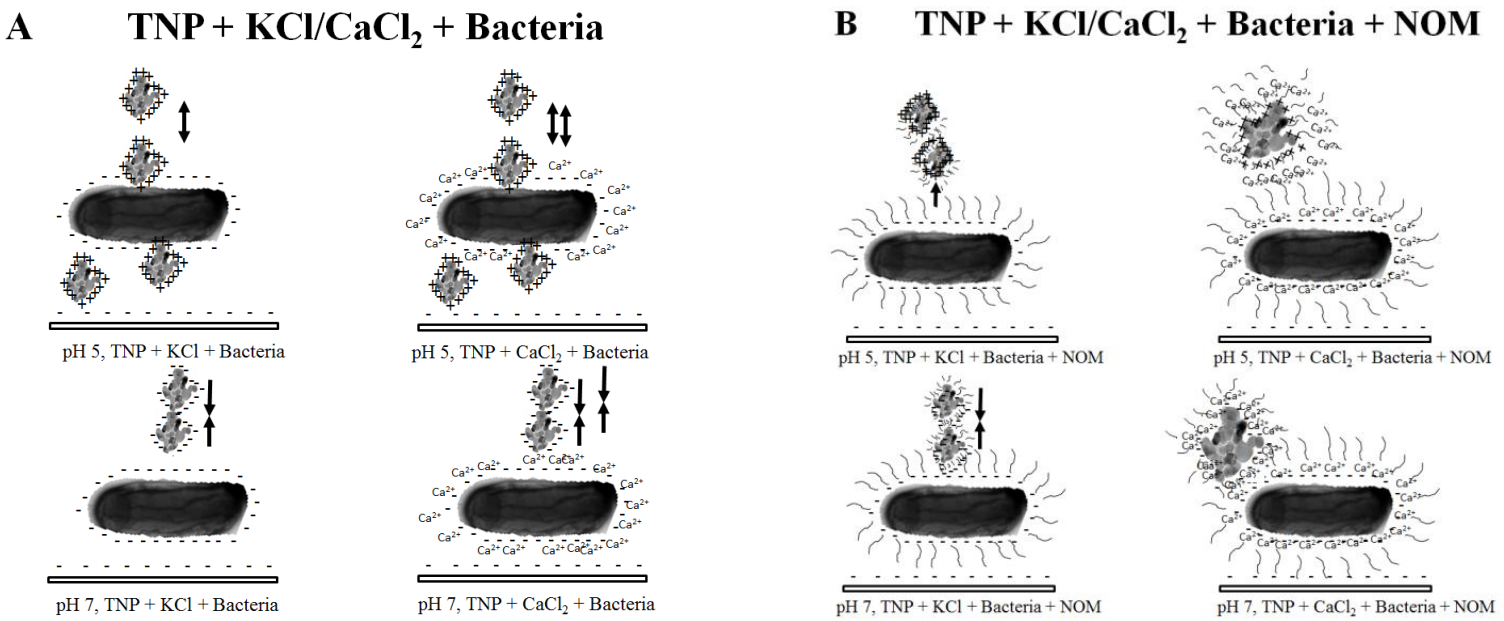

Figure 5.7. Schematic of mechanisms involved in interactions between TNPs, NOM and bacteria and combined effects on deposition of TNPs. A) Interactions between TNPs and bacteria in the absence of SRHA and B) Interactions between TNPs and bacteria in the presence of SRHA. Mechanisms have been shown for pH 5 and 7 in KCl and $CaCl_2$.

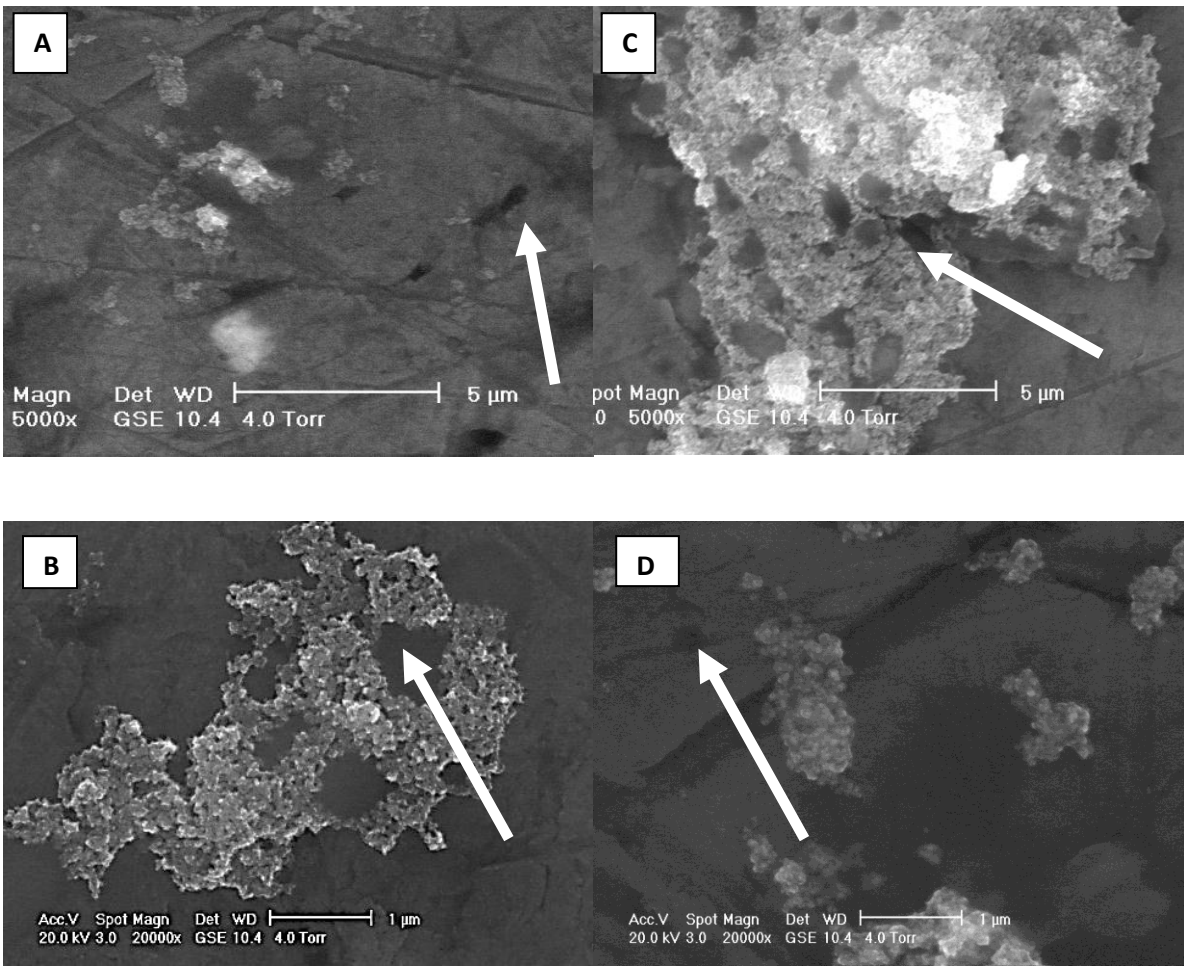

Figure 5.8. Environmental scanning electron microscope (ESEM) Images of TNPs aggregates in presence of *E. coli* and SRHA. A) TNPs and TNPs-*E. coli* aggregate in presence of *E. coli* only at pH 7 and 10 mM KCl; B) TNPs and TNPs-*E. coli* aggregate in presence of *E. coli* only at pH 7 and 10 mM $CaCl_2$; C) TNPs and TNPs-*E. coli* aggregate in presence of *E. coli* and SRHA at pH 7 and 10 mM $CaCl_2$; D) TNPs and TNPs-*E. coli* aggregate in presence of *E. coli* and SRHA at pH 7 and 10 mM KCl. White arrows indicate the *E. coli* not attached to TNPs (Figure A, D) and encrusted by TNPs (Figure B, C).

ESEM images qualitatively are in agreement with our hypotheses (Figure 5.8). At pH 7 and 10 mM KCl, ESEM images indicated that *E. coli* and TNPs did not interact and

TNPs aggregates are small, which is consistent with DLS results (Table 5.4). At pH 7 and 10 mM $CaCl_2$, bacteria attached to TNPs aggregates through Ca^{2+} bridging, forming larger aggregates (Figure 5.8B). Deposition studies of TNPs in the presence of bacteria indicated that changes in aggregation state of TNPs due to bacteria can significantly affect the transport of TNPs in aquatic environment.

5.3.4 Deposition of TNPs in the Presence of Both of SRHA and *E. coli*

Deposition of TNPs was also investigated in the presence of both SRHA and *E. coli* in the PP and column systems. Deposition trends of TNPs in presence of both SRHA and bacteria are: pH 5, $CaCl_2$ + SRHA + *E. coli* > pH 5, KCl + SRHA + *E. coli* > pH 7, $CaCl_2$ + SRHA + *E. coli* ≈ pH 7, KCl + SRHA + *E. coli*.

In the PP, k_{pp} of TNPs decreased quite significantly (~171 times) at pH 5 and KCl in the presence of both SRHA and *E. coli* relative to systems without SRHA or *E. coli*. The bacteria mass transfer rate is higher (10-fold) than that for TNPs under this condition. In $CaCl_2$, addition of *E. coli* and SRHA decreased TNPs mass transfer rate ~6.6 times, whereas the *E. coli* mass transfer rate was an order of magnitude less than TNPs deposition. At pH 7, addition of *E. coli* and SRHA resulted in negligible TNPs deposition in the presence of either monovalent and divalent ions. Overall, in the PP chamber, mass transfer rates of TNPs decreased more significantly with addition of both SRHA and bacteria than with SRHA or bacteria alone.

Results from column studies indicate that bacteria reduce the transport of TNPs through the column (either with or without SRHA). It may be due to complex interaction

among TNPs, SRHA and bacteria influencing the nature of the TNPs and TNPs-bacteria aggregates, which can reduce the mobility of TNPs through porous media by mechanisms such as straining.

Mechanisms likely responsible for interactions among TNPs, bacteria and SRHA have been described schematically in Figure 5.7B. At pH 5 and KCl, both *E. coli* and TNPs aggregates have SRHA on their outer surfaces and both are negatively charged. Hence, electrostatic and electrosteric repulsion between TNPs and bacteria can increase TNPs aggregate size and decrease TNPs-bacteria aggregate size due to change in collisions of TNPs aggregates. At pH 7 and KCl, though, both *E. coli* and TNPs aggregates have SRHA on their outer surfaces, and the layer thickness of SRHA on TNPs is the greatest according to Ohshima Analysis (Table 5.3). Hence, electrostatic and electrosteric repulsion between TNPs and *E. coli* cannot increase TNPs aggregate size. However, in the presence of divalent ions, SRHA can bridge with Ca^{2+} and form clusters of TNPs, *E. coli* and SRHA (Figure 5.7B). DLS results indicated that TNPs and bacteria formed large agglomerates in presence of divalent ions at both pH 5 and pH 7. ESEM images revealed that with addition of SRHA, TNPs and bacteria did not interact at 1 mM KCl and pH 7 (Figure 5.8D). However, with $CaCl_2$ under SRHA, TNPs and bacteria formed much larger aggregate (~5-8 μm) size due to bridging between Ca^{2+} and SRHA (Figure 5.8C). Deposition of TNPs in the presence of both SRHA and bacteria revealed that transport of TNPs can significantly increase due to combined effects of SRHA and bacteria. However, in the presence of divalent ions, large clusters of TNPs, bacteria and

SRHA can significantly reduce the transport through porous media due to straining as observed in column study.

5.4 Conclusions

While we acknowledge that the scope of this study is limited to a narrow range of pH and IS (pH 5 and 7, IS 1-10 mM), these values encompass most natural surface and groundwater conditions. Likewise, the concentration of NOM (1 mg/L) and the two valence conditions (K^+ vs Ca^{2+}) were also within levels typically encountered in groundwater. Therefore, within the experimental parameters of this study, it has been demonstrated that both the presence of NOM and bacterial cells significantly affects TNP deposition and attachment to surfaces due to changes in the physicochemical properties and aggregation state of the TNPs.

In the absence of bacteria or NOM, transport of TNPs through porous media depends primarily on pH, IS and ion valence. The presence of NOM increases the transport of TNPs in the PP chamber under all conditions investigated in this study due to both electrostatic and electrosteric effects. With NOM alone, ion valence shows more significant influence than pH toward removal of TNPs. Addition of bacterial cells reduces the deposition of TNPs in the PP chamber due to changes in TNPs and TNPs-bacterial aggregate formation mainly governed by ion valence. NOM influenced deposition of TNPs more so than bacteria, indicating that organic matter will be the determining factor in TNPs transport. Furthermore, the simultaneous presence of NOM and bacteria in divalent ion solutions results in large TNPs-NOM-bacterial clusters,

significantly influencing the resulting TNPs transport. Deposition in presence of both bacteria and NOM is significantly lower due to change in TNPs aggregation state over the conditions investigated in this study, indicating that bacteria and NOM will increase the transport of TNPs in the aquatic environment.

Transport of TNPs through porous media is different than those observed in the PP chamber, particularly in the presence of bacterial cells. Although the mobility of TNPs through porous media increases significantly in the presence of NOM, addition of bacteria can form large TNPs-bacteria clusters, which in turn reduces the transport of TNPs by straining and pore blocking, promoting removal during treatment via depth/sand filtration. Hence, adjustment of porous media type or filter parameters will be necessary to remove nanoparticles in the presence of NOM and bacterial cells. Considerations of these phenomena are necessary for prediction of nanoparticle transport in both natural and engineered environments.

5.5 References

(1) Dunphy Guzman, K. A.; Finnegan, M. P.; Banfield, J. F., Influence of Surface Potential on Aggregation and Transport of Titania Nanoparticles. *Environmental Science & Technology* **2006,** *40*, (24), 7688-7693.

(2) Wiesner, M. R.; Lowry, G. V.; Alvarez, P.; Dionysiou, D.; Biswas, P., Assessing the Risks of Manufactured Nanomaterials. *Environmental Science & Technology* **2006,** *40*, (14), 4336-4345.

(3) Long, T. C.; Saleh, N.; Tilton, R. D.; Lowry, G. V.; Veronesi, B., Titanium Dioxide (P25) Produces Reactive Oxygen Species in Immortalized Brain Microglia (BV2): Implications for Nanoparticle Neurotoxicity. *Environmental Science & Technology* **2006,** *40*, (14), 4346-4352.

(4) Trouiller, B.; Reliene, R.; Westbrook, A.; Solaimani, P.; Schiestl, R. H., Titanium Dioxide Nanoparticles Induce DNA Damage and Genetic Instability In vivo in Mice. *Cancer Res* **2009,** *69*, (22), 8784-8789.

(5) Adams, L. K.; Lyon, D. Y.; Alvarez, P. J. J., Comparative eco-toxicity of nanoscale TiO2, SiO2, and ZnO water suspensions. *Water Research* **2006,** *40*, (19), 3527.

(6) Crittenden, J. C.; Montgomery Watson, H., *Water treatment principles and design*. J. Wiley: Hoboken, N.J., 2005.

(7) Chen, Z.; Westerhoff, P.; Herckes, P., Quantification of C60 Fullerene Concentrations in Water,. *Environmental Toxicology and Chemistry* **2008,** *27*, (9), 1852-1859.

(8) Chen, K. L.; Mylon, S. E.; Elimelech, M., Enhanced aggregation of alginate-coated iron oxide (hematite) nanoparticles in the presence of calcium, strontium, and barium cations. *Langmuir* **2007,** *23*, (11), 5920-5928.

(9) Chen, K. L.; Mylon, S. E.; Elimelech, M., Aggregation kinetics of alginate-coated hematite nanoparticles in monovalent and divalent electrolytes. *Environmental Science & Technology* **2006,** *40*, (5), 1516-1523.

(10) Chen, K. L.; Elimelech, M., Relating Colloidal Stability of Fullerene (C60) Nanoparticles to Nanoparticle Charge and Electrokinetic Properties. *Environmental Science & Technology* **2009,** *43*, (19), 7270.

(11) Chen, K. L.; Elimelech, M., Interaction of Fullerene (C60) Nanoparticles with Humic Acid and Alginate Coated Silica Surfaces: Measurements, Mechanisms, and Environmental Implications. *Environmental Science & Technology* **2008,** *42*, (20), 7607-7614.

(12) Chen, K. L.; Elimelech, M., Aggregation and Deposition Kinetics of Fullerene (C60) Nanoparticles. *Langmuir* **2006,** *22*, (26), 10994-11001.

(13) Mylon, S. E.; Chen, K. L.; Elimelech, M., Influence of Natural Organic Matter and Ionic Composition on the Kinetics and Structure of Hematite Colloid Aggregation: Implications to Iron Depletion in Estuaries. *Langmuir* **2004,** *20*, (21), 9000-9006.

(14) Stankus, D. P.; Lohse, S. E.; Hutchison, J. E.; Nason, J. A., Interactions between Natural Organic Matter and Gold Nanoparticles Stabilized with Different Organic Capping Agents†. *Environmental Science & Technology* **2010**, *45 (8)*, 3238-3244.

(15) Thio, B. J. R.; Zhou, D.; Keller, A. A., Influence of natural organic matter on the aggregation and deposition of titanium dioxide nanoparticles. *Journal of Hazardous Materials* **2011,** *189*, (1-2), 556-563.

(16) Petosa, A. R.; Jaisi, D. P.; Quevedo, I. R.; Elimelech, M.; Tufenkji, N., Aggregation and Deposition of Engineered Nanomaterials in Aquatic Environments: Role of Physicochemical Interactions. *Environmental Science & Technology* **2010,** *44*, (17), 6532-6549.

(17) Huang, Z.; Zheng, X.; Yan, D.; Yin, G.; Liao, X.; Kang, Y.; Yao, Y.; Huang, D.; Hao, B., Toxicological Effect of ZnO Nanoparticles Based on Bacteria. *Langmuir* **2008,** *24*, (8), 4140.

(18) Li, Z.; Greden, K.; Alvarez, P. J. J.; Gregory, K. B.; Lowry, G. V., Adsorbed Polymer and NOM Limits Adhesion and Toxicity of Nano Scale Zerovalent Iron to E. coli. *Environmental Science & Technology* **2010,** *44*, (9), 3462-3467.

(19) Horst, A. M.; Neal, A. C.; Mielke, R. E.; Sislian, P. R.; Suh, W. H.; Madler, L.; Stucky, G. D.; Holden, P. A., Dispersion of TiO2 Nanoparticle Agglomerates by Pseudomonas aeruginosa. *Appl. Environ. Microbiol.* **2010,** *76*, (21), 7292-7298.

(20) Limbach, L. K.; Bereiter, R.; Müller, E.; Krebs, R.; Gälli, R.; Stark, W. J., Removal of Oxide Nanoparticles in a Model Wastewater Treatment Plant: Influence of Agglomeration and Surfactants on Clearing Efficiency. *Environmental Science & Technology* **2008,** *42*, (15), 5828-5833.

(21) Kiser, M. A.; Westerhoff, P.; Benn, T.; Wang, Y.; Pérez-Rivera, J.; Hristovski, K., Titanium Nanomaterial Removal and Release from Wastewater Treatment Plants. *Environmental Science & Technology* **2009,** *43*, (17), 6757-6763.

(22) Westerhoff, P.; Song, G.; Hristovski, K.; Kiser, M. A., Occurrence and removal of titanium at full scale wastewater treatment plants: implications for TiO2 nanomaterials. *Journal of Environmental Monitoring* **2011,** *13*, (5), 1195-1203.

(23) Kaegi, R.; Voegelin, A.; Sinnet, B.; Zuleeg, S.; Hagendorfer, H.; Burkhardt, M.; Siegrist, H., Behavior of Metallic Silver Nanoparticles in a Pilot Wastewater Treatment Plant. *Environmental Science & Technology* **2011,** *45*, (9), 3902-3908.

(24) Jarvie, H. P.; Al-Obaidi, H.; King, S. M.; Bowes, M. J.; Lawrence, M. J.; Drake, A. F.; Green, M. A.; Dobson, P. J., Fate of Silica Nanoparticles in Simulated Primary Wastewater Treatment. *Environmental Science & Technology* **2009,** *43*, (22), 8622-8628.

(25) Kim, B.; Park, C.-S.; Murayama, M.; Hochella, M. F., Discovery and Characterization of Silver Sulfide Nanoparticles in Final Sewage Sludge Products. *Environmental Science & Technology* **2010,** *44*, (19), 7509-7514.

(26) Chowdhury, I.; Hong, Y.; Honda, R. J.; Walker, S. L., Mechanisms of TiO2 nanoparticle transport in porous media: Role of solution chemistry, nanoparticle concentration, and flowrate. *Journal of Colloid and Interface Science* **2011,** *360*, (2), 548-555.

(27) Xia, T.; Kovochich, M.; Liong, M.; Mädler, L.; Gilbert, B.; Shi, H.; Yeh, J. I.; Zink, J. I.; Nel, A. E., Comparison of the Mechanism of Toxicity of Zinc Oxide and

Cerium Oxide Nanoparticles Based on Dissolution and Oxidative Stress Properties. *ACS Nano* **2008,** *2*, (10), 2121-2134.

(28) Chowdhury, I.; Walker, S. L., Deposition mechanisms of TiO2 nanoparticles in a parallel plate system. *Journal of Colloid and Interface Science* **2012,** *369*, (1), 16-22.

(29) Chowdhury, I.; Hong, Y.; Walker, S. L., Container to characterization: Impacts of metal oxide handling, preparation, and solution chemistry on particle stability. *Colloids and Surfaces A: Physicochemical and Engineering Aspects* **2010,** *368*, (1-3), 91-95.

(30) Phenrat, T.; Saleh, N.; Sirk, K.; Kim, H.-J.; Tilton, R.; Lowry, G., Stabilization of aqueous nanoscale zerovalent iron dispersions by anionic polyelectrolytes: adsorbed anionic polyelectrolyte layer properties and their effect on aggregation and sedimentation. *Journal of Nanoparticle Research* **2008,** *10*, (5), 795-814.

(31) Keller, A. A.; Wang, H.; Zhou, D.; Lenihan, H. S.; Cherr, G.; Cardinale, B. J.; Miller, R.; Ji, Z., Stability and Aggregation of Metal Oxide Nanoparticles in Natural Aqueous Matrices. *Environmental Science & Technology* **2010**, *44*, 1962

(32) Johnson, W. P.; Logan, B. E., Enhanced transport of bacteria in porous media by sediment-phase and aqueous-phase natural organic matter. *Water Research* **1996,** *30*, (4), 923-931.

(33) Hong, Y.; Brown, D. G., Cell surface acid-base properties of *Escherichia coli* and *Bacillus brevis* and variation as a function of growth phase, nitrogen source and C:N ratio. *Colloids and Surfaces B: Biointerfaces* **2006,** *50*, (2), 112.

(34) Kim, H. N.; Hong, Y.; Lee, I.; Bradford, S. A.; Walker, S. L., Surface Characteristics and Adhesion Behavior of *Escherichia coli* O157:H7: Role of Extracellular Macromolecules. *Biomacromolecules* **2009,** *10*, (9), 2556-2564.

(35) Walker, S. L.; Hill, J. E.; Redman, J. A.; Elimelech, M., Influence of Growth Phase on Adhesion Kinetics of *Escherichia coli* D21g. *Appl. Environ. Microbiol.* **2005,** *71*, (6), 3093-3099.

(36) Walker, S.; Elimelech, M.; Redman, J., Influence of Growth Phase on Bacterial Deposition: Interaction Mechanisms in Packed-Bed Column and Radial Stagnation Point Flow Systems. *Environmental Science & Technology* **2006,** *40*, (17), 5586-5586.

(37) Haznedaroglu, B. Z.; Bolster, C. H.; Walker, S. L., The role of starvation on Escherichia coli adhesion and transport in saturated porous media. *Water Research* **2008,** *42*, (6-7), 1547.

(38) Subach, F. V.; Patterson, G. H.; Manley, S.; Gillette, J. M.; Lippincott-Schwartz, J.; Verkhusha, V. V., Photoactivatable mCherry for high-resolution two-color fluorescence microscopy. *Nat Meth* **2009,** *6*, (2), 153-159.

(39) Kim, H. N.; Bradford, S. A.; Walker, S. L., Escherichia coli O157:H7 Transport in Saturated Porous Media: Role of Solution Chemistry and Surface Macromolecules. *Environmental Science & Technology* **2009,** *43*, (12), 4340.

(40) Comte, S.; Guibaud, G.; Baudu, M., Relations between extraction protocols for activated sludge extracellular polymeric substances (EPS) and EPS complexation properties: Part I. Comparison of the efficiency of eight EPS extraction methods. *Enzyme and Microbial Technology* **2006,** *38*, (1-2), 237-245.

(41) DuBois, M.; Gilles, K. A.; Hamilton, J. K.; Rebers, P. A.; Smith, F., Colorimetric Method for Determination of Sugars and Related Substances. *Analytical Chemistry* **1956,** *28*, (3), 350-356.

(42) Markwell, M. A. K.; Haas, S. M.; Bieber, L. L.; Tolbert, N. E., A modification of the Lowry procedure to simplify protein determination in membrane and lipoprotein samples. *Analytical Biochemistry* **1978,** *87*, (1), 206-210.

(43) Chen, G.; Beving, D. E.; Bedi, R. S.; Yan, Y. S.; Walker, S. L., Initial Bacterial Deposition on Bare and Zeolite-Coated Aluminum Alloy and Stainless Steel. *Langmuir* **2009,** *25*, (3), 1620.

(44) Yang, J.; Bos, R.; Poortinga, A.; Wit, P. J.; Belder, G. F.; Busscher, H. J., Comparison of Particle Deposition in a Parallel Plate and a Stagnation Point Flow Chamber. *Langmuir* **1999,** *15*, (13), 4671.

(45) Walker, S. L.; Redman, J. A.; Elimelech, M., Role of cell surface lipopolysaccharides in Escherichia coli K12 adhesion and transport. *Langmuir* **2004,** *20*, (18), 7736-7746.

(46) Hong, Y.; Honda, R. J.; Myung, N. V.; Walker, S. L., Transport of Iron-Based Nanoparticles: Role of Magnetic Properties. *Environmental Science & Technology* **2009,** *43*, (23), 8834.

(47) Gregory, J., *Particles in water : properties and processes*. IWA Pub. ; Taylor & Francis: London; Boca Raton, FL, 2006.

(48) Elimelech, M., Gregory, J., Jia, X., Williams, R.A., *Particle Deposition and Aggregation: Measurement, Modeling and Simulation*. Butterworth-Heinemann: 1995; p 441.

(49) Janjaroen, D.; Liu, Y.; Kuhlenschmidt, M. S.; Kuhlenschmidt, T. B.; Nguyen, T. H., Role of Divalent Cations on Deposition of Cryptosporidium parvum Oocysts on Natural Organic Matter Surfaces. *Environmental Science & Technology* **2010,** *44*, (12), 4519-4524.

(50) Liu, X.; Wazne, M.; Han, Y.; Christodoulatos, C.; Jasinkiewicz, K. L., Effects of natural organic matter on aggregation kinetics of boron nanoparticles in monovalent and divalent electrolytes. *Journal of Colloid and Interface Science* **2010,** *348*, (1), 101-107.

(51) Overbeek, T., DLVO theory - Milestone of 20th century colloid science - Preface. *Advances in Colloid and Interface Science* **1999,** *83*, (1-3), IX-XI.

(52) Derjaguin, B. V., A Theory of the Heterocoagulation, Interaction and Adhesion of Dissimilar Particles in Solutions of Electrolytes. *Discussions of the Faraday Society* **1954**, (18), 85-98.

(53) Pham, M.; Mintz, E. A.; Nguyen, T. H., Deposition kinetics of bacteriophage MS2 to natural organic matter: Role of divalent cations. *Journal of Colloid and Interface Science* **2009,** *338*, (1), 1-9.

(54) Phenrat, T.; Cihan, A.; Kim, H.-J.; Mital, M.; Illangasekare, T.; Lowry, G. V., Transport and Deposition of Polymer-Modified Fe0 Nanoparticles in 2-D Heterogeneous Porous Media: Effects of Particle Concentration, Fe0 Content, and Coatings. *Environmental Science & Technology* **2010,** *44*, (23), 9086-9093.

(55) Ohshima, H., Electrophoresis of soft particles. *Advances in Colloid and Interface Science* **1995,** *62*, (2-3), 189-235.

(56) Phenrat, T.; Song, J. E.; Cisneros, C. M.; Schoenfelder, D. P.; Tilton, R. D.; Lowry, G. V., Estimating Attachment of Nano- and Submicrometer-particles Coated with Organic Macromolecules in Porous Media: Development of an Empirical Model. *Environmental Science & Technology 44*, (12), 4531.

(57) de Kerchove, A. J.; Elimelech, M., Relevance of Electrokinetic Theory for "Soft" Particles to Bacterial Cells: Implications for Bacterial Adhesion. *Langmuir* **2005,** *21*, (14), 6462-6472.

(58) Phenrat, T.; Saleh, N.; Sirk, K.; Tilton, R. D.; Lowry, G. V., Aggregation and Sedimentation of Aqueous Nanoscale Zerovalent Iron Dispersions. *Environmental Science & Technology* **2007,** *41*, (1), 284-290.

(59) Jaisi, D. P.; Saleh, N. B.; Blake, R. E.; Elimelech, M., Transport of Single-Walled Carbon Nanotubes in Porous Media: Filtration Mechanisms and Reversibility. *Environmental Science & Technology* **2008,** *42*, (22), 8317-8323.

(60) Phenrat, T.; Kim, H.-J.; Fagerlund, F.; Illangasekare, T.; Tilton, R. D.; Lowry, G. V., Particle Size Distribution, Concentration, and Magnetic Attraction Affect Transport of Polymer-Modified Fe0 Nanoparticles in Sand Columns. *Environmental Science & Technology* **2009,** *43*, (13), 5079.

Chapter 6

Influence of Primary Particle Size on Nano-TiO_2 Aggregate Formation and Transport

Chowdhury, I., Pokhrel, S., Mädler, L., Mylon, S. E. and Walker, S. L. (2012) Influence of Primary Particle Size on Nano-TiO_2 Aggregate Formation and Transport, *Environmental Science and Technology*.

Abstract

This study set out to determine the influence of primary particle size on the aggregate formation and transport of TiO_2 nanoparticles (TNPs) through porous media. Three distinctly sized TNPs (6, 13, 23 nm) were synthesized using flame spray pyrolysis (FSP). Aggregate formation and transport behavior of these particles were evaluated in a column packed with quartz sand over a range of solution chemistries and in the presence of natural organic matter (NOM). Results indicate that electrokinetic properties of all the TNPs are the function of solution chemistry, but not necessarily dependent on primary particle size. However, aggregation behavior demonstrated significant dependence on size, with 6 nm TNPs forming the largest aggregate. Primary particle size influences transport of the aggregate with a notable dependence on the aggregate size. For small aggregates (<500 nm) under clean bed filtration, the larger the primary particle size within the aggregate is the higher the retention of the aggregates in the porous media. For large aggregates (>800 nm) the transport trend becomes the opposite, which is attributed to straining or blockage of the porous media subsequently giving rise to breakage of the aggregate. Fractal dimension (D_f) showed a linear relationship with respect to specific surface area of indicating that the smallest primary particle has the more compact aggregate in the aquatic environment.

6.1 Introduction

Nanoparticles in water bodies generally deposit more slowly than larger particles making transport feasible over considerable distances along with movement of water (1). However, the distance travelled can be significantly reduced due to the degree of aggregation. The behavior of manufactured or natural nanoparticles in aquatic systems can provide useful basis for prediction of nanoparticle fate and transport. Moreover, the interaction of these NPs such as nano TiO_2, with the natural organics present in the water system also helps to facilitate the transport of these materials. TiO_2 nanoparticles synthesized at a large scale in the industry are used in many consumer product and applications. Hence, TiO_2-based nanoproducts will be ubiquitous and there is considerable likelihood that these nanoparticles will be released in the environment, demanding the investigation of the fate, transport and toxicity.

A suspension of small dense unfunctionalized nanomaterials is likely comprised of assemblages or aggregates of primary particles (2, 3), and although the nanoparticles can form large stable aggregates at the colloidal scale, localized properties of the aggregate can be influenced by the physicochemical features of the primary particles. Nanoparticle aggregates are a relatively loosely bound, physically heterogeneous cluster of primary particles, and they may possess a porous structure through which water and ions may diffuse (4). Fractal dimension is often used to characterize aggregate morphology which can change with the degree of favorability of the process of aggregation (5). Aggregate morphology can influence the drag force on the aggregate

and at times this may be significantly different than that experienced by a single, colloidal particle. For example, Wiesner (4) conducted an investigation of aggregate growth in a rapid mix system with numerical simulations and found that the resulting fractal dimension played a substantial role in the resulting floc volume which subsequently affected removal of aggregates in the basin. Another study (6) investigated aggregation and disruption mechanisms of SiO_2 (7-30 nm), ZrO_2 (12 nm) and TiO_2 (21 nm) nanoparticle aggregates in a stirred vessel. This study revealed that aggregates composed of large primary particle size are more easily broken by applying a combination of external forces compared with those aggregates composed of smaller primary particles

The physicochemical nature of the nanoparticle aggregate also differs from that of a single, colloidal particle. He et al. (7) demonstrated that both point of zero charge and critical coagulation concentration of hematite nanoparticles showed a marked increase with primary particle size. Suttiponparnit et al. (8) found that isoelectric point (IEP) of TiO_2 nanoparticles (TNP) decreased with primary particle size, whereas particle crystal structure showed an insignificant effect on the IEP of TNP. Zhang et al. (9) found that the chemical reactivity of silver particles was sensitive to particle size, notably with the release rate of silver ions increasing with smaller primary particle size.

At the biointerface, aggregates have also been shown to differ from the primary particles that make them up. One study found a size effect on the adsorption of hematite nanoparticles on *E. coli* cells revealed that adsorption of large nanoparticles (98 nm)

reached equilibrium faster than small nanoparticles (26 nm) decreasing adsorption rates with primary particle size (10). Another study (11) revealed that iron from hematite less than a few tens of nm in size were considerably more bioavailable than iron associated with larger particles due to the penetration of sub-10 nm particles through the cell wall.

Baalousha et al. (12) studied the role of natural organic matter (NOM) on aggregation of iron oxide nanoparticles and found that the concentration of Suwanee River Humic Acid significantly affected the structure and aggregation of iron oxide with a more compact aggregate formed in the presence of organic matter. They reported that in the absence of the organic, diffusion limited aggregation dominates, whereas the addition of NOM led to a reaction limited regime. Within the reaction limited regime, particles require a react more slowly finding the lowest energy state that is a more compact aggregate. Mylon et al. (13) investigated influence of NOM on the kinetics and structure of hematite colloid aggregation and also found a significant influence of humic acid in the resulting fractal nature of aggregate. Another study with ZnO and iron-doped ZnO reported that toxicity of ZnO decreased notably in presence of humic acid (14).

Despite the extensive research with nanoparticles of various sizes that has been conducted to date on nanoparticle aggregation and toxicity, there have been no studies to our knowledge on the subsequent role on deposition and transport behavior. The physicochemical properties of the resulting aggregate can contribute to different mechanism and extent of transport in the aquatic environment (15). The few studies available are limited in scope and do not address the heterogeneity within the aggregate

brought about by differring primary particle size. Additionally, there has been no study on the influence of primary particle size within the similarly sized nanoparticle aggregates on transport behavior. So far, most studies have considered nanoparticle aggregates as colloids to interpret the transport results, yet it is not still understood whether overall the contribution of the aggregate size or primary particle size within the aggregates will dominate. Therefore, in this study we investigate the role of primary particle size within the aggregate in aggregation and transport of nanoparticles using model titanium dioxide (TiO_2) nanoparticle (TNPs), as TNPs are one of the widely used nanomaterials in industry and consumer markets (1, 16). This paper seeks to establish what contribution primary particle size will have on aggregate formation and fate in the aquatic environment.

6.2 Materials and Methods

6.2.1 Synthesis of Distinctly Sized TNPs

A flame spray pyrolysis technique(17) was used for the production of TiO_2 powders. The metallorganic precursor titanium (IV) isopropoxide (Strem Chemical, 99.9% pure) diluted in xylene (0.5M by metal) was used for the production of differently sized TNPs. The liquid precursor was delivered at the rate of 4 mL/min to the flame nozzle using a syringe pump and was atomized using 7/min O_2 at a constant pressure drop of 1.5 bar at the nozzle tip to obtain 6 nm particle. Similarly, precursor flow of 5 or 7 mL/min and oxygen flow of 4.5 or 3.5 were adapted to design the primary particle size

of 13 and 23 nm respectively. The spray was ignited by a premixed co-delivery of CH_4 and O_2 (1.5 L/min, 3.2 L/min) forming a spray flame. The ultrafine particles were formed by reaction, nucleation, surface growth, coagulation and coalescence in the flame environment. The particles were collected from the 257 mm glass filter placed in the flame reactor at a distance of 60 cm from the flame.

6.2.2 Characterization of Synthesized TNPs

Wide range of characterization was conducted to determine the physicochemical properties of synthesized TNPs. For the X-ray diffraction measurements, the differently sized TNPs were loaded into a Philips PW1800 diffractometer [Cu-K_α (λ=0.154 nm)], equipped with a secondary monochromator. The variable divergence for a fixed area of illumination, primary and secondary Soller slit with 0.04 rad aperture and circular sample holder with 16 mm diameter was used for the measurements. A receiving slit of 0.2 mm and a scintillation counter applying a continuous scan in the range of 3-100° 2θ and an integration step width of 0.0334° 2θ (15 s for each measuring time step) were the measurement parameters . The structural parameters were extracted using Rietveld refinement by applying BRASS program (18). Background, scale factor, unit cell parameters, Gaussian as well as Lorentzian peak widths parameters were simultaneously refined followed by crystallite size and microstrain analysis. The structural models ICSD -202242 for anatase TiO_2 and ICSD-63710 for rutile TiO_2 with space groups I41/AMD and P 4_2/m n m respectively were

used. The quality of Rietveld refinement was evaluated in terms of the usual R factor (R_{wp}) and the background corrected residual R'_p (19). A volume weighted average crystallite size (d_{XRD}) and the root-mean-square (rms) lattice micro strain for each of the mixed In-Sn-oxide phases was determined from the line-broadening analysis. The instrumental contribution to the peak broadening was taken into account during the full profile fitting by instrumental parameters derived from a fit of standard crystalline LaB_6.

Nitrogen adsorption-desorption measurements (BET) were carried out at 77K using a NOVA system to determine the specific surface areas. Before the measurements, the samples were degassed at 200°C under vacuum to clean the unwanted adsorbants from the surface. The primary particle size was derived using the equation $d_{BET} = 6/(\rho_p \cdot S_A)$, where d_{BET}, ρ_p and S_A are defined as the average diameter of a spherical particle, theoretical density and the measured specific surface area.

Primary particle size and distribution of synthesized TNPs were determined using transmission electron microscopy (TEM, FEI-PHILIPS CM300, Hillsboro, OR) operated at 300 kV. At least 10 different TEM images were taken for each sized TNPs and primary particle size was determined by analyzing more than 500 nanoparticles using ImageJ software (National Institute of Health, US).

Both electrokinetic properties and hydrodynamic diameter of distinctly sized TNPs were determined over a wide range of solution chemistry from pH 4 to 10 using a ZetaPALS analyzer (Brookhaven Instruments Corp., Holtsville, NY). Both monovalent (KCl) and divalent ($CaCl_2$) ions were used at 1 and 10 mM ionic strength. Suwannee River Humic Acid (SRHA) standard II (International humic society substances, Georgia)

was used as model natural organic matter in this study. Hydrodynamic diameter was measured using dynamic light scattering (DLS) (Brookhaven model BI-9000AT Holtsville, NY) at a wavelength of 661 nm and scattering angle of 90^{o}. All solutions were made with ACS reagent grade chemicals (Fisher Scientific, Pittsburgh, PA) and pH was controlled with 10 mM HCl or KOH. Statistical analysis was conducted to compare the difference among different particles using analysis of variance (ANOVA) and student t-test with 95% confidence level ($P < 0.05$). Regression analyses were also done to determine the significant trend among different particles.

Morphology of distinctly sized TNP was determined to understand the influence of primary particle size on aggregate structure. Aggregate morphology of TNP was determined by static angle light scattering technique varying the scattering angle from 30^{o} to 140^{o}. The light scattering unit consisted of a diode-pumped laser (Verdi V-2/V-5, Coherent) operating at 532 nm, an ALV-SP S/N 30 goniometer (ALV-GmbH, Langen, Germany) with an index matching vat filled with doubly filtered (0.1 µm) toluene, and an ALV-500 correlator. Rayleigh-Gans-Debye (RGD) theory was applied to determine fractal dimension from scattering intensities (32). Basic approach of RGD theory is to model the scattering body as a collection of Rayleigh scatterers that do not interact with each other. At low values of q (low scattering angles), 1/q is much larger than the size of the aggregates. . At high values of q (high scattering angles), 1/q is much smaller than size of primary particle. Intermediate values of q (scattering angles), 1/q lies between size of primary particles and aggregate size with the following equations (32):

$$\mathbf{I(q)} \propto q^{-D_f} \qquad (6.1)$$

$$q = \frac{4\pi}{\lambda} \sin\frac{\theta}{2} \quad (6.2)$$

Where θ = scattering angle; λ = wavelength in vacuum; D_f = fractal dimension; q = scattering wave vector; $I(q)$ = scattering intensity.

6.2.3 Transport Experiments

Transport of distinctly sized TNP were investigated in a borosilicate glass column (Omnifit, Boonton, NJ) packed with quartz sand (Iota quartz, Unimin Corp., NC) simulating porous media. The detailed procedure regarding the column experiment is mentioned elsewhere (15, 20). Further details regarding preparation procedures for the sand has been are similar to earlier studies (21-23). The porosity of packed-bed column was determined gravimetrically to be 46.5% (24). The TiO_2 concentration in each of stock nanoparticles effluent was determined by Inductively Coupled Plasma Atomic Emission Spectroscopy (ICP-AES) (Optima 2100 DV, PerkinElmer Inc., Shelton, CT.)(26). Column experiments were conducted with 2 mL/min with a superficial approach velocity of 0.019 cm/s, simulating groundwater or slow sand filtration (27, 28). Injected TNP concentration was 10 mg/L. For column experiments with SRHA, the packed column was equilibrated with SRHA solution for at least 10 PV prior to injection of TNP suspension.

Deposition rate coefficient (k_d) of TNPs in the column were determined by using the following equation(29):

$$k_d = -\frac{U}{fL} ln\left(\frac{C}{C_0}\right) \quad (6.3)$$

where U = approach fluid velocity (0.019 cm/s); L = packed-bed column length (5 cm); f = packed-bed porosity (0.465); and C/C_0 = normalized breakthrough concentration for clean bed conditions. Averaged normalized breakthrough concentrations between 1.8 and 2.0 pore volumes were used as C/C_0 for calculation k_d values following the procedure described elsewhere (30).

Experimental attachment efficiency was calculated by normalizing experimental deposition rate (k_d) with deposition rate under favorable condition ($k_{d,\,fav}$) (24):

$$\alpha = \frac{k_d}{k_{d,fav}} \quad (6.4)$$

$k_{d,\,fav}$ was calculated from the packed-bed column experiments where quartz sand was modified with aminosilane as mentioned elsewhere (30). In brief, the quartz sand was suspended in a 1% (v/v) (3-aminopropyl)triethoxysilane (Sigma Aldrich) for 5 min. Afterwards the quartz sand was rinsed thoroughly with DI water, followed by curing at 80^{o}C for 24 h.

6.3 Results and Discussion

6.3.1 Particle and Aggregate Characterization

6.3.1.1 XRD, BET and TEM

The BET measurements show that the particles have specific surface area of 71, 117 and 173 m^2/g to give particle size of 6, 13 and 23 nm respectively. The primary particle size decreases from 23 to 6 nm with the change in flame parameters. These values reasonably agree with the crystallite size obtained from the XRD refinement. The diffraction peaks at $2\theta \sim 25.48$ (101), 38.07 (112), 48.30 (200), 55.35 (211), 63.03 (204) and 69.21 (116) are attributed to anatase (JCPDS No. 00-021-1272), while those at 2θ ~27.80 (110), 36.36 (101) and 41.48 (111) represent the rutile phase (JCPDS No. 00-021-1276). The XRD patterns (Figure 6.1) of differently sized TiO_2 show that the particles were in anatase or rutile phase with the approximate ratio of 5:1 for 6 and 13 nm particles, and 9.5:1 for 23 nm particles. The XRD patterns were refined using structural model ICSD-63711 for anatase, and ICSD-63710 for rutile phases. Both the anatase and rutile structures crystallize in tetragonal crystal system with space group I41/amd, and P42/mnm respectively.

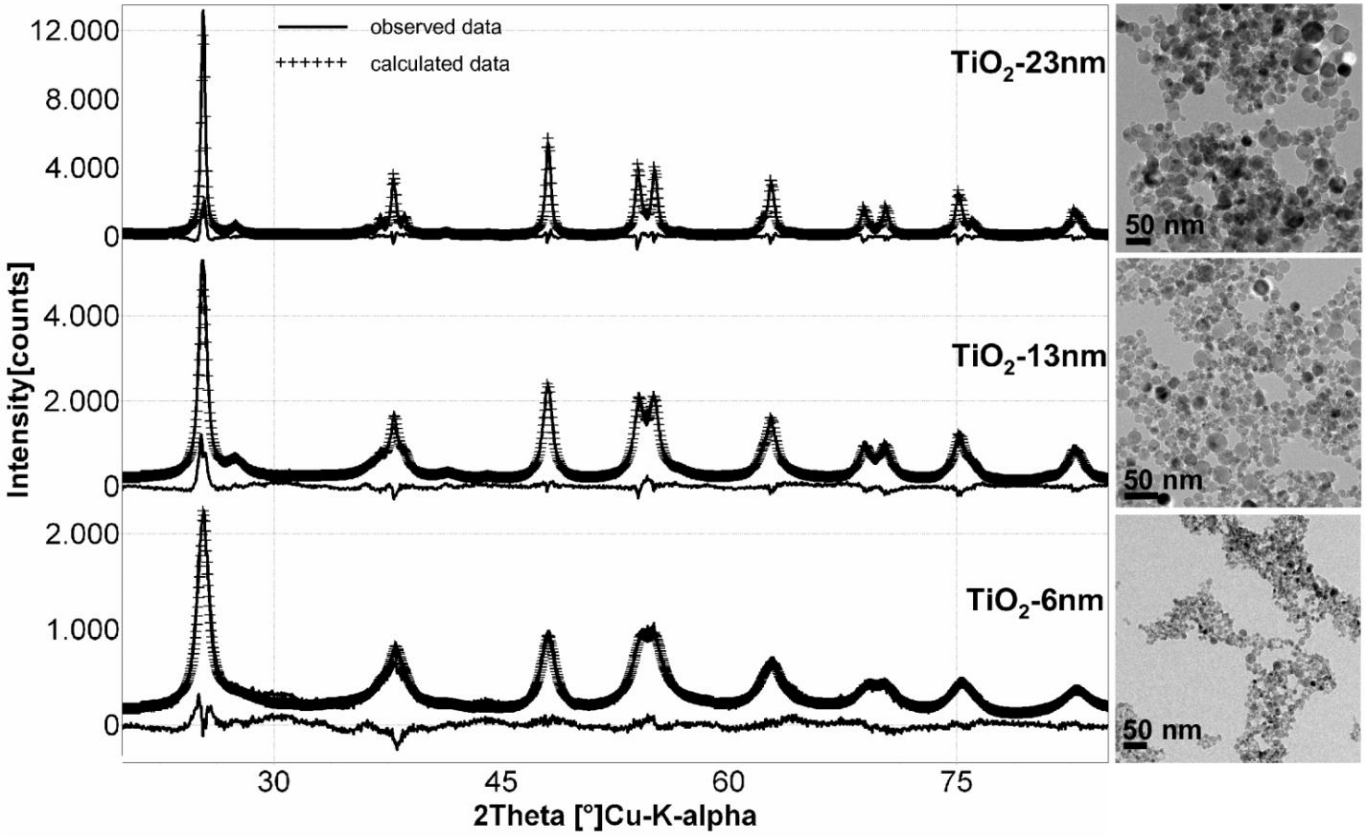

Figure 6.1. The XRD patterns, Rietveld refinement and particle sizes of TiO2 NPs. The crystallite size (d_{XRD}) and particle sizes obtained from TEM (d_{TEM}) and BET (d_{BET}) have a reasonable agreement.

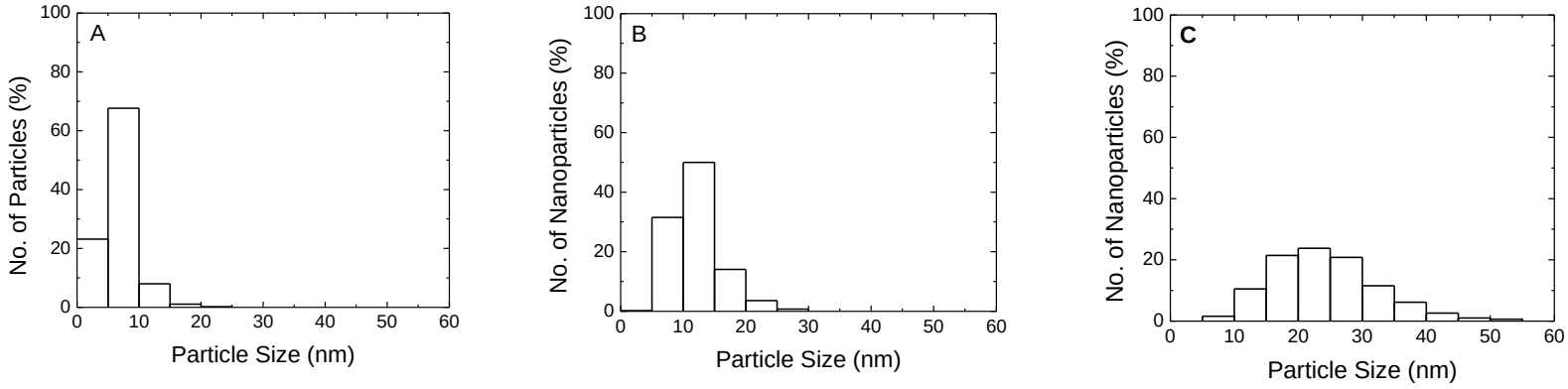

Figure 6.2. Particle size distribution of distinctly sized TNPs for A) 6 nm, B) 13 nm, C) 23 nm. Particle size distribution has been determined by analyzing at least 200 particles from 10 different TEM images using ImageJ software.

TEM images show clear size differences ($P < 0.05$) among synthesized TNPs as determined from ANOVA (Figure 6.1). The smallest sized TNP (6 nm measured from XRD data) had an average size of 6.6 ± 2.5 nm. Size of primary particle ranges from 2 to 25 nm with mostly within 0 - 10 nm range (>90%), indicating that synthesized particles are highly monodispersed (Figure 6.2). Average size of next larger sized TNPs (13 nm measured from XRD data) was determined to be 12.1 ± 3.9 nm. Particle size ranges from 5 nm to 30 nm mostly within 5-15 nm range (>80%). TEM image analysis of the largest synthesized TNP (23 nm as measured from XRD) reveals that average aggregate size is 24.1 ± 8.3 nm. This synthesized TNPs have wide range of particle size from 5 nm to 65 nm with mostly 15-30 nm (>70%).

6.3.1.2 Electrokinetic Characterization and Hydrodynamic Diameter

Electrokinetic properties and hydrodynamic diameter of TNPs are presented in Figures 6.3, 6.4 and 6.5. At 1 mM KCl, all TNPs resulted similar electrophoretic mobility (EPM) over the pH range of 4 to10indicating that all the synthesized particles have similar surface potentials despite the differences in primary particle size (Figure 6.3). Isoelectric point of TNPs is around pH 3.5, which was observed to be insensitive to primary particle size. Aggregate size showed significant dependence on the primary particle size, with 6 nm TNPs forming the largest aggregate followed by 13 nm and 23 nm. Higher surface areas for smaller primary nanoparticles can lead to larger aggregation, which was also observed in case of differently sized hematite nanoparticles

(7). The influence of primary particle size on aggregation decreased with an increasing pH due to a more negative EPM causing larger electrostatic repulsion between TNPs (31). At pH 10, both aggregate size and EPM of all 3 sized TNPs became quite similar. Likewise at higher IS (10 mM KCl), EPM remained similar regardless of the size of TNPs across the pH range of 4-10, though EPM were significantly lower than 1 mM KCl due to electrical double layer compression (31).

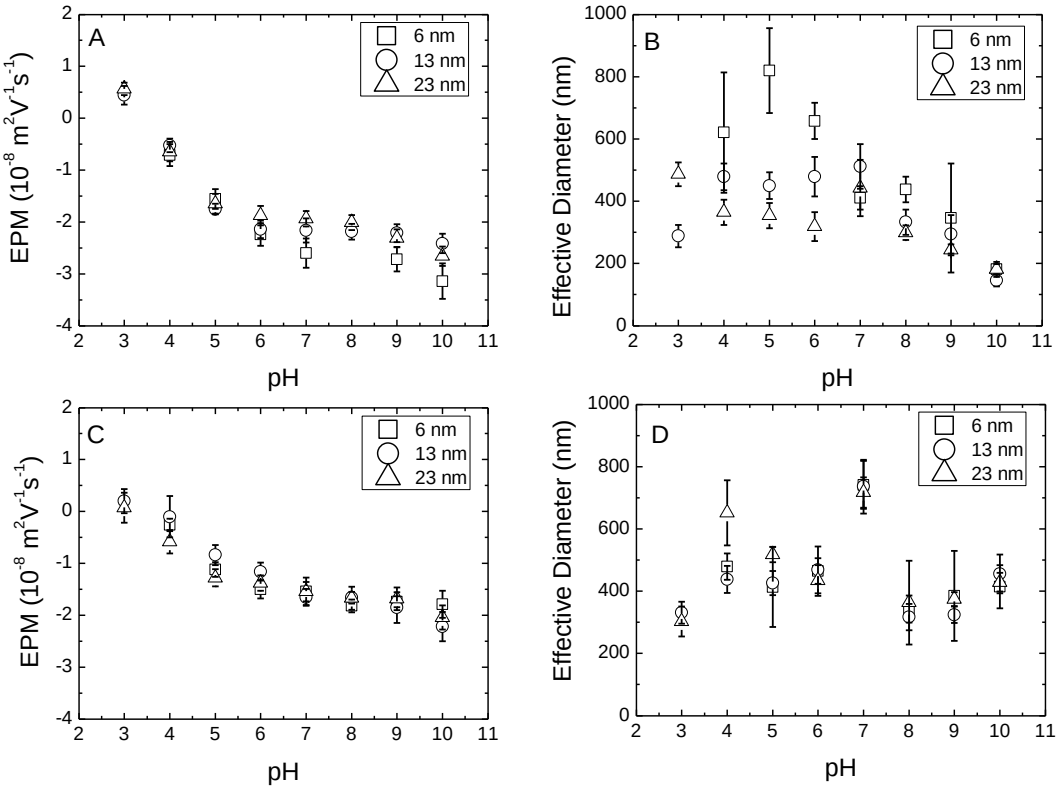

Figure 6.3. Electrokinetic characterization and hydrodynamic diameter of 6, 13, 23 nm TiO_2 particles as a function of pH at 1 and 10 mM KCl. A) Electrophoretic mobilities (EPMs) of TiO_2 at 1 mM KCl; B) Aggregate size of TiO_2 at 1 mM KCl; C) EPMs of TiO_2 at 10 mM KCl; D) Aggregate size of TiO_2 at 10 mM KCl. pH was controlled by adding KOH and HCl. Nanoparticle concentration was 10 mg/L.

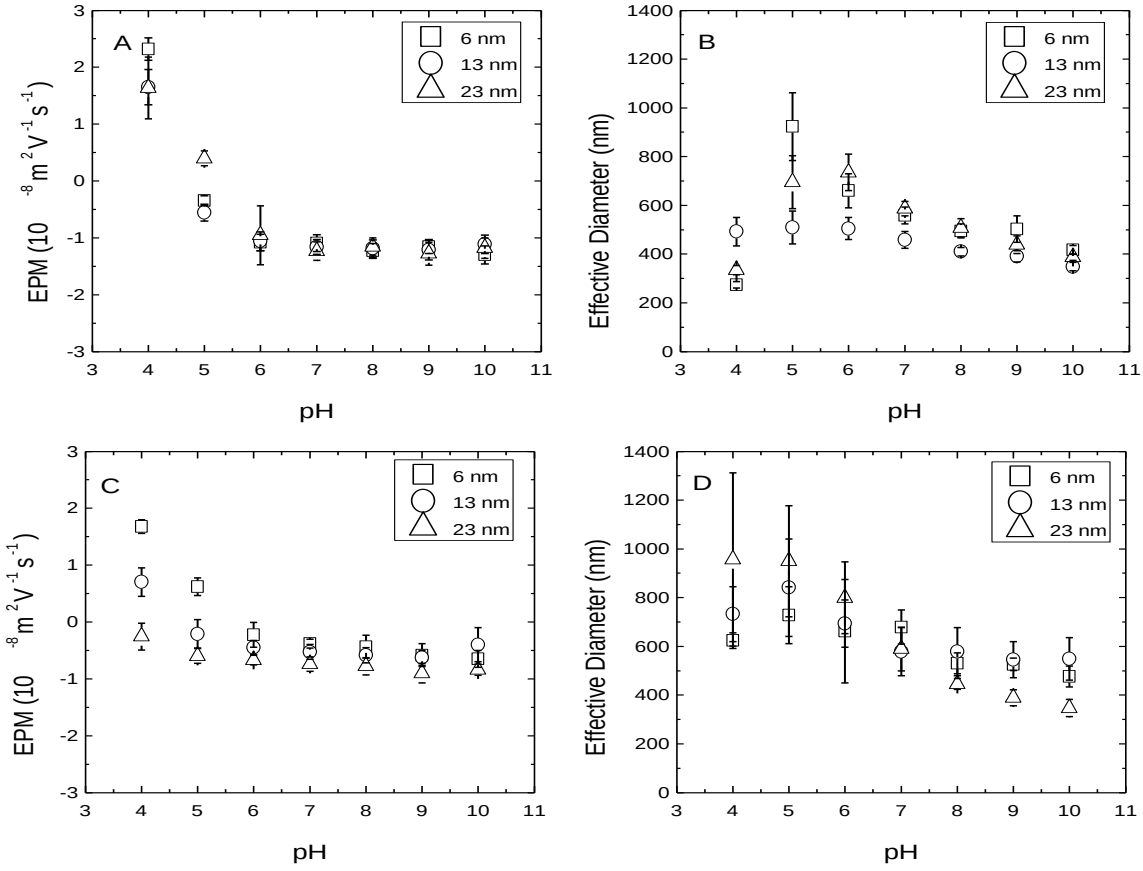

Figure 6.4. Electrokinetic characterization and hydrodynamic diameter of 6, 13, 23 nm TiO_2 particles as a function of pH at 1 and 10 mM $CaCl_2$. A) Electrophoretic mobilities (EPMs) of TiO_2 at 1 mM $CaCl_2$; B) Aggregate size of TiO_2 at 1 mM $CaCl_2$; C) EPMs of TiO_2 at 10 mM $CaCl_2$; D) Aggregate size of TiO_2 at 10 mM $CaCl_2$. pH was controlled by adding KOH and HCl. Nanoparticle concentration was 10 mg/L.

In the presence of divalent ions ($CaCl_2$), there is a slight difference in EPMs below pH 6 among different TNPs, though EPM did not change over the pH range of 6 to 10 for different types of TNPs (Figure 6.4). Aggregate size was significantly larger for $CaCl_2$ with respect to KCl due to the increased electrical double layer compression in the

presence of divalent ions in 10 mM IS (32). There is no significant trend observed in aggregation with respect to the primary particle size.

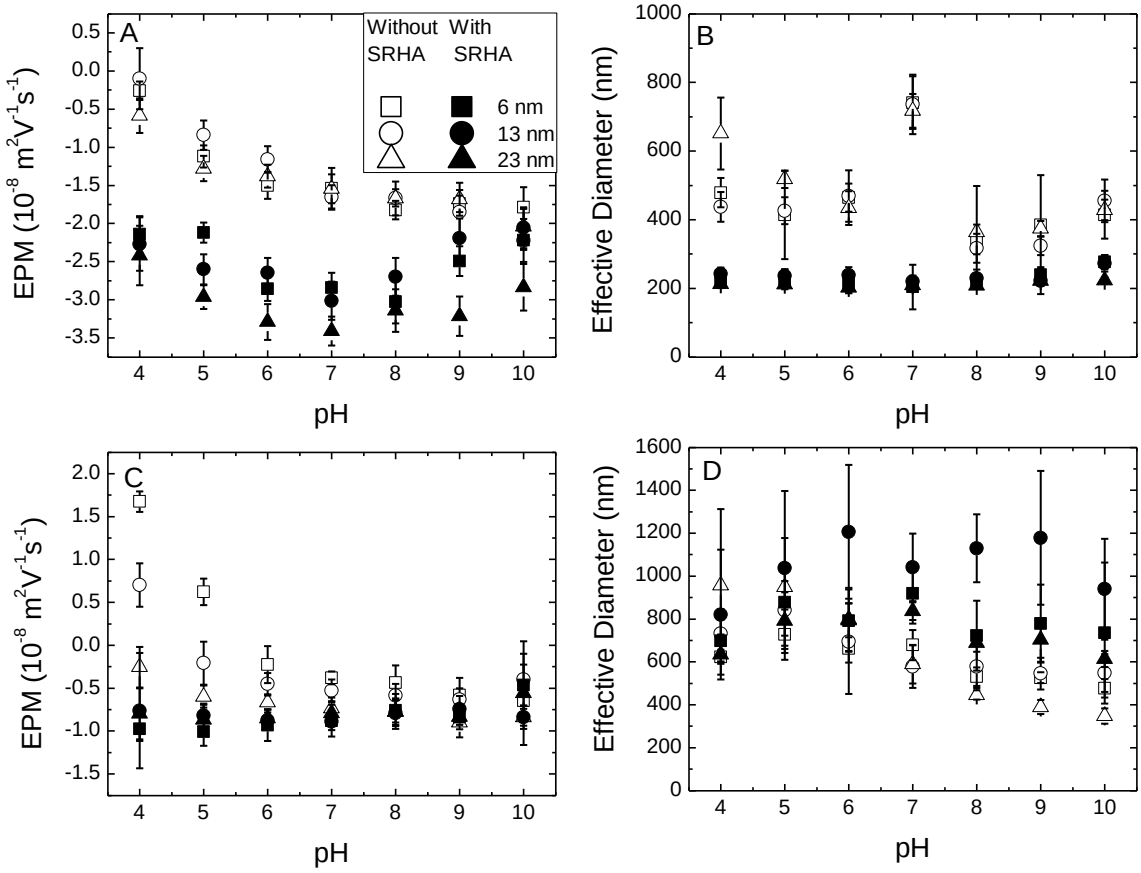

Figure 6.5. Electrokinetic characterization and hydrodynamic diameter of 6, 13, 23 nm TiO_2 particles as a function of pH at 10 mM KCl and 10 mM $CaCl_2$ with and without SRHA. A) Electrophoretic mobility (EPMs) of TiO_2 at 10 mM KCl ; B) Aggregate size of TiO_2 at 10 mM KCl ; C) EPMs of TiO_2 at 10 mM $CaCl_2$; D) Aggregate size of TiO_2 at 10 mM $CaCl_2$. pH was controlled by adding KOH and HCl. Nanoparticle concentration was 10 mg/L. Legends in Figure A are applicable for Figures B, C and D.

Addition of SRHA in 10 mM KCl resulted in more negative surface potentials for all the TNPs regardless of primary particle size (Figure 6.5A). Aggregate diameter decreased significantly to ~200 nm for all TNPs with addition of SRHA due to electrostatic and electrosteric effects (33). Influence of SRHA on the diameter of TNPs diminished with pH, as similarly sized aggregates were formed in the absence and presence of SRHA at pH 10. Upon addition of SRHA in the presence of divalent ions ($CaCl_2$), the surfaces of the TNPs were again more negatively charged similar to observations in KCl. However, TNP aggregate size increased significantly with addition of SRHA in $CaCl_2$ most likely due to bridging of carboxylic functional groups of SRHA in the presence of divalent ions (32, 34) with 13 nm forming the largest aggregate, followed by 6 nm and 23 nm. While increasing pH and adding SRHA reduced the aggregate size considerably, we do note that aggregates were never completely disaggregated to primary particle size in aqueous suspension, forming hard aggregates (35). The minimum aggregate size was ~200 nm for all TNP tested indicating that hard aggregate size of the TNPs used in this study is around 200 nm. Mueller et al. (35) also observed similar phenomenon for non-agglomerated dry silica nanoparticles.

Overall electrokinetic properties of TNPs resulted similar values independent of primary particle size over the pH range investigated in this study, particularly in monovalent ions (KCl). Though ionic strength and presence of SRHA influenced the TNP aggregates considerably, primary particle size affected the aggregate size more significantly particularly in low ionic strength (1 mM KCl). This is likely because primary nanoparticles form larger aggregate size due to higher surface areas. Addition of

SRHA significantly reduced the influence of primary particle size in aggregation due to sorption of SRHA on TNP surfaces (36). At pH 10, both EPMs and aggregate size became very similar for all TNPs, indicating that transport of TNPs at pH 10 will be the same if there is no role of primary particle size. At pH 7, distinctly sized TNPs had similar EPMs but different aggregate sizes indicating that transport of TNPs will be governed by aggregate size at pH 7. Hence, deposition studies were conducted at pH 7 and 10 to understand the role of primary particle size within the aggregate on the subsequent transport.

6.3.1.3 Aggregate Morphology of TNPs

Morphology of TNP aggregates was determined over a wide range of solution chemistry in the absence and presence of SRHA (Figure 6.6). Overall the aggregate morphology shows a notable dependence on primary particle size, pH, IS, and SRHA with D_f varying from 1.05 to 2.5. Fractal dimensions of TNP aggregates have been correlated with specific surface areas of primary nanoparticles (Figure 6.7). D_f of TNP aggregates shows linear dependence on surface areas of particles over the conditions investigated in this study, which indicates that aggregates with smaller primary particles have higher D_f than those with larger primary particles. Slope of D_f vs. surface area plot represents the sensitivity of fractal dimension of TNP aggregates to primary particle size. However sensitivity of compactness of aggregate on primary particle size shows a significant dependence on solution chemistry (pH, IS, ion valence) and presence of SRHA which may be due to change in surface charge and size of TNP aggregates.

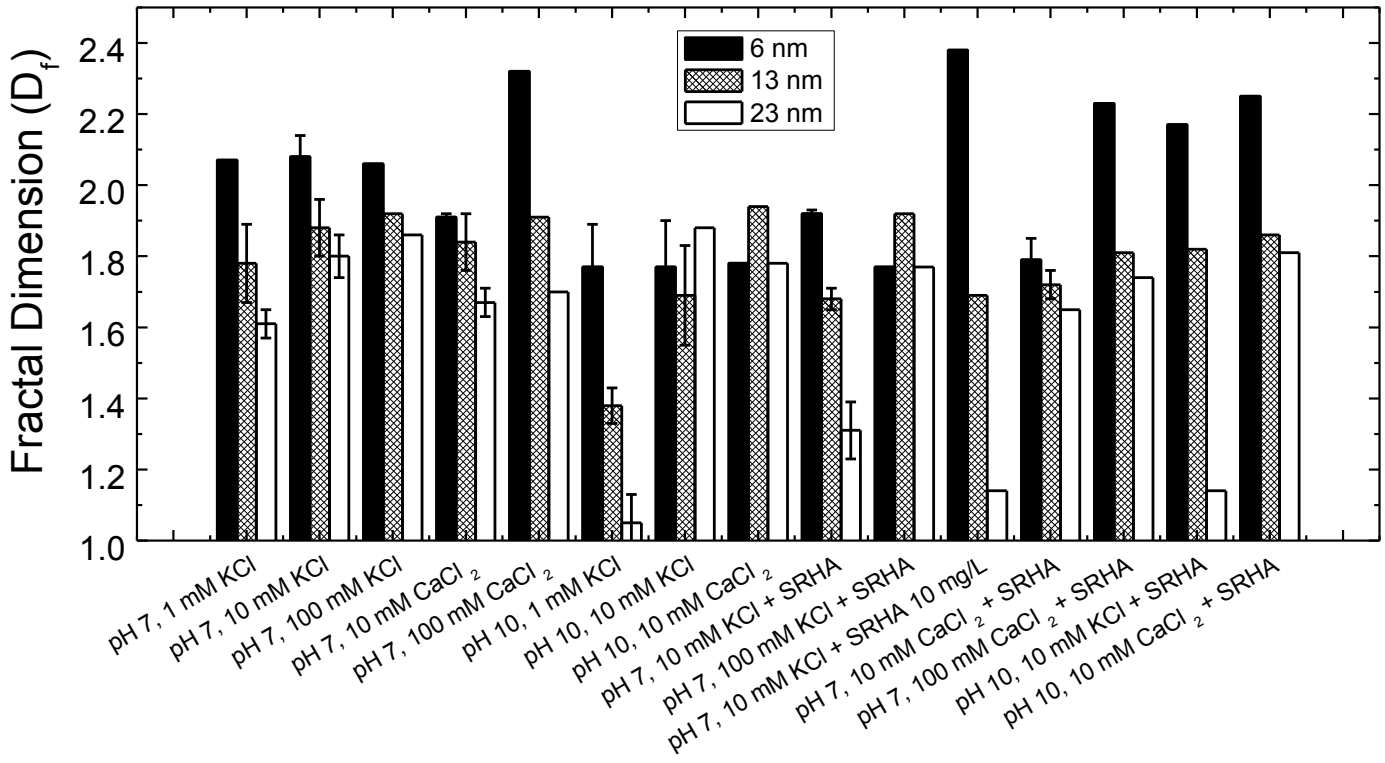

Figure 6.6. Fractal dimensions of distinctly sized TNP aggregates as a function of pH, ionic strength, ion valence and SRHA. Fractal dimensions were calculated using RGD theory from the light scattering data 30^o to 140^o.

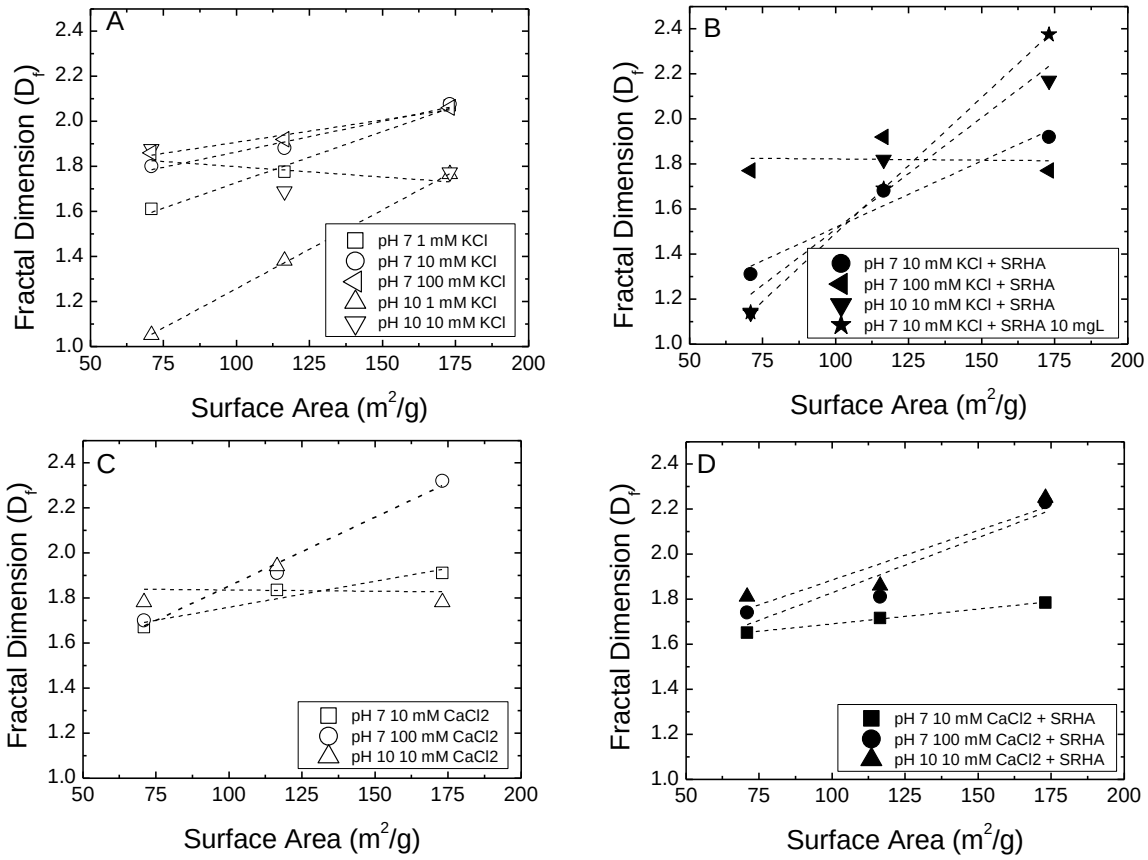

Figure 6.7. Relative dependence of fractal dimension (D_f) on surface area of primary particles as a function of A) KCl only ; B) Both KCl and SRHA; C) $CaCl_2$ only and D) Both $CaCl_2$ and SRHA.

6.3.2 Transport of TNP Aggregate

6.3.2.1 Transport in the Absence of SRHA

Results from the transport of TNP aggregates in the packed-bed column are presented in Figure 6.8 and Table 6.1. At pH 7, significant elution of TNPs (>80%) were observed for all 3 sized-TNPs in 1 mM KCl solution (Figure 6.8A). Almost 100% elution was observed for 6 nm and 13 nm-sized TNPs, while 16% of 23-nm-sized TNPs retained in the column. Higher elution of TNP aggregates may be attributed to the electrostatically repulsive conditions existing between quartz sand and TNP aggregates. Furthermore, deposition rate constants (k_d) as well as attachment efficiency (α) of aggregates comprised of 23 nm TNPs were 2 times higher than aggregates formed from 6 nm and 13 nm particles. Though EPMs were almost identical for all 3 TNPs, significant difference in deposition was observed. TNP aggregate size at pH 7 and 1 mM KCl were 411(±58.8), 512 (±26.9) and 442 (±29.1) nm for aggregates formed with 6, 13 and 23 nm primary particles respectively. Statistical analysis indicates that there are not significant differences among those aggregates sizes considering the standard deviation.

At pH 10 and 1 mM KCl, high elution (>90%) was observed for 6 nm and 13 nm-aggregate, a trend similar to the system maintained at pH 7 with 1 mM KCl (Figure 6.8C). However, significantly lower elution (~66%) was observed for 23 nm-TNP aggregate. α of TNP follows the trend: 6 nm < 13 nm < 23 nm. α of aggregates with 23 nm was almost 4 times greater than those of 6 nm and 13 nm. Both aggregate size (~180 nm) and EPM were quite similar for all TNP types indicating that primary particle size in

aggregates played significant role in deposition. This may be due to the difference in surface areas of primary particles, interaction energy and aggregate morphology of distinctly-sized TNP aggregates.

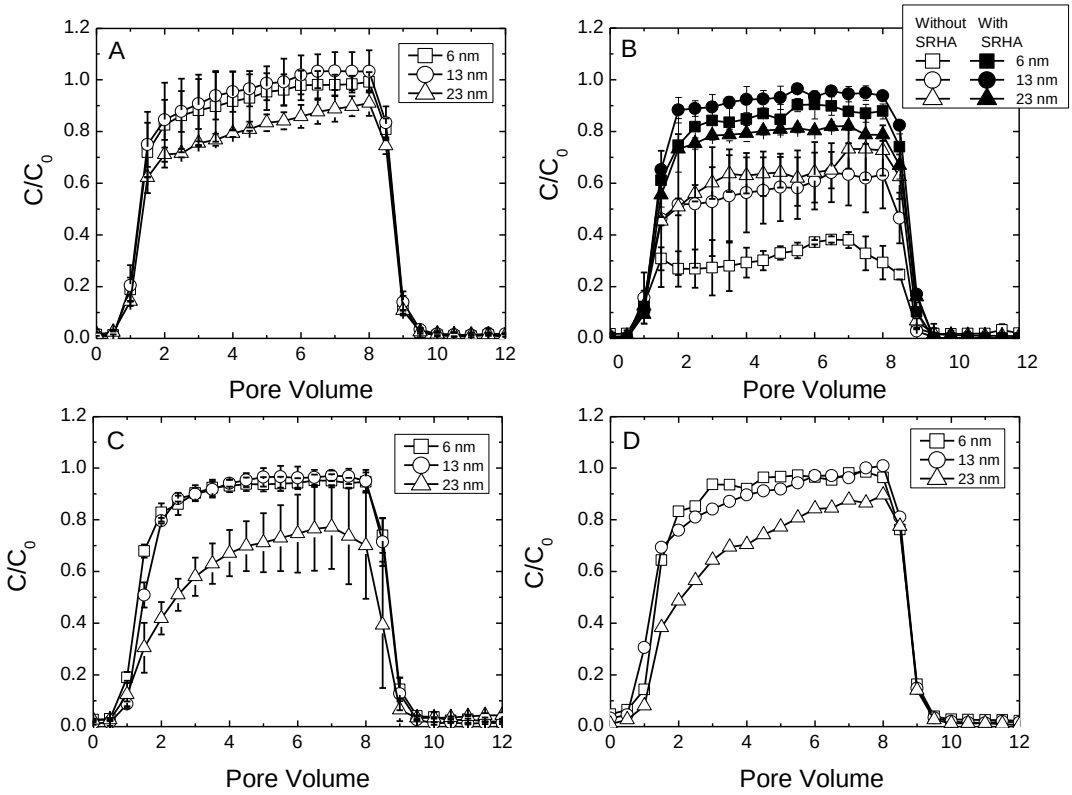

Figure 6.8. Column breakthrough curves for 6, 13 and 23 nm TiO_2 nanoparticles at A) pH 7 and 1 mM KCl, B) pH 7 and 10 mM KCl (with and without SRHA), C) pH 10 and 1 mM KCl, and D) pH 10 and 10 mM KCl. Injected nanoparticle concentration was used as 10 mg/L. Other parameters: Approach velocity= 0.019 cm/s; porosity = 0.465; SRHA concentration = 1 mg/L TOC. pH was controlled by KOH and HCl. Error bars indicate on standard deviation of triplicate measurements.

Table 6.1. Deposition rates of 6 nm, 13 nm and 23 nm TiO_2 nanoparticles in packed-bed column as a function of pH and IS

Primary particle size (nm)	pH	Ionic strength (mM KCl)	Aggregate size (nm)	Fractal dimension, D_f	EPM (10^{-8} $m^2V^{-1}s^{-1}$)	Deposition rate, k_d (s^{-1})	M_E (%)	Attachment efficiency, α
6	7	1	411.1± 58.8	2.07 ± 0.00	-2.60±0.28	1.77×10^{-3}	100.78	0.05
		10	741.2 ± 76.7	2.08 ± 0.06	-1.54 ± 0.27	1.04×10^{-2}	33.74	0.32
		10 (SRHA)	204.1 ±65.1	1.92 ± 0.01	-2.84±0.19	2.67×10^{-3}	84.79	0.08
	10	1	181.5 ± 20.7	1.77±0.12	-3.14 ± 0.34	1.82×10^{-3}	93.59	0.06
		10	414.2 ± 69.8	1.77± 0.13	-1.79 ± 0.26	4.49×10^{-3}	95.24	0.14
13	7	1	512.1 ± 26.9	1.78 ± 0.11	-2.61±0.30	1.55×10^{-3}	99.49	0.05
		10	735.8 ± 86.7	1.88 ± 0.08	-1.66 ± 0.16	5.52×10^{-3}	57.83	0.17
		10 (SRHA)	219.5 ±17.9	1.68 ± 0.03	-3.01±0.25	1.44×10^{-3}	92.00	0.04
	10	1	145.5 ± 25.7	1.38± 0.05	-2.85 ± 0.14	2.46×10^{-3}	91.56	0.08
		10	455.1 ± 62.1	1.69 ± 0.14	-2.22 ± 0.28	2.38×10^{-3}	93	0.07
23	7	1	442.3 ± 29.1	1.61 ± 0.04	-2.66±0.26	2.97×10^{-3}	84.29	0.08
		10	717.1 ± 48.9	1.80 ± 0.06	-1.55 ± 0.19	5.67×10^{-3}	64.70	0.15
		10 (SRHA)	208.5 ±7.4	1.31 ± 0.08	-3.41±0.19	2.94×10^{-3}	78.47	0.08
	10	1	181.2 ± 6.0	1.05 ± 0.08	-3.35 ± 0.43	7.53×10^{-3}	66.29	0.20
		10	428.4 ± 30.0	1.88 ± 0.00	-2.04 ± 0.23	6.21×10^{-3}	74.96	0.17

At pH 10 and 10 mM KCl, both aggregates formed with 6 nm and 13 nm TNPs resulted substantial transport through the packed-bed column with more than 90% of TNPs eluted (Figure 6.8D). However, notably lower elution (~75%) was observed for 23 nm-TNP aggregates. Deposition rate of 23 nm sized TNP aggregate is ~2 times higher than 13 nm-TNP aggregate followed by 6 nm-sized aggregate, a similar trend observed in other two conditions (pH 7 and pH 10 in 1 mM KCl). Though both aggregate size and EPMs are similar for all distinctly sized TNPs, substantial changes in transport properties among TNP aggregates reveals a vital role of primary particle size within aggregate.

Overall, the transport results of TNP aggregates indicate that the larger the primary particle size within TNP aggregates are, the higher the deposition of TNP aggregates are in the porous media. It is to be noted that aggregate size was within the range of 200-500 nm under the conditions mentioned above. To verify whether this transport trend will be applicable for larger aggregate size, we conducted transport experiments in higher IS (10 mM KCl) at pH 7 (Table 6.1). At pH 7 and 10 mM KCl, TNP aggregate size increased to ~800 nm due to an increase in charge screening effect at higher IS (32). Elution of TNPs showed a marked drop with increased IS and aggregate size (Figure 6.8C). Overall, the elution trend follows: 23 nm (65%) > 13 nm (58%) > 6 nm (34%). Despite the similarity in aggregate size (~720 nm) and EPM among TNP aggregates, the deposition rate of aggregates with 6 nm particles was significantly higher than 13 nm and 23 nm (Figure 6.8C). The transport trend under this condition is opposite to what observed for other three conditions. The main difference between pH 7, 10 mM KCl and other three conditions is the aggregate formation, which led to significant larger

aggregate size (~800 nm) in 10 mM KCl, pH 7 relative to other three conditions (200-400 nm).

6.3.2.2 Transport in the Presence of SRHA

We conducted transport study at pH 7, 10 mM KCl in the presence of SRHA, as aggregate size reduced to ~200 nm, similar to aggregate size for other three conditions. Influence of SRHA in the transport of distinctly sized TNPs was investigated at pH 7 in 10 mM KCl, as higher aggregation was observed under this solution chemistry without SRHA (Figure 6.8C). Both aggregate and EPMs are similar for all forms of TNPs in the presence of SRHA. In the presence of SRHA, elution of TNPs through the column increased significantly forms of TNPs. The trend in the transport of TNP follows: 13 nm (92%) > 6 nm (85%) > 23 nm (79%). Increase of elution due to addition of SRHA for: 6 nm: 51% (34% to 85%); 13 nm: 34% (58% to 92%); 23 nm: 14% (65% to 79%), which indicates that interactions of SRHA with TNPs depend on the primary particle size. It is impossible to say whether the 6nm TNPs adsorbed a greater fraction of the SRHA compared with either of the two larger TNPs, but the larger surface area for the 6nm particles is suggestive that this might be the case.

It is to be noted that deposition trend at pH 7 and 10 mM KCl in the presence of SRHA is opposite to the trend observed in the absence of SRHA. However, the transport trend in SRHA is quite similar to observed in other three conditions (pH 7, 1 mM KCl; pH 10, 1 mM KCl; pH 10, 10 mM KCl). The important difference between the

condition at pH 7, 10 mM KCl and other four conditions is aggregate size. Aggregate size has significant influence on trransport but it is the primary particle size that appear to affect the aggregate size for similar particles. For small aggregates (200-500 nm), the larger the primary particle size within the aggregate, the higher the retention of TNP aggregate through the packed-bed column. However, when aggregates becomes larger (>800 nm), increased primary particle size within the aggregate resulted lower retention in the porous media. We explain this as follows: For small aggregates clean bed filtration occurs in the column, whereas larger aggregates can block the pore throat, causing straining (37). As a result, aggregates can break up through the packed-bed column due to straining and pore-blocking. Straining depends on the ratio of particle size to collector diameter which can occur as low as ratio > 0.002 (38). Hence, for a collector of 275 μm, the threshold particle size for straining is 550 nm. In this study, TNP aggregates were under 550 nm under all conditions except pH 7 and 10 mM KCl, where aggregate size exceeded 700 nm. Hence, straining of TNP aggregates could occur at pH 7 in 10 mM KCl, where aggregate breakup may play a role.

6.3.2.3 Aggregate Breakup in Transport

TNP aggregate size in the influent and effluent suspensions was measured during column transport experiment at pH 7 and 10 mM KCl to determine whether aggregate breakup occurred (Figure 6.9). Results indicate that influent aggregate size of all TNPs was around 800 nm, which is above the limit of straining threshold (550 nm) in the packed-bed column used in this study. Multimodal DLS size distribution has been

developed for these aggregates to determine whether there is substantial polydispersity in the aggregate size using the method described elsewhere (34, 39). Volume-based size distribution in the influent and effluent suspension during column experiment indicates that almost all aggregates (>90%) were around the size range of 1200 nm in the influent TNP suspension. However, the effluent aggregate size was within the range of 200 nm and 400 nm, which confirms that TNP aggregates are breaking up in the column during the transport process at pH 7 and 10 mM KCl. We do note that effluent aggregate size shows an important dependence on primary particle size. The size of breakup aggregate decreases with increased primary particle size, even though influent aggregate size is quite similar for all TNP types, which indicates that aggregates formed with larger primary particle size have more propensity to breakup in the column.

Overall deposition of distinctly sized TNP aggregates was significantly different, even though EPM and hydrodynamic diameter of TNP aggregates were quite similar under the conditions investigated in this study, which indicates that primary particles within aggregate are playing significant role in deposition. Notably, the influence of primary particle size within TNP aggregates on the transport through porous media shows a significant dependence of aggregate size. This may be related to difference in aggregate morphology and interaction energy between TNP aggregates and quartz sand.

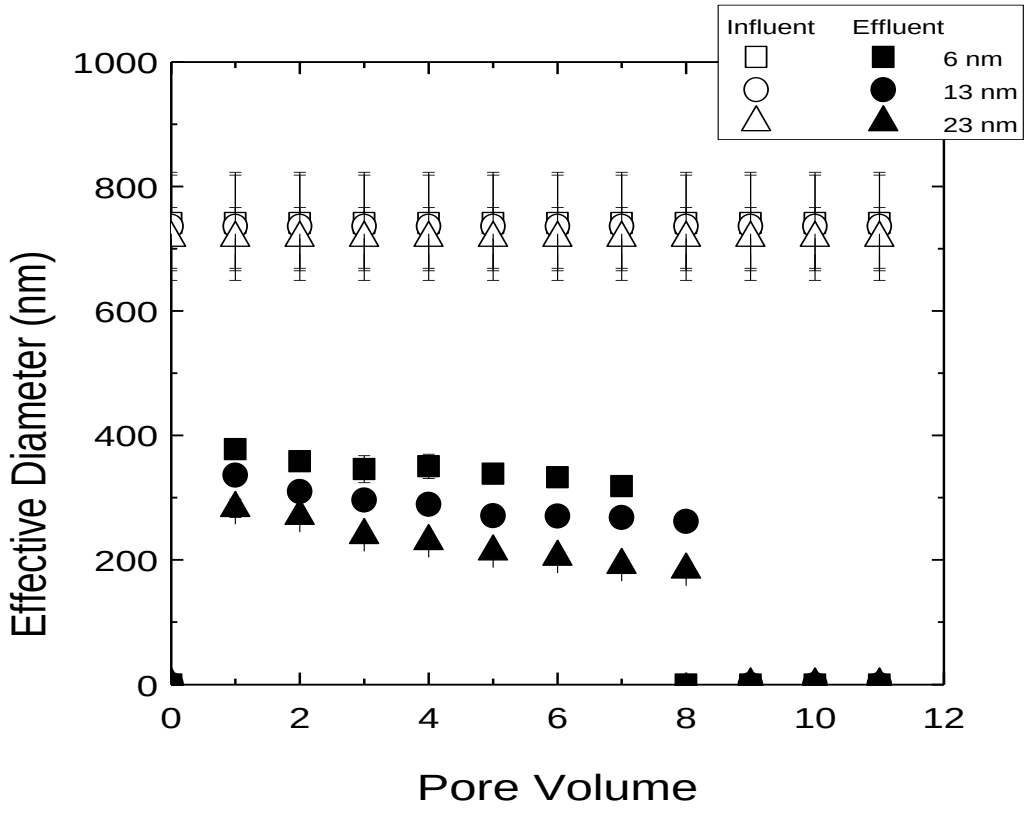

Figure 6.9. Hydrodynamic diameter of nanoparticle aggregates in the influent and effluent TNP suspension during packed-bed column experiments for 6, 13 and 23 nm primary particles at pH 7 and 10 mM KCl.

6.3.3 Possible Mechanisms in Role of Heterogeneity of Aggregate on Transport

6.3.3.1 Interpretation with DLVO Theory

Interaction profiles between TNPs and quartz grain were generated utilizing classical Derjaguin-Landau-Verwey-Overbeek (DLVO) theory (Figure 6.10). Detailed discussion on DLVO results has been mentioned in the Supporting Information. Overall DLVO analysis show that the energy barrier between TNP aggregates and quartz sand is considerably large (> 200 kT) under all conditions with negligible secondary minima (< 2

kT), indicating deposition of TNP aggregates in the column occurred under repulsive conditions. Though deposition of 6 nm and 13 nm TNP aggregates can be qualitatively explained by DLVO theory, deposition of 23 nm-TNP aggregate cannot be explained by DLVO alone. Moreover, deposition of all sized TNP aggregates did not follow DLVO prediction in the presence of SRHA. Hence, additional mechanisms may be related to the morphology of TNP aggregates, which can be considerably affected by primary particle size within TNP aggregate.

6.3.3.2 Role of Roughness of Aggregate due to Primary Particle Size

Previous studies revealed that surface roughness of particles and collectors surfaces can considerably affect the deposition of particles on collectors (40, 41). Aggregate morphology, particularly difference in primary particle size within aggregate can contribute additional roughness to the aggregate surface. Aggregates composed of larger primary particle can result higher surface roughness than those consisted of smaller primary particle size. Elimelech and O'Melia (42) investigated the role of roughness of particle and collector surface on deposition and found that roughness decreased the interaction energy as well as height of energy barrier, indicating that higher surface roughness will increase the deposition of particles on surfaces. However, after certain height of roughness, energy barrier can increase with roughness due to larger repulsion caused by particle-protrusion interaction. Huang et al. (43) conducted a theoretical investigation on interactions energy due to surface roughness and found that surface

roughness is as important as the surface potential of particles for calculating interactions with surfaces.

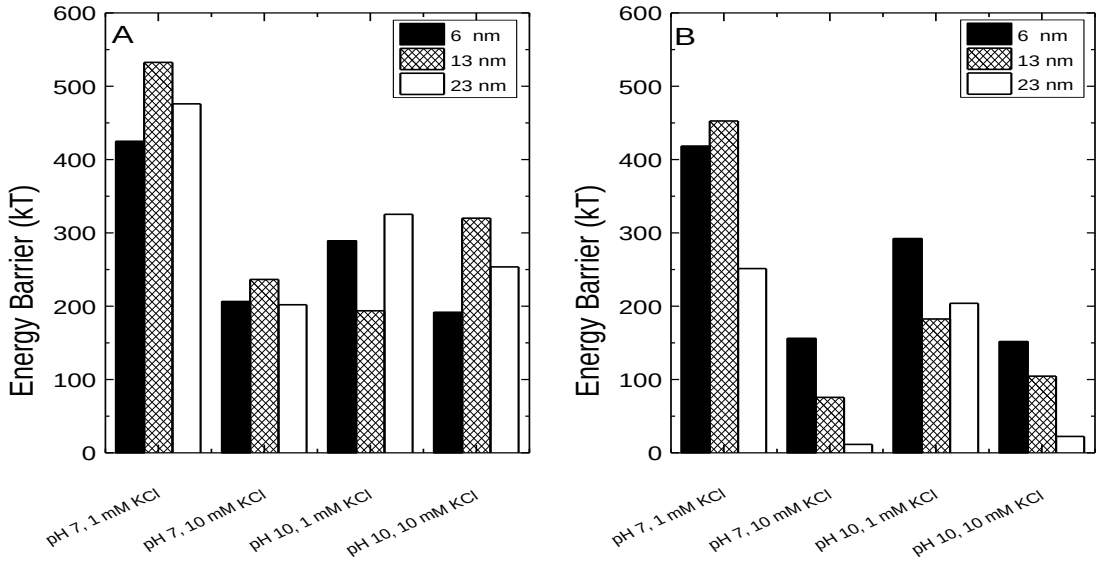

Figure 6.10. DLVO energy barrier between TNP and quartz sand based on A) without roughness, B) with roughness.

Influence of surface roughness on the interaction energy can be calculated using a simple approach as developed by Elimelech and O'Melia (42). In brief, the total interaction energy between rough aggregate and smooth quartz surface can be visualized as the combination of two interactions, notably 1) half-sphere protrusion-smooth surface interaction ($\boldsymbol{\phi}_i$), and 2) smooth aggregate-surface interaction ($\boldsymbol{\phi}_{ii}$). Using this approach, total interaction energy can be calculated with the following equation:

$$\emptyset_T(h) = \emptyset_i(h) + \emptyset_{ii}(h + a) \qquad (6.5)$$

Where h is separation distance and a is half-sphere protrusion, which is assumed as the radius of primary particles. Results have been summarized in Figure 6.10. Even though DLVO interaction energy without considering surface roughness of aggregate is quite similar and highly repulsive for all particle types, addition of surface roughness reduces the energy barrier significantly. When considering roughness of aggregate, the decrease in energy barrier showed a notable dependence on primary particle size. For 6 nm particles, interaction energy with and without roughness is quite similar, indicating that aggregates formed with smaller nanoparticles are behaving like a similar sized colloid. However, energy barrier reduces significantly with aggregates comprised of larger primary particle sizes, particularly 23 nm. This suggests, aggregates composed of 23 nm TNPs will have more attractive interaction energy with quartz surface than those consisted of 13 nm and 6 nm due to higher surface roughness. This change in interaction energy due to surface roughness can lead to higher deposition for 23 nm aggregate followed by 13 nm and 6 nm under clean bed condition, which was also observed in transport study (Figure 6.8).

6.3.3.3 Role of Aggregate Morphology

Study of aggregate morphology reveals that fractal dimension of aggregates was significantly affected by primary particle size. To confirm whether this change in aggregate morphology due to primary particles size has any role in transport, an effort was made to correlate the fractal dimension and transport of TNP aggregates. Overall deposition rates of TNP aggregates showed an increasing trend with fractal dimension.

For aggregates consisted of 6 nm primary particles deposition rates remained independent of fractal dimension. There is a clear increasing trend observed for 23 nm-aggregate with D_f. For 13 nm-aggregate, deposition rates decreased with fractal dimension. However there are notable differences observed among distinctly sized TNP aggregates. Finding from this study indicates that aggregate morphology became more dominant in the transport for TNP aggregates consisted of larger primary particle size. Overall aggregate morphology considerably affected the transport of TNPs through porous media. The influence of fractal dimension on the transport of TNPs showed a significant dependence on primary particle size. Aggregates comprised of larger primary particle size were more impacted by aggregate morphology. This may be due to change in aggregate properties including density, strength, hydrodynamic interaction and surface roughness contributed by altering aggregate morphology.

6.3.3.4 Role of Aggregate Density

Density of colloids is one of the most important parameters controlling the deposition process (44). Recent studies revealed that deposition of bacteria (27) and nanoparticles (45) can be significantly increased with density due to higher gravitational force. Previous studies showed that aggregate morphology has significant influence on the density of aggregate (31, 32). For a constant D_f, density of aggregates reduces with increasing aggregate size. Effective density of an aggregate in a liquid (ρ_E) can be correlated with fractal dimension of aggregate as follows:

$$\rho_E = Bd^{D_f - 3} \tag{6.6}$$

where d is aggregate diameter; B is an experimental constant. Hence for a certain aggregate size, ratio between aggregates with two fractal dimension (D_{f1} and D_{f2}) is:

$$\frac{\rho_{E1}}{\rho_{E2}} = d^{D_{f1}-dD_{f2}} \tag{6.7}$$

Hence aggregate density is significantly higher for large fractal dimension for similarly sized aggregates. In this study fractal dimension of aggregates consisted of 6 nm primary particles is always higher than those consisted of 13 nm followed by 23 nm, though aggregate size remains similar for all 3 sized particles. Hence aggregates composed of 6 nm particles have higher density than 13 nm and 23 nm. Deposition of 6 nm-sized aggregates should be higher than 13 nm followed by 23 nm if gravitational forces dominate. However, transport results show that deposition rates of 23 nm TNPs were significantly higher than those of 6 nm and 13 nm TNPs for small aggregates (200-400 nm), whereas larger aggregates (>800 nm) led to higher deposition for 6 nm than 13 nm and 23 nm in the packed-bed column. Chowdhury and Walker(20) recently showed that gravitational force due to density of metal oxide nanoparticle aggregate (TiO_2 and CeO_2) can dominate over DLVO forces in the deposition for large aggregates, whereas DLVO forces are more important for small aggregates. Hence, in this study, gravitational forces increases the deposition of 6 nm particles for large aggregates (>800 nm), which increases the retention of 6 nm-aggregate in the column. DLVO forces are dominant for small aggregates., which transport trend follows the DLVO interaction forces.

6.3.3.5 Role of Aggregate Strength

The strength of aggregate can have significant effect in the fate and transport of colloids in the aquatic environment (31). The force required to break an aggregate is usually function of particle-particle bonds and the strength of these bonds. Aggregate strength can be defined as:

$$\sigma = \frac{4 f_0}{\pi d^2} \quad (6.8)$$

Where f_0 = force; d = diameter of aggregates; σ = aggregate strength. Number of particle-particle bonds per unit area is directly correlated with aggregate density, which is also function of D_f. Generally strength of aggregates increases with higher fractal dimension for similar sized aggregates (32, 46). Aggregates with low D_f should be less strong due to few bonds per unit area, whereas high D_f can increase the bonds per unit area, forming strong aggregates (32).

Aggregate morphology reveals that TNP aggregates composed of 6 nm primary particles have higher D_f than those with 13 nm and 23 nm. However, the strength of aggregates will be a factor in transport through porous media, when there is a possibility of aggregate breakup. Aggregate breakup study at pH 7 in 10 mM KCl reveals that influent aggregate size became 200-400 nm from 800 nm, which indicates that aggregate is breaking up during the transport. The effluent aggregate size decreases with increased primary particle size within nanoparticle aggregate, which implies that primary particle size within TNP aggregate is playing substantial role in aggregate breakup process. D_f of TNP aggregates at pH 7 in 10 mM KCl follows the trend : 6 nm (2.08) > 13 nm (1.88) >

23 nm (1.80). Hence, aggregates formed with 23 nm primary particles are weaker than those with 6 nm and 13 nm aggregates, which in turn reduces the size of breakup aggregate more significantly for 23 nm particles than 6 nm and 13 nm.

6.3.3.6 Role of Hydrodynamic Interactions

Hydrodynamic interactions due to slow drainage of water from the gap between interacting surfaces can be a function of diameter of particle size and separation distance (40). Due to porous nature of fractal aggregate, water and ions can diffuse through the aggregate, which can alter the hydrodynamic interactions of aggregates with surfaces (32). Previous study (47) showed that deposition of Brownian particles are not significantly affected by hydrodynamic interactions. However, in this study nanoparticles formed large aggregates with varying fractal nature. Adler (48) showed that fractal dimension has insignificant role in drag force of aggregates, which is close to similar sized colloids. Later Adrover and Giona (49) found that drag force is not function of D_f for small aggregates, whereas large aggregates (500-13000x of primary particles) can affect the drag force. In this study the aggregates are still in the Brownian range, it is therefore concluded that hydrodynamic interactions are not playing significant role in the transport.

6.4 Conclusions

This study reveals that transport of TNP aggregates through porous media is significantly influenced by the primary particle size within the aggregate. One notable

finding from this study is that the mechanism, how primary particle size within the aggregate can influence the transport through porous media, is also function of aggregate size. For small aggregates under clean bed condition, aggregates formed with smaller primary particles can transport longer in the environment. However, as aggregate size increased, the aggregates with larger primary particles were observed to travel further due to aggregate breakup, which is attributed to straining. Aggregate breakup is more significant for larger primary particles, which indicates that aggregates with larger primary particles will likely be transported greater distances in the subsurface when experienced pore blocking. The size of the primary particles was also demonstrated to play a vital role on the morphology of aggregate formation, which showed a linear dependence on the surface areas of primary particles. Under all conditions investigated in this study, aggregates composed of small primary particles showed highest fractal dimension among all particles, which indicate that small primary nanoparticles can form more compact aggregate than large primary particles in the aquatic environment. This understanding on the role of primary particles within nanoparticle aggregates will help to better predict the long term fate of nanoparticles in the aquatic environment.

6.5 References

(1) Dunphy Guzman, K. A.; Taylor, M. R.; Banfield, J. F., Environmental Risks of Nanotechnology: National Nanotechnology Initiative Funding, 2000-2004. *Environmental Science & Technology* **2006,** *40*, (5), 1401-1407.

(2) Wiesner, M. R.; Lowry, G. V.; Alvarez, P.; Dionysiou, D.; Biswas, P., Assessing the Risks of Manufactured Nanomaterials. *Environmental Science & Technology* **2006,** *40*, (14), 4336-4345.

(3) Chen, K. L.; Elimelech, M., Relating Colloidal Stability of Fullerene (C60) Nanoparticles to Nanoparticle Charge and Electrokinetic Properties. *Environmental Science & Technology* **2009,** *43*, (19), 7270.

(4) Mark R, W., Kinetics of aggregate formation in rapid mix. *Water Research* **1992,** *26*, (3), 379-387.

(5) Riefler, N.; Mädler, L., Structure–conductivity relations of simulated highly porous nanoparticle aggregate films. *Journal of Nanoparticle Research* **2010,** *12*, (3), 853-863.

(6) Seekkuarachchi, I. N.; Kumazawa, H., Aggregation and Disruption Mechanisms of Nanoparticulate Aggregates. 1. Kinetics of Simultaneous Aggregation and Disruption. *Industrial & Engineering Chemistry Research* **2008,** *47*, (7), 2391-2400.

(7) He, Y.; Wan, J.; Tokunaga, T., Kinetic stability of hematite nanoparticles: the effect of particle sizes. *Journal of Nanoparticle Research* **2008,** *10*, (2), 321-332.

(8) Suttiponparnit, K.; Jiang, J.; Sahu, M.; Suvachittanont, S.; Charinpanitkul, T.; Biswas, P., Role of Surface Area, Primary Particle Size, and Crystal Phase on Titanium Dioxide Nanoparticle Dispersion Properties. *Nanoscale Res Lett* **2011,** *6*, (1), 27.

(9) Zhang, W.; Yao, Y.; Sullivan, N.; Chen, Y., Modeling the Primary Size Effects of Citrate-Coated Silver Nanoparticles on Their Ion Release Kinetics. *Environmental Science & Technology* **2011,** *45*, (10), 4422-4428.

(10) Zhang, W.; Rittmann, B.; Chen, Y., Size Effects on Adsorption of Hematite Nanoparticles on E. coli cells. *Environmental Science & Technology* **2011,** *45*, (6), 2172-2178.

(11) Dehner, C. A.; Barton, L.; Maurice, P. A.; DuBois, J. L., Size-Dependent Bioavailability of Hematite (α-Fe2O3) Nanoparticles to a Common Aerobic Bacterium. *Environmental Science & Technology* **2010,** *45*, (3), 977-983.

(12) Baalousha, M.; Manciulea, A.; Cumberland, S.; Kendall, K.; Lead, J. R., Aggregation and surface properties of iron oxide nanoparticles: Influence of pH and natural organic matter. *Environmental Toxicology and Chemistry* **2008,** *27*, (9), 1875-1882.

(13) Mylon, S. E.; Chen, K. L.; Elimelech, M., Influence of Natural Organic Matter and Ionic Composition on the Kinetics and Structure of Hematite Colloid Aggregation: Implications to Iron Depletion in Estuaries. *Langmuir* **2004,** *20*, (21), 9000-9006.

(14) Li, M.; Pokhrel, S.; Jin, X.; Mädler, L.; Damoiseaux, R.; Hoek, E. M. V., Stability, Bioavailability, and Bacterial Toxicity of ZnO and Iron-Doped ZnO

Nanoparticles in Aquatic Media. *Environmental Science & Technology* **2010,** *45*, (2), 755-761.

(15) Chowdhury, I.; Hong, Y.; Honda, R. J.; Walker, S. L., Mechanisms of TiO_2 nanoparticle transport in porous media: Role of solution chemistry, nanoparticle concentration, and flowrate. *Journal of Colloid and Interface Science* **2011,** *360*, (2), 548-555.

(16) Robichaud, C. O.; Uyar, A. E.; Darby, M. R.; Zucker, L. G.; Wiesner, M. R., Estimates of Upper Bounds and Trends in Nano-TiO2 Production As a Basis for Exposure Assessment. *Environmental Science & Technology* **2009,** *43*, (12), 4227-4233.

(17) Teoh, W. Y.; Amal, R.; Madler, L., Flame spray pyrolysis: An enabling technology for nanoparticles design and fabrication. *Nanoscale* **2010,** *2*, (8), 1324-1347.

(18) Birkenstock, J. F., R. X.; Messner, T. BRASS, The Bremen Rietveld Analysis and Structure Suit. . http://www.brass.uni-bremen.de/

(19) Hill, R. J.; Fischer, R. X., Profile agreement indices in Rietveld and pattern-fitting analysis. *Journal of Applied Crystallography* **1990,** *23*, (6), 462-468.

(20) Chowdhury, I.; Walker, S. L., Deposition mechanisms of TiO2 nanoparticles in a parallel plate system. *Journal of Colloid and Interface Science* **2012,** *369*, (1), 16-22.

(21) Kim, H. N.; Bradford, S. A.; Walker, S. L., *Escherichia coli* O157:H7 Transport in Saturated Porous Media: Role of Solution Chemistry and Surface Macromolecules. *Environmental Science & Technology* **2009,** *43*, (12), 4340.

(22) Haznedaroglu, B. Z.; Kim, H. N.; Bradford, S. A.; Walker, S. L., Relative Transport Behavior of *Escherichia coli* O157:H7 and Salmonella enterica Serovar Pullorum in Packed Bed Column Systems: Influence of Solution Chemistry and Cell Concentration. *Environmental Science & Technology* **2009,** *43*, (6), 1838.

(23) Bradford, S. A.; Kim, H. N.; Haznedaroglu, B. Z.; Torkzaban, S.; Walker, S. L., Coupled Factors Influencing Concentration-Dependent Colloid Transport and Retention in Saturated Porous Media. *Environmental Science & Technology* **2009,** *43*, (18), 6996.

(24) Walker, S. L.; Hill, J. E.; Redman, J. A.; Elimelech, M., Influence of Growth Phase on Adhesion Kinetics of *Escherichia coli* D21g. *Appl. Environ. Microbiol.* **2005,** *71*, (6), 3093-3099.

(25) Hong, Y.; Honda, R. J.; Myung, N. V.; Walker, S. L., Transport of Iron-Based Nanoparticles: Role of Magnetic Properties. *Environmental Science & Technology* **2009,** *43*, (23), 8834.

(26) American Public Health, A.; American Water Works, A.; Water Pollution Control, F., Standard methods for the examination of water and wastewater. *Standard methods for the examination of water and wastewater*. **1905**.

(27) Chen, G.; Hong, Y.; Walker, S. L., Colloidal and Bacterial Deposition: Role of Gravity. *Langmuir* **2009**. *26*, (1), 314-319.

(28) Crittenden, J. C.; Montgomery Watson, H., *Water treatment principles and design*. J. Wiley: Hoboken, N.J., 2005.

(29) Kretzschmar, R.; Borkovec, M.; Grolimund, D.; Elimelech, M., Mobile subsurface colloids and their role in contaminant transport. In *Advances in Agronomy, Vol 66*, 1999; Vol. 66, pp 121-193.

(30) Walker, S. L.; Redman, J. A.; Elimelech, M., Role of Cell Surface Lipopolysaccharides in *Escherichia coli* K12 Adhesion and Transport. *Langmuir* **2004,** *20*, (18), 7736-7746.

(31) Elimelech, M., Gregory, J., Jia, X., Williams, R.A., *Particle Deposition and Aggregation: Measurement, Modeling and Simulation*. Butterworth-Heinemann: 1995; p 441.

(32) Gregory, J., *Particles in water : properties and processes*. IWA Pub. ; Taylor & Francis: London; Boca Raton, FL, 2006.

(33) Thio, B. J. R.; Zhou, D.; Keller, A. A., Influence of natural organic matter on the aggregation and deposition of titanium dioxide nanoparticles. *Journal of Hazardous Materials* **2011,** *189*, (1-2), 556-563.

(34) Chowdhury, I.; Cwiertny, D. M.; Walker, S. L., Combined Factors Influencing the Aggregation and Deposition of nano-TiO_2 in Presence of Humic Acids and Bacteria. *Environmental Science & Technology* **2012** ASAP.

(35) Mueller, R.; Kammler, H. K.; Pratsinis, S. E.; Vital, A.; Beaucage, G.; Burtscher, P., Non-agglomerated dry silica nanoparticles. *Powder Technology* **2004,** *140*, (1–2), 40-48.

(36) Chowdhury, I.; Cwiertny, D. M.; Walker, S. L., Combined Factors Influencing the Aggregation and Deposition of nano-TiO_2 in the Presence of Humic Acid and Bacteria. *Environmental Science & Technology* **2012**.

(37) Bradford, S. A.; Simunek, J.; Bettahar, M.; van Genuchten, M. T.; Yates, S. R., Modeling Colloid Attachment, Straining, and Exclusion in Saturated Porous Media. *Environmental Science & Technology* **2003,** *37*, (10), 2242-2250.

(38) Bradford, S. A.; Simunek, J.; Bettahar, M.; Tadassa, Y. F.; van Genuchten, M. T.; Yates, S. R., Straining of colloids at textural interfaces. *Water Resour. Res.* **2005,** *41*.

(39) Phenrat, T.; Kim, H.-J.; Fagerlund, F.; Illangasekare, T.; Tilton, R. D.; Lowry, G. V., Particle Size Distribution, Concentration, and Magnetic Attraction Affect Transport of Polymer-Modified Fe0 Nanoparticles in Sand Columns. *Environmental Science & Technology* **2009,** *43*, (13), 5079.

(40) Elimelech, M.; O'Melia, C. R., Kinetics of deposition of colloidal particles in porous media. *Environmental Science & Technology* **1990,** *24*, (10), 1528-1536.

(41) Chen, G.; Beving, D. E.; Bedi, R. S.; Yan, Y. S.; Walker, S. L., Initial Bacterial Deposition on Bare and Zeolite-Coated Aluminum Alloy and Stainless Steel. *Langmuir* **2009,** *25*, (3), 1620.

(42) Elimelech, M.; O'Melia, C. R., Effect of particle size on collision efficiency in the deposition of Brownian particles with electrostatic energy barriers. *Langmuir* **1990,** *6*, (6), 1153-1163.

(43) Huang, X.; Bhattacharjee, S.; Hoek, E. M. V., Is Surface Roughness a "Scapegoat" or a Primary Factor When Defining Particle−Substrate Interactions? *Langmuir* **2009,** *26*, (4), 2528-2537.

(44) Hunter, R. J., *Foundation of Colloid Science*. Oxford University Press: Oxford, 2001; Vol. 2.

(45) Chowdhury, I.; Walker, S. L., Deposition mechanisms of TiO_2 nanoparticles in a parallel plate system. *Journal of Colloid and Interface Science*, **2012,** *369*, (1), 16-22.

(46) Ehrl, L.; Soos, M.; Morbidelli, M., Dependence of Aggregate Strength, Structure, and Light Scattering Properties on Primary Particle Size under Turbulent Conditions in Stirred Tank. *Langmuir* **2008,** *24*, (7), 3070-3081.

(47) Prieve, D. C.; Ruckenstein, E., Effect of London forces upon the rate of deposition of Brownian particles. *Aiche Journal* **1974,** *20*, (6), 1178-1187.

(48) Adler, P. M., Hydrodynamic properties of fractal flocs. *Faraday Discussions of the Chemical Society* **1987,** *83*, 145-152.

(49) Adrover, A.; Giona, M., Hydrodynamic properties of fractals: Application of the lattice Boltzmann equation to transverse flow past an array of fractal objects. *International Journal of Multiphase Flow* **1997,** *23*, (1), 25-35.

Chapter 7

Impact of Synthesis and Purification Methods on the Transport of Single Walled Carbon Nanotubes in the Aquatic Environments

Chowdhury, I., Duch, M. C., Gits, C. C., Hersam, M. C. and Walker, S. L. (2012) Synthesis Methods and Residual Catalysts Affecting the Transport of Single Walled Carbon Nanotubes in the Aquatic Environment, *Environmental Science and Technology*.

Abstract

In this study, a systematic approach has been followed to investigate the fate and transport of single walled carbon nanotubes (SWNTs) from synthesis to environmentally relevant conditions. Three widely used SWNT synthesis methods have been investigated in this study including high pressure carbon monoxide (HiPco), chemical vapor deposition (CVD) and electric arc discharge technique (EA). To eliminate the heterogeneity in nanotube length and diameter, a dispersion procedure was utilized using biocompatible triblock copolymer Pluronic, which allowed the comparison in the transport trends among these SWNTs. After purification, the residual metal catalyst between the SWNTs follows the trend: HiPco-D > SG65-D > P2-D. The electrophoretic mobility and hydrodynamic diameter of SWNTs remained insensitive to SWNT type, pH, and presence of natural organic matter (NOM); but were affected by ionic strength and ion valence (K^+, Ca^{2+}). Transport of HiPco-D in the porous media was significantly higher than SG65-D followed by P2-D. Release of HiPco-D from porous media was higher than SG65-D followed byP2-D, though negligible amount of all types of SWNTs (<5%) was released. Both transport and release pattern follow a similar trend to what was observed for residual metal catalysts in SWNTs. HiPco-D is notably more acidic than SG65-D followed by P2-D, which is similar to transport trend. Overall, it was observed that the synthesis methods resulted in distinctive breakthrough trends, which were correlated to metal content.

7.1 Introduction

Unique mechanical, electrical, optical and thermal properties of carbon-based nanomaterials have led the widespread usage of these novel nanomaterials in the industry and consumer products (1). These carbonaceous materials can be manufactured in a variety of shapes including spheres (ie C60 bucky balls) and tubes (ie. single and double walled carbon nanotubes) (2). Carbon nanotubes (CNTs) are allotropes of carbon in hexagonal carbon formed in helical form (3, 4). Both single walled (SWNT) and multi walled carbon nanotubes (MWNT) can be synthesized with nanometer scale diameters, but usually with lengths on the micron scale(1). The unique electrochemical properties of CNTs have led to the increased usage of these novel nanomaterials in the nanocomposites, biosensors, energy devices, nanomedicine and even in the environmental applications (3).

With a projected mass production rate of 55- 1101 t/year in US alone (4, 5), the eventual release of CNTs to aquatic environments is a realistic possibility. Fate and transport of CNTs have not yet been studied well enough to support predictive ability in the actual environmental media. Jaisi et al. (6) found that both physicochemical filtration and straining played significant roles in the transport of SWNTs through porous media, affected by the shape of the SWNTs. The Jaisi study worked with natural soils and showed limited transport of CNTs due to physical straining (7). Another study by Liu et al. (8) observed a significant dependence of MWNTs transport through porous media on pore water velocity. A recent study showed that sodium dodecylsulfate surfactant can

significantly increase the stability and mobility of SWNTs through porous media (9). Smith et al. (10) found that colloidal dispersion of CNTs is significantly dependent on the oxygen-containing functional groups on CNTs. Saleh et al.(11) investigated the aggregation kinetics of MWNTs by using time-resolved dynamic light scattering (DLS) and found that natural aquatic environment can increase the stability and mobility of MWNTs. His study on aggregation kinetics of SWNTs(4) indicated that biomacromolecules and humic acids increased the stability of SWNTs through steric repulsion. Recently, Yi and Chen(12) found that surface oxidation can affect the deposition of MWNTs significantly, largely depending on ion valence.

Most commonly used synthesis methods for SWNTs are high pressure carbon monoxide (HiPco), chemical vapor deposition (CVD) and electric arc discharge (EA) (13, 14). Healy et al.(14) found that HiPco process has the lowest environmental impact under base case yield conditions, whereas for best case yield condition, EA can generate lowest impact. Plata et al.(15) showed the potential environmental risk from synthesis of nanotubes using CVD methods including potential release of greenhouse gas, methane and toxic compounds. Ecotoxicity during CNT production process can be comparable to ecotoxicity from CNT release, which is primarily dominated by toxic metal release (13).

During the synthesis process of SWNTs different metals are commonly used as catalysts(Fe, Co, Mo, Y, Ni), and residuals of these materials can remain in synthesized SWNTs. One study reported that residual metal catalysts can remain in the SWNTs even after washing with nitric acid at an elevated temperature, as these metals can be inside the

channel of nanotubes or protected by graphene sheets (16). Removal of residual metal catalysts on the surface of SWNTs showed a reduced trend in the electrochemical activity of SWNTs (16). However, the amount of residual metal on the SWNTs also varies significantly between different synthesis and purification methods(17). Plata et al.(18) found a significant amount of impurities in the industrially synthesized SWNTs including metals and polycyclic hydrocarbons, which are primarily dominated by residual metal catalysts. These residual metal catalysts can degrade aromatic hydrocarbons through generating radical species (18). Redox properties of SWNTs showed an increasing trend with residual metal catalysts, which needs to be considered in determining the subsequent toxicity of SWNTs (19). For example, pulmonary toxicity tests of SWNTs in mice showed an increasingly harmful trend with residual metal catalysts, as well as variations in the synthesis methods has also significant effect (20).

Previously, research on the transport mechanism of SWNTs primarily considered solution chemistry and presence of organic matter. However, one important aspect of SWNTs was not considered so far for the transport study is physicochemical properties of SWNTs, which is usually governed by synthesis and purification methods. Recent study revealed that cytotoxicity of bacteria is considerably affected by the electronic structure of SWNTs, showing increased bacterial inactivation with higher metal content (21). This type of transport study was not possible in the past due to lack of SWNT purification method to separate SWNTs based on the electronic structure until recently developed ultracentrifugation-based SWNT purification method, which can segregate SWNTs based on band gap, diameter and electronic structure (22). Previous

studies reported that chemical reactivity of SWNTs is a function of electronic structure with metallic SWNTs showing more reactivity(23). The higher reactivity and toxicity of SWNTs are attributed to the faster electron transport.

It is critical to understand how synthesis methods and residual metal catalysts will influence the transport of SWNTs in the aquatic environment, which will control the toxicity exposure of nanotubes. Though transport of carbon nanotubes has been studied(6, 8, 24), so far there has been no study to date on the influence of synthesis methods and purifications in the transport of SWNTs. This comparison among different SWNTs was not possible in the past due to inherent heterogeneity among SWNTs particularly from nanotube diameter and length. In this study, we utilized a novel approach to disperse and sort SWNTs in triblock copolymer, which eliminates the difference in nanotube diameter and length, and allows us to compare differently synthesized SWNTs. In this study, the role of synthesis methods and purifications on the transport of SWNTs was investigated through a well characterized transport system (packed-bed column) coupled with extensive physicochemical characterization. Three types of SWNTs (HiPco-D, SG65-D and P2-D) synthesized by HiPco, CVD and EA methods respectively were used in this study.

7.2 Materials and Methods

7.2.1 Preparation of Dispersed SWNTs

Three SWNTs synthesized by different metal catalysts was used in this study. Purified HiPco, SG65 and P2 SWNTs were purchased from NanoIntegris (Skokie, IL),Southwest Nano Technologies (Norman, OK) and Carbon Solutions, Inc (Riverside, CA) respectively. Each dispersed grade SWNT sample was prepared in multiple batches of 70 mL aqueous solution of 2% w/v Pluronic F108NF (BASF) with 2.5 mg/mL of purified grade SWNT (175 mg). Each batch was sonicated using a Digital Sonic Dismembrator (Model 500, Fisher Scientific, Pittsburgh, PA) at 60% amplitude (~65 W) for 1 hour using a 1/2" immersed horn and cooled with an ice bath. The resulting material was then immediately centrifuged at 41 krpm in a SW41Ti rotor (~288,000 g) for 30 minutes at 22^{o}C to remove aggregates and catalyst particles. The top 80% of the supernatant was retained as final sample.

7.2.2 Physical Characterization of SWNTs

Wide range of characterization was conducted to determine the physicochemical properties of dispersed SWNTs. Details of these characterization techniques are presented in the Supporting Information. Length and diameter of SWNTs were determined from atomic force microscopy and UV-vis near infrared spectroscopy (UV-vis NIR). Transmission electron microscorpy (TEM) was utilized to further confirm

the length and diameter. Amount of residual metal catalysts was also determined using inductively coupled plasma mass spectroscopy (ICP-MS).

7.2.3 Electrokinetic and Hydrodynamic Characterization of Nanotubes

A ZetaPALS analyzer (Brookhaven Instruments Corp., Holtsville, NY) was utilized to determine electrokinetic properties and hydrodynamic diameter of SWNTs over a wide range of solution chemistry from pH 4 to 10 in both monovalent (KCl) and divalent ($CaCl_2$) ions. Dynamic light scattering (DLS) (Brookhaven model BI-9000AT Holtsville, NY) was used to determine hydrodynamic diameter at a wavelength of 661 nm and scattering angle of 90^o. All solutions were made with ACS reagent grade chemicals (Fisher Scientific, Pittsburgh, PA) and pH was controlled with HCl or KOH. NOM is a ubiquitous substance in the aquatic environment and also widely known to significantly affect the transport of colloids, microorganisms and nanomaterials(25-27). Suwannee River humic acid (SRHA) was used as model NOM in this study, as SRHA is one of the most well characterized and widely used models of naturally occuring organic matter. Statistical analysis was conducted to compare the difference among different particles using analysis of variance (ANOVA) and student t-test as mentioned in the Supporting Information.

7.2.4 Potentiometric Titration of Nanotubes

Effect of synthesis methods and residual metal catalysts on the surface charge properties of SWNTs was further investigated by potentiometric titration(28, 29).

Carbon dioxide from background solution (1 mM KCl) was purged using nitrogen gas (Puritan Medical Products, Inc., Overland Park, KS) for at least 50 min prior to experiments. 10 mL of 100 mg/L SWNTs was titrated in a sealed titration vessel. Potentiometric titrations were conducted using an automatic titrator (798 Titrino, Metrohm Ltd., Switzerland) with 0.1 N NaOH titrant over the pH range of 3.0-10.5 at room temperature (23 ± 2 ^{o}C) in the presence of nitrogen gas purging and continuous stirring. All titration experiments were conducted in triplicate. Overall surface charge densities and acidities of SWNTs under the experimental conditions were also determined from the titration study following the procedure mentioned elsewhere (30, 31). FITEQL 4.0 was utilized to determine the surface sites and concentration on SWNTs from titration data (28, 32).

7.2.5 Transport Experiments

Transport behavior of SWNTs was investigated in the column packed with quartz sand, simulating filter media, which can capture the deposition mechanisms of SWNT on the quartz surfaces following the procedure mentioned elsewhere (33, 34). Transport of SWNTs was investigated in a borosilicate glass column (Omnifit, Boonton, NJ) packed with quartz sand (Iota quartz, Unimin Corp., NC) simulating porous media. Quartz sand sieved between 50 and 60 mesh with a resulting average sand size of 275 µm, typical range of sand in filters, was used in transport experiments (35). Further details regarding preparation procedures for the sand have been mentioned elsewhere(36-38). The porosity

of packed-bed column was determined gravimetrically to be 46.5%(30). The SWNT concentration in each of stock nanoparticles suspension, and effluent was determined by UV-vis spectrophotometer at 240 nm wavelength (40). For column experiments with SRHA, the packed column was equilibrated with SRHA solution for at least 10 PV prior to injection of SWNT suspension. Column experiments were conducted 2 mL/min with a superficial approach velocity of 0.019 cm/s, simulating groundwater or slow sand filtration (35, 41). Injected SWNT concentration was 10 mg/L. Reversibility of deposited SWNTs from quartz sand was tested by introducing deionized water in which electrostatic attraction should be eliminated and cause reversibly bound SWNTs to be released following the procedure mentioned elsewhere(6, 42).

Retention profiles of SWNTs in the granular media were developed by following the procedure mentioned elsewhere(43). In brief, the packed-bed column was dissected into five pieces after the experiment. The granular media were extruded in each cm from the column by removing the bottom end piece of the column, and collecting the sand by gravity. The media remained saturated during this dissection process with the background electrolyte to avoid any change in deposition profile during the dissection process. Each cm of dissected media was collected in 50 mL centrifuge tubes and 5 mL of 1 mM NaOH was added in the tube. The dissected media was kept in NaOH solution for 1 hour and then gently shaken to release the SWNTs in the NaOH solution. SWNT concentration was measured in the supernatant suspension by using UV-vis spectrophotometer at 240 nm wavelength from the calibration curve (Supporting

Information). The mass balance of SWNTs from the column experiments was determined by integrating column breakthrough curves and deposition profile. Transport of SWNTs results have been simulated with attachment-detachment model (two kinetic sites model) using HYDRUS 1D (44).

7.2.6 Bacterial Cytotoxicity

Bacterial cytotoxicity of SWNTs was also investigated in this study using standard methods that have been reported elsewhere (21, 46). Briefly, the loss of viability (or outer membrane integrity) was determined in 1 mM KCl background solution after 60 min of incubation at 37^0 C with shaking at 200 rpm. A fluorescence based toxicity assay was used to determine the viability of bacteria using Live/dead Baclight kit (L-13152, Molecular Probes, Eugene, OR) and a fluorescent microscope (BX51, Olympus, Japan) with a red/green fluorescent filter set (Chroma Technology Corp., Brattleboro, VT). *E. coli K12* was used in this study as model bacteria. SWNT concentration was varied from 1 and 10 mg/L and cell concentration was kept constant at 5×10^7 cells/mL.

7.3 Results and Discussion

7.3.1 Physical Characterization of Dispersed SWNTs

Extensive characterization was conducted to determine the physicochemical properties of HiPco-D, SG65-D and P2-D, which are presented in Table 7.1 and Figures

7.1 and 7.2. Visible-near infrared (vis-NIR) spectra showed a characteristic adsorption peak in the S11 regions for both HiPco-D and SG65-D, while P2-D showed the peak in S22 (900-1100 nm) and M11 (600-800 nm) region. Estimated diameter of nanotubes from vis-NIR spectra is within the range of 0.7 to 2.0 nm for all SWNTs, which was further confirmed from TEM images (Supporting Information). Statistical analysis (analysis of variance and t-test) showed insignificant difference ($P >> 0.05$) in diameter for all 3 SWNTs. Distribution of nanotube length is presented in Figure 7.2. Overall, average length of nanotubes is around 400 nm for all SWNTs with a wide range from 50 nm to 1700 nm. ANOVA and t-test analysis revealed that there is no significant difference ($P >> 0.05$) in length of all 3 SWNTs.

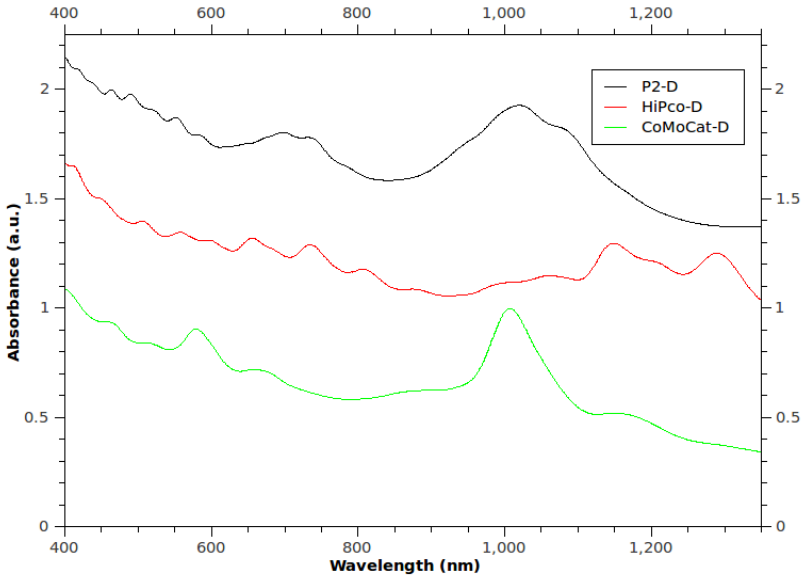

Figure 7.1. UVVis-Near infrared spectra of HiPco-D, SG65-D and P2-D single walled carbon nanotubes (SWNTs)

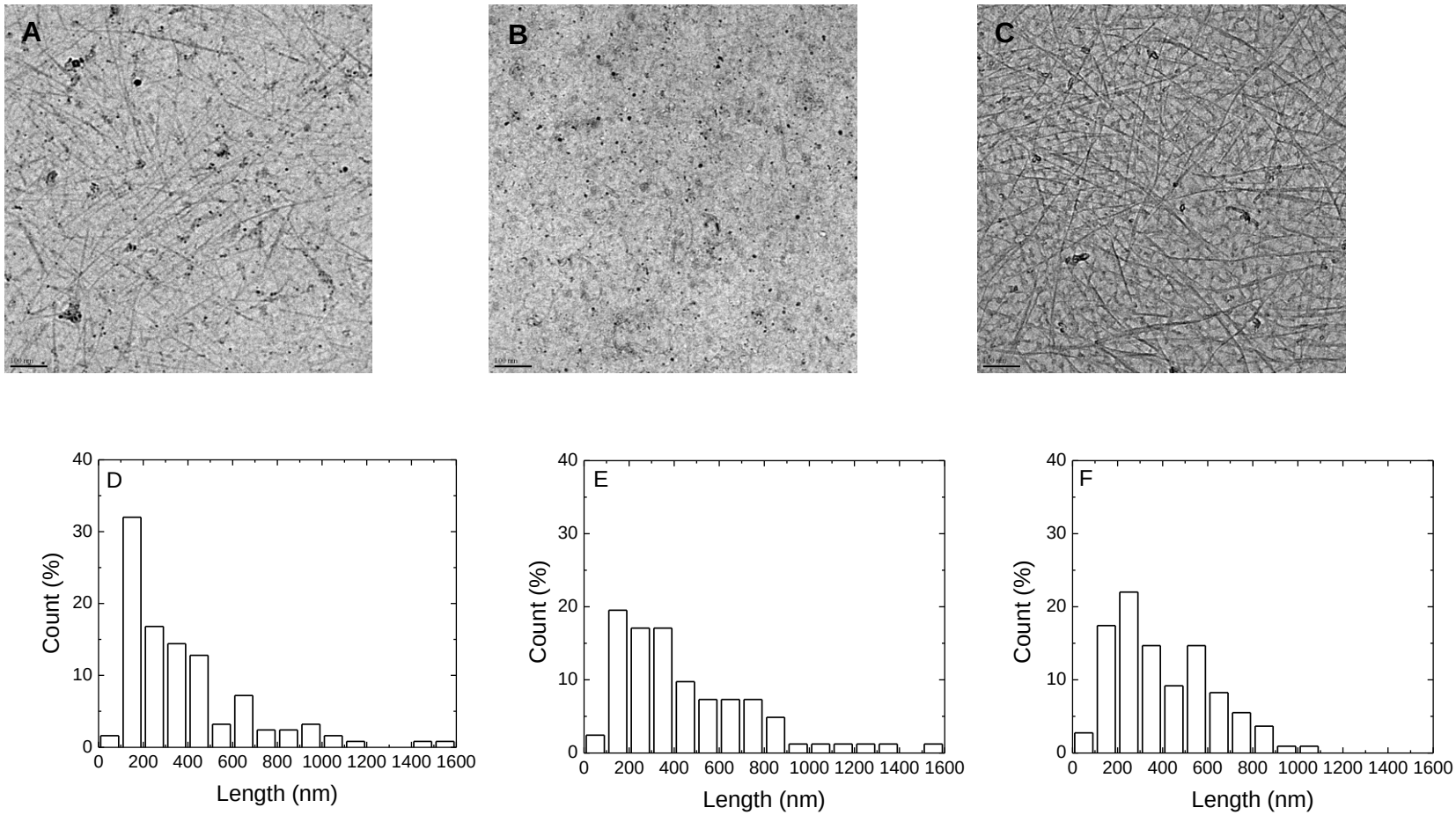

Figure 7.2. Transmission electron microscopy (TEM) images of single walled carbon nanotubes (SWNTs) for A) HiPco-D; B) SG65-D and C) P2-D. Distribution of length for each nanotube are presented for D) HiPco-D; E) SG65-D, and F) P2-D.

Table 7.1. Physical characterization of differently synthesized single walled carbon nanotubes

	Diameter range (nm)nge (nm)	Length (nm)	Metal Mass (%)	Species	Species Mass (%)	Metal Species (%)
HiPco-D	0.696-1.129	383 ± 281	6.52	Fe	6.52	100
SG65-D	0.682-0.981	449 ± 316	1.80	Co	0.22	12.26
				Mo	1.58	87.74
P2-D	1.158-1.699	404 ± 221	0.21	Y	0.06	30.24
				Ni	0.15	69.76

Purity of SWNTs was determined by measuring the residual metal catalysts in SWNTs (Table 7.1). Purifications of SWNTs resulted decrease in metal content by 59%, 67% and 90% for HiPco, SG65 and P2. Overall, the metal content in the SWNTs follows the trend: HiPco-D > SG65-D > P2-D. Metal content of HiPco-D (6.52%) is 4-fold higher than SG65-D (1.80%), followed by 40-fold higher than P2-D (0.21%). While HiPco-D has 100% Fe, distribution of metal species is observed for both SG65-D and P2-D. P2-D resulted higher distribution in metal species (30% Y, 70% Ni) than SG65-D (12% Co, 88% Mo). A metal coating on the CNTs is quite unlikely, yet individual particles attached to the end of a CNT, or scattered along the length of it (in TEM images they appear to usually be inside of the CNT). There are two possible locations for the metal particles: 1) The catalyst particle that seeds the growth of each CNT. This will end up at one end of the CNT after the growth is done, and may or may not be encapsulated

by a carbonaceous shell. 2) In some synthesis methods, as the CNT grows (and if excess catalyst metal is present in the flow of gases, which causes the catalyst particle to grow over time), the catalyst particle may leave behind a portion of itself connected the CNT. The end result is a series of small (~1-3 nm) metal nanoparticles connected to the CNT.

7.3.2 Transport of SWNTs

7.3.2.1 Transport in the Absence of SRHA

Deposition studies of SWNTs were conducted over a wide range of solution chemistry including pH (5, 7), ionic strength (0.1-10 mM), and ion valence (K^+, Ca^{2+}), and results are presented in Figure 7.3 and Table 7.2. This study reveals that elution of SWNTs through the column follows the trend HiPco-D > SG65-D > P2-D under all conditions, which indicates a paramount role of synthesis methods in the transport of SWNTs (Figures 7.3A and 7.3B). In 1 mM KCl, elution of SWNTs through granular media follows the trend: HiPco-D = SG65-D (~58%) >> P2-D (~37%), while deposition rates (assuming first order clean-bed filtration rate(45, 47)) follows: HiPco-D < SG65-D < P2-D (Table 7.2). Similarly, in 1 mM $CaCl_2$, elution of SWNTs trend follows: HiPco-D (~20%) > SG65-D (~6%) > P2-D (~3%), whereas SWNT deposition trend follows HiPco-D < SG65-D < P2-D. These trends indicate that HiPco-D will travel longer distance in the aquatic environment than SG65-D, followed by P2-D.

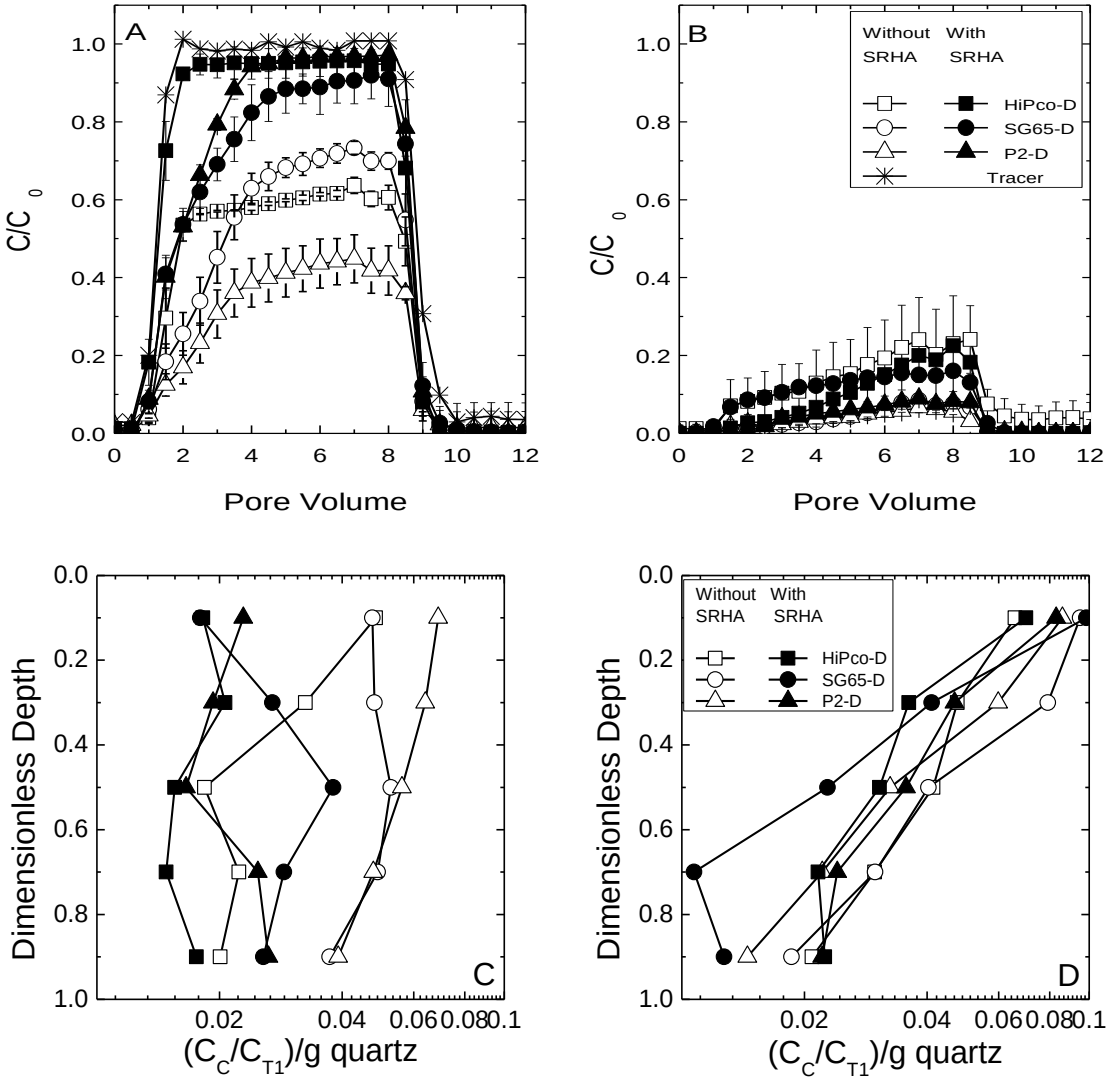

Figure 7.3. Breakthrough curves for 3 differently synthesized SWNTs in absence and presence of SRHA at pH 7 in A) 1 mM KCl and B) 1 mM $CaCl_2$. Deposition profiles for 3 differently synthesized SWNTs in absence and presence of SRHA at pH 7 in C) 1 mM KCl and D) 1 mM $CaCl_2$. Experimental conditions: porosity = 0.465; column length = 5 cm; approach velocity = 0.019 cm/s; mean grain diameter = 275 μm; temperature = 23°C. Injected SWNT concentration (C_0) was 10 mg/L.

Table 7.2. Summary of transport of SWNTs through porous media in the absence and presence of SRHA

Primary particle size (nm)	Condition	Effective Diameter (nm)	EPM (10^{-8} $m^2 V^{-1} s^{-1}$)	Deposition rate, k_d (s^{-1})	M_E (%)	M_c (%)	M_T (%)	%Release[a]
HiPco-D	pH 7, 1 mM KCl	144.1± 17.9	-1.88 ± 0.23	5.08×10^{-3}	57.58	42.74	100.24	3.63
	pH 7, 1 mM KCl + SRHA	147.6 ±14.6	-1.58 ± 0.18	6.48×10^{-4}	91.15	22.04	113.19	4.45
	pH 7, 1 mM $CaCl_2$	125.1±6.8	-0.33±0.28	2.03×10^{-2}	19.35	51.45	70.80	NA
	pH 7, 1 mM $CaCl_2$ + SRHA	123.0± 4.6	-0.66±0.16	2.93×10^{-2}	11.14	45.29	56.43	NA
SG65-D	pH 7, 1 mM KCl	181.2± 25.5	-1.44±0.24	1.11×10^{-2}	58.46	58.77	117.23	1.97
	pH 7, 1 mM KCl + SRHA	136.1± 17.2	-1.27±0.20	5.52×10^{-3}	76.20	21.95	98.15	1.20
	pH 7, 1 mM $CaCl_2$	132.2± 13.4	-0.48±0.17	3.35×10^{-2}	5.23	77.01	82.24	NA
	pH 7, 1 mM $CaCl_2$ + SRHA	142.9±11.3	-0.56±0.12	1.99×10^{-2}	12.86	46.57	59.43	NA
P2-D	pH 7, 1 mM KCl	182.3± 18.7	-0.97±0.47	1.44×10^{-2}	37.53	69.15	106.68	0.91
	pH 7, 1 mM KCl + SRHA	192.1±19.5	-1.41±0.26	4.74×10^{-3}	86.78	27.57	114.35	3.11
	pH 7, 1 mM $CaCl_2$	125.1± 49.8	-0.45±0.32	3.00×10^{-2}	3.21	55.67	58.88	NA
	pH 7, 1 mM $CaCl_2$ + SRHA	141.9± 22.33	-0.60±0.16	4.14×10^{-2}	5.45	NA	NA	NA

[a]%Release is calculated with respect to retained SWNTs in the column

It is to be noted that column breakthrough formed distinctively shaped curves for each SWNT synthesis approach, which indicates that synthesis methods not only control the elution and deposition of SWNTs through granular media, but also affect the shape of breakthrough curves. Shape of breakthrough curves indicate the deposition and interaction phenomena of colloidal materials being transported through the porous media, which in this case is related to the unique transport of each SWNT type(48, 49). Issue of heterogeneity within particle population has been reported particularly in the transport of microbial particles(43, 49). Previous studies on the transport of microbial particles reported that heterogeneity within a bacterial population and cell surfaces can control the shape of breakthrough curves due to mutiple deposition sites, which subsequently deviates from classical colloid filtration theory(43, 49). Since there is a similarity between bacteria and SWNTs in shape and surface chemistry heterogeneity, the distinct breakthrough curves observed for HiPco-D, SG65-D and P2-D may be related to the heterogeneity in SWNTs due to the difference in synthesis methods and residual metal catalysts.

To further understand the mechanisms involved in the transport of SWNTs, retention profiles for deposited SWNTs on the quartz surface in the packed-bed column were developed by dissecting the column in each cm of column length, which were subsequently analyzed to determine the retained SWNTs in each segment (Figures 7.3C and 7.3D). Mass balance of SWNTs was determined from the integration of column breaktrhough curves and retention profiles and is presented in Table 7.2. For monovalent

ions (KCl), mass balance is between 100% and 120%, which implies that almost all SWNTs were successfully separated from the quartz sand. However, in the case of divalent ions ($CaCl_2$) , only 55-85% of total mass of SWNTs was recovered from the quartz sand indicating that SWNTs were more strongly attached with quartz sand in the presnce of $CaCl_2$ than KCl. Such strong and irreversible deposition of SWNTs on the quartz sand in divalent salt solution has been reported by Jaisi et al.(6), which this study attributed due to a primary minimum in the presence of Ca^{2+}.

Retention profile indicates that overall deposition trend follows: HiPco-D < SG65-D < P2-D under all conditions, which further confirms the trend observed from column breakthrough curves (Figures 7.3A and 7.3B). Like what was observed in breakthrough curves, there were distinctive shapes in the retention profiles for each type of SWNTs, further validating the trend observed from elution. Though retention profile of HiPco-D in In 1 mM KCl decreases hyperexponentially with increased depth of porous media, concentration of retained SWNTs showed initially increasing and then decreasing trend with depth for both SG65-D and P2-D. In 1 mM $CaCl_2$, though retention of SWNTs in the sand is higher than in 1 mM KCl, the retention profile decreases exponentially with column depth.

7.3.2.2 Transport in the Presence of SRHA

Whether these findings associated with synthesis techniques and residual metal catalysts in SWNTs in the transport of nanotubes can be translated towards more realistic natural environment, transport of the SWNTs was further investigated in the presence of

natural organic matter. Overall, the transport of SWNTs increased significantly in the presence of SRHA, a similar trend to observations made in other studies with carbon nanotubes(6). In 1 mM KCl with SRHA, elution of SWNTs follows the trend HiPco-D (91%) > P2-D (87%) > SG65-D (77%), while deposition trend follows HiPco-D << P2-D < SG65-D. In divalent ions with SRHA, SWNT elution trend follows: HiPco-D = SG65-D (~12%) > P2-D (~5%), while deposition trend follows HiPco-D = SG65-D < P2-D. Increase of SWNTs transport in the presence of SRHA has been found to be more substantial in monovalent ions than divalent ions. Though addition of NOM increased the transport of SWNTs through the granular media, the distinctive shape of breakthrough curves for each type of SWNTs remains quite similar to those observed in the absence of SRHA, which implies that synthesis and purification methods of SWNTs have singificant effect on the transport of SWNTs. Additional evidence is that similar column retention profiles were observed with the SRHA as compared to without SRHA in both KCl and $CaCl_2$.

7.3.2.3 Release of SWNTs from Porous Media

To further understand the transport of SWNTs, release of SWNTs from the column was conducted to determine the reversibility of deposition and degree of attraction between each SWNT type and quartz surfaces (Figure 7.4). Under all conditions, release of SWNTs was fairly low with less than 5% of the originally deposited nanoparticles being released indicating that SWNTs were irreversibly attached

to the quartz surface under the conditions investigated. Jaisi et al.(6) also found negligble release of SWNTs particularly in the presence of calcium ions. However, the extent of release of SWNTs – even if minor – showed a significant dependence on the synthesis and purification methods, showing the following trend: HiPco-D (3.63%) > SG65-D (1.97%) > P2-D (0.91%). The significance was confirmed with an ANOVA test. In the presence of NOM, the release trend followed a slightly different trend: HiPco-D (4.45%) > P2-D (3.21%) > SG65-D (1.20%).

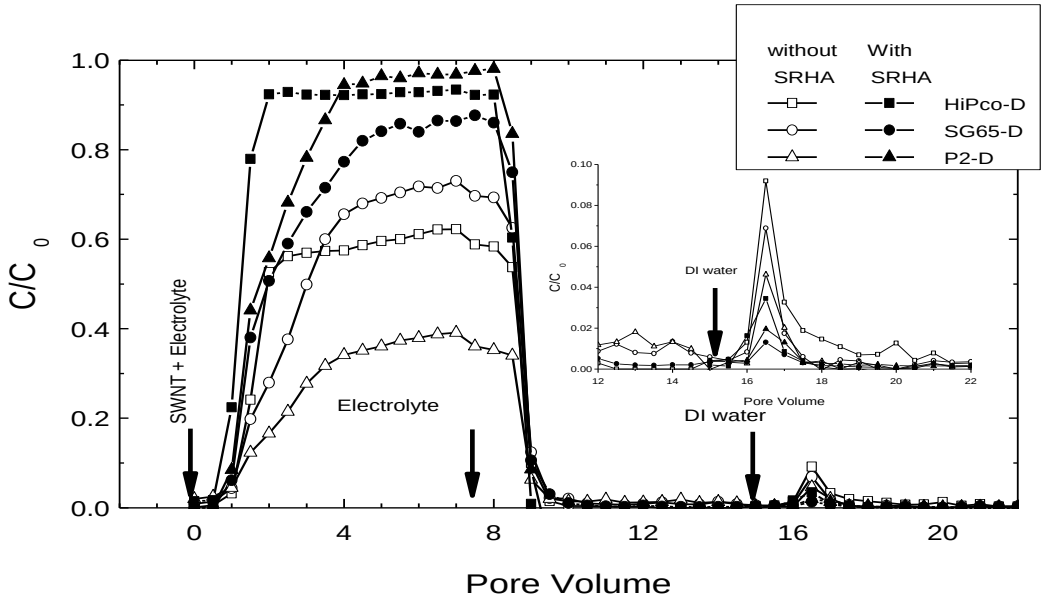

Figure 7.4. Release of previously deposited single walled carbon nanotubes (SWNTs) induced by reduction of background ionic strength. SWNTs were initially injected in 1 mM KCl solution. Nanopure deionized water (10^{18} M-ohm) was introduced after 14 pore volume to reduce ionic strength. Experimental conditions: porosity = 0.465; column length = 5 cm; approach velocity = 0.019 cm/s; mean grain diameter = 275 µm; temperature = 23^0C. Injected SWNT concentration (C_0) was 10 mg/L.

Despite the similar diameter and length of nanotubes (Table 7.1), transport of SWNTs shows a distinctive trend for each type of SWNTs, which implies that other physicochemical parameters of SWNTs may be involved in transport. The metal content in SWNTs follows the similar trend observed in transport, which indicates a dominant role of residual metal content in the transport of SWNTs. Release of SWNTs, like elution, showed an upward trend with metal content indicating that metal content in SWNTs will increase the transport not only through higher elution, but also through higher release from deposited SWNTs. This may be the change in surface properties of SWNTs due to residual metal content. Hence, surface charge properties of SWNTs were further evaluated through electrokinetic characterization and potentiometric titration.

7.3.3 Electrokinetic and Hydrodynamic Characterization of SWNTs

Electrokinetic properties of nanotubes were determined over a wide range of pH in both monovalent (K^+) and divalent (Ca^{2+}) ions with and without SRHA (Figure 7.5). Electrophoretic mobility (EPM) remained very similar over the pH range of 4-10 for all 3 SWNTs, which indicates a relative insensitivity ($P >> 0.05$) of zeta potential of SWNTs to pH. EPM values remains quite similar in both the absence and presence of SRHA, indicating that SRHA did not contribute the charge on SWNTs surface, which is quite opposite to observed in metal oxide nanomaterials(50-52). Overall, in 1 mM KCl, EPMs varied within the range of -1.2×10^{-8} to -1.4×10^{-8} $m^2V^{-1}s^{-1}$, and there is no significant difference ($P >> 0.05$) observed among different SWNT types. In the presence of SRHA

in KCl, the EPM remains similar (-1.2 x 10^{-8} to -1.4 x 10^{-8} $m^2V^{-1}s^{-1}$) for all 3 SWNTs over the pH range of 4-10. Such electrokinetic properties were observed in the case of carbon based nanomaterials including carbon nanotubes(4) and fullerenes at pH 5.5 in both monovalent and divalent ions(25).

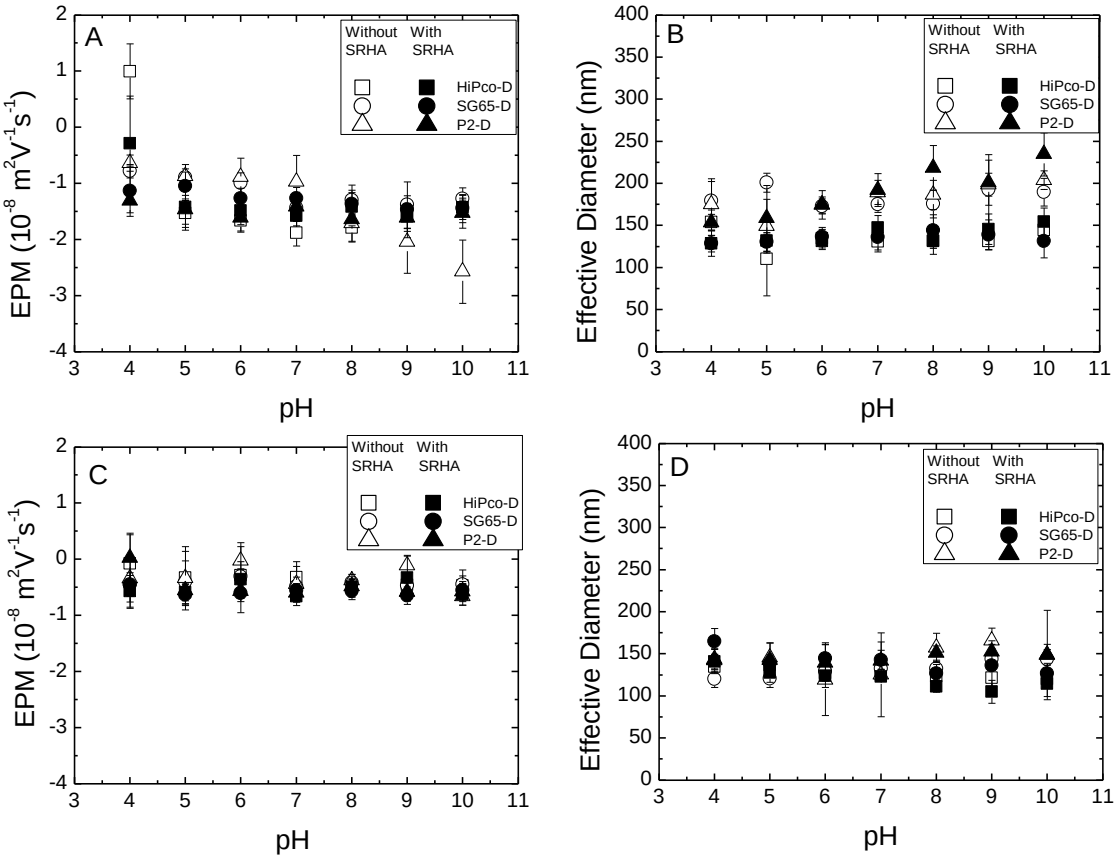

Figure 7.5. Electrokinetic characterization and hydrodynamic diameter of single walled carbon nanotubes (SWNTs) as a function pH in absence and presence of SRHA at A) 1 mM KCl; B) 1 mM KCl; C) 1 mM $CaCl_2$ and D) 1 mM $CaCl_2$. Error bars indicate one standard deviation of at least three measurements.

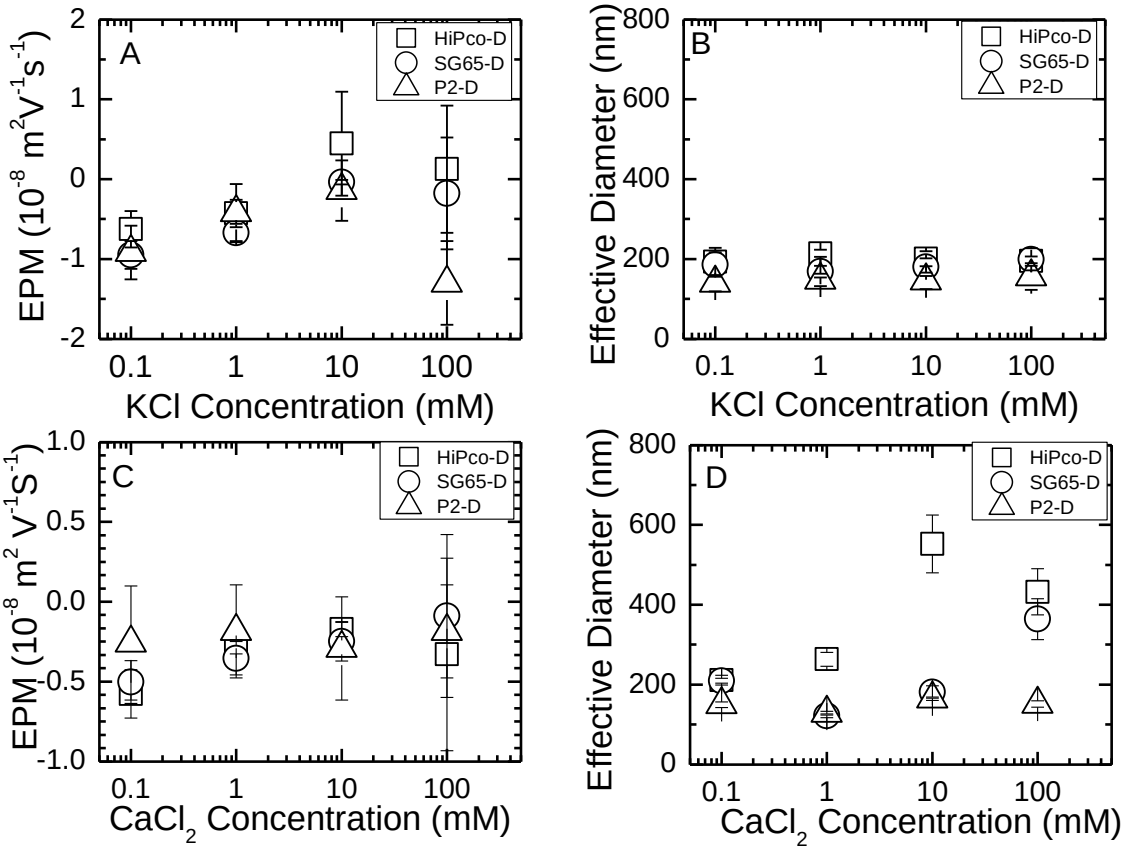

Figure 7.6. Electrokinetic characterization and hydrodynamic diameter of single walled carbon nanotubes (SWNTs) as a function ionic strength for A) EPM in KCl; B) hydrodynamic diameter in KCl; C) EPM in $CaCl_2$ and D) hydrodynamic diameter in $CaCl_2$. Error bars indicate one standard deviation of at least three measurements.

Hydrodynamic diameter of SWNTs was determined over a wide range of solution chemistry (Figure 7.5). Overall the effective diameter of all SWNTs was within the range of 150-200 nm, which remained insensitive to pH, ion valence, SWNT type and SRHA presence investigated in this study. In KCl without SRHA, hydrodynamic

diameter of all 3 SWNTs remained similar (~180 nm) over the pH range 4-10. However, statistical analyses (ANOVA) indicate that there is no significant difference among hydrodynamic diameter for all 3 SWNTs. In KCl with SRHA, hydroynamic diameter of all SWNTs remained insensitive to pH range 4-10. In $CaCl_2$ without SRHA, though EPM remained quite similar for all 3 SWNTs, EPMs were close to neutral indicating compression of electrical double layer in divalent ions(53). In $CaCl_2$ with SRHA, EPMs remained quite similar to observed without SRHA, indicating SRHA is not contributing surface charge on SWNT. Overall, EPM and hydrodynamic diameter of SWNTs remained insensitive to pH, SWNT type, and SRHA in divalent ions.

To confirm whether these findings regarding the electrokinetic properties and hydrodynamic diameter of SWNTs are still applicable to wide range of solution IS, characterization of SWNTs was conducted from 0.1 to 100 mM (Figure 7.6). Overall in monovalent ions (KCl), despite the decrease in EPM, hydrodynamic diameter of all SWNTs remained insensitive to IS, which indicates that the SWNTs used in this study remained stable over a wide range of IS. In KCl, EPM of SWNTs decreased with IS due to electrical double layer compression(53). Furthermore, hydrodynamic diameter of HiPco-D was higher than SG65-D and P2-D. In $CaCl_2$, EPM decreased until 1 mM IS and then became constant. P2-D remained similar hydrodynamic diameter from 0.1-100 mM $CaCl_2$; however, the effective diameter of SWNTs increased for HiPco-D and SG65-D, possibly due to the higher metal content leading to more aggregation.

7.3.4 Factors Affecting Transport

7.3.4.1 Synthesis Methods and Residual Metal Catalysts

To confirm the contribution of SWNT synthesis method on the transport, another surface characterization technique was employed, which is potentiometric titration(54-56). Each type of SWNT was titrated with NaOH from pH 3.0 to 10.5. Acidities and surface charge densities calculated from the potentiometric titration results are presented in Figure 7.7 and Table 7.3. Over the pH conditions investigated in this study (pH 4-10), acidities of SWNTs follows the trend: HiPco-D > SG65-D > P2-D in both the absence and presence of SRHA, though addition of SRHA resulted an increase in acidities for all SWNT types (Figure 7.7). To quantitatively compare among these SWNTs, average acidities and surface charge densities were calculated between pH 4 and 10 (Table 7.3). Acidities and surface charge densities of HiPco-D were ~5-fold and 8-fold higher than those of SG65-D and P2-D respectively, while electrokinetic characterization resulted in similar EPMs for all 3 SWNTs. Overall, acidities as well as surface charge densities of SWNTs showed an upward trend from HiPco-D to P2-D indicating a remarkable role of synthesis methods and residual metal catalysts in physicochemical properties of SWNTs.

A notable trend has been observed in potentiometric titration curves (Figure 7.7) that SG65-D and P2-D showed more inflection points than HiPco-D. Hence, relative site concentrations of each metal type in SWNTs were determined by further analyzing the potentiometric titration data with FITEQL 4.0, as detailed analysis mentioned elsewhere (28, 32). Total site concentration of SWNTs follows the trend: HiPco-D >> SG65-D >

P2-D, which is similar to metal content trend. Previous studies with microbial transport found that increased surface charge density and acidity on bacterial surface is attributed to the functional groups, which eventually leads to longer transport of bacteria. Likewise, higher surface charge density and site concentration resulted longer transport for HiPco-D, followed by SG65-D and P2-D.

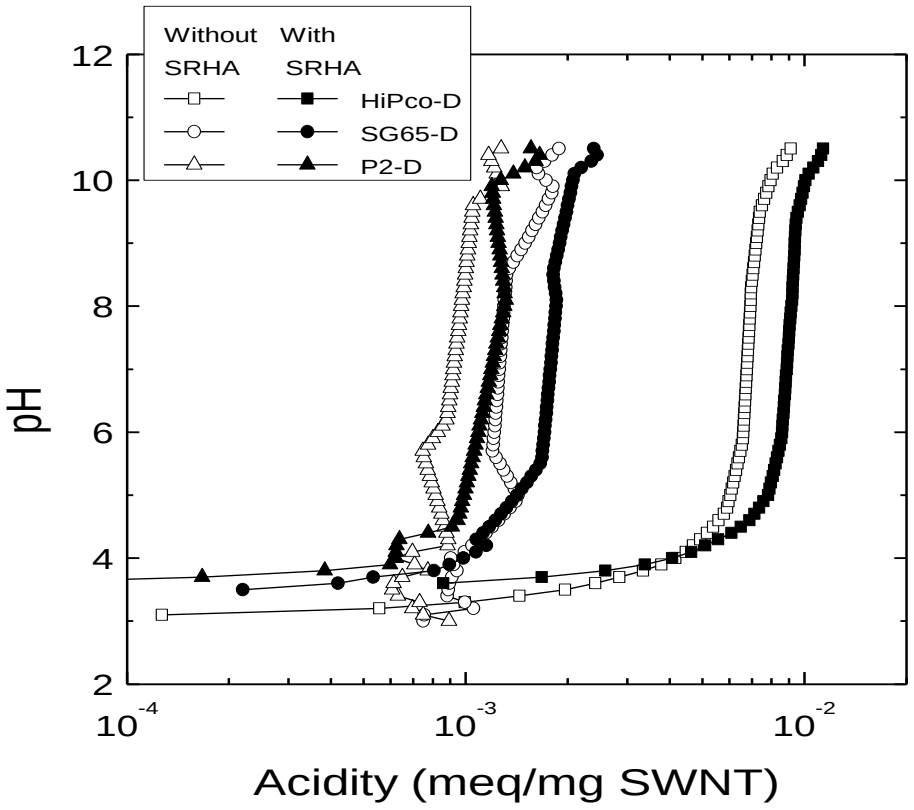

Figure 7.7. Potentiometric titrations of HiPco-D, SG65-D and P2-D SWNTs in absence and presence of SRHA. Acidities are determined from the amount of NaOH (0.1 N) consumed during titration. Titrations were performed in 1 mM KCl and at 25^{o}C.

Table 7.3. Potentiometric titration of SWNTs in the absence of SRHA with calculated values from pH 4 to 10.

SWNT Type		**Acidity (meq/mg SWNT)**	**Surface charge density (μC/mg SWNT)**	**Total site concentration, C_T (10^{-6} mol/mg SWNTs)**	**pK_{a1}**	**pK_{a2}**	**pK_{a3}**	**C_1/C_T**	**C_2/C_T**	**C_3/C_T**
HiPCo-D	Without SRHA	(4.41 ± 0.87) x 10^{-3}	(4.25 ± 0.84)x 10^5	10.62 ± 1.01	3.94 ± 0.52	10.18 ± 0.41	NA	0.67± 0.09	0.33±0.09	NA
SG65-D	Without SRHA	(9.17 ± 1.34) x 10^{-4}	(8.85± 1.30) x 10^4	2.07	4.57 ±	6.06 ±	10.27	0.12	0.17	0.71
P2-D	Without SRHA	(5.83 ± 0.76) x 10^{-4}	(5.62± 0.73) x 10^4	1.45 ± 1.47	6.71± 1.35	10.80± 0.06	NA	0.19± 0.10	0.81± 0.10	NA

C_i/C_T : Relative concentration of each sit

FITEQL analysis indicates that HiPco-D showed two distinctive ion dissociable sites with pK_a values around 3.9 and 10.0, which corresponds to carboxylic and hydroxyl functional groups respectively. In HiPco-D, the dominant functional group is carboxylic (70%). However, SG65-D shows three separate sites with pKa values around 4.6, 6.1 and 10.3, which denotes carboxylic, phosphoric and hydroxyl functional groups. In SG65-D, hydroxyl functional group is the most dominant (71%). Additional pK_a in SG65-D may be due to two residual metal catalysts (Co and Mo) found in SG65-D., which caused the inflection in the potentiometric curve as well as distinctively shaped breakthrough curve (as discussed before). In P2-D, two functional groups are observed with pKa values of 6.7 and 10.8 corresponding to phosphoric and hydroxyl, which is primarily dominated by hydroxyl functional groups (81%).

From the SWNT transport of results, it is observed that each SWNT type shows distinctive breakthrough curve, though there was no observable difference in length, diameter, hydrodynamic diameter and zeta potential among these SWNTs. The notable difference among these SWNTs was observed in synthesis methods and residual metal catalysts. These differences contributed to the additional acidities and charge densities to SWNT surface, which in turn increases the mobility of SWNTs through granular media. Although higher elution of HiPco-D with respect to P2-D and SG65-D can be explained from the higher charge densities observed for HiPco-D, the question still remains why each SWNT type resulted distinctive breakthrough curve. Potentiometric titration analysis reveals that number of residual metal catalysts may have notable role on the

physicochemical characteristics of SWNTs. SWNTs synthesized by two metal catalysts (SG65-D and P2-D) have one more surface site than SWNTs with single metal catalyst (HiPco-D). These differences in physicochemical properties of SWNTs due to the number of residual metal catalysts observed from potentiometric titration results may have influence on the distinctive transport of SWNTs.

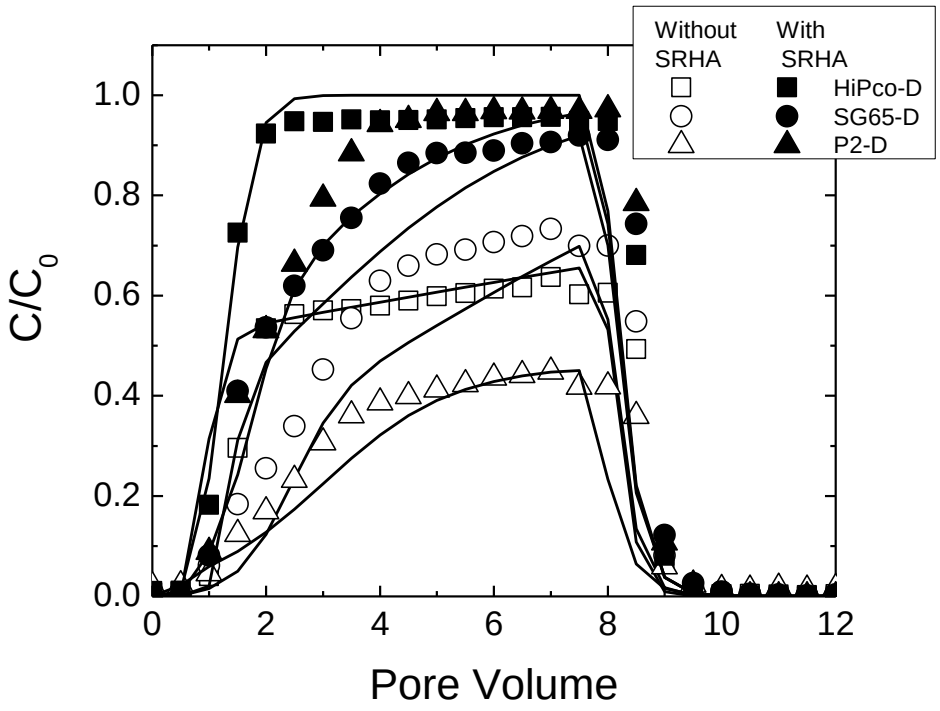

Figure 7.8. Observed and model fitted breakthrough curves for SWNTs in presence and absence of SRHA at pH 7 and 1 mM KCl. The lines are fitted using HYDRUS 1-D model. Two kinetic site model is used in modeling. Experimental conditions: porosity = 0.465; column length = 5 cm; approach velocity = 0.019 cm/s; mean grain diameter = 275 μm; temperature = 23^0C. Injected SWNT concentration (C_0) was 10 mg/L.

Table 7.4. HYDRUS Modeling Results for transport of SWNTs at pH 7 and 1 mM KCl

SWNT Type		RMSE	S_{max1} (cm^3/g)	k_{a1} (s^{-1})	S_{max2} (cm^3/g)	k_{a2} (s^{-1})
HiPCo-D	Without SRHA	0.090	2.42	5.36×10^{-3}	NA	NA
	With SRHA	0.096	0.11	1.67×10^{-3}	NA	NA
SG65-D	Without SRHA	0.079	1.33	9.70×10^{-3}	0.27	4.12×10^{-3}
	With SRHA	0.096	0.65	8.03×10^{-3}	0.09	1.10×10^{-1}
P2-D	Without SRHA	0.057	10.00	7.79×10^{-3}	0.49	2.83×10^{-3}
	With SRHA	0.103	0.40	5.58×10^{-3}	1.32	2.20×10^{-3}

RMSE: Root mean squared error

To investigate this role, we utilized HYDRUS 1D (44) model to fit the transport data using the one and two kinetic site model. Details of this model are mentioned in the Materials and Methods section and Supporting Information. HYDRUS results are presented in Table 7.4 and Figure 7.8. Both one and two site models were utilized to optimize the fitting parameters (Table 7.4). Overall modeling results show that transport of HiPco-D can be best described with one kinetic site model, while both SG65-D and P2-D requires two sites to fit the transport data. For HiPco-D, the origin of one site is from residual Fe catalyst, while two sites in SG65-D and P2-D result from Co, Mo and Y, Ni respectively. The deposition rates (k_d) and maximum solid phase concentration (S_{max}) also show a notable dependence on the residual metal catalysts. For SG65-D and P2-D,

most of the deposition of SWNTs occurred in one site, which further relates to the distribution of residual metal catalyst of these SWNTs. Both SG65-D and P2-D are mainly dominated by one residual metal catalyst (for SG65-D, Mo 88% and P2-D, Ni 70%). While It is still not certain whether residual metal catalysts or difference in synthesis methods are responsible for the difference in transport, the observed results confirms the vital role of synthesis methods and residual metal catalysts on the mobility of SWNTs in the aquatic environment.

7.3.4.2 Metallic and Semiconducting Properties of SWNTs

Although there is a significant amount of metal, the electronic behavior of the nanotubes is dominated by their structure. Most SWCNT as produced will be a mix of ~1/3 metallic tubes and ~2/3 semiconducting (1 out of 3 tube structures as determined by their (n,m) indices are metallic, and the rest semiconducting). HiPco and P2 tubes follow this rule (as the (n,m) index of a SWNT is a random distribution over a diameter range). SG65 material on the other hand is synthesized in such a way as to significantly favor semiconducting tubes during growth, resulting in ~90% of tubes being semiconducting, with the rest metallic. The procedures we followed to prepare the SWNT dispersed material will not favor dispersion of either type, resulting in material that is representative of the starting powder.

Metal content should not have a significant effect on the electronic properties of nanotubes. Electronic structure of SWNTs can be modified by doping (both n and p

types of SWNT can be produced by addition of specific molecules and acids), and this change affects the optical properties of SWNTs (damping optical absorption bands, modifying emission and absorption peaks), which can easily be measured by UV-Vis-NIR absorbance or photoluminescence experiments. Nothing was observed in the absorption or fluorescence spectra of SWNTs that would indicate that the bands differ from a pristine carbon-only sample. Although local behavior may be modified (metal particulates would probably act as exciton recombination centers when in contact with semiconducting SWNTs, but these would only affect a local section of a SWNT rather than the entire SWNT "molecule"). In general,metal contamination at this level is not expected to significantly alter the electronic properties of a SWNT.

7.3.4.3 Presence of a Dispersing Agent

Pluronic F108 triblock copolymer was used to disperse the SWNTs in aqueous solution as mentioned elsewhere(57, 58). Pluronic copolymer composes of two hydrophilic polyethylene oxide (PEO) chains with a central hydrophobic polypropylene oxide (PPO) group(57). Hydrophobic PPO group binds with SWNT surface, while hydrophilic PEO chains extend to the solution. Both PPO and PEO segments control the dispersion ability of SWNTs in Pluronic copolymers(59). Interactions of Pluronic with SWNTs depend not only on pluronic type(60), but also on temperature(61, 62) and SWNT properties including diameter and length(63, 64). While it is experimentally impossible to measure how much Pluronic is sorbed to each SWNT type and whether

Pluronic has specific sorption towards particular SWNT type, it is certain that our dispersion of SWNTs with Pluronic F108 sorts the similar sized (diameter and length) nanotubes from differently synthesized SWNTs.

7.3.5 Bacterial Cytotxicity of SWNTs

Bacterial cytotoxicity of SWNTs was also investigated to confirm whether this change in transport of SWNTs due to synthesis methods and residual metal catalysts has any influence on bacterial viability. Results from bacterial cytotoxicity of SWNTs are summarized in Figure 7.9. Overall, viability results indicated a greater toxic response of *E. coli* cells to the HiPco-D as compared to SG65-D and P2-D. Notably, the viability loss was 60% for HiPco-D as compared to others (at less than 10%) in the one hour exposure test. Vecitis et al.(21) proposed a three-step antimicrobial mechanism for SWNTs with initial cell-nanotube contact, membrane rupture and oxidation. While exact mechanism for this greater toxicity is still unknown, it is certain that both transport and toxicity of HiPco-D is the highest among the SWNTs investigated in this study and this may be attributed to the higher acidity and residual metal catalyst.

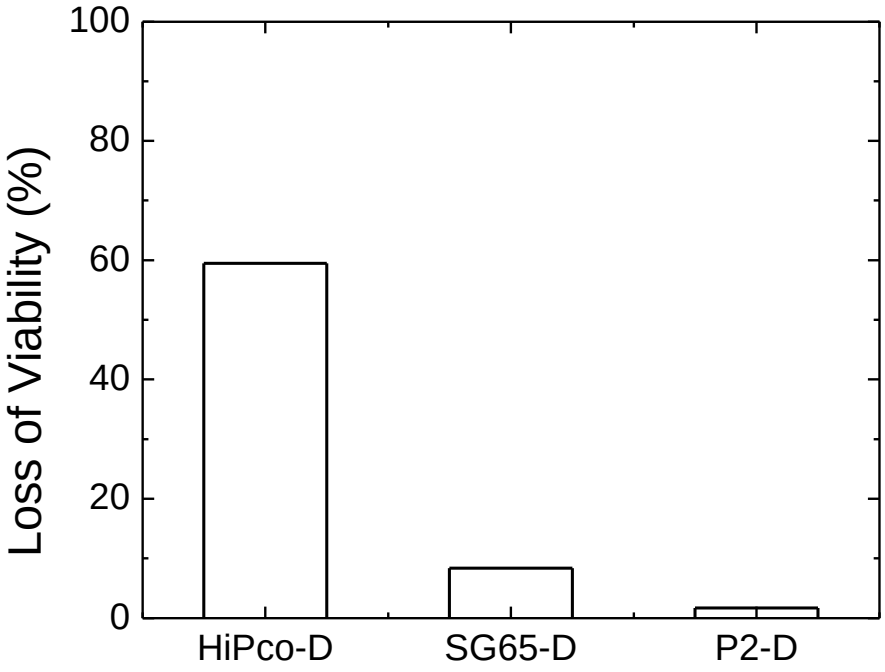

Figure 7.9. Bacterial cytotoxicity of single walled carbon nanotubes. *E. coli K12* is used in this study as model bacteria at 5 x 10^7 cells/mL. SWNT concentration was 10 mg/L. Loss of viability has been determined after 60 min of incubation at 37^0 C. Fluorescence based toxicity assay was used to determine the viability of bacteria using Live-dead Baclight kit.

7.4 Conclusions

While we still do not know the exact mechanisms and extent to which residual metal catalysts affect the transport of SWNTs, herein we found a vital role of synthesis and purification approaches on the transport and toxicity of three representative SWNTs. This study reveals that SWNTs synthesized by the HiPco method are removed in porous

media less than those synthesized with CVD and EA methods. This higher transport potential for HiPco SWNTs is attributed to its acidity due to residual metal catalyst. Overall, transport of SWNTs increases with higher metal content indicating that the more toxic SWNTs (greater metal content) will be transported further in the environment than less toxic SWNTs (lower metal content). The hydrodynamic diameter and zeta potential of SWNTs remain insensitive to pH, which indicates that transport of nanotubes in the environment will not be governed by pH. Significantly higher deposition was observed in the presence of divalent ions than monovalent ions, implying that ion valence will play a substantial role in determining the transport of SWNTs in the aquatic environment. NOM also was found to increase the transport of SWNTs, and the extent to which was sensitive to ion valence. The combination of these findings will allow for safe design of environmental friendly SWNTs by identifying properties that can be exploited to reduce their subsequent transport potential in water. Reducing the metal content will reduce the mobility and toxicity of SWNTs, which in turn will limit the exposure of SWNTs.

7.5 References

(1) Hyung, H.; Fortner, J. D.; Hughes, J. B.; Kim, J.-H., Natural Organic Matter Stabilizes Carbon Nanotubes in the Aqueous Phase. *Environmental Science & Technology* **2007,** *41*, (1), 179-184.

(2) Wiesner, M. R.; Hotze, E. M.; Brant, J. A.; Espinasse, B., Nanomaterials as possible contaminants: the fullerene example. *Water Science and Technology* **2008,** *57*, (3), 305-310.

(3) Mauter, M. S.; Elimelech, M., Environmental Applications of Carbon-Based Nanomaterials. *Environmental Science & Technology* **2008,** *42*, (16), 5843-5859.

(4) Saleh, N. B.; Pfefferle, L. D.; Elimelech, M., Influence of Biomacromolecules and Humic Acid on the Aggregation Kinetics of Single-Walled Carbon Nanotubes. *Environmental Science & Technology* **2010,** *44*, (7), 2412-2418.

(5) Hendren, C. O.; Mesnard, X.; Dröge, J.; Wiesner, M. R., Estimating Production Data for Five Engineered Nanomaterials As a Basis for Exposure Assessment. *Environmental Science & Technology* **2011,** *45*, (7), 2562-2569.

(6) Jaisi, D. P.; Saleh, N. B.; Blake, R. E.; Elimelech, M., Transport of Single-Walled Carbon Nanotubes in Porous Media: Filtration Mechanisms and Reversibility. *Environmental Science & Technology* **2008,** *42*, (22), 8317-8323.

(7) Jaisi, D. P.; Elimelech, M., Single-Walled Carbon Nanotubes Exhibit Limited Transport in Soil Columns. *Environmental Science & Technology* **2009,** *43*, (24), 9161.

(8) Liu, X.; O'Carroll, D. M.; Petersen, E. J.; Huang, Q.; Anderson, C. L., Mobility of Multiwalled Carbon Nanotubes in Porous Media. *Environmental Science & Technology* **2009**, *43*, 8153.

(9) Bouchard, D.; Zhang, W.; Powell, T.; Rattanaudompol, U. s., Aggregation Kinetics and Transport of Single-Walled Carbon Nanotubes at Low Surfactant Concentrations. *Environmental Science & Technology* **2012**, *46*, 4458

(10) Smith, B.; Wepasnick, K.; Schrote, K. E.; Bertele, A. R.; Ball, W. P.; O'Melia, C.; Fairbrother, D. H., Colloidal Properties of Aqueous Suspensions of Acid-Treated, Multi-Walled Carbon Nanotubes. *Environmental Science & Technology* **2008,** *43*, (3), 819-825.

(11) Saleh, N. B.; Pfefferle, L. D.; Elimelech, M., Aggregation Kinetics of Multiwalled Carbon Nanotubes in Aquatic Systems: Measurements and Environmental Implications. *Environmental Science & Technology* **2008,** *42*, (21), 7963-7969.

(12) Yi, P.; Chen, K. L., Influence of Surface Oxidation on the Aggregation and Deposition Kinetics of Multiwalled Carbon Nanotubes in Monovalent and Divalent Electrolytes. *Langmuir* **2011,** *27*, (7), 3588-3599.

(13) Eckelman, M. J.; Mauter, M. S.; Isaacs, J. A.; Elimelech, M., New Perspectives on Nanomaterial Aquatic Ecotoxicity: Production Impacts Exceed Direct Exposure Impacts for Carbon Nanotoubes. *Environmental Science & Technology* **2012,** *46*, (5), 2902-2910.

(14) Healy, M. L.; Dahlben, L. J.; Isaacs, J. A., Environmental Assessment of Single-Walled Carbon Nanotube Processes. *Journal of Industrial Ecology* **2008,** *12*, (3), 376-393.

(15) Plata, D. e. L.; Hart, A. J.; Reddy, C. M.; Gschwend, P. M., Early Evaluation of Potential Environmental Impacts of Carbon Nanotube Synthesis by Chemical Vapor Deposition. *Environmental Science & Technology* **2009,** *43*, (21), 8367-8373.

(16) Pumera, M., Carbon Nanotubes Contain Residual Metal Catalyst Nanoparticles even after Washing with Nitric Acid at Elevated Temperature Because These Metal Nanoparticles Are Sheathed by Several Graphene Sheets. *Langmuir* **2007,** *23*, (11), 6453-6458.

(17) Chiang, I. W.; Brinson, B. E.; Smalley, R. E.; Margrave, J. L.; Hauge, R. H., Purification and Characterization of Single-Wall Carbon Nanotubes. *The Journal of Physical Chemistry B* **2001,** *105*, (6), 1157-1161.

(18) Plata, D. L.; Gschwend, P. M.; Reddy, C. M., Industrially synthesized single-walled carbon nanotubes: compositional data for users, environmental risk assessments, and source apportionment. In IOP PUBLISHING LTD: **2008**.

(19) Pumera, M.; Miyahara, Y., What amount of metallic impurities in carbon nanotubes is small enough not to dominate their redox properties? *Nanoscale* **2009,** *1*, (2).

(20) Lam, C.-W.; James, J. T.; McCluskey, R.; Hunter, R. L., Pulmonary Toxicity of Single-Wall Carbon Nanotubes in Mice 7 and 90 Days After Intratracheal Instillation. *Toxicological Sciences* **2004,** *77*, (1), 126-134.

(21) Vecitis, C. D.; Zodrow, K. R.; Kang, S.; Elimelech, M., Electronic-Structure-Dependent Bacterial Cytotoxicity of Single-Walled Carbon Nanotubes. *ACS Nano* **2010,** *4*, (9), 5471-5479.

(22) Arnold, M. S.; Green, A. A.; Hulvat, J. F.; Stupp, S. I.; Hersam, M. C., Sorting carbon nanotubes by electronic structure using density differentiation. *Nat Nano* **2006,** *1*, (1), 60-65.

(23) Strano, M. S.; Dyke, C. A.; Usrey, M. L.; Barone, P. W.; Allen, M. J.; Shan, H.; Kittrell, C.; Hauge, R. H.; Tour, J. M.; Smalley, R. E., Electronic Structure Control of Single-Walled Carbon Nanotube Functionalization. *Science* **2003,** *301*, (5639), 1519-1522.

(24) Petersen, E. J.; Zhang, L.; Mattison, N. T.; O'Carroll, D. M.; Whelton, A. J.; Uddin, N.; Nguyen, T.; Huang, Q.; Henry, T. B.; Holbrook, R. D.; Chen, K. L., Potential Release Pathways, Environmental Fate, And Ecological Risks of Carbon Nanotubes. *Environmental Science & Technology* **2011,** *45*, (23), 9837-9856.

(25) Chen, K. L.; Elimelech, M., Interaction of Fullerene (C60) Nanoparticles with Humic Acid and Alginate Coated Silica Surfaces: Measurements, Mechanisms, and Environmental Implications. *Environmental Science & Technology* **2008,** *42*, (20), 7607-7614.

(26) Johnson, W. P.; Logan, B. E., Enhanced transport of bacteria in porous media by sediment-phase and aqueous-phase natural organic matter. *Water Research* **1996,** *30*, (4), 923-931.

(27) Tiller, C. L.; O'Melia, C. R., Natural organic matter and colloidal stability: Models and measurements. *Colloids and Surfaces A: Physicochemical and Engineering Aspects* **1993,** *73*, 89-102.

(28) Hong, Y.; Brown, D. G., Cell surface acid-base properties of *Escherichia coli* and *Bacillus brevis* and variation as a function of growth phase, nitrogen source and C:N ratio. *Colloids and Surfaces B: Biointerfaces* **2006,** *50*, (2), 112.

(29) Kim, H. N.; Hong, Y.; Lee, I.; Bradford, S. A.; Walker, S. L., Surface Characteristics and Adhesion Behavior of *Escherichia coli* O157:H7: Role of Extracellular Macromolecules. *Biomacromolecules* **2009,** *10*, (9), 2556-2564.

(30) Walker, S. L.; Hill, J. E.; Redman, J. A.; Elimelech, M., Influence of Growth Phase on Adhesion Kinetics of *Escherichia coli* D21g. *Appl. Environ. Microbiol.* **2005,** *71*, (6), 3093-3099.

(31) Walker, S.; Elimelech, M.; Redman, J., Influence of Growth Phase on Bacterial Deposition: Interaction Mechanisms in Packed-Bed Column and Radial Stagnation Point Flow Systems. *Environmental Science & Technology* **2006,** *40*, (17), 5586-5586.

(32) Westall, J. C.; Jones, J. D.; Turner, G. D.; Zachara, J. M., Models for Association of Metal Ions with Heterogeneous Environmental Sorbents. 1. Complexation of Co(II) by Leonardite Humic Acid as a Function of pH and NaClO4 Concentration. *Environmental Science & Technology* **1995,** *29*, (4), 951-959.

(33) Chowdhury, I.; Hong, Y.; Honda, R. J.; Walker, S. L., Mechanisms of TiO_2 nanoparticle transport in porous media: Role of solution chemistry, nanoparticle

concentration, and flowrate. *Journal of Colloid and Interface Science* **2011,** *360*, (2), 548-555.

(34) Chae, S.-R.; Badireddy, A. R.; Farner Budarz, J.; Lin, S.; Xiao, Y.; Therezien, M.; Wiesner, M. R., Heterogeneities in Fullerene Nanoparticle Aggregates Affecting Reactivity, Bioactivity, and Transport. *ACS Nano* **2010,** *4*, (9), 5011-5018.

(35) Crittenden, J. C.; Montgomery Watson, H., *Water treatment principles and design*. J. Wiley: Hoboken, N.J., 2005.

(36) Kim, H. N.; Bradford, S. A.; Walker, S. L., *Escherichia coli* O157:H7 Transport in Saturated Porous Media: Role of Solution Chemistry and Surface Macromolecules. *Environmental Science & Technology* **2009,** *43*, (12), 4340.

(37) Haznedaroglu, B. Z.; Kim, H. N.; Bradford, S. A.; Walker, S. L., Relative Transport Behavior of *Escherichia col*i O157:H7 and Salmonella enterica Serovar Pullorum in Packed Bed Column Systems: Influence of Solution Chemistry and Cell Concentration. *Environmental Science & Technology* **2009,** *43*, (6), 1838.

(38) Bradford, S. A.; Kim, H. N.; Haznedaroglu, B. Z.; Torkzaban, S.; Walker, S. L., Coupled Factors Influencing Concentration-Dependent Colloid Transport and Retention in Saturated Porous Media. *Environmental Science & Technology* **2009,** *43*, (18), 6996.

(39) Hong, Y.; Honda, R. J.; Myung, N. V.; Walker, S. L., Transport of Iron-Based Nanoparticles: Role of Magnetic Properties. *Environmental Science & Technology* **2009,** *43*, (23), 8834.

(40) American Public Health, A.; American Water Works, A.; Water Pollution Control, F., Standard methods for the examination of water and wastewater. *Standard methods for the examination of water and wastewater*. **1905**.

(41) Chen, G.; Hong, Y.; Walker, S. L., Colloidal and Bacterial Deposition: Role of Gravity. *Langmuir* **2009,** *26*, (1), 314-319.

(42) Walker, S. L.; Redman, J. A.; Elimelech, M., Role of Cell Surface Lipopolysaccharides in *Escherichia coli* K12 Adhesion and Transport. *Langmuir* **2004,** *20*, (18), 7736-7746.

(43) Tufenkji, N.; Elimelech, M., Deviation from the Classical Colloid Filtration Theory in the Presence of Repulsive DLVO Interactions. *Langmuir* **2004,** *20*, (25), 10818-10828.

(44) Simunek, J., Van Genuchten, M.T., Sejna, M., The HYDRUS-1D software package for simulating the one-dimensional movement of water, heat, and multiple solutes in variably-saturated media. *University of California-Riverside Research Reports* **2005**, pp. 240.

(45) Tufenkji, N.; Elimelech, M., Correlation Equation for Predicting Single-Collector Efficiency in Physicochemical Filtration in Saturated Porous Media. *Environmental Science & Technology* **2003,** *38*, (2), 529.

(46) Gong, A. S.; Lanzl, C. A.; Cwiertny, D. M.; Walker, S. L., Lack of Influence of Extracellular Polymeric Substances (EPS) Level on Hydroxyl Radical Mediated Disinfection of *Escherichia coli*. *Environmental Science & Technology* **2011,** *46*, (1), 241-249.

(47) Yao, K.-M.; Habibian, M. T.; O'Melia, C. R., Water and waste water filtration. Concepts and applications. *Environmental Science & Technology* **1971,** *5*, (11), 1105.

(48) Tufenkji, N.; Redman, J. A.; Elimelech, M., Interpreting Deposition Patterns of Microbial Particles in Laboratory-Scale Column Experiments. *Environmental Science & Technology* **2003,** *37*, (3), 616-623.

(49) Baygents, J. C.; Glynn, J. R.; Albinger, O.; Biesemeyer, B. K.; Ogden, K. L.; Arnold, R. G., Variation of Surface Charge Density in Monoclonal Bacterial Populations: Implications for Transport through Porous Media. *Environmental Science & Technology* **1998,** *32*, (11), 1596-1603.

(50) Thio, B. J. R.; Zhou, D.; Keller, A. A., Influence of natural organic matter on the aggregation and deposition of titanium dioxide nanoparticles. *Journal of Hazardous Materials* **2011,** *189*, (1-2), 556-563.

(51) Chen, K. L.; Mylon, S. E.; Elimelech, M., Aggregation kinetics of alginate-coated hematite nanoparticles in monovalent and divalent electrolytes. *Environmental Science & Technology* **2006,** *40*, (5), 1516-1523.

(52) Chowdhury, I.; Cwiertny, D. M.; Walker, S. L., Combined Factors Influencing the Aggregation and Deposition of nano-TiO_2 in Presence of Humic Acids and Bacteria. *Environmental Science & Technology* **2012** ASAP

(53) Elimelech, M., Gregory, J., Jia, X., Williams, R.A., *Particle Deposition and Aggregation: Measurement, Modeling and Simulation*. Butterworth-Heinemann: 1995; p 441.

(54) Hong, Y.; Brown, D. G., Electrostatic Behavior of the Charge-Regulated Bacterial Cell Surface. *Langmuir* **2008,** *24*, (9), 5003-5009.

(55) Zarzycki, P.; Rosso, K. M., Origin of Two Time-Scale Regimes in Potentiometric Titration of Metal Oxides. A Replica Kinetic Monte Carlo Study. *Langmuir* **2009,** *25*, (12), 6841-6848.

(56) Castro, F. D.; Sedman, J.; Ismail, A. A.; Asadishad, B.; Tufenkji, N., Effect of Dissolved Oxygen on Two Bacterial Pathogens Examined using ATR-FTIR Spectroscopy, Microelectrophoresis, and Potentiometric Titration. *Environmental Science & Technology* **2010,** *44*, (11), 4136-4141.

(57) Antaris, A. L.; Seo, J.-W. T.; Green, A. A.; Hersam, M. C., Sorting Single-Walled Carbon Nanotubes by Electronic Type Using Nonionic, Biocompatible Block Copolymers. *ACS Nano* **2010,** *4*, (8), 4725-4732.

(58) Duch, M. C.; Budinger, G. R. S.; Liang, Y. T.; Soberanes, S.; Urich, D.; Chiarella, S. E.; Campochiaro, L. A.; Gonzalez, A.; Chandel, N. S.; Hersam, M. C.; Mutlu, G. M., Minimizing Oxidation and Stable Nanoscale Dispersion Improves the Biocompatibility of Graphene in the Lung. *Nano Letters* **2011,** *11*, (12), 5201-5207.

(59) Moore, V. C.; Strano, M. S.; Haroz, E. H.; Hauge, R. H.; Smalley, R. E.; Schmidt, J.; Talmon, Y., Individually Suspended Single-Walled Carbon Nanotubes in Various Surfactants. *Nano Letters* **2003,** *3*, (10), 1379-1382.

(60) Shvartzman-Cohen, R.; Nativ-Roth, E.; Baskaran, E.; Levi-Kalisman, Y.; Szleifer, I.; Yerushalmi-Rozen, R., Selective Dispersion of Single-Walled Carbon

Nanotubes in the Presence of Polymers: the Role of Molecular and Colloidal Length Scales. *Journal of the American Chemical Society* **2004,** *126*, (45), 14850-14857.

(61) Lin, Y.; Alexandridis, P., Temperature-Dependent Adsorption of Pluronic F127 Block Copolymers onto Carbon Black Particles Dispersed in Aqueous Media. *The Journal of Physical Chemistry B* **2002,** *106*, (42), 10834-10844.

(62) Shvartzman-Cohen, R.; Florent, M.; Goldfarb, D.; Szleifer, I.; Yerushalmi-Rozen, R., Aggregation and Self-Assembly of Amphiphilic Block Copolymers in Aqueous Dispersions of Carbon Nanotubes. *Langmuir* **2008,** *24*, (9), 4625-4632.

(63) Nagarajan, R.; Bradley, R. A.; Nair, B. R., Thermodynamically stable, size selective solubilization of carbon nanotubes in aqueous solutions of amphiphilic block copolymers. *The Journal of Chemical Physics* **2009,** *131*, (10), 104906-13.

(64) Kusner, I.; Srebnik, S., Conformational behavior of semi-flexible polymers confined to a cylindrical surface. *Chemical Physics Letters* **2006,** *430*, (1–3), 84-88.

Chapter 8

Summary and Conclusions

The overall goal of this doctoral work was to shed a light on the fundamental mechanisms involved in the fate, transport, and removal of nanomaterials in both natural and engineered environments. Nine different nanomaterials were used in this study including three different metal oxide (TiO_2, CeO_2, ZnO), three differently sized TiO_2 (6, 13, 23 nm) and three different single walled carbon nanotubes (HiPco-D, SG65-D, P2-D). Wide variation in physicochemical properties among these nanomaterials allowed the comparison among the nanomaterials with respect to size, shape, types, and synthesis methods. The transport studies were investigated over a wide range of solution chemistry including pH, ionic strength, and ion valence. Presence of natural organic matter and bacteria on the transport of nanomaterials were also investigated in this study. Both macroscopic packed-bed column and microscopic flow cell systems were utilized to investigate the transport of nanomaterials.

As discussed in Chapter 2, a handling approach was developed for dispersion of metal oxide nanomaterials in aqueous solution for transport and toxicity studies. This study showed that sonication dispersed the nanoparticles, which reached the optimization after 30 min for initial breakup of dried nanoparticles in water. After certain time, extensive sonication led to reaggregation due to higher collisions. Since aggregation was evident in metal oxide nanoparticles, sonication to achieve a proper dispersion of nanoparticles in solution was necessary prior to further experimentation. No more than 30 s sonication was needed for preparing well dispersed test sample from the diluted stock suspension. TiO_2 or CeO_2 addition reduced pH with the increase of nanoparticle

concentration, whereas pH increased with ZnO concentration. It is concluded from the results in this chapter that consideration of these parameters (effects of sonication, nanoparticle concentration, and solution chemistry) is necessary to ensure successful subsequent toxicity and transport studies.

Chapter 3 highlighted the role of solution chemistry, nanoparticle concentration and hydrodynamic effects in the transport and deposition of TiO_2 nanoparticles through porous media. Two solution chemistry variables, pH and ionic strength, showed a significant influence on the transport due to their involvement in the aggregation of the nanoparticles and interaction with quartz sand. An electrostatically unfavorable condition for deposition existed at pH 7, at which the greatest retention occurred in the column, likely due to aggregation (>1000 nm) and straining effects. Under electrostatically favorable conditions (pH 5) significant elution from the column was observed and attributed to smaller aggregate size (~300 nm) and blocking effects. Nanoparticle concentration was found to contribute to the increased breakthrough of nanoparticles at pH 5 due to blocking and subsequent particle-particle repulsion. Increased flowrate resulted in greater elution of nanoparticles due to hydrodynamic forces acting on aggregates and subsequently contributed to blocking. Breakup of aggregate was observed to lead the higher elution through porous media at high flowrate. Aggregate breakup also showed a significant dependence on solution chemistry. Higher potential for aggregate breakup was observed under favorable condition than unfavorable condition. Overall, a combination of mechanisms including straining, blocking, and

DLVO-type forces were involved over the range of solution chemistry and nanoparticle concentrations tested. Consideration of these mechanisms is necessary for improved removal of TiO_2 nanoparticles via filtration and reliable prediction of transport of these potentially problematic nanoparticles through the subsurface.

Chapter 4 described a novel microscope-based technique to understand the fundamental mechanisms involved in the deposition of TiO_2 nanoparticles in parallel plate chamber. Findings from this study showed that higher deposition of TiO_2 nanoparticles was observed at pH 5 versus pH 7 due to favorable conditions for deposition at pH 5 as compared to pH 7, as predicted by DLVO theory. Additionally, deposition rates at pH 5 were reduced with IS below 10 mM due to the decrease in the range of electrostatic attractive forces. Above 10 mM, aggregate size increased, resulting in higher deposition rates. At pH 7, no deposition was observed below 10 mM and above this concentration, deposition increased with IS. Like the transport results in Chapter 3, the impact of flowrate was also observed, with decreasing flowrate leading to greater deposition due to the reduction in drag force acting on the aggregate (regardless of pH). Comparisons between experimental and theoretical approximations indicate that non-DLVO type forces also play a significant role. Overall these findings from this study suggest that the deposition of these model nanoparticles on the collector surfaces was controlled by a combination of DLVO and non-DLVO-type forces, shear rate, aggregation state, and gravitational force acting on nanoparticles.

Chapter 5 investigated the contributions of natural organic matter (NOM) and bacteria to the aggregation and deposition of TiO_2 nanoparticles in the aquatic environments. Results from both packed-bed column and parallel plate chamber revealed that interactions among TiO_2 nanoparticles, NOM and bacteria exhibited a significant dependence on solution chemistry (pH 5 and 7) and ion valence (K^+ and Ca^{2+}), and that these interactions subsequently affected the deposition of TiO_2 nanoparticles. NOM and *E. coli* significantly reduced deposition of TiO_2 nanoparticles, with NOM having a greater stabilizing influence than bacteria. Ca^{2+} ions played a significant role in these interactions, promoting formation of large clusters of TiO_2 nanoparticles, NOM and bacteria. TNPs transport in the presence of both NOM and *E. coli* resulted in much less deposition than in the presence of NOM or *E. coli* alone, indicating a complex combination of interactions involved in stabilization. Generally, over the aquatic conditions considered, the extent of TNPs deposition follows: without NOM or bacteria > with bacteria only > with NOM only > combined bacteria and NOM. This trend should allow better prediction of the fate of TNPs in complex aquatic systems.

Chapter 6 set out to determine the influence of primary particle size on the aggregate formation and transport of TiO_2 nanoparticles through porous media. The motivation for this study was generated from the vital role of nanoparticle aggregate in transport as observed in Chapters 3,4 and 5. However, so far focus had been on the aggregate size, not how the aggregates were formed. Results indicated that electrokinetic properties of TiO_2 nanoparticles were a function of solution chemistry, but not necessarily sensitive to primary particle size. Aggregation behavior, however,

demonstrated significant dependence on size, with 6 nm TiO_2 nanoparticles forming the largest aggregate. Transport results revealed deposition rates of TiO_2 nanoparticles aggregates composed with three distinctly sized primary nanoparticles were significantly different, despite the similarity in the aggregate size and electrokinetic properties of these particles. Primary particle size influenced transport of the aggregates with a notable dependence on the aggregate size. For small aggregates (<500 nm) under clean bed filtration, the larger the size of the primary particles within the aggregate was, the higher the retention of the aggregates in the porous media was found. For large aggregates (>800 nm), this trend was reverse. This shift in transport trend for large aggregates was attributed to straining or pore blocking in the porous media, which subsequently resulted in breakup of the aggregates. The size of primary nanoparticles was demonstrated to play a significant role on the aggregate breakup process as aggregates formed with larger primary particle size showed higher propensity to breakup during the transport process under straining conditions. Morphology of the aggregates was significantly dependent on primary particle size. Fractal dimension showed a linear relationship with specific surface areas (6 nm < 13 nm < 23nm) indicating that the smallest primary particles formed the most compact aggregates in the aquatic environment. Aggregates formed from the smaller primary particle size appeared to interact with NOM to a greater extent than those formed from the larger primary particles implying that NOM will play an important role in the fate of smaller nanoparticles. Primary nanoparticle affected the aggregate density, surface roughness, hydrodynamic force and strength, which subsequently impacted the transport of TiO_2 nanoparticles aggregates.

Chapter 7 investigated the fate and transport of single walled carbon nanotubes (SWNTs) from synthesis to environmentally relevant conditions. After purification, the residual metal catalyst between the SWNTs follows the trend: HiPco-D > SG65-D > P2-D. The electrophoretic mobility (EPM) and hydrodynamic diameter of SWNTs remained insensitive to SWNT type, pH, and presence of natural organic matter (NOM); but were affected by ionic strength (IS) and ion valence (K^+, Ca^{2+}). In monovalent ions, the hydrodynamic diameter of SWNTs was not influenced by IS, while larger aggregation was observed for HiPco-D with IS than P2-D and SG65-D in the presence of Ca^{2+}. Transport of HiPco-D in the porous media was significantly higher than SG65-D followed by P2-D. Release of HiPco-D from porous media was higher than SG65-D followed byP2-D, though negligible amount of all types of SWNTs (<5%) was released. Both transport and release pattern followed a similar trend to what was observed for residual metal catalysts in SWNTs. Addition of NOM increased the transport of all SWNTs primarily due to electrosteric repulsion. HiPco-D was notably more acidic than SG65-D followed by P2-D, which was similar to transport trend. Overall SWNTs synthesized by different methods resulted in distinctive breakthrough curves attributed to the catalysts used in synthesis, whereas metal content of SWNTs affected the relative elution of SWNTs through column. These findings will allow for the safe design of environmental friendly SWNTs such that they can be generated to be the least mobile in the aquatic environment.

The findings from this dissertation suggest the following critical insights throughout the life cycle of nanomaterials (synthesis to environment): First, the paramount role of synthesis methods and purifications on physicochemical properties and transport of nanomaterials, particularly carbon nanotubes. Second, the influence of handling and preparation approach on the physicochemical properties of metal oxide nanomaterials, which need to be considered for reproducible and consistent transport and toxicity studies. Third, aggregate formation and breakup is the dominant factor in the transport of metal oxide nanoparticles, which is highly sensitive to solution chemistry, nanoparticle physical properties (size, density), hydrodynamic condition and presence of NOM and bacteria.

There are lot of opportunities and challenges ahead which needs to be resolved for environmental regulations as well as sustainable development of nanotechnology. First, nanomaterials are often incorporated in the products with other chemicals and materials or in composite form with multiple nanomaterials. Though this doctoral research investigated nanomaterials individually, future work is needed to understand how these nanomaterials will behave from synthesis to integrated product form. Second, the transformation of nanomaterials will need to be investigated for the long term fate of these advanced materials in the environment. Third, there are substantial challenges ahead in establishing environmental regulations regarding nanomaterials. Particularly, monitoring approaches for nanomaterials in the complex environment will need to be developed. So far most of environmental regulations for contaminants are based on

concentration, the unique size and shape dependent properties of nanomaterials require different regulatory criteria (concentration, size, shape, properties), which can capture the transport and toxicities of nanomaterials.

This doctoral work has clearly demonstrated the fundamental mechanisms involved in the fate, transport and removal of both metal oxide and carbon-based nanomaterials in the aquatic environment. These results have implications in the development of predictive fate and transport model of engineered nanomaterials in the aquatic environment. Findings from this study can also be useful for the future design of removal of nanomaterials via filtration. Finally, this study supports the concept that systematic design of engineered nanomaterials including type (metal oxide, carbon-based), size (three different TiO_2), shape (sphere vs wire), and synthesis methods, can be useful for the future design of environmental friendly nanomaterials by reducing the extent of transport in the aquatic environment, which in turn can reduce exposure.